The final inclusive and semi-inclusive longitudinal double-spin asymmetries at HERMES. Extraction of quark helicity distributions of the nucleon from deep-inelastic scattering.

Der Naturwissenschaftlichen Fakultät

der Friedrich-Alexander-Universität Erlangen-Nürnberg

zur

Erlangung des Doktorgrades

vorgelegt von

Polina Kravchenko

aus Sankt Petersburg, Russland

Als Dissertation genehmigt von der Naturwissenschaftlichen Fakultät der Universität Erlangen-Nürnberg

Tag der mündlichen Prüfung:

Vorsitzender der Promotionskommision:	Prof. Dr. Eberhard Bänsch
Erstberichterstatter:	Prof. Dr. Klaus Rith
Zweitberichterstatter:	Prof. Dr. Michael Thies

Contents

List of Tables vi

List of Figures viii

1 Introduction 1

2 Spin Structure of the Nucleon 4

2.1 Deep Inelastic Scattering . . . 4

2.1.1 Kinematics of the Deep-Inelastic Scattering . . . 4

2.1.2 The Deep-Inelastic Scattering Cross section . . . 8

2.1.3 The photon-nucleon asymmetries . . . 16

2.2 The parton model . . . 18

2.2.1 The simple parton model . . . 18

2.2.2 The spin crisis in the parton model . . . 20

2.3 Semi-Inclusive Deep Inelastic Scattering . . . 23

3 The HERMES experiment 25

3.1 The polarized lepton beam of the HERA storage ring . . . 25

3.2 The internal gas target . . . 26

3.3 The HERMES spectrometer . . . 28

3.3.1 Magnet and tracking detectors . . . 30

3.3.2 Particle IDentification detectors . . . 31

3.4 Data Structure and Data Acquisition System . . . 36

3.4.1 Data structure . . . 36

3.4.2 Data Acquisition and Production . . . 37

4 Data Selection and Particle Identification 39

4.1 Burst-level data selection . . . 39

4.2 Particle identification . . . 41

4.2.1 Discriminating leptons and hadrons . . . 41

4.2.2 Identification of hadrons with the RICH . . . 43

4.3 Event selection . . . 46

4.3.1 Inclusive requirements . . . 46

4.3.2 Geometric requirements . . . 46

4.3.3 Semi-inclusive requirements . . . 48
4.4 Binning . . . 49

5 Double spin asymmetries **52**
5.1 Determination of the double-spin asymmetries . . . 52
5.1.1 Correction of yields . . . 54
5.2 Extraction of Born asymmetries . . . 55
5.2.1 Smearing correction and QED radiative correction . . . 56
5.2.2 Acceptance correction . . . 61
5.3 Systematic uncertainties . . . 67
5.3.1 Polarization . . . 67
5.3.2 RICH unfolding . . . 70
5.3.3 Azimuthal correction . . . 70
5.4 Results . . . 71
5.4.1 $A_1(x)$ . . . 71
5.4.2 3D asymmetries $A_1(x, z, p_{\perp h})$ . . . 72
5.4.3 $A_1(x, p_{\perp h})$ . . . 72
5.4.4 2D asymmetries $A_1(x, Q^2)$ . . . 79
5.4.5 Hadron charge difference asymmetries . . . 84
5.4.6 Comparison of result to COMPASS experiment . . . 91

6 Quark Helicity Distributions **92**
6.1 Formalism of Helicity-Distribution Extraction . . . 92
6.2 Extraction of the Purities . . . 95
6.3 Systematic studies on the purity uncertainties. . . . 99
6.3.1 The influence of the spectrometer acceptance on the purities . . . 100
6.3.2 NLO effects . . . 100
6.3.3 Dependence of purities on fragmentation functions . . . 100
6.4 Systematic studies on the quark polarizations . . . 103
6.5 Results . . . 109
6.5.1 The quark polarizations $\Delta q/q$: 3D extraction . . . 109
6.5.2 The quark polarizations . . . 113
6.5.3 The polarized parton densities . . . 115
6.5.4 Comparison with theoretical prediction . . . 115
6.5.5 Final result for quark helicity distributions . . . 115
6.6 The Hadron-Charge-Difference-Asymmetry Method . . . 118
6.6.1 The hadron-charge-difference asymmetry. Formalism. . . . 118
6.6.2 Determination of moments of the distributions . . . 122

7 Conclusions **126**

8 Zusammenfassung **128**

A Results: Asymmetries $A_1(x)$ **130**

B Results: Asymmetries $A_1(x, p_{h\perp})$ **137**

C Results: Asymmetries $A_1(x, z, p_{h\perp})$ **141**

D Results: Asymmetries $A_1(x, Q^2)$ **154**

E Hadron charge difference asymmetry **160**

Bibliography **162**

List of Tables

1.1 Overview of investigations of the nucleon structure 3

2.1 A legend of kinematic quantities used in the description of deep-inelastic charged-lepton nucleon scattering. 7

3.1 Refractive indices and Čerenkov light thresholds of the RICH 32

4.1 Burst-level data quality requirements. 40
4.2 Beam, target and Čerenkov detector type for each year of HERMES running. 43
4.3 Inclusive kinematic requirements. 47
4.4 Geometric requirements for inclusive and semi-inclusive events. 48
4.5 Semi-inclusive requirements. 49
4.6 Count numbers of DIS leptons and SIDIS hadrons for the hydrogen and deuterium data. 50

5.1 Kinematics of final state radiation. 56
5.2 Fractional uncertainties of beam and target and their quadratic sum by year 70
5.3 The value of χ^2 for each functional form fit to the $A_1(x, p_{h\perp})$ data points for each target–final-state-hadron combination. 80

6.1 First moments of various helicity distributions in the measured range at a scale of $Q^2 = 2.5\ GeV^2$. 125

A.1 1-Dimensional x binning. 130
A.2 Inclusive Born level asymmetries on the proton target 131
A.3 Inclusive Born level asymmetries on the deuteron target 131
A.4 Born level asymmetries for hadrons on the proton target 132
A.5 Born level asymmetries for pions on the proton target 133
A.6 Born level asymmetries for hadrons on the deuteron target 134
A.7 Born level asymmetries for pions on the deuteron target 135
A.8 Born level asymmetries for kaons on the deuteron target 136

B.1 2-Dimensional $x - p_{h\perp}$ binning. 137
B.2 Semi-Inclusive Born level asymmetries for positive and negative pions on the proton target 138

B.3 Semi-Inclusive Born level asymmetries for positive and negative pions on the deuteron target . . . 139
B.4 Semi-Inclusive Born level asymmetries for positive and negative kaons on the deuteron target . . . 140

C.1 The bin edges for z and $p_{h\perp}$ added to form a 3D binning . . . 141
C.2 Born level asymmetry for positive pions on the proton target . . . 142
C.3 Born level asymmetries for negative pions on the proton target . . . 144
C.4 Born level asymmetries for positive pions on the deuteron target . . . 146
C.5 Born level asymmetries for negative pions on the deuteron target . . . 148
C.6 Born level asymmetries for positive kaons on the deuteron target . . . 150
C.7 Born level asymmetries for negative kaons on the deuteron target . . . 152

D.1 2-Dimensional $x - Q^2$ binning. . . . 154
D.2 Semi-Inclusive Born level asymmetries for positive and negative hadrons on the proton target . . . 155
D.3 Semi-Inclusive Born level asymmetries for positive and negative pions on the proton target . . . 156
D.4 Semi-Inclusive Born level asymmetries for positive and negative hadrons on the deuteron target . . . 157
D.5 Semi-Inclusive Born level asymmetries for positive and negative pions on the deuteron target . . . 158
D.6 Semi-Inclusive Born level asymmetries for positive and negative kaons on the deuteron target . . . 159

E.1 Pions charge difference asymmetry on the proton target . . . 160
E.2 Hadrons charge difference asymmetry on the deutron target . . . 161
E.3 Pions charge difference asymmetry on the deutron target . . . 161
E.4 Kaons charge difference asymmetry on the deutron target . . . 161

List of Figures

2.1 Sketch of the deep-inelastic scattering process in the one-photon approximation as seen in the laboratory system. The definitions of the kinematic variables are summarized in Tab. 2.1. 5

2.2 As the energy of the virtual photon increases, increasingly small sub-structures (partons) can be resolved. 6

2.3 An overview of the proton structure function F_2^p [33] measured in lepton-proton scattering with positrons by HERMES, the collider experiments (H1 and ZEUS) in the kinematic domain of HERA for $x > 0.00006$, and for electrons (SLAC, JLAB[31]) and muons (BCMS, NMC and E665). The world data of F_2^p is compared to phenomenological parameterizations. The Q^2 dependence of F_2^p is shown in bins of x. The values of F_2^p were scaled by powers of 1.6. 11

2.4 The world data of F_2^d is compared to the SMC phenomenological parameterization[32]. The Q^2 dependence of F_2^d is shown in bins of x. The values of F_2^d were scaled by powers of 1.6. 12

2.5 The ratio of longitudinal and transverse cross sections $R = \sigma_L/\sigma_T$ as a function of x in three ranges of Q^2. The solid line shows the parameterization R1998[34]. Also shown are measurements from various experiments. The dashed lines show the results of a next-to-next-to-leading order calculation in perturbative QCD. 13

2.6 The definition of angles. Here $\vec{k}$ and $\vec{k}'$ are momentum vectors of the incoming and scattered lepton respectively. Angles θ and ϕ represent the polar angle with respect to $\vec{k}$ and azimuthal angle which is defined by an angle between scattering plane and polarization plane. 14

2.7 The spin-dependent structure function $xg_1(x)$ of the proton and deuteron shown on separate panels measured as a function of x in deep inelastic scattering of polarized electrons/positrons. The HERMES result [14] is compared to the data from SMC [36][37][38], E143[39], E155[40][41], and COMPASS[16]. The error bars represent the sum in quadrature of statistical and systematic uncertainties. For the HERMES data the closed (open) symbols represent values derived by selecting events with $Q^2 > 1\ GeV^2$ ($Q^2 < 1\ GeV^2$). 15

2.8 Top panel : xg_1^n from data for g_1^p and g_1^d, compared with similar data from SMC [36],[37],[38], E143 [39], E155 [40],[41] in the HERMES x-range. Middle panel: xg_1^n as obtained from a ^3He target by JLab [20], HERMES [42], E142 [43] and E154 [44]. Bottom panel: average Q^2 versus x. For the HERMES data the closed (open) symbols represent values derived by selecting events with $Q^2 > 1\ GeV^2$ ($Q^2 < 1\ GeV^2$). 16
2.9 Schematic diagram of the polarizad DIS in Quark Parton Model. The arrows indicate the spins of the virtual photon, the partons and the nucleon. 17
2.10 Visualization of parton density $q(\xi)$. 19
2.11 Lepton-quark elastic scattering. 20
2.12 Visualization of the longitudinally polarized parton density $\Delta q(x)$. The upper arrows show the spin direction. 21

3.1 Sketch of the HERA facility at DESY 26
3.2 Example for a measurement of the polarization build-up of the HERA positron beam as measured by both the Transverse and the Longitudinal Polarimeter. 27
3.3 Diagram of the target chamber. 28
3.4 Schematic view of the HERMES spectrometer. 29
3.5 Front scheme of HERMES spectrometer: the angular acceptance is limited in the azimuthal angle ϕ by the blue dotted lines, and in the polar angle θ by the red dotted circles. 30
3.6 A perspective view of the upper RICH detector setup. 32
3.7 Distribution of reconstructed angles in the HERMES RICH. The upper triplet of curves corresponds to aerogel events, and the lower to gas events. From left to right the contours in each case are for π, K and p. 33
3.8 Side view of the TOP half of the TRD: when an electron track and a pion track pass through the six modules of the TRD, only the electron is emitting transition radiation photons. 34
3.9 Responses of three PID detectors: Number of counts for positrons (empty histograms) and hadrons (shaded histograms) in TRD, hodoscope H2 and the calorimeter. 35
3.10 Overview of the preshower and the calorimeter. 36

4.1 A 3-dimensional view of the positron-hadron separation due to all the four PID detectors. 42
4.2 The p-matrix represents the conditional probability that a hadron of true type h_t will be identified by the RICH as type h_i. The momenta p_h are given in GeV. 44
4.3 The distribution of the selected DIS events in the $x - Q^2$ plane. 47

5.1 DIS process in first order QED (Born level). The scattering kinematics are well defined by the properties of the incident and scattered electron. 55
5.2 Second order QED radiative corrections for the DIS process. 57
5.3 Diagram of final state radiation. The diagram illustrates the emission of an undetected photon with energy ω before the detection of the scattered lepton. 58

5.4 Migration matrices for a pure x binning. The matrices were extracted from a fully reconstructed Monte Carlo data set simulating both QED radiative and detector effects for inclusive (left panel) DIS and semi-inclusive production of positive pions (right panel) on a proton target. 59
5.5 Monte Carlo asymmetries for the proton in HERMES acceptance (red triangles) and in 4π (green diamonds). The black points represent the differences in the asymmetries $\Delta A_1 = A_1^{acc} - A_1^{4\pi}$ which can be attributed entirely to the difference in average kinematics. 62
5.6 Monte Carlo asymmetries for the deuteron in HERMES acceptance (red triangles) and in 4π (green diamonds). The black points represent the differences in the asymmetries $\Delta A_1 = A_1^{acc} - A_1^{4\pi}$ which can be attributed entirely to the difference in average kinematics. 63
5.7 Definition of azimuthal angle of the hadron ϕ (here named ϕ_h) for semi-inclusive deep inelastic scattering in the target rest frame. $P_{h\perp}$ is the transverse part of P_h with respect to the photon momentum. 64
5.8 Comparison of 4π Born Monte Carlo samples with and without $\cos(\phi)$ weighting. Asymmetries for charged pions from the proton target and both pions and kaons from the deuteron target are shown. Since there is no ϕ-dependent acceptance included, the cosine moments of the unpolarized cross section integrate out over the full ϕ range. . . 68
5.9 Comparison of Born Monte Carlo samples with and without $\cos(\phi)$ weighting in acceptance. Unlike the 4π comparison shown in Fig. 5.8, the nonuniform acceptance of the spectrometer in ϕ creates significant differences between the weighted and unweighted asymmetries. The azimuthal correction factor C_ϕ^h, which is simply the ratio of the two asymmetries, is also shown. 69
5.10 The inclusive and semi-inclusive Born level asymmetries on the proton, corrected for instrumental smearing and QED radiative effects. The error bars give the statistical uncertainties, and the colored bands indicate the systematic uncertainty. 73
5.11 The inclusive and semi-inclusive Born level asymmetries on the deuteron, corrected for instrumental smearing and QED radiative effects. The error bars give the statistical uncertainties, and the colored bands indicate the systematic uncertainty. Black triangles and the lowermost bands are taken from the COMPASS publication[85]. 74
5.12 The charged hadrons Born level asymmetries for both targets , corrected for instrumental smearing and QED radiative effects. The error bars give the statistical uncertainties, and the colored bands indicate the systematic uncertainty. 75
5.13 The inclusive and semi-inclusive Born level asymmetries on the proton in comparison with previous published HERMES result. 76
5.14 The charged hadrons Born level asymmetries for both targets in comparison with previous published HERMES result. 77
5.15 The inclusive and semi-inclusive Born level asymmetries on the deuteron in comparison with previous published HERMES result. 78
5.16 $A_1(x, p_{h\perp})$ for charged pion production for proton and deuteron targets and charge kaon production for deuteron target, in three different x ranges. 80

5.17 Final result for $A_1(x, p_{\perp h})$ fit with a simple linear function in x (dashed) with no $p_{h_\perp}$ dependence. Each fit curve is bounded by a 1-σ error band of the same color. The small solid rectangles represent the systematic uncertainty for the associated data point. The reduced χ^2 values given suggest that this parameterization is adequate to describe the data. 81
5.18 Final result for $A_1(x, p_{\perp h})$ fit with a simple linear function in x (dashed) with no $p_{h_\perp}$ dependence. Each fit curve is bounded by a 1-σ error band of the same color. The small solid rectangles represent the systematic uncertainty for the associated data point. The reduced χ^2 values given suggest that this parameterization is adequate to describe the data. 82
5.19 Final result for $A_1(x, p_{\perp h})$ fit with a simple linear function in x (dashed) with no $p_{h_\perp}$ dependence. Each fit curve is bounded by a 1-σ error band of the same color. The small solid rectangles represent the systematic uncertainty for the associated data point. The reduced χ^2 values given suggest that this parameterization is adequate to describe the data. 83
5.20 The pion-charge-difference asymmetry $A_{1p}^{\pi^+-\pi^-}$ for the proton target. The error bars give the statistical uncertainties, and the colored band indicates the systematic uncertainty. 84
5.21 The hadron-charge-difference asymmetry $A_{1d}^{h^+-h^-}$ for the deuteron target. The error bars give the statistical uncertainties, and the colored band indicates the systematic uncertainty. The difference between Fig. 5.29 and this plot is that also protons and antiproton are included. 85
5.22 The pion-charge-difference asymmetry $A_{1d}^{\pi^+-\pi^-}$ for the deuteron target. The error bars give the statistical uncertainties, and the colored band indicates the systematic uncertainty. 86
5.23 The kaon charge-difference asymmetry $A_{1d}^{K^+-K^-}$ for the deuteron target. The error bars give the statistical uncertainties, and the colored band indicates the systematic uncertainty. 86
5.24 Migration matrices $n_{\rightarrow\Rightarrow}^{\pi^+}$ (top left) and $n_{\rightarrow\Leftarrow}^{\pi^+}$ (top right) and smearing matrices $S_{\rightarrow\Rightarrow}^{\pi^+}$ (bottom left) and $S_{\rightarrow\Leftarrow}^{\pi^+}$ (bottom right) 87
5.25 Migration matrices $n_{\rightarrow\Rightarrow}^{\pi^-}$ (top left) and $n_{\rightarrow\Leftarrow}^{\pi^-}$ (top right) and smearing matrices $S_{\rightarrow\Rightarrow}^{\pi^-}$ (bottom left) and $S_{\rightarrow\Leftarrow}^{\pi^-}$ (bottom right) 87
5.26 Differences of migration matrices $n_{\rightarrow\Rightarrow}^{\pi^+} - n_{\rightarrow\Rightarrow}^{\pi^-}$ (top left) and $n_{\rightarrow\Leftarrow}^{\pi^+} - n_{\rightarrow\Leftarrow}^{\pi^-}$ (top right) and differences of smearing matrices $S_{\rightarrow\Rightarrow}^{\pi^+} - S_{\rightarrow\Rightarrow}^{\pi^-}$ (bottom left) and $S_{\rightarrow\Leftarrow}^{\pi^+} - S_{\rightarrow\Leftarrow}^{\pi^-}$ (bottom right) 89
5.27 Migration matrices $n_{\rightarrow\Rightarrow}^{\pi^+-\pi^-}$ (top left) and $n_{\rightarrow\Leftarrow}^{\pi^+-\pi^-}$ (top right) and smearing matrices $S_{\rightarrow\Rightarrow}^{\pi^+-\pi^-}$ (bottom left) and $S_{\rightarrow\Leftarrow}^{\pi^+-\pi^-}$ (bottom right) 89
5.28 Difference of smearing matrices $S_{\rightarrow\Rightarrow}^{\pi^+} - S_{\rightarrow\Rightarrow}^{\pi^+-\pi^-}$ (top left) and $S_{\rightarrow\Leftarrow}^{\pi^+} - S_{\rightarrow\Leftarrow}^{\pi^+-\pi^-}$ (top right), $S_{\rightarrow\Rightarrow}^{\pi^-} - S_{\rightarrow\Rightarrow}^{\pi^+-\pi^-}$ (bottom left) and $S_{\rightarrow\Leftarrow}^{\pi^-} - S_{\rightarrow\Leftarrow}^{\pi^+-\pi^-}$ (bottom right) 90
5.29 The hadron charge-difference asymmetry for deuteron target in comparison with the COMPASS result. 91

6.1 A schematic diagram of the generation of purities. 94
6.2 Purities in x-bins for the proton target (solid black circles) and deuteron target (solid red triangles) for each quark and asymmetry type for $Q^2 > 1\ GeV^2$. The tuned LUND fragmentation model and the CTEQ6L parameterization of the unpolarized quark distributions have been used in the MC for the generation of the extracted events. Each column corresponds to scattering off a certain quark flavor. Note: for strange quarks (last two columns) the values of purities are increased by a factor of 4. In addition, open symbols show the purities for the range $Q^2 < 1\ GeV^2$. 96
6.3 Comparison of pion and kaon purities evaluated in the HERMES acceptance (black circles) and in 4π (red triangles) for a proton target. The blue open crosses show the ratio of two purity sets. Note: for strange quarks (last two columns) the values of purities are increased by a factor of 4. 97
6.4 The differences between the purity for the proton target calculated using the standard HERMES MC and three purity sets : "LO" (black open circles), "GRV" (red triangles) and "CTEQ modif" (red open triangles). The details are described in the text. For comparison of the differences and the mean values of the purity, black full points represent the purity itself. 98
6.5 Same as for Fig. 6.4 on the deuteron target 99
6.6 Purities for the proton target computed analytically using CTEQ6LO and two fragmentation function parameterizations (Kretzer[74](red dashed line) and Sassot[75](blue solid line)) compared with the HERMES MC-based purities(black points) used in this analysis. 101
6.7 Same as for Fig. 6.6 for the deuteron target 102
6.8 The quark polarizations extracted using the analytic purities based on the Kretzer FFs (left) and the Sassot FFs (right) times the CTEQ6LO PDFs varied to the upper and lower edges of their error bars. The red triangles and blue squares were offset in x for presentation. Note: for sea quarks the last three x points are not shown, due to the huge error bars. 104
6.9 Quark polarizations computed from HERMES MC purities (black circles) and from analytically extracted purities with Kretzer FF (red triangles) and Sassot FF (blue squares). The red and blue points were offset in x for presentation. 105
6.10 The ratio of the uncertainties of the quark polarizations computed from analytically extracted purities with Kretzer FFs (red stars), with Sassot FFs (blue crosses) and from HERMES MC purities. 106
6.11 Quark polarizations computed assuming zero anti-strange polarization $\Delta\bar{s}(x) = 0$ (black circles) and computed with no assumption on the strange sea (red triangles). The error bars show the statistical uncertainties. The red points were offset in x for presentation. Note: last three x points for sea quarks are not shown, because their uncertainties are large. 107
6.12 The difference (blue crosses) and the ratio (red stars) of quark polarizations computed with and without the inclusive asymmetries. 108

6.13 Purity in x-bins for the deuteron target. At each x position there are nine points, representing each of the nine $z - p_{\perp h}$ bin combinations. The "leading", high-z-low-$p_{\perp h}$ is plotted in red circles, the "remnant", low-z-high-$p_{\perp h}$, is plotted in blue triangles, and the "central", middle bin of each semi-inclusive variable, is plotted in black squares. All other combinations are shown in gray open circles. 110

6.14 Purity in x-bins for the deuteron target. Only five of the nine x-bins are shown in order to make space for points representing all nine semi-inclusive bins. Three z bins are shown in different colors and symbols: $0.1 < z < 0.35$ (blue triangles), $0.35 < z < 0.5$ (black squares) and $0.5 < z < 0.8$ (red circles). The increasing of the size of the each type of symbols demonstrates $p_{\perp h}$ dependence of purities. The first $p_{\perp h}$-bin ($0.0\ GeV < p_{\perp h} < 0.3\ GeV$) is shown using small symbols, the second bin ($0.3\ GeV < p_{\perp h} < 0.5\ GeV$) is shown with the middle symbols. The large symbols represent the third ($0.5\ GeV < p_{\perp h} < 2.0\ GeV$) bin. 111

6.15 Comparison between 1D and 3D $\Delta q/q$. The ratio of the uncertainties $\delta(\Delta q/q)_{3D}/\delta(\Delta q/q)_{1D}$ (blue crosses) shows the improvement of errors at low x for u and d-quarks and at high x for sea quarks. 112

6.16 The result of polarizations of the quark flavors in the proton for $Q^2 > 1\ GeV^2$ (red squares) and for $Q^2 < 1\ GeV^2$ (red open circles) using the 3D extraction method as a function of x. The published HERMES result[13] (black circles) is shown for comparison. The error bars represent the statistical uncertainties. The upper red bands show the systematic uncertainties due to the using of assumption on the sea quarks, the error on the unpolarized PDFs and the uncertainties on the asymmetries. For the low Q^2 points and for two last x points the systematic uncertainties are not shown (see text). The lower black bands are the published systematic uncertainties. 114

6.17 The x-weighted helicity distributions from the data for $Q^2 < 1\ GeV^2$ (black circles) and $Q^2 > 1\ GeV^2$ (red squares). The error bars show the statistical uncertainties. Systematic uncertainties are not shown. The data are shown together with the theoretical prediction from the GRSV2000 parameterization[79] for various Q^2 values scaled with $\frac{1}{1+R}$. 116

6.18 The quark helicity distributions $x\Delta q(x)$ for $Q^2 > 1\ GeV^2$ (red squares) and $Q^2 < 1\ GeV^2$ (red open circles) regions evaluated at a common value of $Q^2 = 2.5\ GeV^2$ as a function of x from 3D extraction method are shown in comparison with previous HERMES published result (black circles). The systematic errors are displayed separately as the upper red band. For low Q^2 points and for the sea-quark helicity distributions for two last x points (red open squares) the systematic uncertainties are not shown. The lower black bands are the published systematic uncertainties. 117

6.19 Left panel: The pion-charge-difference asymmetry $A_{1p}^{\pi^+-\pi^-}$ (red circles) from proton data in comparison with values for $\frac{4\Delta u_v(x)-\Delta d_v(x)}{4u_v(x)-d_v(x)}$ extracted from the purity method (black squares). Right panel: the combined pion and kaon charge difference asymmetry $A_{1d}^{K^+(\pi)^+-K^-(\pi)^-}$ (red circles) in comparison with extracted from the purity method values for $\frac{\Delta u_v(x)+\Delta d_v(x)}{u_v(x)+d_v(x)}$ from deuteron data. The error bars show the statistical uncertainties. Systematical uncertainties for asymmetries are shown as a red bands. Systematical uncertainties for the purity method are omitted. 118

6.20 Polarized valence quark distributions computed from the charge difference asymmetries (red circles) at $Q^2 = 2.5\ GeV^2$. For comparison, the same densities extracted with the purity algorithm (black squares) are shown slightly offset in x. The error bars represent the statistical uncertainties. 121

6.21 Top: Polarized valence quark distribution $x(\Delta u_v(x) + \Delta d_v(x))$ (red circles) evolved to $Q^2 = 2.5\ GeV^2$ according to the DNS fit at LO[75] (line) in comparison with the result obtained from the purity method (black squares). The four additional points (red open circles) at high x are obtained from g_1^d[14]. Bottom: The integral of $\Delta u_v(x) + \Delta d_v(x)$ over the range $0.023 \leq x \leq 0.9$ as a function of the lower x limit, evaluated at $Q^2 = 2.5\ GeV^2$. 124

“ To my family ”

—

" for more recipes visit http://particleadventure.org/index.html "

—

Chapter 1

Introduction

Throughout the last 40 years the spin structure of the nucleon is one of the intensively discussed topics in particle physics. While spin-independent effects of lepton scattering on a nucleon have been well studied, there are still many open questions in the understanding of spin-dependent processes. The structure of nucleons is described in the Standard Model of particle physics. In this model, the electron is one of six elementary leptons - the electron, the muon, the tau and three corresponding neutrinos. The nucleons are composite particles of quarks. There are six different types of quarks or quarks flavors - up (u), down (d), strange (s), charm (c), bottom (b), and top (t). Leptons and quarks and their corresponding anti-particles are fermions, they interact through the exchange of gauge bosons. Neutrinos interact only weakly. Quarks are subject to the electro-weak interaction and the strong interaction that is mediated by the gluon. Nucleons are composed of three valence quarks (proton: uud, neutron:udd) which exchange gluons that can fluctuate into quark/anti-quark pairs, the sea-quarks.

For high-energy processes, which probe the structure and interaction of particles at short distances, the interplay of the quarks and gluons is well described in the framework of **Q**uantum **C**hromo **D**ynamics (QCD), the quantum field theory of the strong interaction. The strong force becomes weaker at short distances and vanishes in the limit of zero distance, a feature called asymptotic freedom. At high energies the strong coupling constant is small enough to allow the calculation of QCD processes by perturbative expansions. However, at low energies the perturbative expansions diverge due to the rise of the coupling constant. Thus QCD does not allow quantitative predictions for processes like confinement of quarks inside hadrons.

Like the quarks, a nucleon is a fermion characterized by a spin-expectation value of 1/2 in units of $\hbar$. Spin is a very important quantity as it poses symmetry requirements on the wave function used to describe a particle in quantum mechanics. In a naive model the nucleon is composed of only three valence quarks, which are bound together by gluons. The total spin of the nucleon could be explained by the simple vector sum of the spins of the three valence quarks. This model also describes the measured magnetic moments of the proton and the neutron remarkably well. First experiments that investigated the spin structure of the nucleon

were carried out at SLAC [4], verifying theoretical expectations in principle. However, the subsequent CERN experiment (EMC) measured the contribution by the quark spins to the spin of the nucleon to be close to zero [5], contrary to the naive model expectation. This result became known as the "proton spin crisis".

In a general approach, the spin of the nucleon can be decomposed into contributions from quark and gluon spins and orbital angular momenta. In a system where the nucleon moves with very high longitudinal momentum they represent the individual terms in the sum rule for the helicity s_z^N of the nucleon:

$$s_z^N/\hbar = \frac{1}{2} = \frac{1}{2}\Delta\Sigma + \Delta g + L_z^q + L_z^g. \tag{1.1}$$

Neglecting heavy quarks,

$$\Delta\Sigma = \Delta u + \Delta\bar{u} + \Delta d + \Delta\bar{d} + \Delta s + \Delta\bar{s} \tag{1.2}$$

is the contribution from the quarks spins, Δg is the component due to the gluon spin, and L_z^q and L_z^g are the orbital angular momenta of the quarks and the gluons, respectively.

The HERMES experiment is a second generation experiment designed to investigate the contribution of quark spins to the nucleon in detail [19]. HERMES was one of the four experiments at the HERA electron-proton collider at DESY. It used the high current longitudinally polarized electron beam of HERA with a beam energy of about 27.6 GeV together with polarized and unpolarized gas targets internal to the storage ring.

This thesis focuses on two aspects of the HERMES data analysis: the measurement of the semi-inclusive double spin asymmetries and the extraction of quark helicity distributions and quark polarizations, as a possible interpretation of the HERMES data. The asymmetries from the 1996-2000 dataset (Run I) are presented using all possible and accessible information about the HERMES data, including the latest systematic studies provided during the last years by HERMES collaboration.

The outline of this thesis is as follows: In Chapter 2, the framework of deep-inelastic scattering and the quark parton model are reviewed. The HERMES experiment is described in the following part. Chapter 4 describes the data selection and particle identification. The measurement of the asymmetries and the asymmetries, including the corrections and systematic studies, are presented in Chapter 5. The extraction of quark polarizations and quark helicity distributions is described and the result is compared to theoretical prediction in Chapter 6. Conclusions are given in Chapter 7.

Table 1.1: Overview of investigations of the nucleon structure

Theory			
Year	Theorist	Prediction	Ref.
1964	Gell-Mann and Zweig	Quark Model: proposed independently by Gell-Mann and Zweig	[1]
1969	Feynman	Parton Model: the nucleon is constructed by pointlike constituents.	[3]
1972	Feynman	Quark Parton Model: charged parton are quarks.	[6]
1973	Ellis and Jaffe	Sum Rule: $\int dx g_1(x) \simeq 0.2$	[9]
Experiment			
Year	Collaboration	Main Results	Ref.
1950s		A number of new particles were discovered.	
1969	SLAC	(Weak Q^2 dependence of DIS cross section with increasing Q^2.) Scaling of unpolarized structure function.	[7, 8]
1976,1978	SLAC E80	Measurement of double spin asymmetries in polarized DIS.	[4, 10]
1983	SLAC E130	Result consistents with the Ellis-Jaffe Sum Rule.	[11]
1988	EMC	Spin crisis: The contribution of quark spin to the nucleon spin is only $\sim 12\%$ of the nucleon spin.	[5, 12]
1995-	HERMES, DESY	Measurement of inclusive and semi-inclusive double spin asymmetries in polarized DIS. First extractions of quark helicity distribution functions. Precise determination of the spin structure function g_1.	[13, 14]
	COMPASS, CERN	Measurement of inclusive double spin asymmetry A_1^d and structure function g_1^d.	[15, 16]
	JLAB Hall A	Measurement of the neutron spin asymmetries and spin-dependent structure functions in the valence quark region.	[20]

Chapter 2

Spin Structure of the Nucleon

2.1 Deep Inelastic Scattering

Deep-inelastic lepton-nucleon scattering (DIS) can be used to investigate the structure of the nucleon. In first order QED, the DIS process is described by one-photon exchange[1]. Figure 2.1 shows a schematic view of the DIS process. An incoming charged lepton $l = e^{\pm}$ interacts with a nucleon N in such a way that the nucleon is broken up and forms a final hadronic state X,

$$\ell + N \rightarrow \ell^{'} + X. \tag{2.1}$$

Here ℓ and $\ell^{'}$ are the incident and the scattered lepton respectively, N is the nucleon and X is the final hadronic state. DIS experiments in which only the final state electron is detected are referred to as *inclusive*. Additional information becomes available in *semi-inclusive* DIS (SIDIS), where a final state hadron h is detected in coincidence with the scattered lepton:

$$\ell + N \rightarrow \ell^{'} + h + X. \tag{2.2}$$

2.1.1 Kinematics of the Deep-Inelastic Scattering

The kinematic quantities used to describe the DIS process are defined in Table 2.1. The DIS process can be characterized by two independent kinematic variables. In this thesis mainly the

[1]The DIS process is mediated by the exchange of a virtual boson (γ^*, Z^0) between the charge lepton and one of the partons inside the target nucleon.
At HERMES, where the center-of-mass energy $\sqrt{s} \sim 7.3\ GeV$ is small compared to the Z-boson mass, the contributions due to the weak interaction can be neglected, the dominant process is one-photon exchange.

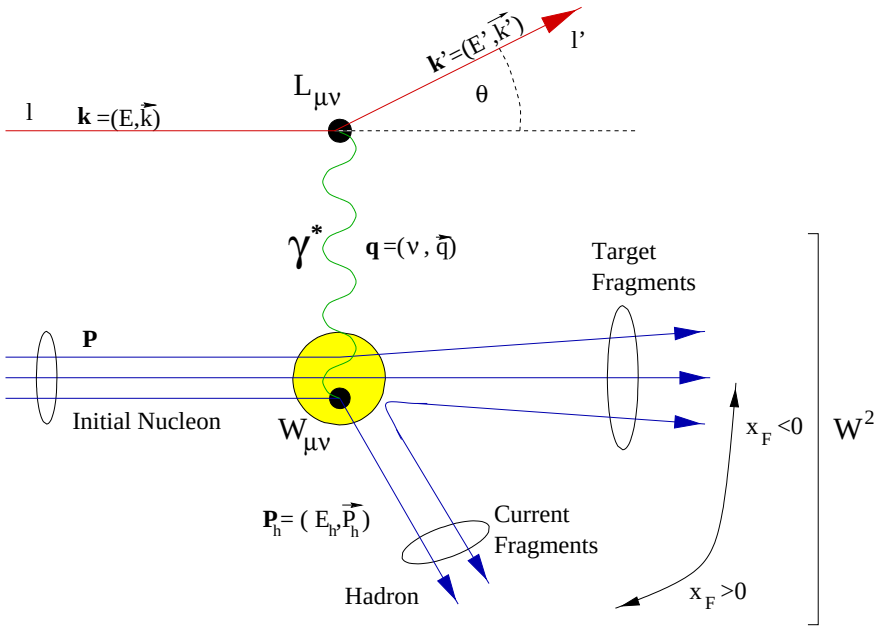

Figure 2.1: Sketch of the deep-inelastic scattering process in the one-photon approximation as seen in the laboratory system. The definitions of the kinematic variables are summarized in Tab. 2.1.

following two variables are used[2]:

$$Q^2 = -q^2 = -(k - k')^2 \stackrel{lab}{=} 4EE' sin^2\frac{\theta}{2}, \tag{2.3}$$

$$x = \frac{Q^2}{2P \cdot q} = \frac{Q^2}{2M\nu}, \tag{2.4}$$

where $k \stackrel{lab}{=} (E, \vec{k})$ and $k' \stackrel{lab}{=} (E, \vec{k'})$ are the four-momenta of the incoming and the scattered lepton respectively, θ is the polar angle of the scattered lepton in the laboratory system and M is the mass of the nucleon. In Eq. 2.4 P and q are the four momenta of the target nucleon and the virtual photon exchanged between the lepton and the nucleon, and ν is the energy transfer to the target

$$\nu = \frac{P \cdot q}{M} \stackrel{lab}{=} E - E'. \tag{2.5}$$

The negative squared invariant mass of the virtual photon, Q^2 (Eq. 2.3), is the measure of the spatial resolution in the scattering process. In analogy to diffraction in optics, the virtual photon can resolve objects whose extension perpendicular to the direction of the photon is comparable to or larger than the reduced wavelength λ of the photon. This quantity λ is not Lorentz-invariant, but depends on the reference frame. In the *Breit* frame, where no energy is transfered from the virtual photon to the target ($\nu = 0$), the reduced wavelength of the virtual

[2]Since the energies of incident and scattered leptons are large compared to their mass, the lepton mass may be neglected. This approximation is used in the derivation of the DIS kinematic quantities listed in Table 2.1

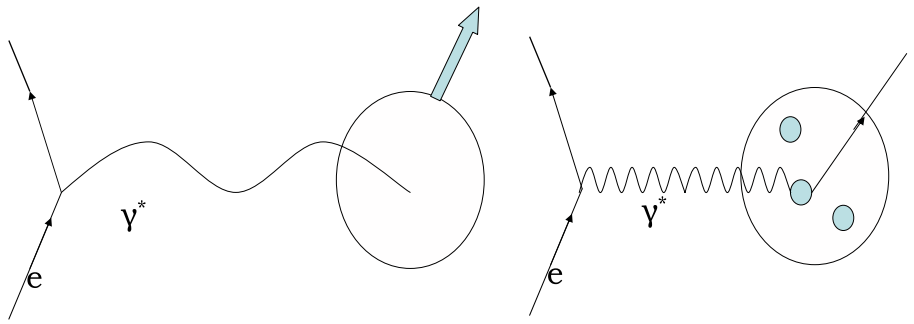

Figure 2.2: As the energy of the virtual photon increases, increasingly small substructures (partons) can be resolved.

photon is simply given by:

$$\lambda\!\!\!^{-} = \frac{1}{|\vec{q}|} \stackrel{\nu=0}{=} \frac{1}{\sqrt{Q^2}}. \tag{2.6}$$

Figure 2.2 is a cartoon illustration of *ep* scattering in two different Q^2 regimes. If Q^2 is significantly smaller than 1 GeV^2 (a scale comparable with *size* of the proton), the nucleon is probed as a whole. The right panel of Figure 2.2 shows a large-Q^2 probe in which the virtual photon has wavelength small enough to resolve the individual elements of the nucleon's substructure. The dimensionless variable x is called *Bjorken scaling variable* (Eq. 2.4), and is a measure of the inelasticity of the scattering process. The squared center-of-mass energy W^2 of the photon-nucleon system is given by

$$W^2 = (P+q)^2 = M^2 + 2P\cdot q - Q^2 = M^2 + 2M\nu - Q^2. \tag{2.7}$$

In an elastic scattering process the target nucleon remains intact and, consequently, the squared mass of the final state (see Tab. 2.1) is equal to the squared nucleon mass $W^2 = M^2$. This results in $2M\nu = Q^2$ or $x = 1$. For inelastic processes, when the target breaks up, the mass of the final hadronic state is larger than the target mass, $W^2 > M^2$ and $0 < x < 1$.

The second dimensionless variable y is the fractional energy transfer from the incident lepton to the target nucleon ($0 \leq y \leq 1$):

$$y = \frac{P\cdot q}{P\cdot k} \stackrel{lab}{=} \frac{\nu}{E}. \tag{2.8}$$

In semi-inclusive scattering processes, additional kinematic variables are required for each detected hadron. The dimensionless variable z gives the fractional energy of the virtual photon, carried by the detected hadron. The *Feynman scaling variable* $x_F \simeq 2P^*_{||}/W$ is defined in the center-of-mass system of the virtual photon and the nucleon, where $P^*_{||}$ is the hadron's longitudinal momentum with respect to the virtual-photon momentum in the photon-nucleon center-of-mass system. The kinematically allowed ranges for the above quantities are $0 \leq z \leq 1$ and $-1 \leq x_F \leq 1$. In this thesis mainly z is used.

Table 2.1: A legend of kinematic quantities used in the description of deep-inelastic charged-lepton nucleon scattering.

Initial and scattered leptons	
$k^\mu \stackrel{lab}{=} (E, \vec{k})$	Four-momentum of the incident lepton
$k'^\mu \stackrel{lab}{=} (E, \vec{k'})$	Four-momentum of the scattered lepton
θ, ϕ	Polar and azimuthal angles of scattered lepton in the laboratory frame
$s_\mu \stackrel{lab}{=} \frac{1}{m_e}(\lvert\vec{k}\rvert, \hat{\vec{k}}E); \hat{\vec{k}} := \frac{\vec{k}}{\lvert\vec{k}\rvert}$	Spin four-vector of the incident **longitudinally** polarized lepton in the laboratory frame.
Target nucleon	
$P^\mu \stackrel{lab}{=} (M, \vec{0})$	Four-momentum of the target nucleon
$S^\mu \stackrel{lab}{=} (0, \vec{S})$	Spin four-vector of the target nucleon
Inclusive DIS	
$\nu = \frac{P_\mu q^\mu}{M} \stackrel{lab}{=} E - E'$	Energy transfer to the target
$q^\mu = k^\mu - k'^\mu = (\nu, \vec{q})$	Four-momentum transfer to the target
$Q^2 = -q_\mu q^\mu \stackrel{lab}{\simeq} 4EE' sin^2\frac{\theta}{2}$	Negative squared invariant mass of the virtual photon
$s = (P^\mu + k^\mu)^2 \stackrel{lab}{\simeq} 2ME + M^2$	Squared center of mass energy
$W^2 = (P^\mu + q^\mu)^2 \stackrel{lab}{=} M^2 + 2M\nu - Q^2$	Squared mass of the final hadronic state
$x = \frac{Q^2}{2P_\mu q^\mu} \stackrel{lab}{=} \frac{Q^2}{2M\nu}$	Bjorken scaling variable
$y = \frac{2P_\mu q^\mu}{2P_\mu k^\mu} \stackrel{lab}{=} \frac{\nu}{E}$	Fractional energy transfer of the virtual photon
Semi-inclusive DIS	
$P^*_{\lvert\rvert} = \vec{P}_h \cdot \frac{\vec{q}}{\lvert\vec{q}\rvert}\Big\rvert_{\gamma^* N - system}$	Longitudinal momentum of a hadron h in the $\gamma^* N$ center of mass system
$x_F = \frac{P^*_{\lvert\rvert}}{\lvert\vec{q}\rvert} \simeq \frac{2P^*_{\lvert\rvert}}{W}$	Feynman scaling variable
$z = \frac{P_\mu P_h^\mu}{P_\mu q^\mu} \stackrel{lab}{=} \frac{E_h}{\nu}$	Fraction of the virtual photon energy carried by hadron h.

2.1.2 The Deep-Inelastic Scattering Cross section

The differential cross section of lepton nucleon scattering in the approximation of one-photon exchange[3] is given as [21],

$$\frac{d^2\sigma}{d\Omega dE'} = \frac{\alpha^2}{2MQ^4}\frac{E'}{E}L_{\mu\nu}W^{\mu\nu}, \tag{2.9}$$

where α represents the electromagnetic coupling constant and $L_{\mu\nu}$ and $W^{\mu\nu}$ represent the leptonic and hadronic tensors, respectively. The leptonic tensor $L_{\mu\nu}$ describes the photon radiation by the lepton and can be calculated exactly in Quantum Electrodynamics (QED) [17]. The hadronic tensor $W^{\mu\nu}$ [18] describes the interaction of the virtual photon with the nucleon and therefore depends on its a priori unknown, i.e. presently not calculable, inner structure that can be parameterized with structure functions as shown below.

Both tensors can be split into symmetric and anti-symmetric parts (indicated by superscripts (S) and (A) respectively) under μ, ν interchange,

$$L_{\mu\nu} = L^{(S)}_{\mu\nu} + iL^{(A)}_{\mu\nu}, \tag{2.10}$$

$$W_{\mu\nu} = W^{(S)}_{\mu\nu} + iW^{(A)}_{\mu\nu}, \tag{2.11}$$

resulting in the following equation for the cross section:

$$\frac{d^2\sigma}{d\Omega dE'} = \frac{\alpha^2}{2MQ^4}\frac{E'}{E}[L^{(S)}_{\mu\nu}W^{\mu\nu(S)} - L^{(A)}_{\mu\nu}W^{\mu\nu(A)}]. \tag{2.12}$$

The tensor of the point-like lepton is given to first order by

$$L_{\mu\nu} = L^{(S)}_{\mu\nu} + L^{(A)}_{\mu\nu} = 2[k_\mu k'_\nu + k_\nu k'_\mu - g_{\mu\nu}k\cdot k' + i\epsilon_{\mu\nu\alpha\beta}s^\alpha q^\beta], \tag{2.13}$$

where $g_{\mu\nu}$ is the Minkowski metric tensor and $\epsilon_{\mu\nu\alpha\beta}$ the totally anti-symmetric Levi-Civita tensor. The first three terms are symmetric in μ, ν and define $L^S_{\mu\nu}$, the spin-independent part of $L_{\mu\nu}$. The last term $L^A_{\mu\nu}$ is the anti-symmetric, spin-dependent part of $L_{\mu\nu}$, which vanishes in unpolarized scattering.

The hadronic tensor that describes the composite structure of the nucleon cannot be calculated exactly. However, Lorentz invariance, gauge invariance, and parity conservation of the

[3]The corrections due to multi-photon exchange are suppressed by the smallness of the fine structure constant $\alpha \sim 1/137$.

electromagnetic interaction lead to the general form of the hadronic tensor:

$$W_{\mu\nu} = W^S_{\mu\nu} + W^A_{\mu\nu} = \tag{2.14}$$

$$= \Big(-g_{\mu\nu} - \frac{q_\mu q_\nu}{Q^2}\Big)\frac{F_1(x,Q^2)}{M} + \Big(P_\mu + \frac{P\cdot q}{Q^2}q_\mu\Big)\Big(P_\nu + \frac{P\cdot q}{Q^2}q_\nu\Big)\frac{F_2(x,Q^2)}{M(P\cdot q)} \tag{2.15}$$

$$+ i\epsilon_{\mu\nu\alpha\beta}q^\alpha \frac{1}{P\cdot q}\Big[S^\beta g_1(x,Q^2) + \Big(S^\beta - \frac{S\cdot q}{P\cdot q}P^\beta\Big)g_2(x,Q^2)\Big]. \tag{2.16}$$

The structure functions $F_1(x,Q^2)$ and $F_2(x,Q^2)$ account for the spin-independent nucleon structure. These terms comprise the symmetric tensor $W^S_{\mu\nu}$. The spin-dependent nucleon structure is contained in the functions $g_1(x,Q^2)$ and $g_2(x,Q^2)$. The two corresponding terms in Eq. 2.16 make up the anti-symmetric tensor $W^A_{\mu\nu}$.

In contrast to the leptonic tensor, the hadronic tensor $W_{\mu\nu}$ which describes the interaction at the virtual-photon nucleon vertex, is unknown. It represents the internal structure of the nucleon whose understanding in a specific aspect is the aim of this thesis.

The Unpolarized Cross Section

In case of unpolarized beam and target, the differential cross section is given as a product of the symmetric parts of leptonic and hadronic tensors,

$$\frac{d^2\sigma}{d\Omega dE'} = \frac{\alpha^2}{2MQ^4}\frac{E'}{E}L^{(S)}_{\mu\nu}W^{\mu\nu}_{(S)}, \tag{2.17}$$

where

$$W^{\mu\nu}_{(S)} = 2\Big(-g_{\mu\nu} - \frac{q_\mu q_\nu}{Q^2}\Big)F_1(x,Q^2) + \Big(P_\mu + \frac{P\cdot q}{Q^2}q_\mu\Big)\Big(P_\nu + \frac{P\cdot q}{Q^2}q_\nu\Big)\frac{F_2(x,Q^2)}{(P\cdot q)}. \tag{2.18}$$

Here $F_1(x,Q^2)$ and $F_2(x,Q^2)$ are spin-independent unpolarized structure functions which are Lorentz-invariant and explain the internal structure of the nucleon. In the Bjorken limit, or DIS regime, where $\nu\to\infty$ and $Q^2\to\infty$, such that $x = Q^2/2M\nu$ remains constant, the two structure functions cannot depend on two variables such as Q^2 and ν but should be expressible in terms of a single parameter such as x:

$$\lim_{\nu,Q^2\to\infty} F_1(x,Q^2) = F_1(x), \tag{2.19}$$

$$\lim_{\nu,Q^2\to\infty} F_2(x,Q^2) = F_2(x). \tag{2.20}$$

. This property is known as the Bjorken scaling hypothesis, and states that in the limit where Q^2 and ν tend to infinity the structure functions depend only on the *ratio* of these quantities determined by the parameter x. The scaling was observed by a Rutherford-type deep inelastic scattering experiment at SLAC. This effect has been interpreted as that the nucleon appears as

a collection of point-like constituents when probed at very high energies in DIS. This opening promoted development of parton model (see Chap. 2.2), according to which the nucleon is composed of point-like constituents - partons.

The spin-independent DIS cross section (2.17) can be alternatively represented it terms of the inclusive variables x and Q^2:

$$\frac{d^2\sigma}{dxdQ^2} = \frac{4\pi\alpha^2}{Q^4}\Big[y^2 \cdot F_1(x,Q^2) + (1 - y - \frac{My}{2E}) \cdot \frac{F_2(x,Q^2)}{x}\Big] \tag{2.21}$$

or with respect to x and y:

$$\frac{d^2\sigma}{dxdy} = \frac{4\pi\alpha^2}{sx^2y^2}\Big[xy^2F_1(x,Q^2) + \Big(1 - y - \frac{\gamma^2y^2}{4}\Big)F_2(x,Q^2)\Big], \tag{2.22}$$

where $s = (P + k)^2$ denotes the squared center-of-mass energy and $\gamma = (2Mx)/Q$.

Precise measurements of the proton and deuterium structure functions F_2^p and F_2^d have been performed by various fixed target experiments with electrons (SLAC [23], HERMES [27]) and muons (BCDMS [24], EMC [22], NMC [25] and E665 [26]) and by the *ep* collider experiments H1 [28] and ZEUS [29], [30]. The HERMES experiment has collected an outstanding amount of lepton nucleon scattering data on a variety of light and heavy targets. World data on the structure functions F_2^p and F_2^d are shown in Figures 2.3, 2.4.

Photon absorption cross section

The unpolarized cross section can alternatively be expressed in terms of the absorption cross sections for transversely (T) σ_T and longitudinally (L) σ_L polarized virtual photons,

$$\frac{d^2\sigma^{unpol}}{dxdQ^2} = \Gamma\Big[\sigma_T(x,Q^2) + \epsilon\sigma_L(x,Q^2)\Big]. \tag{2.23}$$

Here Γ is the flux of transverse virtual photons, that originate from the lepton beam,

$$\Gamma = \frac{\alpha}{2\pi^2Q^2}\frac{E'}{E}\frac{K}{1-\epsilon}, \tag{2.24}$$

where the factor K is given by

$$K = \frac{W^2 - M^2}{2M} = \nu(1 - x). \tag{2.25}$$

The virtual photon polarization parameter ϵ is the ratio of virtual photon fluxes for longitudinal and transverse polarizations. Neglecting the lepton rest mass m_e, ϵ is given by

$$\epsilon \overset{Q^2>>2me^2}{\simeq} \frac{1 - y - \frac{1}{4}\gamma^2y^2}{1 - y - \frac{1}{4}y^2(\gamma^2 + 2)}. \tag{2.26}$$

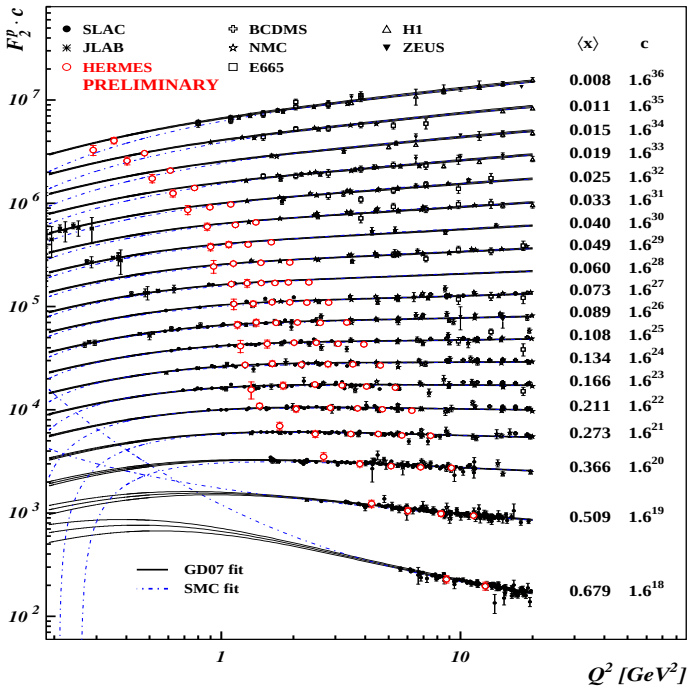

Figure 2.3: An overview of the proton structure function F_2^p [33] measured in lepton-proton scattering with positrons by HERMES, the collider experiments (H1 and ZEUS) in the kinematic domain of HERA for $x > 0.00006$, and for electrons (SLAC, JLAB [31]) and muons (BCMS, NMC and E665). The world data of F_2^p is compared to phenomenological parameterizations. The Q^2 dependence of F_2^p is shown in bins of x. The values of F_2^p were scaled by powers of 1.6.

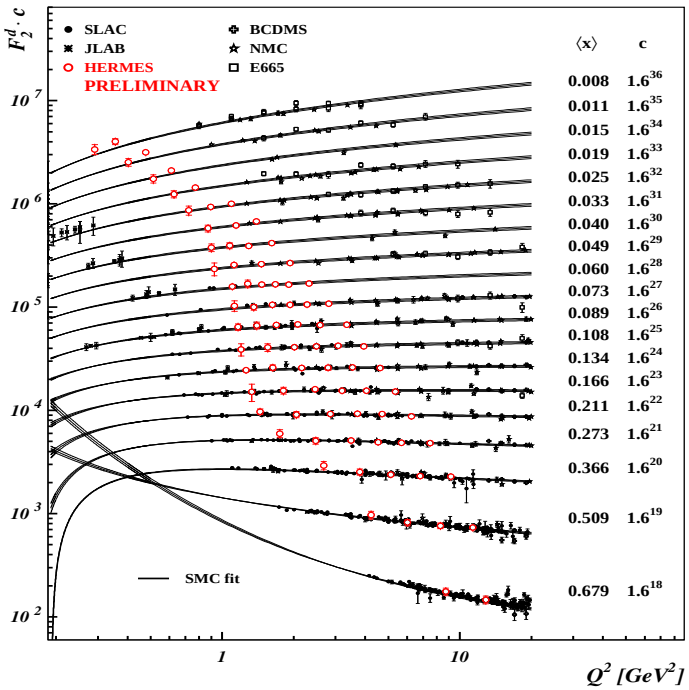

Figure 2.4: The world data of F_2^d is compared to the SMC phenomenological parameterization [32]. The Q^2 dependence of F_2^d is shown in bins of x. The values of F_2^d were scaled by powers of 1.6.

Introducing the ratio $R(x, Q^2)$ of the photon absorption cross section

$$R(x, Q^2) = \frac{\sigma_L(x, Q^2)}{\sigma_T(x, Q^2)} \tag{2.27}$$

the structure functions $F_1(x, Q^2)$ and $F_2(x, Q^2)$ can be related to each other by the longitudinal structure function $F_L(x, Q^2)$

$$R(x, Q^2) = \frac{F_L(x, Q^2)}{2xF_1(x, Q^2)} = \frac{(1+\gamma^2)F_2(x, Q^2) - 2xF_1(x, Q^2)}{2xF_1(x, Q^2)} \tag{2.28}$$

or

$$F_1(x, Q^2) = F_2(x, Q^2) \cdot \frac{1+\gamma^2}{2x[1+R(x, Q^2)]}. \tag{2.29}$$

The cross section ratio $R(x, Q^2)$ has been measured by several DIS experiments in the HERMES kinematic range and found to be identical for proton and neutron targets within the experimental uncertainties. The available data and a parameterization of R [34] are shown in Fig. 2.5, which is used in extracting the photon-nucleon asymmetries in the analysis of this thesis.

In the Bjorken limit ($Q^2 \to \infty$ and $\nu \to \infty$, $x = const$) and for longitudinally polarized photons, the photo absorption cross section σ_L vanishes as a consequence of the requirement of

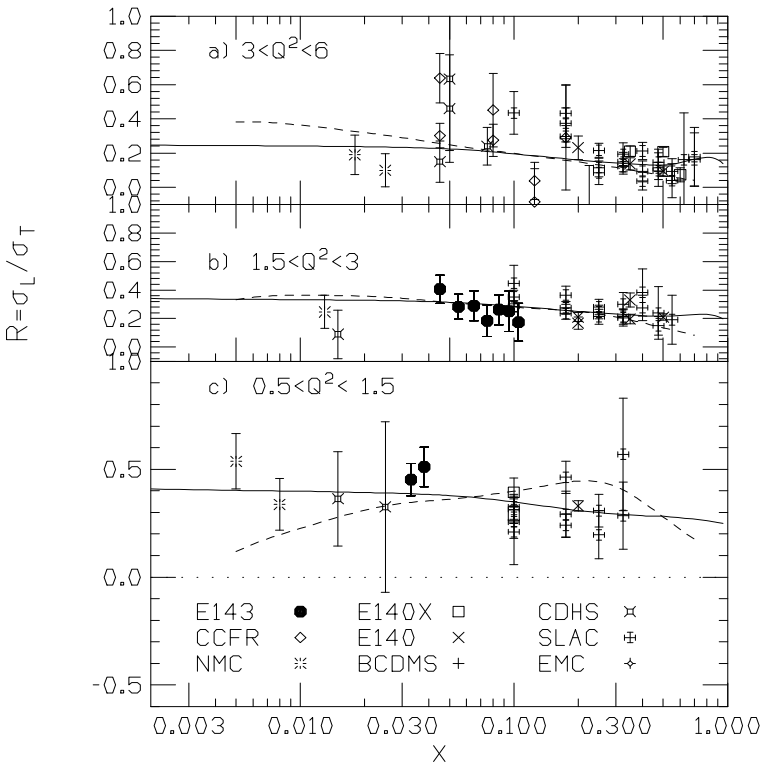

Figure 2.5: The ratio of longitudinal and transverse cross sections $R = \sigma_L/\sigma_T$ as a function of x in three ranges of Q^2. The solid line shows the parameterization R1998 [34]. Also shown are measurements from various experiments. The dashed lines show the results of a next-to-next-to-leading order calculation in perturbative QCD.

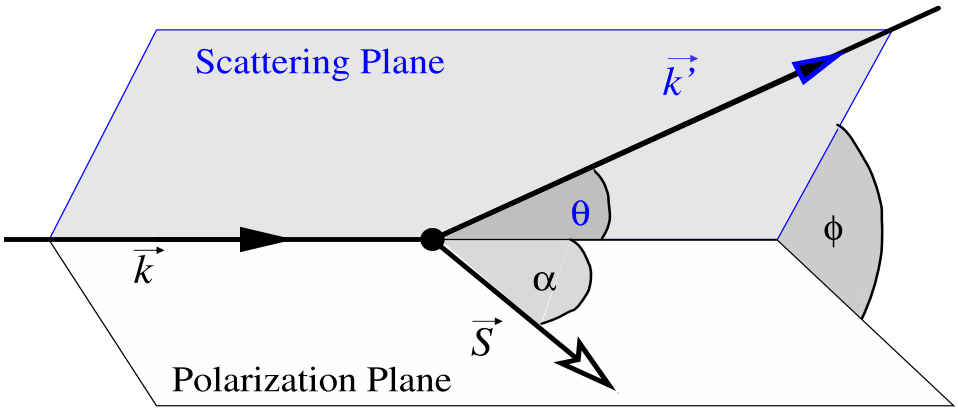

Figure 2.6: The definition of angles. Here $\vec{k}$ and $\vec{k'}$ are momentum vectors of the incoming and scattered lepton respectively. Angles θ and ϕ represent the polar angle with respect to $\vec{k}$ and azimuthal angle which is defined by an angle between scattering plane and polarization plane.

helicity conservation at the virtual photon-quark scattering vertex. In this limit, $R \to 0$, and Eq. 2.29 reduces to the Callan-Gross relation [35]:

$$2xF_1(x) = F_2(x). \tag{2.30}$$

The Polarized Cross Section

In case of longitudinally polarized lepton beam and longitudinally polarized target, the anti-symmetric hadron tensor

$$W_{\mu\nu} = \frac{\epsilon_{\mu\nu\alpha\beta}q^\alpha}{\nu}\Big[S^\beta g_1(x,Q^2) + \Big(S^\beta - \frac{S\cdot q}{P\cdot q}P^\beta\Big)g_2(x,Q^2)\Big] \tag{2.31}$$

appears in the DIS cross section. Here $g_1(x,Q^2)$ and $g_2(x,Q^2)$ are the polarized structure functions and S represents the spin polarization vector of the nucleon target. The polarized structure functions $g_1(x,Q^2)$ and $g_2(x,Q^2)$ can be isolated by considering the difference in cross section upon reversal of the target spin orientation. The two most useful configurations are a longitudinally polarized lepton beam, denoted by $\to$ and a longitudinally or transversely polarized target, denoted by $\Rightarrow$ and $\Leftarrow$ for the parallel and anti-parallel longitudinal orientation, or $\Uparrow$ and $\Downarrow$ for the two transverse orientations. The two polarized structure functions can be obtained by the cross section difference as

$$\frac{d^2\sigma^{\vec{\Leftarrow}}}{dxdQ^2} - \frac{d^2\sigma^{\vec{\Rightarrow}}}{dxdQ^2} = \frac{8\pi\alpha^2}{Q^4}\frac{y}{E}\cdot\Big[(E+E'\cos\theta)g_1(x,Q^2) - \frac{Q^2}{\nu}g_2(x,Q^2)\Big]. \tag{2.32}$$

The definition of the angles between the various vectors is shown in Fig. 2.6. When the target is transversely polarized with respect to the beam direction, the cross section difference can be

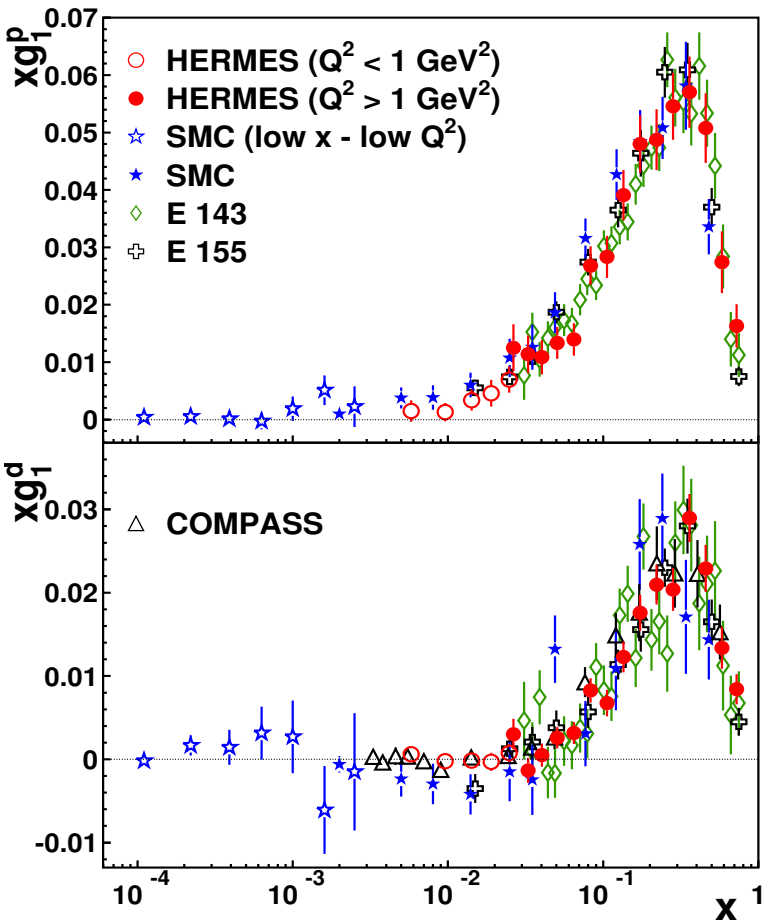

Figure 2.7: The spin-dependent structure function $xg_1(x)$ of the proton and deuteron shown on separate panels measured as a function of x in deep inelastic scattering of polarized electrons/positrons. The HERMES result [14] is compared to the data from SMC [36], [37], [38], E143 [39], E155 [40], [41], and COMPASS [16]. The error bars represent the sum in quadrature of statistical and systematic uncertainties. For the HERMES data the closed (open) symbols represent values derived by selecting events with $Q^2 > 1\ GeV^2$ ($Q^2 < 1\ GeV^2$).

written as

$$\frac{d^2\sigma^{\rightarrow\Uparrow}}{dxdQ^2} - \frac{d^2\sigma^{\rightarrow\Downarrow}}{dxdQ^2} = \frac{8\pi\alpha^2}{Q^4}\frac{y}{E}\cdot E^{'}\cdot \sin\theta\cos\phi\Big[g_1(x,Q^2) + \frac{2E}{\nu}g_2(x,Q^2)\Big]. \tag{2.33}$$

These two cases allow measurement of both g_1 and g_2. Rather than measuring cross section differences it is advantageous from an experimental point of view to measure the following cross section asymmetries:

$$A_{||}(x,Q^2) = \frac{\sigma^{\vec{\Leftarrow}} - \sigma^{\vec{\Rightarrow}}}{\sigma^{\vec{\Leftarrow}} + \sigma^{\vec{\Rightarrow}}}, \qquad A_{\perp}(x,Q^2) = \frac{\sigma^{\rightarrow\Downarrow} - \sigma^{\rightarrow\Uparrow}}{\sigma^{\rightarrow\Downarrow} + \sigma^{\rightarrow\Uparrow}}. \tag{2.34}$$

Here, $\sigma^{\vec{\Leftarrow}(\vec{\Rightarrow})}$ is a short notation for the differential cross sections $\frac{d^2\sigma^{\vec{\Leftarrow}(\vec{\Rightarrow})}}{dxdQ^2}$ for anti-parallel (parallel) alignments of beam and target spin. The $\sigma^{\rightarrow\Downarrow(\rightarrow\Uparrow)}$ are defined accordingly. Provided

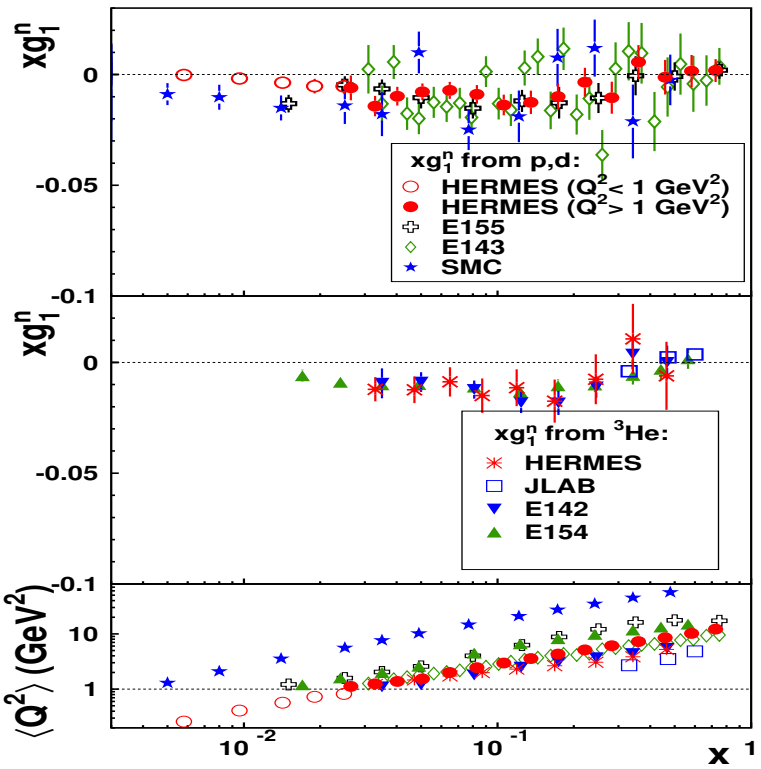

Figure 2.8: Top panel : xg_1^n from data for g_1^p and g_1^d, compared with similar data from SMC [36], [37], [38], E143 [39], E155 [40], [41] in the HERMES x-range. Middle panel: xg_1^n as obtained from a ^3He target by JLab [20], HERMES [42], E142 [43] and E154 [44]. Bottom panel: average Q^2 versus x. For the HERMES data the closed (open) symbols represent values derived by selecting events with $Q^2 > 1\ GeV^2$ ($Q^2 < 1\ GeV^2$).

the time intervals between the flipping of the target or beam spin are short enough, efficiency and acceptance effects, which are not correlated to the relative orientation of the beam and target spins, cancel out by measuring cross section asymmetries instead of cross section differences.

The transverse asymmetry is much smaller than the longitudinal one and therefore difficult to measure. In the past few years it has been possible to gather information on g_2. Figures 2.7 and 2.8 show the results of measurements of spin-dependent structure functions $g_1^{p,d,n}$ on longitudinally polarized proton and deuteron targets of HERMES in comparison with various other experiments.

2.1.3 The photon-nucleon asymmetries

The asymmetries $A_{||}$ and $A_{\perp}$ from Eqs. 2.34 measure the cross section difference with respect to the relative orientations of the lepton and the nucleon spin. However, the fundamental process in DIS is interpreted as the interaction of a virtual photon with the target in lowest order QED,

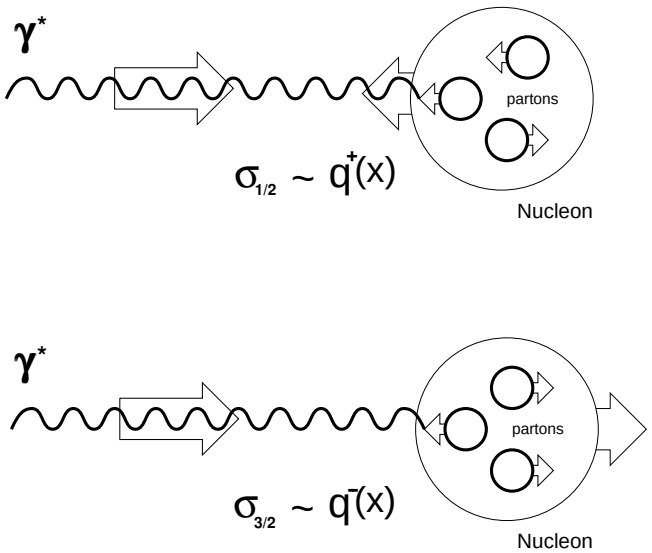

Figure 2.9: Schematic diagram of the polarizad DIS in Quark Parton Model. The arrows indicate the spins of the virtual photon, the partons and the nucleon.

as illustrated in Fig. 2.9 for the longitudinal case.

In a reference frame, known as the Breit frame, in which the struck parton recoils with its momentum reversed, the photon is absorbed by the parton in a head-on collision. In the absorption process of a virtual photon by a quark, the photon can only couple to quarks whose spin is aligned opposite to the spin of the photon because helicity must be conserved and because a quark can only have spin 1/2 and not 3/2. In both panels of Fig. 2.9, the incoming polarized lepton emits a virtual photon at the left with spin projection "pointing" to the right in this picture. In the top panel of Fig. 2.9, the target polarization points to the left so that we measure the cross section for photon and target polarization directions anti-parallel. This cross section is labeled[4] $\sigma_{1/2}$ and is sensitive to the distribution of quarks with their spins in the same direction as the spin of the nucleon, or $q^+(x)$. In the bottom panel of Fig. 2.9 the target spin direction has been reversed so that we measure the cross section for photon and target polarizations parallel ($\sigma_{3/2}$). However, the elementary process is not changed. The photon is absorbed by a quark with spin projection pointing to the left and this process is sensitive to $q^-(x)$.

The difference of the two cross section, $\sigma_{1/2} - \sigma_{3/2}$, is proportional to g_1, while the sum is proportional to F_1. The photo-absorption asymmetries which are the cross section asymmetries for parallel and anti-parallel alignment of the target and virtual photon spins are given by

$$A_1 = \frac{\sigma_{1/2} - \sigma_{3/2}}{\sigma_{1/2} + \sigma_{3/2}} = \frac{g_1 - \gamma^2 g_2}{F_1}, \tag{2.35}$$

[4]The subscript 1/2 refers to the total spin of the virtual photon and target, in order to avoid confusion with the notation $\sigma^{\rightarrow}_{\Leftarrow}$ where the arrows refer to the spin of the lepton and target.

$$A_2 = \frac{2\sigma_{TL}}{\sigma_{1/2} + \sigma_{3/2}} = \frac{\gamma(g_1 + g_2)}{F_1}, \tag{2.36}$$

where σ_{TL} measures the interference of longitudinal transverse photo-absorption amplitudes and the relation to the nucleon structure functions are also given. These asymmetries are related to the experimentally accessible asymmetries $A_{||}$ and $A_{\perp}$ via

$$A_{||} = D(A_1 + \eta A_2), \qquad A_{\perp} = D(-\frac{\eta}{\xi}A_1 + \xi A_2). \tag{2.37}$$

The asymmetry of interest in the analysis is the photon-nucleon asymmetry A_1. It is related to the measured asymmetry $A_{||}$ (from Eqs. 2.35, 2.36 and 2.37):

$$A_1 = \frac{A_{||}}{D(1+\eta\gamma)} - \frac{\eta\gamma(1+\gamma^2)}{1+\eta\gamma}\frac{g_2}{F_1} \overset{g_2=0}{\simeq} \frac{g_1}{F_1} \simeq \frac{A_{||}}{D(1+\eta\gamma)}, \tag{2.38}$$

where the kinematic factor D as defined as

$$D = \frac{1-(1-y)\varepsilon}{1+\varepsilon R}. \tag{2.39}$$

The kinematic factor D accounts for the depolarization of the virtual photon with respect to the polarization of the positron beam. The kinematic factors η, γ and ξ are given as:

$$\eta = \frac{\varepsilon\gamma y}{1-(1-y)\varepsilon}, \tag{2.40}$$

$$\xi = \sqrt{\frac{2\varepsilon}{1+\varepsilon}}. \tag{2.41}$$

2.2 The parton model

2.2.1 The simple parton model

The observation of Bjorken scaling (see Eqs. 2.19, 2.20) at SLAC provided experimental verification of Feynmans parton model [3]. In this model, the nucleon is viewed as being composed of point-like non-interacting constituents, i.e. partons, which absorb the virtual photon in the deep-inelastic scattering reaction. The DIS lepton nucleon cross section can be calculated as the incoherent sum of elastic scattering off quarks in the nucleon.

In a reference frame where the proton is moving very fast with high momentum P in the positive z-direction, the proton can be viewed as a beam of *collinear partons*, as shown in Fig. 2.10. Lorentz invariance of the structure functions ensures that their values in this frame is valid in any other frame. The photon momentum q in this frame is fixed by Lorentz invariance of $-Q^2 \overset{lab}{=} -2xM\nu$ and $P \cdot q \overset{lab}{=} M\nu$. In the hard interaction with the photon, the quark-partons are treated as free, massless particles with momentum $p_i = \xi_i P$ (see Fig. 2.11).

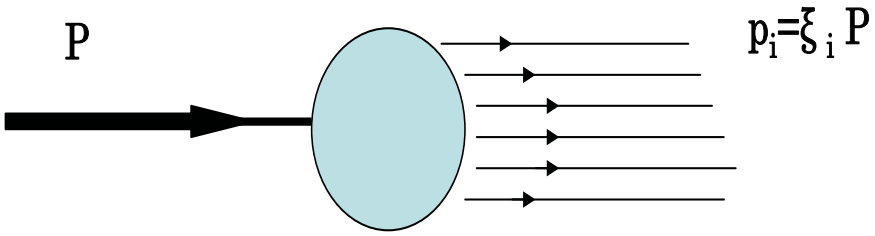

Figure 2.10: Visualization of parton density $q(\xi)$.

The four-momentum of a struck parton can be expressed as

$$(\xi P + q)^2 = m_q^2, \tag{2.42}$$

where m_q is the mass of the parton which can be neglected. Hence the momentum fraction ξ becomes

$$\xi = \frac{Q^2}{2M\nu}\frac{2}{1+\sqrt{1+\frac{Q^2}{\nu^2}}} = \frac{2x}{1+\sqrt{1+\frac{4(Mx)^2}{Q^2}}}. \tag{2.43}$$

In the limit of $Q^2 \gg M^2$,

$$\xi \simeq \frac{x}{1+\frac{(Mx)^2}{Q^2}} \simeq x. \tag{2.44}$$

Hence the Bjorken x indicates the fractional momentum of proton carried by the struck quark.

The cross section for elastic electron-parton scattering can be exactly calculated in QED. Assuming that each parton in the nucleon contributes to the inclusive DIS cross section incoherently, the structure function $F_1(x)$ and $F_2(x)$ can be related to the charge of the parton e_q in units of the elementary charge $|e|$ and to the quark densities $q(x)$:

$$F_1(x) = \frac{1}{2}\sum_q e_q^2[q(x) + \bar{q}(x)], \tag{2.45}$$

$$F_2(x) = x\sum_q e_q^2[q(x) + \bar{q}(x)], \tag{2.46}$$

where the sum runs over all quark flavors ($q = u,\ d,\ s,\ \bar{u},\ \bar{d},\ \bar{s},\ ...$). At HERMES energies, u-, d-, s-quarks, and the corresponding anti-quarks are enough to express the structure functions. Analogously the polarized structure function $g_1(x)$ can be written as

$$g_1(x) = \frac{1}{2}\sum_q e_q^2[\Delta q(x) + \Delta\bar{q}(x)], \tag{2.47}$$

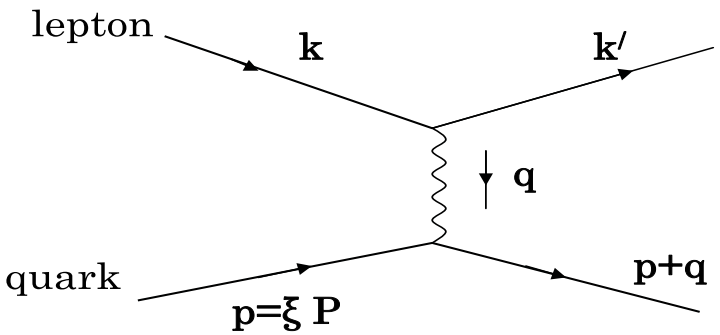

Figure 2.11: Lepton-quark elastic scattering.

where $\Delta q(x)$ is the longitudinally polarized quark density. It is the difference of quark densities with spin orientation parallel or antiparallel to the spin direction of the proton (see Fig. 2.12):

$$\Delta q(x) = q^{(+)}(x) - q^{(-)}(x). \tag{2.48}$$

The usual unpolarized parton densities $q(x)$ are the sum of polarized parton densities:

$$q(x) = q^{(+)}(x) + q^{(-)}(x). \tag{2.49}$$

The densities of the three valence quarks in the nucleon that carry its electric charge and baryon quantum number are similarly expressed in terms of these parton distributions,

$$u_v(x) \equiv u(x) - \bar{u}(x), \qquad d_v(x) \equiv d(x) - \bar{d}(x), \tag{2.50}$$

$$\Delta u_v(x) \equiv \Delta u(x) - \Delta\bar{u}(x), \qquad \Delta d_v(x) \equiv \Delta d(x) - \Delta\bar{d}(x). \tag{2.51}$$

2.2.2 The spin crisis in the parton model

Analogously to the unpolarized structure function F_1, the structure function g_1 can be expressed as the incoherent sum of helicity-dependent or polarized parton densities:

$$g_1(x) = \frac{1}{2}\Big[\frac{4}{9}(\Delta u(x) + \Delta\bar{u}(x)) + \frac{1}{9}(\Delta d(x)\Delta d(x)) + \frac{1}{9}(\Delta s(x) + \Delta\bar{s}(x))\Big]. \tag{2.52}$$

Usually one defines combinations of quark densities which have specific transformation properties under the group of flavor transformations $SU(3)_F$ as:

$$\Delta q_3(x) = [\Delta u(x) + \Delta\bar{u}(x)) - (\Delta d(x) + \Delta\bar{d}(x)], \tag{2.53}$$

$$\Delta q_8(x) = [\Delta u(x) + \Delta\bar{u}(x)) + (\Delta d(x) + \Delta\bar{d}(x)) - 2(\Delta s(x) + \Delta\bar{s}(x)], \tag{2.54}$$

$$\Delta\Sigma(x) = [\Delta u(x) + \Delta\bar{u}(x)) + (\Delta d(x) + \Delta\bar{d}(x)) + (\Delta s(x) + \Delta\bar{s}(x)], \tag{2.55}$$

which transform, respectively, as the third component of an isotopic spin triplet, the eighth

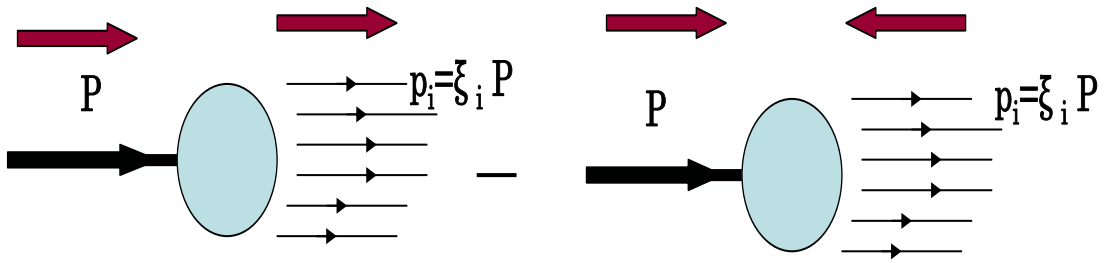

Figure 2.12: Visualization of the longitudinally polarized parton density $\Delta q(x)$. The upper arrows show the spin direction.

component of an $SU(3)_F$ octet and a flavor singlet. Then

$$g_1(x) = \frac{1}{9}\Big[\frac{3}{4}\Delta q_3(x) + \frac{1}{4}\Delta q_8(x) + \Delta\Sigma(x)\Big]. \tag{2.56}$$

The first moment of the polarized structure function g_1 is

$$\Gamma_1 \equiv \int_0^1 g_1(x)dx = \frac{1}{12}\Big[a_3 + \frac{1}{\sqrt{3}}a_8 + \frac{4}{3}a_0\Big], \tag{2.57}$$

where

$$a_3 = \int_0^1 dx\Delta q_3(x), \tag{2.58}$$

$$a_8 = \frac{1}{\sqrt{3}}\int_0^1 dx\Delta q_8(x), \tag{2.59}$$

$$a_0 = \Delta\Sigma = \int_0^1 dx\Delta\Sigma(x). \tag{2.60}$$

Via the operator product expansion these moments can be related to hadronic matrix elements of currents which are *measurable* in other processes [76]. The quantity a_3 is the axial charge of the nucleon. Its value can be measured from neutron β decay [64]:

$$a_3 = 1.2670 \pm 0.0030. \tag{2.61}$$

The value of the matrix element a_8 is obtained from hyperon β decay [77]:

$$a_8 = 0.585 \pm 0.025. \tag{2.62}$$

With the known values of a_3 and a_8 the measurement of Γ_1 (see Eq. 2.57) can be considered as possibility to obtain the value of the flavor singlet a_0. The European Muon Collaboration, working at CERN, measured the first moment of the spin dependent structure function g_1 of

the proton in polarized muon-nucleon scattering and in 1988 announced their startling result at a mean Q^2 of 10.7 GeV^2 [5]:

$$\Gamma_{1,p} = \int_0^1 g_1^p(x)dx = 0.114 \pm 0.012(stat.) \pm 0.026(syst.). \tag{2.63}$$

This result was in contrast to the expectations from the naive parton model. In 1974 Ellis and Jaffe [9] had suggested that one could ignore the contribution from the strange quark, $\Delta s + \Delta\bar{s} = 0$, which is equivalent to

$$a_0 \simeq a_8 \simeq 0.59. \tag{2.64}$$

Then the expected value for $\Gamma_{1,p}$ is

$$\Gamma_{1,p}^{Ellis-Jaffe} = 0.185 \pm 0.004. \tag{2.65}$$

Thus the EMC result was in big contradiction with the Ellis-Jaffe assumption. It was this unexpected result which was termed *"spin crisis in the parton model"*.

A possible explanation of the effect comes from the triangle anomaly of QCD. It has been pointed out that the picture presented by Eqs. 2.53-2.55 is too naive, since QCD radiative corrections arising from the Adler, Bell, Jackiw triangle anomaly [78] have been neglected. When this is taken into account, each of the terms $\Delta q + \Delta\bar{q}$ in Eqs. 2.53-2.55 is replaced by $\Delta q + \Delta\bar{q} - (\alpha_s/2\pi)\Delta G$, where $\Delta G = \int_0^1 [G^+(x) - G^-(x)]dx$ is the mean z-component of spin of the gluons in a proton with $S_z = +\frac{1}{2}$.

The matrix element a_0 is not more related to $\Delta\Sigma$ which depends on the renormalization and factorization scheme used. Two common choices are the $\overline{MS}$ scheme and the Adler-Bardeen (AB) scheme. In the AB scheme a_0 is given as

$$a_0(Q^2) = \Delta\Sigma_{AB} - 3\frac{\alpha_s(Q^2)}{2\pi}\Delta G(Q^2). \tag{2.66}$$

Adler's expression, modified to QCD, gives the possibility to compute the gluonic contribution to the first moment of g_1:

$$\Gamma_1^{gluons}(Q^2) = -\frac{1}{3}\frac{\alpha_s(Q^2)}{2\pi}\Delta G(Q^2). \tag{2.67}$$

The $\overline{MS}$ scheme is defined in such a way that the contribution of gluons cancels in Γ_1 and $\Delta\Sigma_{\overline{MS}}$ depends on Q^2, whereas $\Delta\Sigma_{AB}$ does not

$$a_0(Q^2) = \Delta\Sigma_{\overline{MS}}(Q^2). \tag{2.68}$$

The individual quark spin contributions to the nucleon spin is more directly accessed in semi-inclusive DIS, where the additional information on the hadronic final state allows to determine the polarized parton densities individually. The results, based on technique, called *quark flavor*

tagging, which is described in next chapter, could be useful in our understanding of the internal structure of the nucleon, particularly of the spin structure.

2.3 Semi-Inclusive Deep Inelastic Scattering

In semi-inclusive DIS, $lN \to l'hX$, a final state hadron h is detected in coincidence with the scattered lepton (see Fig. 2.1). The quark is ejected along the direction of the virtual photon in the laboratory frame and its original energy is the same as the energy of the photon. Due to the confinement property of QCD the struck quark and the target remnant will fragment into hadrons. Hadrons produced from the fragmentation of the struck quark are called *current fragments* while those produced from the fragmentation of the target remnant are called *target fragments*. In the current fragmentation region, one expects a large correlation between the flavor of the struck quark and the types of produce hadrons, in particular hadrons whose valence quarks contain the flavor of the struck quark. The existence of such a correlation is necessary in order for quark flavor tagging to work.

The process of the fragmentation of the struck quark is parameterized by fragmentation functions $D_q^h(Q^2, z)$ which are defined as the probability density that a struck quark q, probed at a particular Q^2, fragments into a hadron h with energy fraction z. Since the fragmentation process involves long distance (small Q^2) processes, the fragmentation functions cannot be calculated by perturbative QCD. A clean separation between the current and target fragmentation regions is typically regarded as a necessary criterion for quark flavor tagging. Current fragmentation includes selecting hadrons which are (**a**) forward in the $\gamma^* N$ center of mass system ($x_F > 0$), (**b**) forward in the Breit frame, or (**c**) fast in the laboratory system (e.g. $z > 0.1$). These kinematic requirements cannot identify the current fragments, but allow a significant enhancement of the correlation of the detected hadron with the struck quark. The separation of the two fragmentation regions improves with increasing values of W.

In LO QCD, the differential cross section $d\sigma^h/dz$ for the production of a particular hadron h from the current fragmentation region can be expressed in terms of fragmentation functions and unpolarized quark distributions,

$$\frac{1}{\sigma_{inc}} \frac{d\sigma^h}{dz}(x, Q^2, z) = \frac{\sum_q e_q^2 q(x, Q^2) D_q^h(Q^2, z)}{\sum_q e_q^2 q(x, Q^2)}, \tag{2.69}$$

where σ_{inc} denotes the inclusive DIS cross section. Further, based on Eqs. 2.45 and 2.69, the LO semi-inclusive structure function F_1^h is defined as

$$F_1^h(x, Q^2, z) = \frac{1}{2} \sum_q e_q^2 q(x, Q^2) D_q^h(Q^2, z). \tag{2.70}$$

Under the assumption that the fragmentation process is spin-independent, i.e. that the proba-

bility to produce a hadron of type h by scattering from a quark q is independent of the relative orientations of the quark spin and the nucleon spin, the LO semi-inclusive spin structure function g_1^h can similarly be written as :

$$g_1^h(x, Q^2, z) = \frac{1}{2} \sum_q e_q^2 \Delta q(x, Q^2) D_q^h(Q^2, z). \tag{2.71}$$

Assuming $g_2^h = 0$, the z-integrated semi-inclusive spin asymmetries are given by :

$$A_1^h(x, Q^2) \overset{g_2^h=0}{=} \frac{\int dz g_1^h(x, Q^2, z)}{\int dz F_1^h(x, Q^2, z)} = \frac{\sum_q e_q^2 \Delta q(x, Q^2) \int dz D_q^h(Q^2, z)}{\sum_q e_q^2 q(x, Q^2) \int dz D_q^h(Q^2, z)}. \tag{2.72}$$

This equation relates the measured spin asymmetries A_1^h to the polarized and unpolarized quark distributions and fragmentation functions. The region over which z is integrated is determined by cuts on the hadron kinematics to select hadrons from the current fragmentation region. Given the fragmentation functions D_q^h and the unpolarized quark distributions q, Eq. 2.72 together with the corresponding expression for the inclusive asymmetry

$$A_1(x, Q^2) \overset{g_2^h=0}{=} \frac{g_1(x, Q^2)}{F_1(x, Q^2)} = \frac{\sum_q e_q^2 \Delta q(x, Q^2)}{\sum_q e_q^2 q(x, Q^2)} \tag{2.73}$$

can be used to extract the polarized quark distribution Δq_f from a set of measured inclusive and semi-inclusive asymmetries. The extraction of the polarized parton densities from the measured inclusive and semi-inclusive asymmetries is presented in Chap. 6.

Chapter 3

The HERMES experiment

HERMES was one of the four experiments at HERA at the DESY laboratory in Hamburg, Germany. The HERMES experiment (HERa MEasurement of Spin) [45] is a second generation polarized deep inelastic scattering (DIS) experiment to study the spin structure of the nucleon. For this high beam current, high values of target and beam polarization, high target density and a large detector acceptance are needed. HERMES used the high current longitudinally polarized electron beam of HERA with a beam energy of about 27.6 GeV together with polarized and unpolarized gas targets internal to the electron storage ring. The scattered electron and particles produced in the deep-inelastic electron-nucleon interactions are detected and identified by an open-geometry forward spectrometer with large momentum and solid angle acceptance.

HERMES is based on two novel techniques: longitudinal electron polarization in a high-energy storage ring, which is achieved by a system of spin-rotator magnets, and a storage-cell target where the polarized atoms from a high-intensity polarized source are present as pure atomic species without dilution from unpolarized target material.

In this chapter, the components of the HERA accelerator relevant to the HERMES experiment, the HERMES target, the HERMES spectrometer and the data acquisition system are described. More detailed information is found in ref. [45].

3.1 The polarized lepton beam of the HERA storage ring

Figure 3.1 shows an overview of the HERA accelerator. It consists of a electron beam running clock-wise with an energy of 27.6 GeV and a proton beam running in the opposite direction with an energy of 920 GeV. Both rings have a circumference of 6.3 km. While H1 and ZEUS are located at the interaction points of the electron and proton beam lines, HERMES only uses the electrons.

HERA operation can be split into a number of consecutive steps. The beams are filled and ramped to their operational energies. Initial electron currents of up to 50 mA have been achieved. Due to interactions with residual gas in the beam line, and also due to the influence of

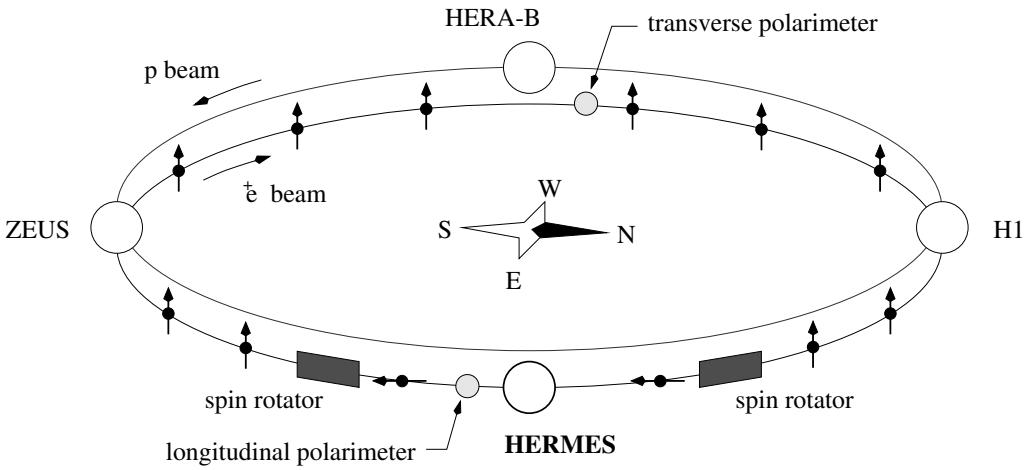

Figure 3.1: Sketch of the HERA facility at DESY

the experiments the electron beam life time is limited to about 12-14 hours. During this time, the current decreases exponentially. HERA runs with both electrons and positrons and in fact most of the HERMES data have been taken with a positron beam. For simplicity throughout the whole paper *electrons* are used for both lepton species.

In high-energy storage rings, electron beams can become transversely polarized through the emission of spin-flip synchrotron radiation [46], the so-called Sokolov-Ternov mechanism. This process is due to an asymmetry in the synchrotron radiation cross section. This polarization develops in time according to

$$P(t) = P_{\infty}(1 - e^{-t/\tau}), \tag{3.1}$$

where the asymptotic polarization P_{∞} and the time constant τ are characteristics of the storage ring. The theoretical limit for polarization is 92.4%. The real polarization reaches typically about 55% approximately 40 minutes after the start of the fill.

Spin rotators have been installed upstream and downstream of the HERMES experiment, since for the measurement of the double spin asymmetries, longitudinal polarization is required. The polarization of the beam is measured by two laser backscattering polarimeters. The transverse polarimeter is located in the West Hall and the longitudinal polarimeter is inside the spin rotator at the East Hall. A typical rise-time curve, measured simultaneously with both polarimeters is shown in Fig. 3.2

3.2 The internal gas target

A fixed target in a storage ring needs a special setup to preserve a reasonable life time of the stored beam, without causing significant disruption to the beam life time. This immediately excluded any possibility of using solid materials for the target in HERMES. In fact, the target density is limited to 10^{15}atoms/cm^2. In order to fulfill the requirement of HERA, a gaseous

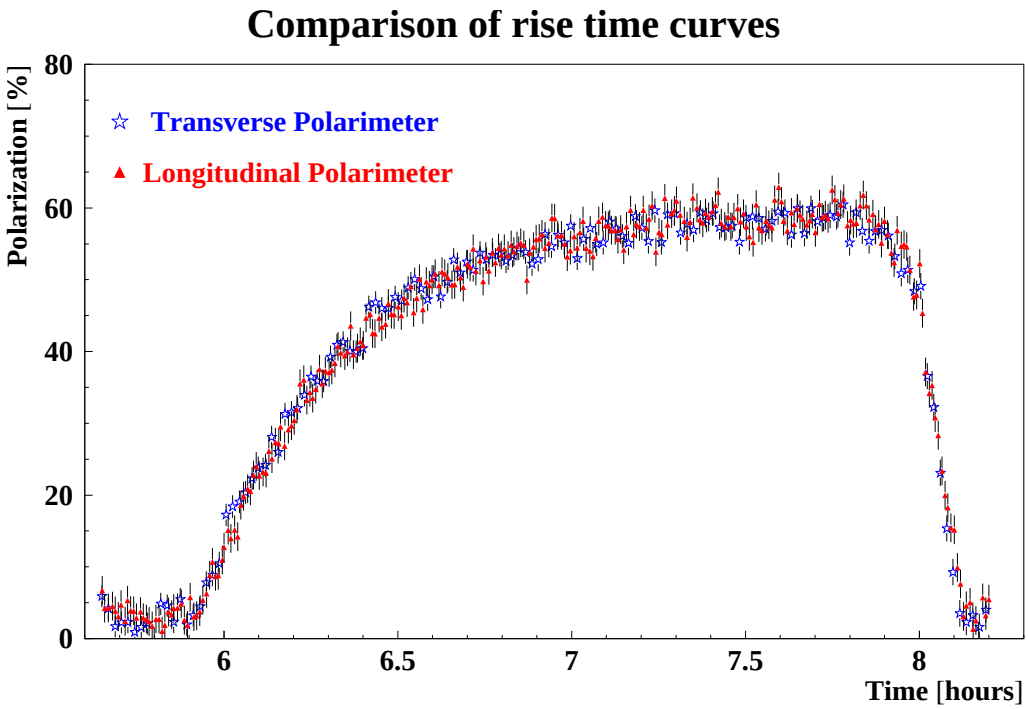

Figure 3.2: Example for a measurement of the polarization build-up of the HERA positron beam as measured by both the Transverse and the Longitudinal Polarimeter.

target [47] cell was designed for use in the experiment.

The HERMES experiment uses an innovative technique for the polarized target, which is very different from other polarized deep-inelastic scattering experiments, that is a polarized gas target internal to the HERA storage ring. This technique permits essentially background-free measurements from highly polarized nucleons with little or no dilution of the signal from unpolarized nucleons in the target.

The HERMES experiment uses both polarized and unpolarized targets. The longitudinal polarized target consisted of Hydrogen, Deuterium or ^{3}He and H_2, D_2, ^{3}He, N_2, Ne, Kr and Xe were used as unpolarized targets. A polarized ^{3}He target was used in 1995, a longitudinally polarized hydrogen target was used in 1996-1997 and in 1998-2000 a longitudinally polarized deuterium target. The transversally polarized hydrogen target, which was installed during a HERA upgrade in 2001, was used in 2002-2005.

The polarized hydrogen(deuterium) atoms are produced by means of an atomic beam source (ABS) [51]. This device consists of a dissociator, a powerful differential pumping system, a beam forming system, a sextupole magnet system and adiabatic high-frequency transitions.

Molecular hydrogen/deuterium gas is dissociated by a radio frequency of 13.56 MHz in a pyrex-type tube. The degree of produced dissociation is up to 80%. Atomic gas flows through a conical nozzle with an opening diameter of 2 mm, which is cooled to 100 K. Five sextupole permanent magnets split this beam into hyperfine states. The particular polarization state of interest is selected by a combination of strong field transitions (SFT), medium field transitions

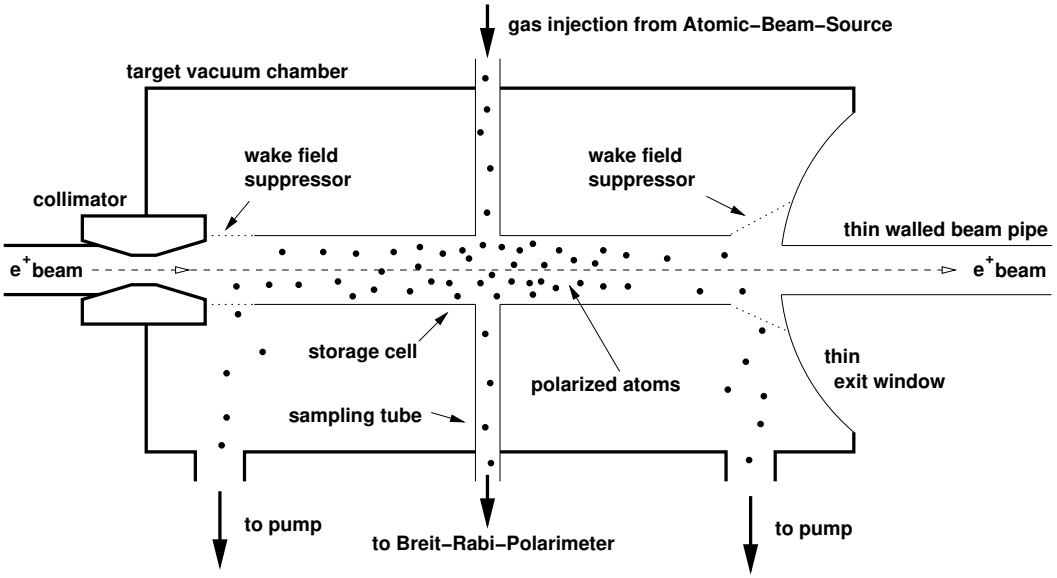

Figure 3.3: Diagram of the target chamber.

(MFT) and weak field transitions (WFT). The polarized atomic beam is injected into the target cell with a pressure of about 10^{-7}mbar. The target cell is an elliptical tube with open ends which holds the gas at the lepton beam position. At the end of the target cell two powerful turbo-pumps are installed in order to protect the ultra-high vacuum in the accelerator ring.

For polarized gas, there are two instruments installed for monitoring: a Breit-Rabi Polarimeter (BRP) [48] and Target Gas Analyser (TGA) [49], [50]. The former measures the polarization of the gas and the latter gives an estimate of the degree of dissociation. For unpolarized gas, neither measurement is needed, so the gas is filled directly into the target cell.

3.3 The HERMES spectrometer

A schematic side view of the HERMES spectrometer is shown in Fig. 3.4. It is a forward spectrometer that consists of two identically constructed halves, one above and one below the HERA beam pipes. Both the positron and the proton beam pass through the central plane of the spectrometer and are shielded from the magnetic field of a dipole magnet by a steel plate. Each spectrometer half consists of a set of tracking chambers, hodoscopes and four particle identification detectors. The coordinate system used by HERMES has the z axis along the beam direction, the y axis pointing upwards, and the x axis horizontal, pointing towards the outside of the storage rings.

The acceptance of the spectrometer extends vertically from 40 to 140 mrad and horizontally to ± 170 mrad, resulting in a total angular acceptance from 40 to 220 mrad (see Fig. 3.5).

The luminosity of the experiment is determined with the use of a luminosity monitor [52] located left and right from the beam pipe at the electromagnetic calorimeter position. It consists

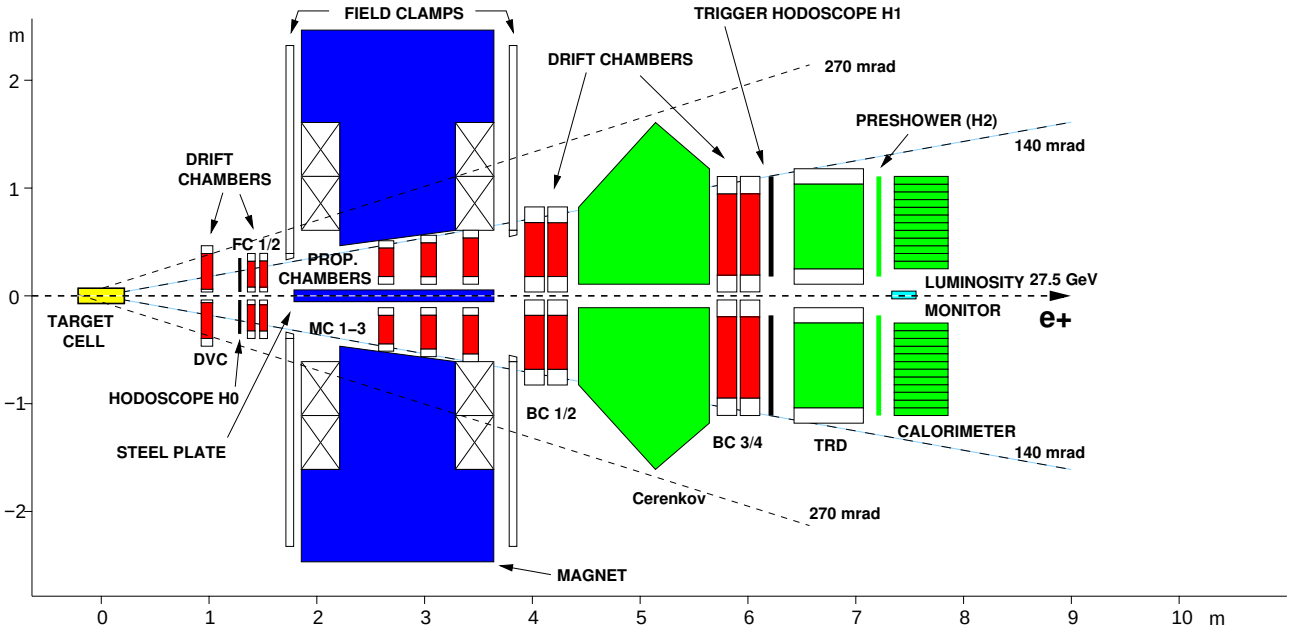

Figure 3.4: Schematic view of the HERMES spectrometer.

of two calorimeters on either side of beam pipe, each made of 12 $NaBi(WO_4)_2$ crystals that are read out by photomultipliers. Since its position is so close to the beam pipe, during the beam injection it is shifted away from the beam pipe to avoid radiation damage.

The luminosity monitor measures the scattering rate of the lepton beam off the atomic electrons of the gas target for three processes:
Bhabha scattering

$$e^+e^- \rightarrow e^+e^-,$$

pair annihilation,

$$e^+e^- \rightarrow \gamma\gamma,$$

when the positron beam is used and the Møller scattering

$$e^-e^- \rightarrow e^-e^-,$$

for the electron-beam data taking periods. The cross section of these three processes is well known, thus the luminosity is obtained from the measured rate of events normalized to the known cross section, and finally corrected for the luminosity monitor acceptance and efficiency.

The spectrometer should serve two fundamental tasks, the reconstruction of the particle tracks, and the identification of the particle types: its components can therefore be grouped in two different categories: the tracking detectors and the Particle IDentification (PID) detectors, both described in the following sections.

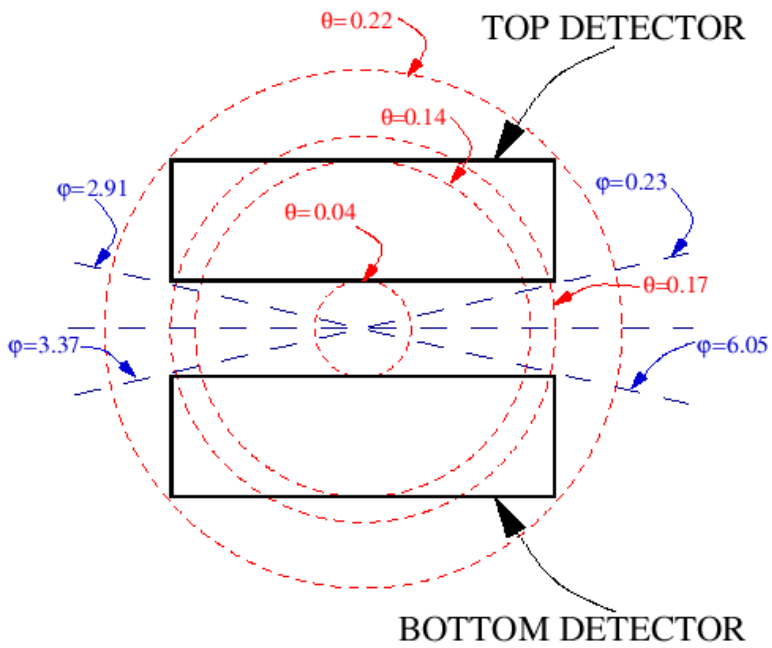

Figure 3.5: Front scheme of HERMES spectrometer: the angular acceptance is limited in the azimuthal angle ϕ by the blue dotted lines, and in the polar angle θ by the red dotted circles.

3.3.1 Magnet and tracking detectors

The tracking system consists of a set of drift vertex chambers DVC, two front chambers FC1/2, three magnet chambers MC1/3 and four back chambers BC1/2 and BC3/4 per detector half. First, it provides a measurement of the position of the scattering vertex in the target. Second, through the bending of the track in the magnetic field, it gives the track's momentum. Third, it has to associate tracks to hits in the particle identification detectors. The overall tracking efficiency is larger than 95%, with a momentum resolution of 0.7 to 1.25% in the total kinematical range, and an angular resolution $\delta\theta$ better than 0.6 mrad. Many tracking chambers have wires oriented along three planes, of which one is the vertical direction (X plane) to provide the x coordinate, while the other two are tilted by $+30^o$ and -30^o (U and V planes).

The front chambers. The DVC's were proposed in 1995 to improve the tracking in front of the magnet. They became operational in 1997. Both the FC and DVC are drift chamber consisting of 6 planes of alternating anode and cathode wires, separated by cathode planes. The DVC and FC are 1.1 m and 1.6 m away from the target, and their resolutions are of the order of 220 μm.

The back chambers. The Back Chambers (BC's)are drift chambers, which form the tracking system behind the magnet. They are arranged in four sets, two directly behind the magnet and two further downstream, after the RICH. Each chamber consists of six wire planes alternated with cathode foils. They measure the track direction after the magnet field, thus providing a measurement of momentum. Their resolutions are approximately 210 μm for BC1/2 and 250

μm for BC3/4.

The magnet. The HERMES magnet provides an integrated magnetic field of 1.5 Tm, with the magnetic field in the vertical direction, so that the particles are deflected in the horizontal direction. The magnet size sets the limits on the geometrical acceptance to the spectrometer: ± 170 mrad in the horizontal direction and ± 140 mrad in the vertical direction, while the shielding plate gives the lower limit to the vertical acceptance, setting it to $\pm$ 40mrad. The tracks are reconstructed independently in the front and back tracking system and then they are matched to the center of the magnet by a fitting procedure.

The magnet chambers. The magnet chambers (MC's) are multiwire proportional chambers. Three sets of magnet chambers are located in the gap of the magnet. Each chamber is made of 3 planes in the XUV orientations. They were designed to help match the front and back tracks, but they turned out to be very useful also in the detection of low-energy particles that are deflected away by the magnetic field, and then not detected by the back chambers. Their resolution is on the order of 1 mm.

3.3.2 Particle IDentification detectors

The HERMES spectrometer includes four particle identification detectors: a Čerenkov detector, a Transition Radiation Detector (TRD), a preshower (H2) and an electromagnetic calorimeter (CALO).

The RICH. The threshold gas Čerenkov detector present at HERMES from 1995 to 1997 was replaced in 1998 with a dual-radiator Ring Imaging Čerenkov Detector (RICH), see Fig. 3.6. The RICH is the first particle identification detector a particle meets. It is located between the drift chambers BC1/2 and BC3/4. It allows the identification of pions, kaons and protons over a large momentum range, with a low cross-contamination and high efficiency. Most of the hadrons produced at HERMES have a momentum between 2 and 15 GeV. The scattered particles encounter a first radiator consisting of an array of 17x5 silica aerogel tiles, followed by a 4000 l volume of C_4F_{10} radiator gas.

When a charged particle in a material medium moves faster than the speed of light in that same medium, it emits Čerenkov radiation on a cone with a characteristic opening angle θ_c given by [53]:

$$cos\theta_c = \frac{1}{n\beta}, \tag{3.2}$$

where n is the index of refraction of the material and $\beta = \frac{v}{c}$ is the ratio of the velocity v of the particle and the speed of light in vacuum c. The Čerenkov threshold momentum p_{thresh} for the particle emitting the Čerenkov radiation in a material medium is given by

$$p_{thresh} = \frac{m}{\sqrt{(n^2-1)}}, \tag{3.3}$$

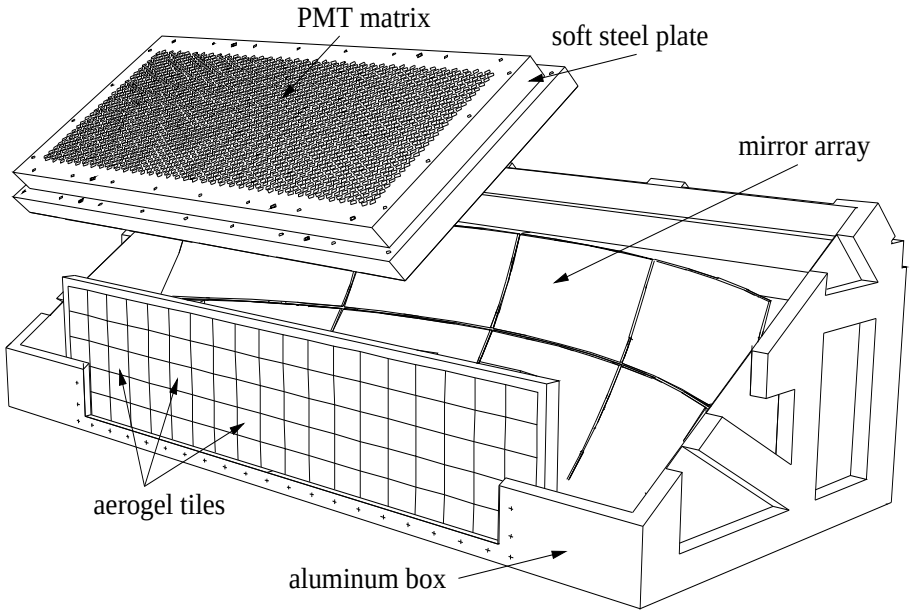

Figure 3.6: A perspective view of the upper RICH detector setup.

Table 3.1: Refractive indices and Čerenkov light thresholds of the RICH

	n	p^{π}_{thresh}	p^{K}_{thresh}	p^{p}_{thresh}
Aerogel	1.0304	0.6 GeV	2.0 GeV	3.8 GeV
C_4F_{10}	1.00137	2.7 GeV	9.4 GeV	17.9 GeV

where m is the mass of the particle. The refractive indices of the radiators for the HERMES dual-radiator RICH and the threshold momenta are shown in Table 3.1.

In the RICH detectors, the Čerenkov cone is focused by an array of spherical mirrors on a matrix of photon detectors where a ring pattern is created. The diameter of the ring is proportional to the Čerenkov angle θ_c.

The RICH particle identification is based on reconstruction of the Čerenkov angle and the particle momentum which is determined from track reconstruction in BC and FC and the deflection radius in the spectrometer magnet. Since the position of the track is known from the track reconstruction and the Čerenkov photons are detected by the RICH PMTs, the Čerenkov photon's angle θ_c can be calculated. The resulting distribution of Čerenkov angles is shown in Fig. 3.7. The combination of two radiators, a clear silica aerogel (refractive index $n = 1.03$) and a C_4F_{10} radiator gas ($n = 1.0014$), allows to span the kinematically difficult region between 2 and 15 GeV, which contains most of the hadrons at HERMES. The upper band on the plot corresponds to the aerogel angles, the lower band shows the C_4F_{10} gas angles.

At HERMES, hadrons are separated from leptons with the TRD and calorimeter components of the spectrometer.

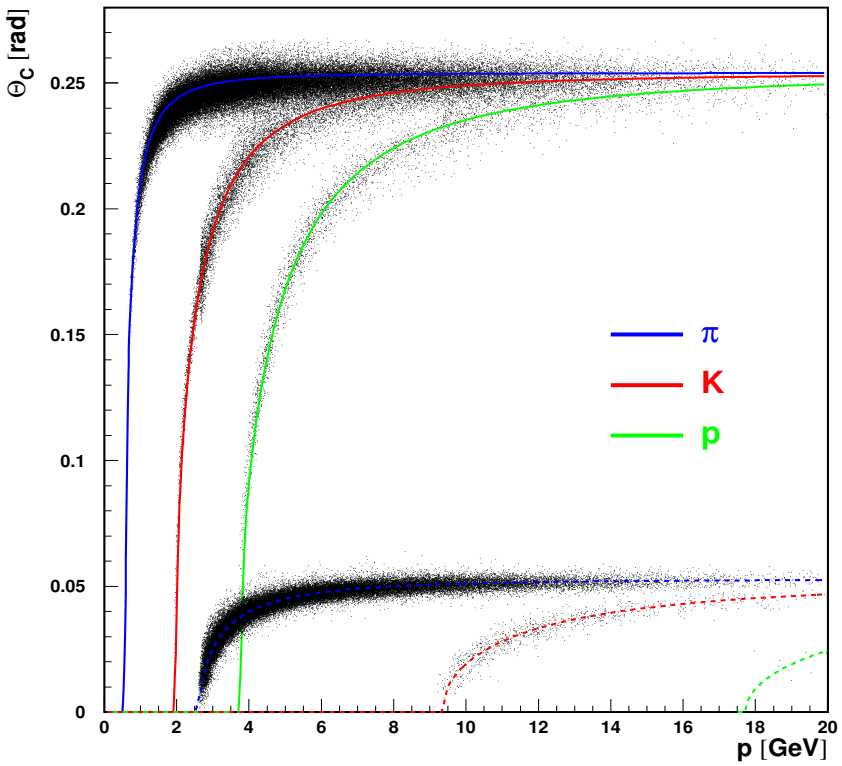

Figure 3.7: Distribution of reconstructed angles in the HERMES RICH. The upper triplet of curves corresponds to aerogel events, and the lower to gas events. From left to right the contours in each case are for π, K and p.

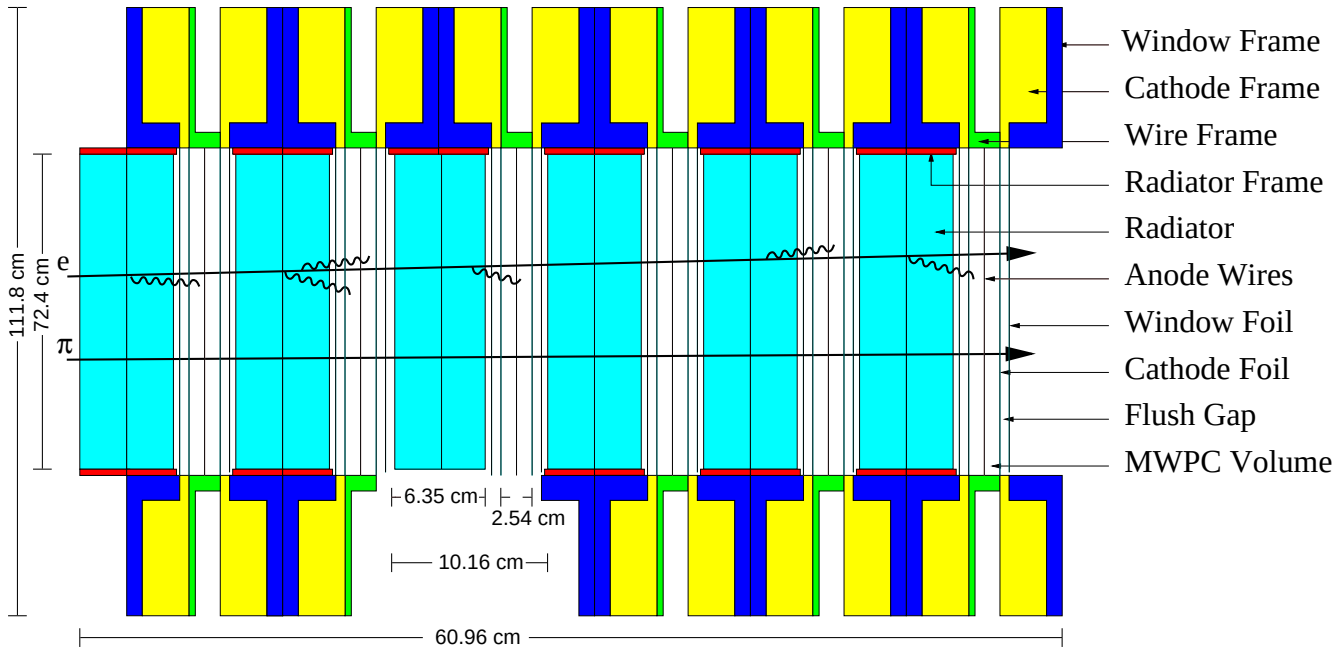

Figure 3.8: Side view of the TOP half of the TRD: when an electron track and a pion track pass through the six modules of the TRD, only the electron is emitting transition radiation photons.

For the hadron identification with the RICH, two different concepts are employed: *Indirect Ray-Tracing Method (IRT) and Direct Ray-Tracing Method (DRT).* (The technical details will be left for the next chapter).

Transition Radiation Detector (TRD). The Transition Radiation detector (TRD) [45] is mainly used to distinguish the electrons from the hadrons. The transition radiation is emitted when a relativistic particle is propagating through the boundary between materials with different dielectric constant ϵ. The threshold is related to the Lorentz factor and lies at about $\gamma = E/mc^2 = 100$. For leptons and hadrons with energy of 5 GeV, the factors are $\gamma_l \approx 10000$ and $\gamma_h \approx 35$, so that only leptons emit transition radiation. For ultra-relativistic particles the radiation is in the range of X-rays. Due to low emission probability in a single boundary, the HERMES TRD was build with six identical layers in a sandwich-like structure Fig. 3.8, each module consisting of a radiator of polypropylene fibers with a diameter of about $20\mu m$ followed by a proportional wire chamber filled with a mixture of 90% Xe and 10% CH_4. In the wire chambers both leptons and hadrons produce a signal due to ionization losses, but only leptons emit the transition radiation, therefore two distinct peaks can be observed in the TRD response, as in the left plot of Fig. 3.9, when the response of the six modules is combined.

A high-energy lepton or photon, when passing through a thick absorber initiates an electromagnetic shower by means of bremsstrahlung and pair production, generating more leptons and photons of lower energy. The secondary leptons and photons continue to produce a cascade of particles until their energy falls below the critical energy ($\sim 100\ MeV$), when they start to

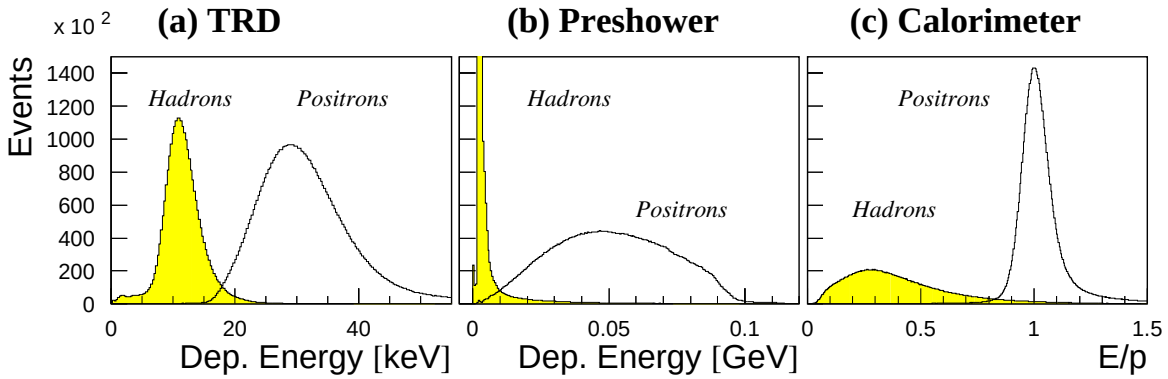

Figure 3.9: Responses of three PID detectors: Number of counts for positrons (empty histograms) and hadrons (shaded histograms) in TRD, hodoscope H2 and the calorimeter.

dissipate their energy primarily by ionization and excitation rather than by the generation of new shower particles. The characteristic scale of an electromagnetic cascade is the so called radiation length X_0, defined as the mean distance over which a high energy lepton looses all except $1/e$ of its energy by Bremsstrahlung. On the contrary the hadrons, due to their higher mass, loose energy mostly through inelastic collisions, and this results in a much slower energy dissipation of hadrons with respect to the leptons. This difference was exploited both by the preshower detector and the Calorimeter to identify the lepton and the hadron among the detected particles.

The preshower hodoscope. In the back spectrometer region there are two identical plastic scintillator hodoscopes, H1 and H2, that, together with the front-region hodoscope H0, are used for the physics triggers and for time of flight measurements. Both hodoscopes consist of 42 vertical scintillator panels with a width of 9.3 cm, that overlap by 1.5 mm to avoid acceptance gaps. The hodoscope H2 is preceded by 1.1 cm of lead, corresponding to two radiation lengths (see Fig. 3.10).

While hadrons deposit only a few MeV in this detector, showering electrons or positrons give rise to a much higher signal, initiated by electromagnetic showers that will develop in the adjacent calorimeter, and for this reason it was called preshower detector. The energy deposition in the preshower from leptons and hadrons are shown in the middle plot of Fig. 3.9: hadrons are responsible for the peak below 5 MeV, while the deposit of leptons is higher in average (about 20-60 MeV) and broader.

The electromagnetic calorimeter. Similar to the preshower detector the calorimeter exploits the difference in energy loss of leptons and hadrons to identify the particles detected. Each half of the HERMES calorimeter consists of 420 lead-glass blocks each with an area of 9x9 cm^2 (Fig. 3.10), coupled to a photomultiplier. The lead-glass thickness of 50 cm, corresponding to 18 radiation lengths, combined with the lead plate of H2, guarantees the electromagnetic showers to be almost fully contained within the preshower and the calorimeter. The energy

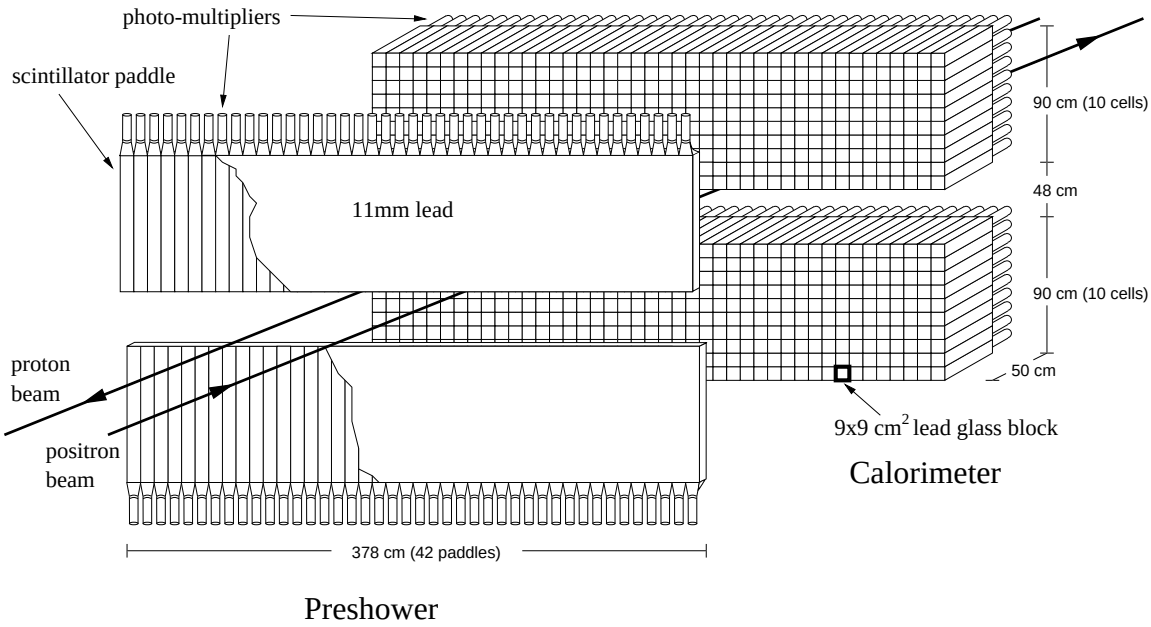

Figure 3.10: Overview of the preshower and the calorimeter.

deposited in the preshower and the calorimeter divided by the particle momentum is very close to 1 for electrons and positrons , while is much less than 1 for hadrons, as shown in the right plot of Figure 3.9.

To avoid radiation damage each calorimeter half is moved 50 cm away from the beam pipe vertically during the beam injection.

3.4 Data Structure and Data Acquisition System

In the following section a brief overview over the structure of the HERMES data and its data acquisition system is given. The purpose is mainly to introduce some jargon used in this work; and also for completeness. Ref. [45] contains more information about the particle tracking and the read-out electronics. A detailed review of the HERMES data processing can be found in [19].

3.4.1 Data structure

The largest logical unit to group the HERMES data is given by the *data taking period*, usually labeled by the year of running. It is basically defined by the time between to major shutdowns, in which HERMES is running with a fixed configuration. During major shutdowns experimental components might change, e.g. by the addition or replacement of detectors. Also HERA might change its operation mode, like for example switching from positron to electron running. The data taken during one period is processed several times, taking advantage of increased understanding of the experimental conditions. This *productions* are labeled with the data

taking period and a letter denoting the production generation. The data in this thesis was taken from 96d0, 97d1, 98d1, 99c1, 00d2 productions.

The next unit - the *fill* - is defined by the operation of the HERA storage ring. During one fill, the shift crew might switch operation modes, a common example is the switch from normal polarized running to unpolarized running with a high-density gas target at the end of fill.

When HERMES is running, the recorded data are stored in chunks of about 460 MByte size, the *runs*. A new run is also started by the shift crews when the conditions change considerably, e.g., when switching from normal to high-density target operation.

Runs are divided into 10 second units called *burst*. In these intervals, slowly varying quantities like beam current and target polarization are read out and stored in the slow control data tables.

3.4.2 Data Acquisition and Production

Particles of numerous sources are traversing the spectrometer at any given time, causing signals in the various detectors. A trigger system is used to filter out events whose structures indicate a physical process of interest. If a trigger is generated, a read out of all detector components is initiated. During the read out, no new data can be accepted, so that the number of generated and accepted triggers might differ. The ratio defines the dead time correction of the experiment:

$$\delta_{dead} = 1 - \frac{T_{acc}}{T_{gen}}. \tag{3.4}$$

Several triggers are defined, requiring different sets of signals. *Trigger 21* is the main physics trigger, designed to filter out DIS events from the background noise. It requires:

- Coincident signals in the hodoscopes H0, H1 and H2;
- An energy deposition in the calorimeter above a certain threshold (usually 1.4 GeV for polarized and 3.5 GeV for unpolarized operation). This signal is usually caused by the scattered beam particle;
- A reasonable timing of the signals. This filters out e.g., particle showers initiated by the proton beam which go backwards in the detector.

The detector read out is performed by the data-acquisition system (DAQ). At this stage, the data is still in a raw format, containing channel numbers and digital signal values stored in the EPIO format (Experimental Physics Input Output Package). In the first step, the data is converted by the HERMES decoder (HDC) into the ADAMO format. HDC takes into account further input like calibration data and information about the detector geometry, which are optimized with each generation of data production.

The numerous read-out values of the different components have to be converted into information which is usable for the data analysis. This is done by the HERMES reconstruction software (HRC). Using a tree-search algorithm, particle tracks are reconstructed from the hit locations in the wire chambers. By combining the front and back partial tracks, the momentum is determined [54]. Based on the reconstructed tracks, the responses of the individual PID detectors are associated with the corresponding particles.

Apart from the time-critical detector signals, there are other parameters of interest which are only slowly changing over time. These values are recorded by the slow control system. Examples are information about the state of the HERA beam (current, polarization, ..) as well as various HERMES operation parameters like voltages, target state and pressure gauges. The parameters are read out in regular intervals in the order of seconds or minutes, and stored chronologically in ADAMO tables. One file per fill is produced. Similar to the physical data, the slow control data is subsequently supplemented with additional expert information (e.g. smoothed polarimeter measurements).

The last step of the data production combines the HRC output and the slow control data to provide a uniform source of information for the analysis programs. During this step, the amount of data is further reduced by leaving out information only relevant for detector studies and not for physics analysis. Also the particle identification is performed at this point, relying on the PID detector responses and calibration information provided by the detector experts. Further input is concerned with data quality. The detector experts identify periods with faulty or unreliable detector operation. The corresponding data sets are marked accordingly or even left out of the production. The output is stored run-wise in so called μDST (micro Data Summary Tape) files, which are then used as input for the physics-analysis programs.

Chapter 4

Data Selection and Particle Identification

The analysis presented in this thesis is based on data collected with the longitudinally polarized hydrogen and deuterium targets in the years 1996 through 2000. In the first part of this chapter, the selection of the high-quality data that were used for physics analysis is discussed. The second part of the chapter describes the process by which the individual events and tracks contained in the HERMES μDST data files are interpreted, selected or rejected, and counted in various kinematic bins to produce yield histograms of a particular data quality and particle identity.

To ensure good quality of the analyzed data, numerous cuts and requirements are necessary. As a first step, a run list is compiled which selects the data taking periods with the desired target gas type and operation modes. The available run information also allows a first selection on the data quality, since data runs with unstable or unclear experimental conditions can be excluded. All cuts can be divided into three groups:

- *Burst level cuts* ensure an overall good performance of HERA, the target and spectrometer.
- *Event level cuts* select (as much as possible) DIS events from the data and avoid specific kinematic regions, like e.g., the region of nucleon resonances.
- *Track level cuts* require that the individual particle tracks originate in the target chamber and traverse the spectrometer within the geometrical acceptance, avoiding problematic regions at the edge of the detector acceptance.

4.1 Burst-level data selection

As already mentioned above, burst-level cuts aim to guarantee that all important detector and target components were operational and working. There are different soures of information on which these decision are based. Many parameters, such as target operation mode, beam conditions, burst length etc. are recorded by the slow control part of the data acquisition. Furthermore, the data-quality group and the detector experts collect information from logbook

Table 4.1: Burst-level data quality requirements.

DataQuality Flag	Burst Selection criteria	*DataQuality Flag*	Burst Selection criteria
0	Target spin parallel or antiparallel to beam	18	Hodoscope H2 or luminosity monitor are good.
1	Smoothed beam polarization $30\% < P_B < 80\%$	19	TRD data quality good.
2	Reasonable DAQ dead-times.	20	No high voltage trips in wire chambers.
3	Reasonable burst lengths.	21	Various problems by year (target, tracking, calorimeter or RICH).
4	Beam current reasonably large.	22	No trips in RICH.
5	Varies by year. Count rates or target density fluctuations reasonably.	23	α_0[5] value is reasonable.
6	First burst of each run rejected.	24	α_R[6] value is reasonable.
7	Last burst of each run and bursts with undefined DAQ state rejected.	25	Čerenkov or RICH data quality good.
8	Varies by year. Nominal DAQ or PID detector states.	26	Various. Runs are rejected due to synchronization, read out, or high voltage problems.
9	Runs marked analyzable by shift crew.	27	Valid target polarization measurement by BRP.
10	Polarized target mode.	28	Beam polarization measurement not older then five minutes.
15	Polarized target mode (determined from value state of target).	29	Target magnet current in reasonable range.
16	Target state good.	30	Dead-time in reasonable range.
17	All calorimeters blocks good.	31	This cut rejects data with low α_R values.

entries, data quality analyses and other sources to identify periods with non-working or unreliable equipment. This knowledge is encoded in status bit patterns which can be checked by the analyzer in the program. The data quality criteria are listed in Table 4.1.

[5]The atomic fraction for the gas injected into cell by ABS. This quantity indicates the degree to which the dissociator works and the recombination with the ABS structure.

[6]The atomic fraction for the gas which recombine in the target cell.

4.2 Particle identification

Particle identification (PID) is a crucial part of any analysis, especially if - like in this case - a clean separation of different hadron types is required. Based on the fact that different particle types produce different responses in the PID detectors (see Chap. 3.3.2), the combination of these signals allows for a highly efficient discrimination of leptons and hadrons. In a second step, tracks identified as hadrons are further classified as pions, kaons and protons, depending on the measured Čerenkov opening angles in the RICH detector.

4.2.1 Discriminating leptons and hadrons

From each response of the four PID detectors it is possible to define the probability for a particle to be an electron (positron) or a hadron. For each PID detector D it is possible to define the probability $P_D(T, p|X)$ that a particle of type T with momentum p causes the detector response X. The particle type T can be *lepton (l)* or *hadron (h)*, and the response X corresponds to the Čerenkov angle θ_c in case of the RICH, or to the particle's energy deposition for the other detectors. The $P_D(T, p|X)$, called the *parent distribution*, can be determined by measuring the detectors response to a clean sample of leptons or hadrons, that are selected by imposing hard requirements on the PID detectors other than the one under consideration. If $P(p|T)$ is the probability that a particle with momentum p is of type T then the Bayes theorem provides the probability for the measured detector response X originated by a particle with momentum p, to be caused by a particle type T:

$$P_D(X, p|T) = \frac{P(p|T) \cdot P_D(T, p|X)}{\Sigma_T P(p|T) \cdot P_D(T, p|X)}. \tag{4.1}$$

Hence the probability that the measured response X in the detector D is due to a lepton l (hadron h) with momentum p becomes:

$$P_D(X, p|l(h)) = \frac{P(p|l(h)) \cdot P_D(l(h), p|X)}{P(p|l) \cdot P_D(l, p|X) + P(p|h) \cdot P_D(h, p|X)}, \tag{4.2}$$

where $P(p|l(h))$ corresponds to the incident lepton and hadron fluxes $\phi_{l(h)}$.

The probabilities described in Eq. 4.2 for the lepton and the hadron can be combined into a logarithmic ratio:

$$PID'_D = log_{10} \frac{P_D(X, p|l)}{P_D(X, p|h)} \tag{4.3}$$

that in terms of *parent distributions* and lepton-hadron fluxes becomes:

$$PID'_D = log_{10} \frac{P_D(l, p|X) \cdot P(p|l)}{P_D(h, p|X) \cdot P(p|h)} = PID_D - log_{10}\Phi, \tag{4.4}$$

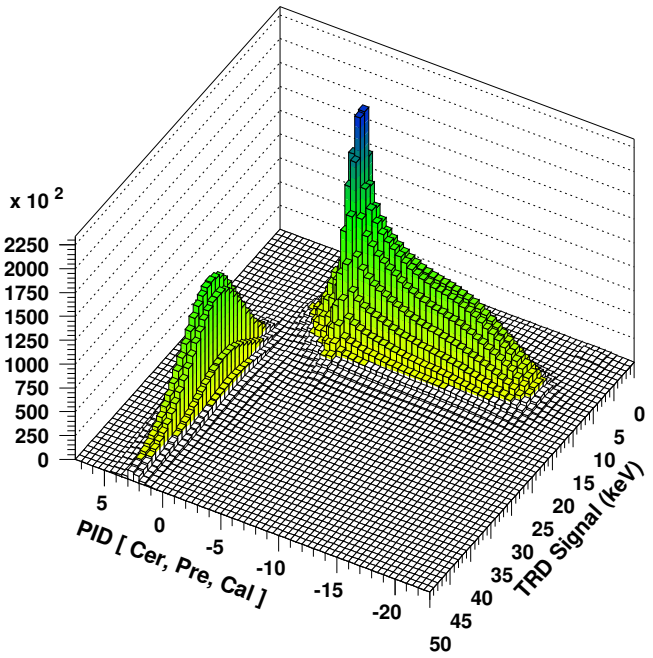

Figure 4.1: A 3-dimensional view of the positron-hadron separation due to all the four PID detectors.

where

$$PID_D \equiv log_{10} \frac{P_D(l,p|X)}{P_D(h,p|X)}. \tag{4.5}$$

The flux factor Φ is:

$$\Phi \equiv \frac{P(p,l)}{P(p,h)} = \frac{\phi_l}{\phi_h}, \tag{4.6}$$

where ϕ_l and ϕ_h are the particle fluxes of leptons and hadrons respectively. This factor is computed and made available in a set of tables for each year. These tables are computed by PID experts using an iterative technique by which responses of the different PID subsystems are compared with another one. Applying this process separately for each year's dataset helps to control uncertainties associated with the aging of the experimental apparatus.

The responses of the four PID detectors can be combined to maximize the sensitivity to the particle type. The combination commonly used at HERMES are:

$$\begin{aligned} PID_2 &\equiv PID_{calo} + PID_{pre}, \\ PID_3 &\equiv PID_{calo} + PID_{pre} + PID_{RICH}, \\ PID_5 &\equiv PID_{TRD} = \textstyle\sum_{i=1,6} PID_{TRDi}, \end{aligned} \tag{4.7}$$

where for the TRD the sum runs over the six modules in each detector half. Taking into account the flux factor and all the detector responses the standard criteria used at HERMES for the

Table 4.2: Beam, target and Čerenkov detector type for each year of HERMES running.

Year	Beam	Target	Hadron ID
1996	e^+	H_2	Threshold Čerenkov
1997	e^+	H_2	Threshold Čerenkov
1998	e^-	D_2	RICH
1999	e^+	D_2	RICH
2000	e^+	D_2	RICH

lepton-hadron separation are:

$$\begin{aligned} PID_3 + PID_5 - log_{10}(\Phi) > \ 1 \qquad & leptons \\ PID_3 + PID_5 - log_{10}(\Phi) < \ 0 \qquad & hadrons, \end{aligned} \tag{4.8}$$

where the interval between 0 and 1, corresponding to a poor identification, is eliminated from the data sample. With the use of the above criteria the efficiency in lepton-hadron separation is larger then 98% and the cross-contaminations smaller than 1%. A 3-dimensional view of the positron-hadron separation using PID_3 and PID_5 is shown in Fig. 4.1.

A detailed description of particle identification and PID probabilistic algorithm at HERMES can be found in Ref. [55].

4.2.2 Identification of hadrons with the RICH

As described previously, of the five years of running with longitudinally polarized H and D targets, hadron identification was performed using a threshold Čerenkov detector for the first two and by the ring imaging Čerenkov detector (RICH) for the latter three (see Tab. 4.2).

The Threshold Čerenkov (1996-1997). Interpreting the response of the threshold Čerenkov counter is relatively straightforward. Each track in the data files has an entry which corresponds to the number of photons, N_γ, in the Čerenkov associated with that track. The number of photons produced by Čerenkov radiation is a function of the momentum and mass of the particle. Moreover, there is a characteristic threshold momentum for each type of particle, below which no photons are produced.

This detector was designed to distinguish pions from heavier hadrons. To do this, tracks (previously identified as hadrons) in a specific momentum range are selected. $p_h > 4\ GeV$ to be just above the pion Čerenkov threshold. For $p_h > 13.8\ GeV$ the kaon threshold is reached and the pion sample becomes contaminated. Finally, $N_\gamma > 0.25$ is required to select pion tracks that are well differentiated from the noise associated with heavy hadron tracks, that produce

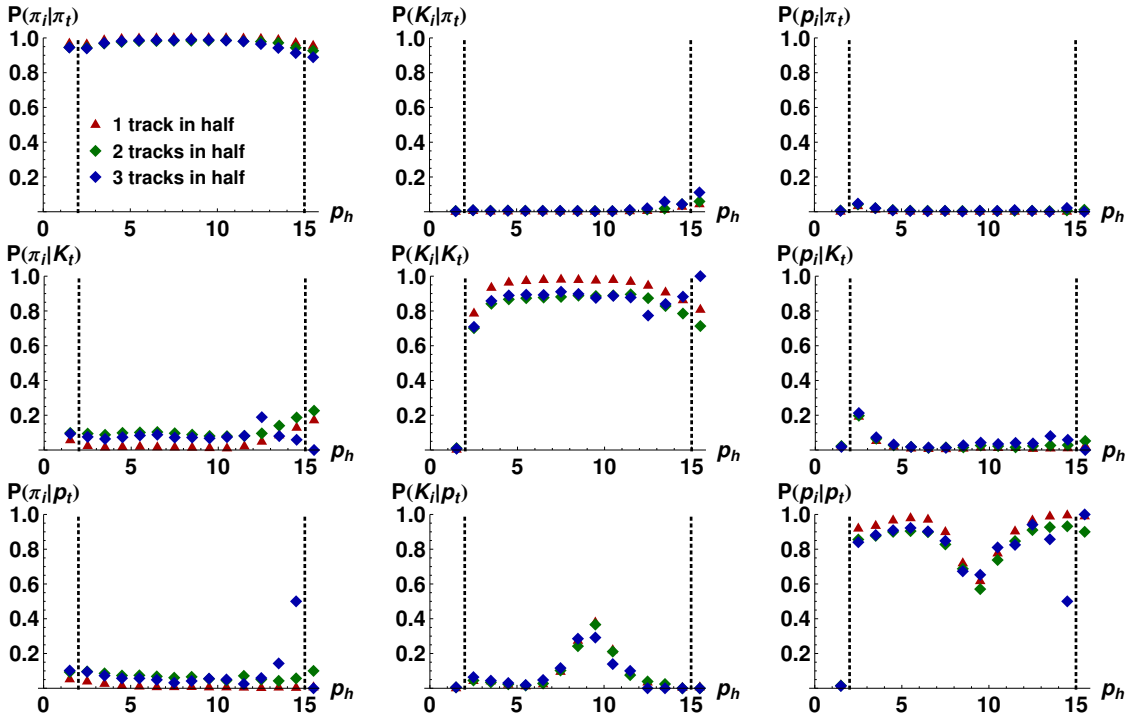

Figure 4.2: The p-matrix represents the conditional probability that a hadron of true type h_t will be identified by the RICH as type h_i. The momenta p_h are given in GeV.

little or no response in the detector.

The RICH (1998-2000). The dual-radiator ring imaging Čerenkov counter (RICH) replaced the threshold Čerenkov in 1998. Because of its careful selected radiator materials, it has the ability to differentiate pions, kaons and protons over the momentum range $2\ GeV < p_h < 15\ GeV$. While for the threshold Čerenkov counter a hadron track is designated either a pion or a heavier hadron, with the RICH a probability is produced for each of the three possible hypotheses: pion, kaon or proton. As described below, weights are calculated for each hypothesis and fractional counts are then recorded in yield histograms during data analysis.

While the RICH produces a single favored hypothesis for each track, a *P-matrix* is provided by the HERMES RICH group which is used to produce weights for all different hypotheses, providing more accurate yields. The P-matrix contains the conditional probabilities, $P(h_i|h_t)$ that a hadron of true identity, h_t, is identified by the RICH as being of type h_i. The probability entries of the P-matrix are plotted in Fig. 4.2. From this, one obtains:

$$\vec{N}_i = P\vec{N}_t, \tag{4.9}$$

where

$$\vec{N}_i = \begin{pmatrix} N_i^\pi \\ N_i^K \\ N_i^P \end{pmatrix}, \ \vec{N}_t = \begin{pmatrix} N_t^\pi \\ N_t^K \\ N_t^P \end{pmatrix}, \ and \ P = \begin{pmatrix} P(\pi_i|\pi_t) & P(K_i|\pi_t) & P(P_i|\pi_t) \\ P(\pi_i|K_t) & P(K_i|K_t) & P(P_i|K_t) \\ P(\pi_i|P_t) & P(K_i|P_t) & P(P_i|P_t) \end{pmatrix}, \quad (4.10)$$

$N_{i(t)}^h$ being an identified (true) yield of hadron of type h. The true yield of identified hadrons can be obtained by inversion of the P-matrix:

$$P^{-1}\vec{N}_i = \vec{N}_t. \quad (4.11)$$

Because of this, the inverted P-matrix can be applied to the RICH's hypothesis to produce the vector of weights to be added to the final hadron yield histograms. It should be noted that unlike the P-matrix, P^{-1}, sometimes referred to as the $Q-matrix$ doesn't contain probabilities. It's entries need not be bounded by one and can also be negative.

The procedure for processing the RICH response is as follows:

- The rQp (RICH Quality Parameter) value is checked.

$$rQp \equiv log_{10}\frac{P(h_1)}{P(h_2)}, \quad (4.12)$$

  where $P(h_1)$ and $P(h_2)$ are the probabilities of the RICH's first and second hadron hypothesis for the observed response pattern. If rQp is zero, more than one track identity hypothesis could have produced the observed pattern with equal likelihood in which case the track is rejected.

- The $iType$ value is checked. The value of this variable represents the hypothesis most favored by the response of the detector to the track.

- The inverted P-matrix is consulted which contains the appropriate true pion, kaon and proton weights for each observed $iType$, track momentum bin and track multiplicity in each detector half.

- Finally, for each of the three possible hadron identities, kinematic variables that depend on the hadron's mass must be computed. This means that for certain semi-inclusive variables, z and x_F for example, the fractional counts for the different hadron hypotheses may be placed in different kinematic bins.

4.3 Event selection

In addition to the responses of the PID detectors, the μDST files contain several parameters for each track including vertex position, vertex angle, momentum, charge and the position and angle of the track leaving the spectrometer magnet. Once the lepton-hadron separation is complete and a track is designated to be the scattered lepton, it can be used to compute inclusive parameters for the event.

4.3.1 Inclusive requirements

The cuts imposed to identify DIS events are listed in Table 4.3. If more than one lepton track passes all DIS cuts, the lepton with the highest energy is taken as the scattered one.

With a fixed beam energy, a DIS event can be described completely with two parameters. Q^2 and Bjorken-x are common choices. The fraction of the beam energy carried by the virtual photon, y, and the invariant mass of the hadronic final state, W, also computed. These additional variables have particular physical meanings and while they are completely constrained by x and Q^2, allow to place specific physical restrictions on the data sample.

The first requirement is imposed through $Q^2 > 1\ GeV^2$. This requirement allows to believe that we have a probe of sufficiently small wavelength to resolve the substructure of the nucleon (whose mass and size correspond to 1 GeV). In other words, Q^2 represents the *scale* of the interaction.

To extend the kinematic range to low values of x, a lower cut of $Q^2 < 0.5\ GeV^2$ is used. At the same time the binning is chosen such that the traditional DIS region $Q^2 > 1\ GeV^2$ can easily be separated from the region $0.5\ GeV^2 < Q^2 < 1\ GeV^2$. A large invariant mass of the hadronic final state $W^2 > 10\ GeV^2$ further rejects events from the resonance region of the photon-nucleon system. This cut additionally improves the separation of the target and current fragments for the identification of the semi-inclusive hadrons. Finally the requirement $y < 0.85$ rejects DIS events in a region where the contribution by higher order QED effects to the cross section is large.

The distribution of the selected DIS events is shown in Fig. 4.3 in the kinematic $x - Q^2$ plane.

4.3.2 Geometric requirements

To ensure that the events originate from interactions of the positron beam and the target, geometrical cuts are applied. The location of the target cell was between $-20\ cm < z < 20\ cm$ in the present analysis. A cut of $|z_{vertex}| < 18\ cm$ efficiently selects events originating from the target cell. A less restrictive cut on the radial distance between reconstructed track and beam is applied at $d_{vertex} < 0.75\ cm$.

Table 4.3: Inclusive kinematic requirements.

Variable	Requirement	Reason
Squared invariant mass of the virtual photon	$0.5 < Q^2 < 1\ GeV^2$	To extend the kinematic range to low values of x
	$Q^2 > 1\ GeV^2$	Virtual photon momentum of suitable scale to resolve the nucleons substructure
Invariant mass of the final hadron state	$W^2 > 10.0\ GeV^2$	Exclude the resonance region of the photon-nucleon system
Fractional energy transfer	$y < 0.85$	Constrain the influence of higher order QED effects

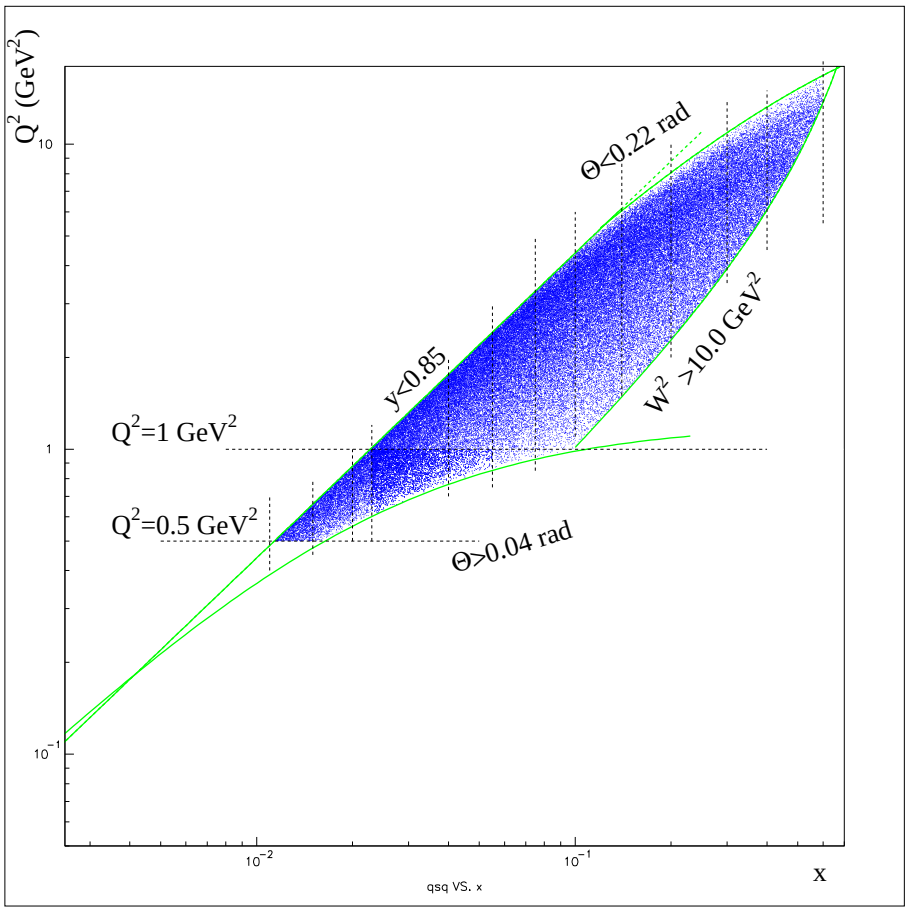

Figure 4.3: The distribution of the selected DIS events in the $x - Q^2$ plane.

Table 4.4: Geometric requirements for inclusive and semi-inclusive events.

Variable	Requirement	Reason
$\lvert z_{vertex}\rvert$	$< 18\ cm$	Lepton originated inside target cell.
d_{vertex}	$< 0.75\ cm$	Event originated from the beam.
p	$> 0.5\ GeV$	Lower limit of spectrometer momentum acceptance.
x_{calo}	$< 175\ cm$	Energy deposition inside of active calorimeter volume.
y_{calo}	$> 30\ cm$	
y_{calo}	$< 100\ cm$	
$\lvert x_{z=172cm}\rvert$	$< 31\ cm$	Track inside front clamp aperture.
$\lvert y_{z=181cm}\rvert$	$> 7\ cm$	Track clears septum plate.
$\lvert x_{z=383cm}\rvert$	$< 54\ cm$	Track inside rear field clamp aperture.

The geometric acceptance of the HERMES spectrometer covers a polar region between $0.04\ rad < \theta < 0.22\ rad$ for events originating in the center of the target. Since the geometric acceptance depends on the longitudinal vertex position z_{vertex} and the magnet bend of a particular track, no general cuts are imposed on the angular acceptance of the detector. The *fiducial volume cuts* are more accurately applied to the individual front and back partial tracks in order to exclude tracks going through the magnet-chamber frames or hitting the field clamps in front or behind the spectrometer magnet. Furthermore, a vertical inner cut is applied to exclude the volume of the septum plate. The requirements are summarized in Tab. 4.4.

4.3.3 Semi-inclusive requirements

To select a SIDIS event it is required that the track with highest momentum is identified as a lepton by the PID algorithm (sec 4.2.1): $PID_3 + PID_5 - log_{10}\Phi > 1$. In coincidence with the lepton, a second track, identified as a hadron ($PID_3 + PID_5 - log_{10}\Phi < 0$), should satisfy requirements on the SIDIS kinematics.

Semi-inclusive hadron measurements are a method to directly separate the spin content of the different quark flavors. There are two variables which will provide an indication of the *forwardness* of a given hadron by which we mean its likelihood to contain the struck quark. The first, z, is simply the ratio of the energy carried by the hadron to the energy of the virtual photon:

$$z = \frac{E_h}{\nu} = \frac{\sqrt{p_h^2 + M_h^2}}{\nu}. \tag{4.13}$$

The second indicator of forwardness, x-Feynman, or x_F, is defined to be the ratio of the momentum, parallel to the q-vector, to its maximum possible value in the center-of-mass reference frame of the virtual photon and the struck nucleon.

Table 4.5: Semi-inclusive requirements.

Variable	Requirement	Reason
z	> 0.1	Select a sample strongly correlated with a struck quark.
	< 0.8	Reject exclusive events - not DIS
x_F	> 0.1	Further emphasis on current fragmentation region.
z_{vertex}	$< 100\ cm$	Include hadrons produced from downstream decays (e.g. K_s).
$\mathrm{p}^{hadrons}$	$> 0.5\ GeV$	Momentum cuts for hadrons
$\mathrm{p}^{pions}_{\check{C}erenkov}$	$> 4\ GeV$	Momentum cuts for pions identified
	$< 13.8\ GeV$	by Čerenkov detector.
$p^{pions,kaons}_{RICH}$	$> 2\ GeV$	Momentum cuts for pions and kaons
	$< 15\ GeV$	by HERMES RICH detector

Semi-inclusive hadrons were selected from the data sample with a cut on the fractional energy of the hadron, $0.1 < z < 0.8$, and a cut on x-Feynman, $x_F > 0.1$. The lower boundaries of both requirements in combination lead to a large probability that the hadron is part of the current fragments that contain the struck quark. The upper boundary on z discarded hadrons from exclusive events such as diffractive vector meson production, where the virtual photon fluctuates into an (off-shell) $q\bar{q}$ pair which is scattered onto the mass shell by diffractive interaction with the target. For hadrons, the requirement $z_{vertex} < 100\ cm$ is relaxed to allow for the possibility that these hadrons were not produced in the primary interaction in the target cell, but subsequently by decay of one of the primary hadrons (e.g. K_s). The semi-inclusive requirements are summarized in Tab. 4.5.

The numbers of the DIS events and the SIDIS hadrons are summarized in Tab. 4.6 after applying all the inclusive and semi-inclusive DIS cuts.

4.4 Binning

One of the main points of this work was to present a multi-dimensional analysis of the measured double-spin asymmetries. In a multi-dimensional analysis, more information can be found about kinematical dependences of the measured asymmetries. Nevertheless, the number of bins should be compatible with the limited statistics provided by the experiment. For the event sample, presented in this analysis, the different possibilities for bin selection in different combinations of variables are given.

1-dimensional or traditional binning In the HERMES kinematic region of $0.023 < x < 0.6$ and $1.0\ GeV^2 < Q^2 < 15.0\ GeV^2$, for the given value of x, the polarized structure function

Table 4.6: Count numbers of DIS leptons and SIDIS hadrons for the hydrogen and deuterium data.

	Proton target		Deuteron target	
	$Q^2 > 1\ GeV^2$	$Q^2 < 1\ GeV^2$	$Q^2 > 1\ GeV^2$	$Q^2 < 1\ GeV^2$
DIS $e^\pm$	1,851,038	621,729	6,944,361	2,304,074
h^+	415,546	137,843	1,540,506	521,577
h^-	252,118	99,992	1,056,008	412,466
π^+	131,784	54,339	1,036,338	397,301
π^-	92,945	44,191	862,496	359,556
K^+			152,339	47,907
K^-			69,482	27,704

g_1 [14] is independent of Q^2 or has only a weak dependence on Q^2 as it is the case for the unpolarized structure function F_1 [27]. In the Bjorken limit, the photo-absorption asymmetry A_1 depends only on x:

$$A_1^{(h)} \overset{g_2=0}{\simeq} \frac{g_1^h(x,Q^2)}{F_1^h(x,Q^2)} \to A_1^{(h)}(x). \tag{4.14}$$

Therefore the measurements of the asymmetries can be performed in each x bin defined in Table A.1.

For the case of x-binning, it was important to produce the result, which can be compared easily to those produced in the past by other HERMES collaborators. To extend the kinematic range to low values of x, 4 x-bins were chosen in addition for the low-Q^2 kinematic region ($0.5\ GeV^2 < Q^2 < 1\ GeV^2$). This binning was used for the extraction of quark polarizations and quark helicity distribution functions, described in Chap. 6.

2-dimensional or $x - p_{h\perp}$ binning This binning was used to produce semi-inclusive asymmetries with 18 bins ($3x \times 6p_{h\perp}$) to compute the $p_{h\perp}$ dependence of the A_1^h. The result is presented in x-slices, to account for the strong $xp_{h\perp}$ correlation. The bin edges are given in Table B.1.

3-dimensional $x - z - p_{h\perp}$ binning For the three dimensional binning 3 intervals in z and 3 intervals in $p_{h\perp}$ were used in addition to the traditional x binning described previously. This binning was used for the semi-inclusive yields. They have 81 bins each ($9x \times 3z \times 3p_{h\perp}$) where the inclusive yields still have the nine traditional x bins. The bin limits are presented in Table C.1. The average values of x, z and $p_{h\perp}$ for 3-dimensional binning are presented in App. C.

The quark polarization and quark helicity distribution functions were extracted using 3-dimensional binning in addition and the comparison with the result from traditional binning in Chap. 6 is presented.

2-dimensional $x - Q^2$ binning In addition to the simple 1-dimensional x binning, the set of asymmetries with 2-dimensional $x - Q^2$ binning has been added for completeness. The bin limits are presented in Table D.1. The average values of x, Q^2, z and $p_{h\perp}$ for 2-dimensional binning are presented in App. D.

Chapter 5

Double spin asymmetries

5.1 Determination of the double-spin asymmetries

As was mentioned in Chap. 2, the longitudinal double-spin asymmetry $A_{||}(x, Q^2)$ is defined as the difference of the cross sections for anti-parallel $\sigma^{\vec{}}_{\Leftarrow}$ and parallel $\sigma^{\vec{}}_{\Rightarrow}$ alignments of the beam and target spins, normalized to the sum of these two cross sections:

$$A_{||}(x, Q^2) = \frac{\sigma^{\vec{}}_{\Leftarrow} - \sigma^{\vec{}}_{\Rightarrow}}{\sigma^{\vec{}}_{\Leftarrow} + \sigma^{\vec{}}_{\Rightarrow}}. \tag{5.1}$$

The unpolarized differential cross section σ_0 equals the average of the polarized cross sections:

$$\sigma_0 = \frac{1}{2}(\sigma^{\vec{}}_{\Leftarrow} + \sigma^{\vec{}}_{\Rightarrow}). \tag{5.2}$$

Here σ_0, $\sigma^{\vec{}}_{\Leftarrow}$ and $\sigma^{\vec{}}_{\Rightarrow}$ indicate the differential cross section $\frac{d\sigma_0}{dxdQ^2}$, $\frac{d\sigma^{\vec{}}_{\Leftarrow}}{dxdQ^2}$ and $\frac{d\sigma^{\vec{}}_{\Rightarrow}}{dxdQ^2}$ respectively.

The measured experimental asymmetry $A_{||}^{exp}(x, Q^2)$ is proportional to the asymmetry $A_{||}(x, Q^2)$:

$$A_{||}^{exp}(x, Q^2) = f \cdot P_B \cdot P_T \cdot A_{||}(x, Q^2), \tag{5.3}$$

where f is the target dilution factor, P_B and P_T denote the beam and target polarizations, respectively. The target dilution factor f is the cross section fraction that is due to polarizable nucleons in the target. For the polarized pure hydrogen gas target at HERMES $f_H = 1$, which is unique compared to all other previous experiments on polarized DIS. Other experiments (SMC [56], E143 [39], etc.) use polarized solid state targets with dilution factor in the range of $f \simeq 0.04 \rightarrow 0.2$, which significantly reduced the size of their measured experimental asymmetries. As the present analysis only deals with data taken on polarized proton and deuteron targets, f_H is neglected, $f_D = 1 - \frac{3}{2}\omega_D = 0.925$ is used, where $\omega_D = 0.05$ represents the deuteron D-state probability.

The cross section asymmetry $A_{||}$ given in Eq. 5.1 can be related to the measured number of counts in two configurations of beam and target polarization. The number of inclusive events

$N^{\vec{\Leftarrow}(\vec{\Rightarrow})}$ and of semi-inclusive hadrons $N_h^{\vec{\Leftarrow}(\vec{\Rightarrow})}$ in the anti-aligned (aligned) configuration of beam and target polarizations is given by:

$$N_{(h)}^{\vec{\Leftarrow}(\vec{\Rightarrow})}(x,Q^2) = \sigma_0(x,Q^2)\int_{\vec{\Leftarrow}(\vec{\Rightarrow})} dt\mathcal{A}(t,x,Q^2)\mathcal{L}(t)\Big(1 \pm P_T(t)P_B(t)A_{||}^{(h)}(x,Q^2)\Big) \tag{5.4}$$

where the negative sign is for the parallel configuration. The unpolarized cross section σ_0 and the asymmetry $A_{||}^{(h)}$ are time independent, instead, $P_B(t)$ and $P_T(t)$ are time dependent. The acceptance of the spectrometer, $\mathcal{A}(t,x,Q^2)$, which includes any DAQ inefficiencies is assumed to be constant for each data-taking period, $\mathcal{A}(t,x,Q^2) \equiv \mathcal{A}(x,Q^2)$. The calculation of the luminosity $\mathcal{L}(t)$ is carried out using the response of the luminosity monitor. The following formula is used to calculate the luminosity for each burst:

$$\mathcal{L}(t) = < R_{lumi}(t) > \times C_{lumi}(year) \times A(target) \times \tau_{DAQ} \times t_{burst}. \tag{5.5}$$

Here $< R_{lumi}(t) >$ is the average rate measured by the luminosity monitor, C_{lumi} is a luminosity constant, a year dependent conversion factor. The luminosity constant comprises the acceptance of the luminosity monitor. As it depends on the beam parameters (positions and slopes) and charge, it is provided separately for each data taking year. The mass number of the target nucleus is indicated as A, τ_{DAQ} is the time-dependent efficiency factor accounting for dead time effects of the detectors, and t_{burst} is the length of the burst.

Equation 5.4 can be solved for $A_{||}$, eliminating the unpolarized cross section σ_0 and the acceptance $\mathcal{A}$. In terms of the numbers of counts, the asymmetry is given by

$$A_{||}^{(h)} = \frac{N_{(h)}^{\vec{\Leftarrow}} L^{\vec{\Rightarrow}} - N_{(h)}^{\vec{\Rightarrow}} L^{\vec{\Leftarrow}}}{N_{(h)}^{\vec{\Leftarrow}} L_P^{\vec{\Rightarrow}} + N_{(h)}^{\vec{\Rightarrow}} L_P^{\vec{\Leftarrow}}}, \tag{5.6}$$

for the inclusive asymmetry $A_{||}$ and the semi-inclusive asymmetries $A_{||}^h$ for various types of hadrons, $h = h^{\pm}, \pi^{\pm}, K^{\pm}$. The counts are normalized by the integrated luminosities $L^{\vec{\Rightarrow}}$ and $L^{\vec{\Leftarrow}}$,

$$L^{\vec{\Leftarrow}(\vec{\Rightarrow})} = \int_{\vec{\Leftarrow}(\vec{\Rightarrow})} dt\mathcal{L}(t). \tag{5.7}$$

Similarly $L_P^{\vec{\Rightarrow}}$ and $L_P^{\vec{\Leftarrow}}$ are the luminosities weighted by the target polarization $P_T(t)$ and the beam polarization $P_B(t)$ integrated over time t,

$$L_P^{\vec{\Leftarrow}(\vec{\Rightarrow})} = \int_{\vec{\Leftarrow}(\vec{\Rightarrow})} dt P_T(t)P_B(t)\mathcal{L}(t). \tag{5.8}$$

The photon-nucleon asymmetry A_1 can be written from the Eq. 2.38 as:

$$A_1 = \frac{1}{(1+\eta\gamma)} \cdot \frac{N^{\vec{\Leftarrow}} L^{\vec{\Rightarrow}} - N^{\vec{\Rightarrow}} L^{\vec{\Leftarrow}}}{N^{\vec{\Leftarrow}} L^{\vec{\Rightarrow}} D^{\vec{\Rightarrow}} + N^{\vec{\Rightarrow}} L^{\vec{\Leftarrow}} D^{\vec{\Leftarrow}}}. \tag{5.9}$$

The difference of the values for the depolarization factor $D^{\vec{\Rightarrow}}(D^{\vec{\Leftarrow}})$ for both relative orientations of the polarizations of beam and target was found to be negligibly small. Therefore, the statistical uncertainty δA_1 on the asymmetry A_1 is given as:

$$\sigma(A_1) = \frac{1}{(1+\eta\gamma)D}\sigma(A_{||}) = \frac{1}{(1+\eta\gamma)D} \cdot \frac{L^{\vec{\Rightarrow}}L_P^{\vec{\Leftarrow}} + L^{\vec{\Leftarrow}}L_P^{\vec{\Rightarrow}}}{(N^{\vec{\Leftarrow}}L_P^{\vec{\Rightarrow}} + N^{\vec{\Rightarrow}}L_P^{\vec{\Leftarrow}})^2} \sqrt{[N^{\vec{\Rightarrow}}\sigma(N^{\vec{\Leftarrow}})]^2 + [N^{\vec{\Leftarrow}}\sigma(N^{\vec{\Rightarrow}})]^2}. \tag{5.10}$$

The semi-inclusive asymmetries A_1^h are extracted in complete analogy to the inclusive A_1, with $N^{\vec{\Leftarrow}(\vec{\Rightarrow})}$ substituted by $N_h^{\vec{\Leftarrow}(\vec{\Rightarrow})}$, the number of events with a hadron of type h in coincidence with a electron.

It is necessary to notice, that the measured quantity in polarized DIS is $A_{||}$, related to A_1 by Eq. 2.38, where the depolarization factor D is obtained from the measured value of R. The information on the polarized parton distributions, whose extraction is the goal of this work, is based on the inclusive and semi-inclusive asymmetries. Therefore we need consistency between the normalization of the inclusive and semi-inclusive asymmetries. For the time being no experimental values of R^h are avaible and we have just assumed that the same values of R applies for both inclusive and semi-inclusive data.

5.1.1 Correction of yields

In this analysis the process of interest is the deep-inelastic scattering process. Some of the cuts discussed in Chap. 4.3 have been introduced to exclude the areas where the physics processes are dominated by resonance excitations. However, further measures have to be taken to suppress the influence of undesired processes.

Correction for charge symmetric background

One possible source of background contamination is the charge symmetric background, e.g., from $\gamma \to e^+e^-$ pair production in the detector material or from the decay $\pi^0 \to e^+e^-\gamma$. The rate for this background was estimated by considering lepton tracks with a charge opposite to the beam charge as a DIS lepton. It was assumed that these leptons stemmed from pair production processes and that the associated anti-lepton was not detected. The rate for the charge-symmetric process where the particle is detected with the same charge as the beam but originated from pair production is the same. The number of events with an opposite sign lepton is therefore an estimate of the number of charge-symmetric events that masquerade as DIS events. This number was subtracted from the inclusive DIS count rate.

Hadrons coincident with the background DIS track, that passed the SIDIS cuts (see Tab. 4.5), were also subtracted from the corresponding SIDIS hadron sample. The DIS background rate was 6% with respect to the total DIS rate in the smallest x-bin and decreased rapidly with increasing x. The overall background fraction from this source was only 1.5%.

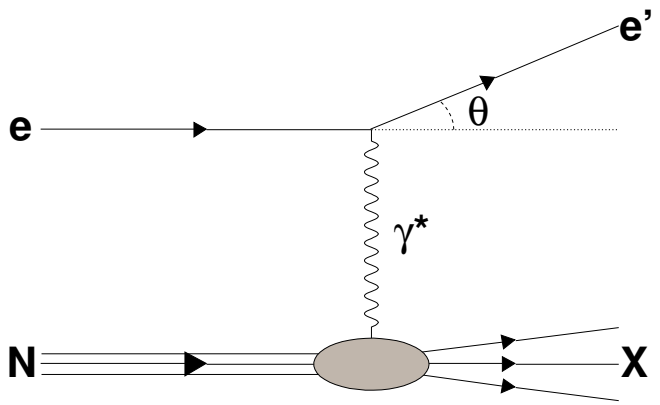

Figure 5.1: DIS process in first order QED (Born level). The scattering kinematics are well defined by the properties of the incident and scattered electron.

The particle count numbers

The particle count numbers for analyzed data-productions analyzed are summarized in Tab. 4.6. The numbers are presented in terms of "equivalent" numbers of events N_{eq} summed over two orientations of target and beam polarizations. The equivalent count number is the number of unweighted events with the same relative errors as the sum of weighted events N,

$$\frac{\sigma(N_{eq})}{N_{eq}} \equiv \frac{\sqrt{N_{eq}}}{N_{eq}} = \frac{\sqrt{\sum_i (\omega)^2}}{\sum_{i'} \omega_{i'}} \equiv \frac{\sigma(N)}{N}, \tag{5.11}$$

where weights ω_i are defined in Sec.4.2.2 for hadrons identified by the RICH detector in semi-inclusive events. The uncertainties on the counts,

$$\sigma(N) = \sqrt{\sum\nolimits_i \omega_i^2}, \tag{5.12}$$

is a consequence of the Poisson distribution of the events. For pions identified by the threshold Čerenkov counter, for undifferentiated hadrons, and for inclusive DIS events the weight is unity, $\omega_i = 1$.

5.2 Extraction of Born asymmetries

The asymmetries discussed in the previous section are subject to instrumental and QED processes (see sec. 5.2.1). The physical quantities of interest, however, are asymmetries of the two DIS processes shown in Fig. 2.9. The measured asymmetries therefore have to be corrected in order to find the asymmetries at lowest order in α or Born asymmetries. In section 5.2.1 two sources of corrections, namely higher-order QED effects and detector-smearing effects are discussed. Then in section 5.2.2 the azimuthal-acceptance correction due to non-zero ϕ_h dependence of the unpolarized semi-inclusive cross section is presented.

Table 5.1: Kinematics of final state radiation.

Measured		Born
$\nu_X = (E - E^{'})$	$\geq$	$\nu_B = (E - (E^{'} + \omega))$
$Q^2_X = 4EE^{'}sin^2\frac{\theta_X}{2}$	$\leq$	$Q^2_B = 4E(E^{'} + \omega)sin^2\frac{\theta_B}{2}$
$x_X = \frac{Q^2_X}{2M\nu_X}$	$\leq$	$x_B = \frac{Q^2_B}{2M\nu_B}$
$W^2_X = M^2 + 2M\nu_X - Q^2_X$		$W^2_B = M^2 + 2M\nu_B - Q^2_B$

5.2.1 Smearing correction and QED radiative correction

The DIS process at first order QED, is depicted in Fig. 5.1. The lepton reacts with the nucleon by exchange of a virtual photon. The kinematics of the scattered lepton (namely the energy $E^{'}$ and the scattering angle θ) are measured in the detector. With the known initial energy of the initial lepton, E, the kinematics of the virtual photon - and thus the kinematics of the entire scattering process - are well defined by this measurement.

QED radiative effects

In addition to the first order or Born level processes, there is an infinite number of possibilities for higher order processes, which are suppressed by at least $O(\alpha)$. Possible higher order processes are shown in Fig. 5.2. While the processes with vertex corrections (Fig. 5.2c) and vacuum polarizations (Fig. 5.2d) affect the overall normalization of the DIS cross section only, initial (Fig. 5.2a) and final (Fig. 5.2b) state radiation also hide the true kinematics of the event. They introduce a systematic bias of the observed kinematics with respect to the true Born level kinematics. This effect is illustrated in Fig. 5.3 for an event with final state radiation. The scattered lepton emits a photon with energy ω and the measured kinematics allow to calculate the experimental kinematic variables ν_X, Q^2_X. The connection of these kinematic quantities with the Born kinematic quantities is given in the Table 5.1. The measured value of the energy transfer ν_X is larger than the energy of the virtual photon ν_B. The kinematic variables Q^2_X and x_X are smaller than their Born analogies. There is no such an inequality for W^2. This discussion is the same for initial state radiation and the expressions for the measured and the Born kinematics are identical except for $Q^2_B = 4(E - \omega)E^{'}sin^2\frac{\theta_B}{2}$.

Detector effects

Another class of uncertainties is introduced by the measuring process itself. While traversing the target and the detector, the final-state particles are subject to interactions with material which influence the energy and direction of the track. The tracking algorithm assumes the particle tracks to be straight lines in the sections before and after the spectrometer magnet.

Figure 5.2: Second order QED radiative corrections for the DIS process.

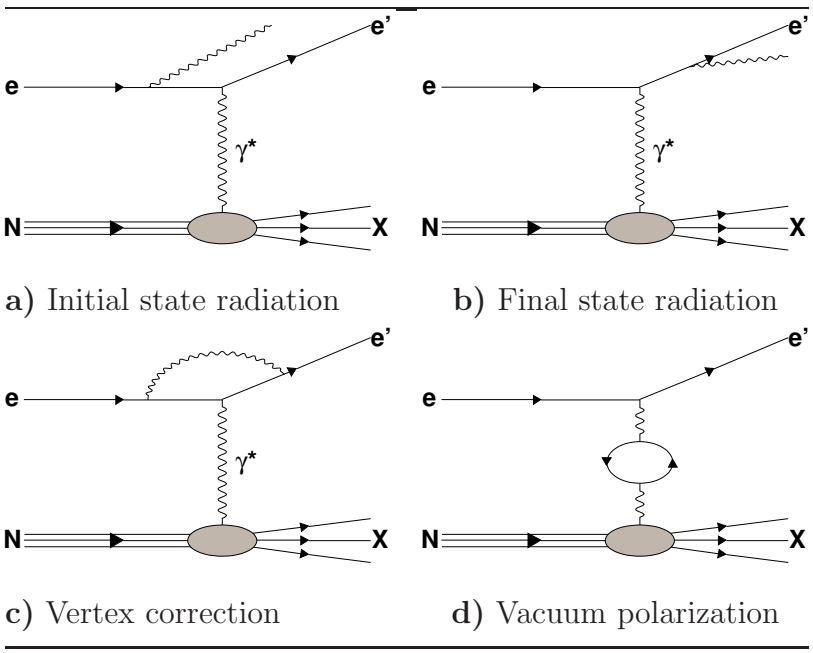

Their real behavior causes, e.g., deviations between the measured and the true scattering angle. The determination of the particle momentum is affected, since this is done by an algorithm matching the partial tracks in the front and the back half of the detector.

The HERMES spectrometer allows detection of particles that leave the target area in a certain solid angle $\delta\Omega$. In order to compare the results with other experiments, this spectrometer dependent restrictions have to be accounted for.

All of the effects mentioned above can be generated by a Monte Carlo simulation. In the HERMES Monte Carlo framework, the radiative corrections are usually handled by the RADGEN program [57] which was specifically designed to simulate radiative corrections for deep-inelastic scattering events with a sufficiently low energy scale, so that electroweak contributions and corrections are negligible.

Interactions of the particles with the detector are accounted for by HMC, that is the GEANT simulation of the HERMES detector. This program uses a model of the detector to simulate the particle interactions with the different materials they traverse. The calculated detector responses are then passed on to the tracking algorithm.

The correction method

The unfolding formalism used to correct for QED radiative effects, detector smearing and acceptance effects was originally described in [58]. It involves the information from two separate Monte Carlo productions:

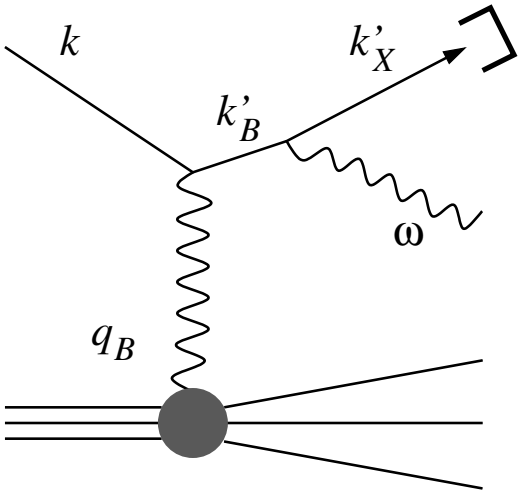

Figure 5.3: Diagram of final state radiation. The diagram illustrates the emission of an undetected photon with energy ω before the detection of the scattered lepton.

- a tracked MC production, including QED effects and a simulation of the detector effects (and thus automatically limited to the HERMES acceptance) and
- a Born Monte Carlo, without the simulation of radiative effects and without any further detector effects.

By design, the tracked Monte Carlo production provides not only the observed kinematics after simulating all effects, but also the true (Born level) kinematics. For the kinematic variables this allows to extract the $N_X \times (N_B{+}1)$ migration matrices $n^{\rightarrow}_{\Rightarrow(\overleftarrow{\Rightarrow})}(i,j)$ for parallel (antiparallel) spin orientations. These matrices contain the count rates which fall into bin i of eXperimental kinematics and bin j of Born kinematics, respectively. The indices run from

$$i \;=\; 1 \;...\; n_{bins} \tag{5.13}$$

and

$$j \;=\; 0 \;...\; n_{bins}, \tag{5.14}$$

where n_{bins} denotes the number of bins for both observed and true values of kinematic variables.

The square sub-matrices of $n^{\rightarrow}_{\Rightarrow(\overleftarrow{\Rightarrow})}(i,j)$ with $1{\leq}i,j{\leq}n_{bins}$ describe events which remain inside the acceptance: diagonal elements ($i = j$) correspond to events which are reconstructed in the same bin in which they belong to on Born level whereas off-diagonal matrix elements describe events which migrated from Born bin j to eXperimental bin i. As in reference [58], bin $j = 0$ is used for events which would have been excluded from the sample by the original kinematics but subsequently migrated into the acceptance.

Fig. 5.4 illustrates an example of migration matrices for DIS events and production of positive pions, in a case of antiparallel spin orientation.

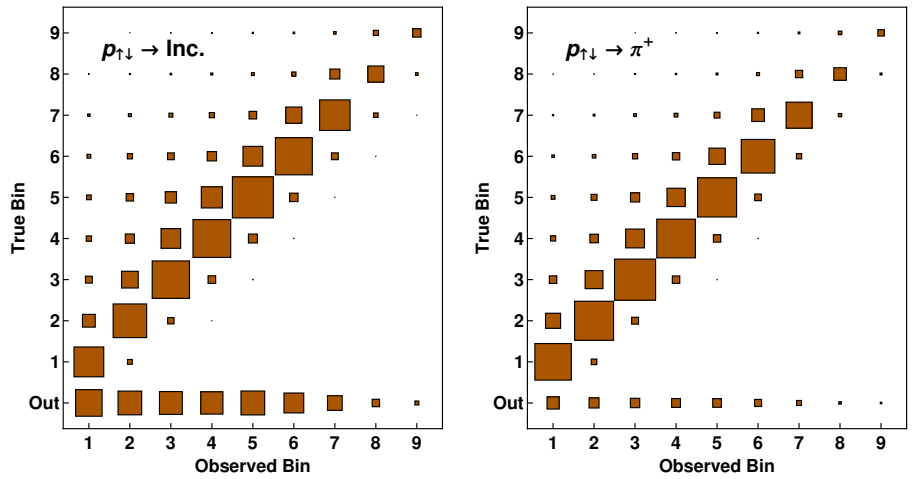

Figure 5.4: Migration matrices for a pure x binning. The matrices were extracted from a fully reconstructed Monte Carlo data set simulating both QED radiative and detector effects for inclusive (left panel) DIS and semi-inclusive production of positive pions (right panel) on a proton target.

The spin-dependent eXperimental count rates $n^X_{\overrightarrow{\Rightarrow}}(i)$ and $n^X_{\overrightarrow{\Leftarrow}}(i)$ can be calculated from the migration matrices by summing up columns,

$$n^X_{\overrightarrow{\Rightarrow}}(i) = \sum_{j=0}^{n_{bins}} n_{\overrightarrow{\Rightarrow}}(i,j) \quad and \quad n^X_{\overrightarrow{\Leftarrow}}(i) = \sum_{j=0}^{n_{bins}} n_{\overrightarrow{\Leftarrow}}(i,j), \tag{5.15}$$

and the spin-independent count rates are given by

$$n^X_u(i) = n^X_{\overrightarrow{\Rightarrow}}(i) + n^X_{\overrightarrow{\Leftarrow}}(i). \tag{5.16}$$

The corresponding Born count rates, $n^B_{\overrightarrow{\Rightarrow}(\overrightarrow{\Leftarrow})}(j)$, in each spin state and bin j are extracted from Born Monte Carlo data. Based on these count rates, the cross section normalized migration matrices are given as

$$S_{\overrightarrow{\Rightarrow}(\overrightarrow{\Leftarrow})}(i,j) \equiv \frac{\partial\sigma^X_{\overrightarrow{\Rightarrow}(\overrightarrow{\Leftarrow})}(i)}{\partial\sigma^B_{\overrightarrow{\Rightarrow}(\overrightarrow{\Leftarrow})}(j)} = \frac{n_{\overrightarrow{\Rightarrow}(\overrightarrow{\Leftarrow})}(i,j)}{n^B_{\overrightarrow{\Rightarrow}(\overrightarrow{\Leftarrow})}(j)}, \qquad i,j = 1,...,n_{bins}. \tag{5.17}$$

The $S_{\overrightarrow{\Rightarrow}(\overrightarrow{\Leftarrow})}$ matrices are insensitive to the Monte Carlo model of the Born distributions, because both the numerator and the denominator scale with the relative number of Born events generated in bin number j.

The relation between the Monte Carlo yields for eXperimental kinematics and the Monte Carlo yields for Born level kinematics is

$$n^{X}_{\underset{\Rightarrow}{\rightarrow}(\underset{\Leftarrow}{\rightarrow})}(i) = \sum_{j=0}^{n_{bins}} S_{\underset{\Rightarrow}{\rightarrow}(\underset{\Leftarrow}{\rightarrow})}(i,j) n^{B}_{\underset{\Rightarrow}{\rightarrow}(\underset{\Leftarrow}{\rightarrow})}(j), \qquad i = 1, ..., n_{bins}, \tag{5.18}$$

which leads to the following expression for the spin dependent Monte Carlo asymmetry $A_{||}^{X_{MC}}$:

$$\begin{aligned} A_{||}^{X_{MC}}(i) &= \frac{n^{X}_{\underset{\Leftarrow}{\rightarrow}}(i) - n^{X}_{\underset{\Rightarrow}{\rightarrow}}(i)}{n^{X}_{\underset{\Leftarrow}{\rightarrow}}(i) + n^{X}_{\underset{\Rightarrow}{\rightarrow}}(i)} = \frac{n^{X}_{\underset{\Leftarrow}{\rightarrow}}(i) - n^{X}_{\underset{\Rightarrow}{\rightarrow}}(i)}{n_u^X(i)} = \\ &= \frac{1}{n_u^X(i)} \sum_{j=0}^{n_{bins}} \Big[S_{\underset{\Leftarrow}{\rightarrow}}(i,j) n^{B}_{\underset{\Leftarrow}{\rightarrow}}(j) - S_{\underset{\Rightarrow}{\rightarrow}}(i,j) n^{B}_{\underset{\Rightarrow}{\rightarrow}}(j) \Big]. \end{aligned} \tag{5.19}$$

The background term $n_p(i,0) \equiv n_{\underset{\Leftarrow}{\rightarrow}}(i,0) - n_{\underset{\Rightarrow}{\rightarrow}}(i,0)$ can be separated from the sum and moved to the other side of the equation:

$$\begin{aligned} &\sum_{j=1}^{n_{bins}} \Big[S_{\underset{\Leftarrow}{\rightarrow}}(i,j) n^{B}_{\underset{\Leftarrow}{\rightarrow}}(j) - S_{\underset{\Rightarrow}{\rightarrow}}(i,j) n^{B}_{\underset{\Rightarrow}{\rightarrow}}(j) \Big] = \\ &\qquad = A_{||}^{X}(i) n_u^X(i) - \Big[S_{\underset{\Leftarrow}{\rightarrow}}(i,0) n^{B}_{\underset{\Leftarrow}{\rightarrow}}(0) - S_{\underset{\Rightarrow}{\rightarrow}}(i,0) n^{B}_{\underset{\Rightarrow}{\rightarrow}}(0) \Big] = \\ &\qquad = A_{||}^{X}(i) n_u^X(i) - n_p(i,0), \qquad i = 1, ..., n_{bins}. \end{aligned} \tag{5.20}$$

The rate $n^{B}_{\underset{\Rightarrow}{\rightarrow}}(j)$ may by eliminated in favor of $n^{B}_{\underset{\Leftarrow}{\rightarrow}}(j)$ and $n_u^B(j)$ using

$$n_u^B(j) = n^{B}_{\underset{\Leftarrow}{\rightarrow}}(j) + n^{B}_{\underset{\Rightarrow}{\rightarrow}}(j). \tag{5.21}$$

The equation 5.20 can be written as

$$\begin{aligned} &\sum_{j=1}^{n_{bins}} \Big[S_{\underset{\Leftarrow}{\rightarrow}}(i,j) + S_{\underset{\Rightarrow}{\rightarrow}}(i,j) \Big] n^{B}_{\underset{\Leftarrow}{\rightarrow}}(j) = \\ &\qquad = A_{||}^{X}(i) n_u^X(i) - n_p(i,0) + \sum_{j=1}^{n_{bins}} S_{\underset{\Rightarrow}{\rightarrow}}(i,j) n_u^B(j). \end{aligned} \tag{5.22}$$

The Born asymmetry $A_{||}^{B_{MC}}(j)$ can be found by solving Eq. 5.22 for $n^{B}_{\underset{\Leftarrow}{\rightarrow}}(j)$ and substituting into

$$A_{||}^{B_{MC}}(j) = \frac{2 n^{B}_{\underset{\Leftarrow}{\rightarrow}}(j) - n_u^B(j)}{n_u^B(j)}. \tag{5.23}$$

The expression for the unfolded asymmetry $A_{||}^{B_{MC}}(j)$ is :

$$A_{||}^{B_{MC}}(j) = -1 + \frac{2}{n_u^B(j)} \sum_{i=1}^{n_{bins}} [S]^{-1}(j,i) \Big[A_{||}^{X_{MC}}(i) n_u^X(i) - n_p(i,0) + \sum_{k=1}^{n_{bins}} S_{\underset{\Rightarrow}{\rightarrow}}(i,k) n_u^B(k) \Big], \tag{5.24}$$

where $S(i,j)$ was defined as a sum of two smearing matrices $S_{\underset{\Leftarrow}{\rightarrow}}(i,j)$ and $S_{\underset{\Rightarrow}{\rightarrow}}(i,j)$.

The relation in Eq. 5.24 is applicable to a *measured* asymmetry $A_{||}$. Then the final expression for the unfolded asymmetry is :

$$A_{||}^{B}(j) = -1 + \frac{2}{n_u^B(j)} \sum_{i=1}^{n_{bins}} [S]^{-1}(j,i) \Big[A_{||}(i) n_u^X(i) - n_p(i,0) + \sum_{k=1}^{n_{bins}} S_{\Rightarrow}^{\rightarrow}(i,k) n_u^B(k) \Big]. \quad (5.25)$$

The covariance matrix C which follows from Eq. 5.25 describes the dependence between any given two x bins of the unfolded Born asymmetry $A_{||}^{B}$:

$$C\Big(A_{||}^{B}(j), A_{||}^{B}(k)\Big) = \sum_{i=1}^{n_{bins}} D(j,i) D(k,i) \sigma^2\Big(A_{||}(i)\Big), \quad (5.26)$$

with the dilution matrix $D(j,i)$ being defined as

$$D(j,i) \equiv \frac{\partial A_{||}^{B}(j)}{\partial A_{||}(j)} = \frac{2[S]^{-1}(j,i) n_u^X(i)}{n_u^B(j)} \quad (5.27)$$

and $\sigma(A_{||}(i))$ being the statistical error on the measured asymmetry $A_{||}(i)$.

5.2.2 Acceptance correction

Effect of the acceptance

The measurement of asymmetries as opposed to total cross sections has the advantage that acceptance effects largely cancel. Possible effects on the asymmetries due to the acceptance of the HERMES spectrometer were studied with the HERMES Monte Carlo simulation.

The inclusive $A_{1,p(d)}^{inc}$ and semi-inclusive $A_{1,p(d)}^{\pi^{\pm},\,K^{\pm}}$ Monte Carlo asymmetries were calculated in HERMES acceptance and in 4π for both targets, and the result is shown on Figs. 5.5 and 5.6. Each case is presented by a set of three panels. While, the red triangles show the Monte Carlo asymmetries extracted in HERMES acceptance, green diamonds correspond to the asymmetries calculated in 4π. In addition, two small panels, which contain the average value for Q^2 calculated separately from the Monte Carlo data samples in 4π (red triangles) and in acceptance (green triangles) and the difference in the asymmetries $\Delta A_1 = A_1^{acc} - A_1^{4\pi}$ (black circles), are shown.

As can be seen in Figs. 5.5 (proton) and 5.6 (deuterium), there are differences between asymmetries in acceptance and 4π. There are also differences in average x and Q^2 values of the bins. The Monte Carlo data sample simulated in 4π contains more events with high Q^2. For the inclusive case, for which the cross section depends on two variables *only*, this kinematic differences can be the only source of discrepancy between asymmetries, and as we provide data points with bin-averaged kinematics, provides no confusion. One can also see that the semi-inclusive asymmetries, which could potentially differ for other reasons, show discrepancies of similar scale in semi-inclusive asymmetries and kinematics to the inclusive case. This suggests

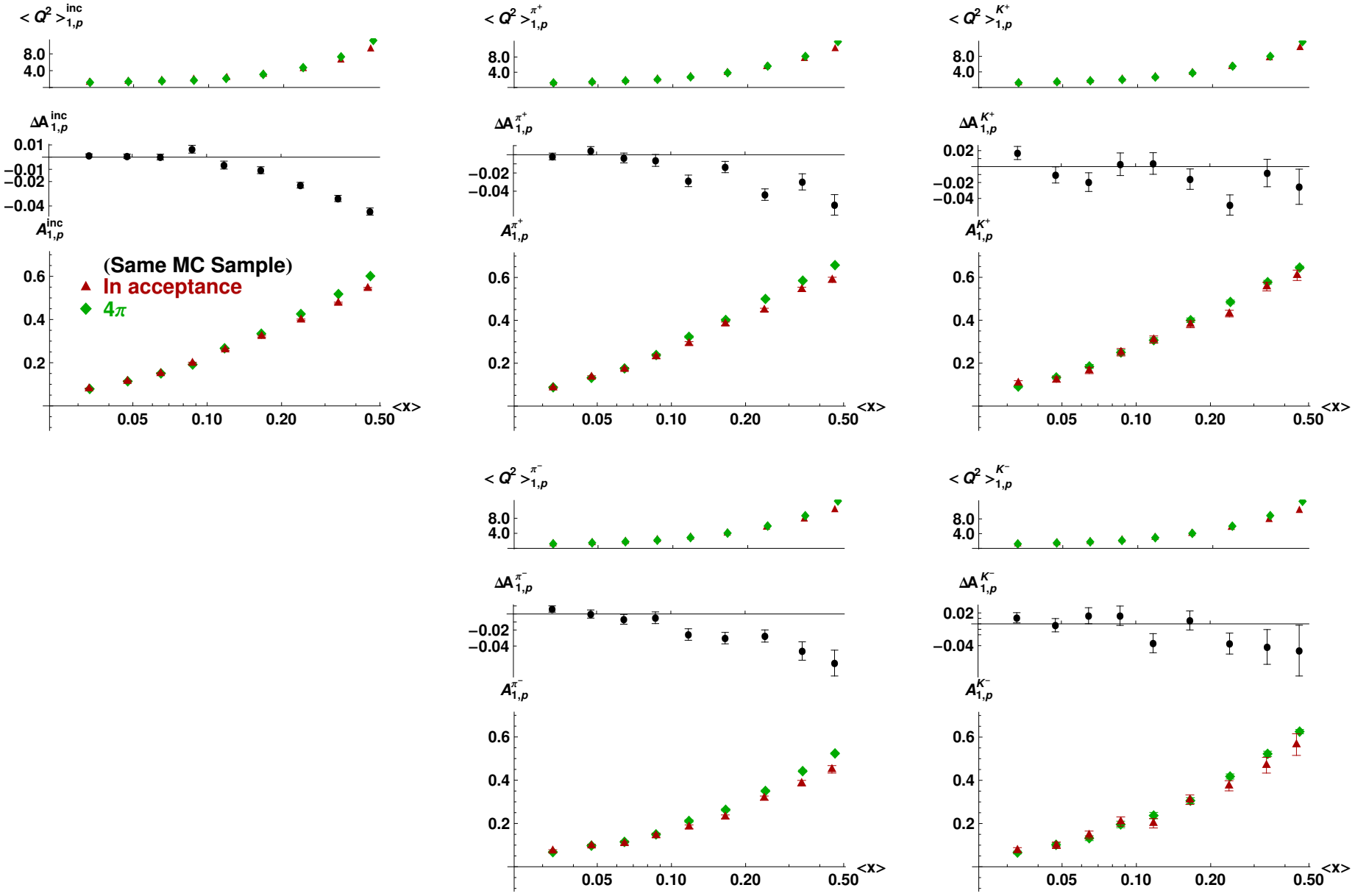

Figure 5.5: Monte Carlo asymmetries for the proton in HERMES acceptance (red triangles) and in 4π (green diamonds). The black points represent the differences in the asymmetries $\Delta A_1 = A_1^{acc} - A_1^{4\pi}$ which can be attributed entirely to the difference in average kinematics.

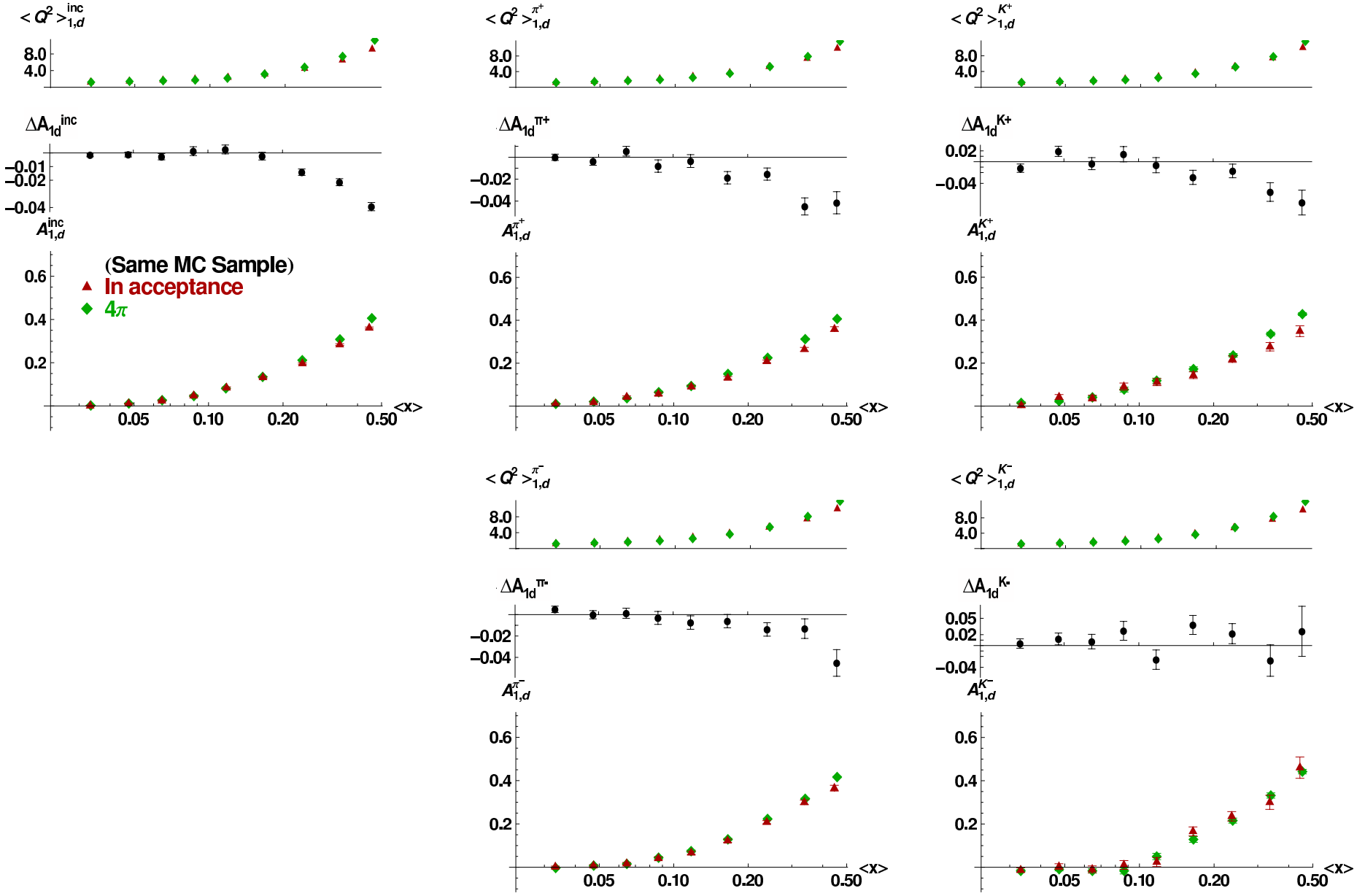

Figure 5.6: Monte Carlo asymmetries for the deuteron in HERMES acceptance (red triangles) and in 4π (green diamonds). The black points represent the differences in the asymmetries $\Delta A_1 = A_1^{acc} - A_1^{4\pi}$ which can be attributed entirely to the difference in average kinematics.

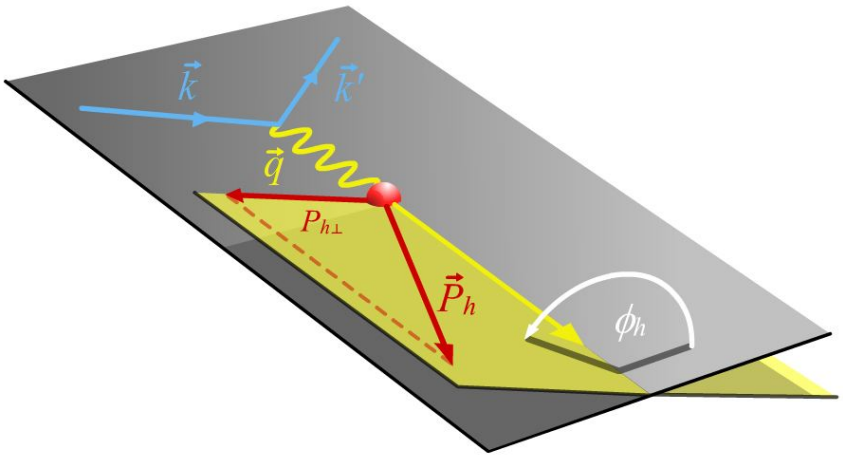

Figure 5.7: Definition of azimuthal angle of the hadron ϕ (here named ϕ_h) for semi-inclusive deep inelastic scattering in the target rest frame. $P_{h\perp}$ is the transverse part of P_h with respect to the photon momentum.

that computing of asymmetries (and further derivative results) in acceptance is save as long as average kinematics are given.

Azimuthal acceptance correction

In semi-inclusive deep inelastic scattering a lepton scatters off a nucleon, after the collision one of the produced hadrons produced is detected. In a naive parton model with quark momenta collinear with the momentum of the proton, the cross section does not depend on the azimuthal angle ϕ between the lepton scattering plane and the hadron production plane. However, this is no longer the case, if also transverse momenta of these partons are taken into account which introduce a dependence of the cross section on ϕ (see Fig. 5.7), as well as on the azimuthal angle of the target polarization.

Two mechanisms are expected to give important contributions to the azimuthal dependence of the unpolarized cross-section in the hadron transverse-momentum range accessed at HERMES:

- **Boer-Mulders mechanism.** This mechanism, introduced by D.Boer and P.J.Mulders [59], is generated when the quark transverse momentum couples to the quark transverse spin.

- **Cahn effect.** A pure kinematic effect, generated by the non-zero intrinsic transverse motion of quarks [60].

While an inclusive cross section can be written as a function of two kinematic variables, e.g. $\sigma(x, Q^2)$, the semi-inclusive cross section is a function of five variables: $\sigma^h(x, Q^2, z, p_{h\perp}, \phi)$.

The semi-inclusive asymmetry can be written explicitly including all these dependences:

$$A_1^h = \frac{\int d\phi\ \Delta\sigma(x, Q^2, z, p_{h\perp}, \phi)\ \mathcal{A}(\phi)}{\int d\phi\ \sigma(x, Q^2, z, p_{h\perp}, \phi)\ \mathcal{A}(\phi)}, \tag{5.28}$$

where $\mathcal{A}(\phi)$ represents the spectrometer acceptance, $\Delta\sigma(x, Q^2, z, p_{h\perp}, \phi)$ is the polarized semi-inclusive cross section for longitudinal beam and target polarizations and $\sigma(x, Q^2, z, p_{h\perp}, \phi)$ is the corresponding unpolarized cross section. Assuming single-photon exchange, the lepton-hadron cross section can be expressed in a model-independent way where the ϕ dependence is given [63] by $\cos(\phi)$ and $\cos(2\phi)$ harmonics:

$$\begin{aligned}\frac{d\sigma}{dx\ dQ^2\ dz\ dp_{h\perp}\ d\phi} \quad \propto \quad & \sigma_{UU}(x, Q^2, z, p_{h\perp}) + \\ + \ \sigma_{UU}^{\cos(\phi)}(x, Q^2, z, p_{h\perp})\ \cos(\phi) + \sigma_{UU}^{\cos(2\phi)}(x, Q^2, z, p_{h\perp})\ \cos(2\phi) + & \\ + P_B\ P_T \Big[\sigma_{LL}(x, Q^2, z, p_{h\perp}) + & \\ + \ \sigma_{LL}^{\cos(\phi)}(x, Q^2, z, p_{h\perp})\ \cos(\phi) + \sigma_{LL}^{\cos(2\phi)}(x, Q^2, z, p_{h\perp})\ \cos(2\phi)\Big], & \end{aligned} \tag{5.29}$$

where σ_{UU}, $\sigma_{UU}^{\cos(\phi)}$, $\sigma_{UU}^{\cos(2\phi)}$, and σ_{LL} represent unpolarized beam, unpolarized target or longitudinally polarized beam, longitudinally polarized target ϕ-moment coefficient functions. The first and second subscripts indicate the respective polarization of beam and target. There are potentially $\sigma_{LL}^{\cos(\phi)}$ and $\sigma_{LL}^{\cos(2\phi)}$ terms in the polarized cross section in Eq. 5.29. But, there are no known mechanisms for producing such a longitudinal-spin spin-dependent ϕ modulation. P_B and P_T represent the longitudinal polarizations of beam and target – which are zero in the unpolarized case.

Given that the unpolarized ϕ dependence of the numerator in Eq. 5.28 disappears since $\Delta\sigma = \sigma_{\Leftarrow}^{\rightarrow} - \sigma_{\Rightarrow}^{\rightarrow}$, only the desired σ_{LL} term is left. What we measure then can be written as follows:

$$\tilde{A}_1^h = \frac{\Delta\sigma(x, Q^2, z, p_{h\perp})}{\int d\phi\ \sigma(x, Q^2, z, p_{h\perp}, \phi)\ \mathcal{A}(\phi)}, \tag{5.30}$$

where we seek for,

$$A_1^h = \frac{\Delta\sigma(x, Q^2, z, p_{h\perp})}{\sigma(x, Q^2, z, p_{h\perp})}, \tag{5.31}$$

which is independent of the HERMES acceptance.

To accomplish this, the following correction is done,

$$A_1^h = C_\phi^h \tilde{A}_1^h, \tag{5.32}$$

where

$$C_\phi^h = \frac{\mathcal{A}_1^h}{\tilde{\mathcal{A}}_1^h}. \tag{5.33}$$

Calligraphic characters are used to denote quantities which were estimated using Monte Carlo

simulation. We take advantage of 1) the $\cos(\phi)$ dependence of the acceptance present in the Monte Carlo and 2) a parameterization of the unpolarized $\cos(\phi)$ moments which are otherwise missing from the Monte Carlo to achieve this. These $\cos(\phi)$ moments have been extracted in another recent HERMES analysis [61, 62].

In oder to correct the semi-inclusive asymmetries for non-zero ϕ dependence of the unpolarized semi-inclusive cross section, we construct the correction factor by producing asymmetries with and without $\cos(\phi)$ weights (see Eq. 5.33), where

$$\mathcal{A}^h = \frac{\mathcal{N}^h_{\stackrel{\rightarrow}{\Leftarrow}} - \mathcal{N}^h_{\stackrel{\rightarrow}{\Rightarrow}}}{\mathcal{N}^h_{\stackrel{\rightarrow}{\Leftarrow}} + \mathcal{N}^h_{\stackrel{\rightarrow}{\Rightarrow}}}, \qquad \tilde{\mathcal{A}}^h = \frac{\mathcal{N}^h_{\stackrel{\rightarrow}{\Leftarrow}} - \mathcal{N}^h_{\stackrel{\rightarrow}{\Rightarrow}}}{\tilde{\mathcal{N}}^h_{\stackrel{\rightarrow}{\Leftarrow}} + \tilde{\mathcal{N}}^h_{\stackrel{\rightarrow}{\Rightarrow}}}. \tag{5.34}$$

A semi-inclusive DIS event was simulated with a weight ω_i, that reflects the Born cross section, and each hadron track was assigned this weight. The Monte Carlo yields $\mathcal{N}^h_{(\stackrel{\rightarrow}{\Leftarrow})\stackrel{\rightarrow}{\Rightarrow}}$ in both spin states are computed as the sum of these weights,

$$\mathcal{N}^h_{(\stackrel{\rightarrow}{\Leftarrow})\stackrel{\rightarrow}{\Rightarrow}} = \sum_{i=1}^{N_{gen}} \omega_i, \tag{5.35}$$

where the sum runs over all hadron tracks. The yields $\tilde{N}^h_{(\stackrel{\rightarrow}{\Leftarrow})\stackrel{\rightarrow}{\Rightarrow}}$ are the ones with $\cos(n\phi)$ weights in addition:

$$\tilde{N}^h_{(\stackrel{\rightarrow}{\Leftarrow})\stackrel{\rightarrow}{\Rightarrow}} = \sum_{i=1}^{N_{gen}} \omega_i \; \omega^h_{i\;t}(x, y, z, p_{h\perp}, \phi) \tag{5.36}$$

where the weight $\omega^h_t(x, y, z, p_{h\perp}, \phi)$ is given by:

$$\omega^h_t(x, y, z, p_{h\perp}, \phi) = 1 \; + \; 2\langle cos\phi\rangle^h_t cos(\phi) + 2\langle cos2\phi\rangle^h_t cos(2\phi). \tag{5.37}$$

Here the indices t and h denote the target and hadron type. The $\langle cosn\phi\rangle^h_t$-moments are extracted using the parameterization

$$\begin{aligned}\langle cos(2)\phi\rangle^h = A_1^{h(2)\phi} + A_2^{h(2)\phi}\; x + A_3^{h(2)\phi}\; y + A_4^{h(2)\phi}\; z + A_5^{h(2)\phi}\; p_{h\perp} \\ + A_6^{h(2)\phi}\; x^2 + A_7^{h(2)\phi}\; z^2 + A_8^{h(2)\phi}\; p_{h\perp}^2 + A_9^{h(2)\phi}\; x\; z \\ + A_{10}^{h(2)\phi}\; x\; p_{h\perp} + A_{11}^{h(2)\phi}\; z\; p_{h\perp} + A_{12}^{h(2)\phi}\; y\; p_{h\perp} \\ + A_{13}^{h(2)\phi}\; x\; y + A_{14}^{h(2)\phi}\; y\; z + A_{15}^{h(2)\phi}\; y^2.\end{aligned} \tag{5.38}$$

In order to create this parameterization [61], unpolarized semi-inclusive data were binned in five kinematic dimensions $(x, y, z, p_{h\perp}, \phi)$ and unfolded in all of these dimensions simultaneously. The benefit of this technique is that, as none of the variables are integrated out, there is no convolution of the kinematic dependence with the acceptance of the spectrometer. The difficulty, however, is that in five dimensions - or 6000 kinematic bins ($5x \times 4y \times 5z \times 5p_{h\perp} \times 12\phi$),

even large Monte Carlo statistics yield migration matrices sparsely populated in its corners.

Graphs in Fig. 5.8 show the comparison of the $\pi^{\pm}$ and $K^{\pm}$ Born Monte Carlo asymmetries in 4π (i.e. without imposing any geometric acceptance requirements) $\tilde{\mathcal{A}}^h$ (blue squares) with and $\mathcal{A}^h$ (green triangles) without weighting for both targets. The plot shows the full coincidence of the asymmetries, because the unpolarized cross section (see Eq. 5.30) is integrated over the full ϕ range. The same semi-inclusive Born asymmetries, but extracted from the Monte Carlo data sample, where the particles were registered in acceptance, are shown in Fig. 5.9. Whereas blue squares represent the asymmetry in acceptance with $cos(\phi)$ weighting, the red triangles show the asymmetry without $cos(\phi)$ weighting. Graphs in Fig. 5.9 demonstrate that with the ϕ dependent acceptance imposed, the $cos(\phi)$ weighting changes the integral of the $cos(\phi)$ and thus the value of the asymmetry.

Finally, the correction factor C_{ϕ}^{h}, which is the ratio of two asymmetries calculated from Born Monte Carlo samples with and without $\cos(\phi)$ weights in acceptance, is also shown in Fig. 5.9. The correction to the asymmetries is small at low x and becomes larger, about 10% for $x > 0.2$. For positive pions and positive and negative kaons the correction factor C_{ϕ}^{h} raises the value of asymmetry for larger x. For negative pions the asymmetries become smaller, if the $\cos(\phi)$ dependence is taken into account. In addition, the values of C_{ϕ}^{h} are given in App A-E. The correction is applied to the measured asymmetries given by Eq. 2.38:

$$A_1 = C_{\phi}^{h} \frac{A_{||}}{D(1+\eta\gamma)}. \tag{5.39}$$

5.3 Systematic uncertainties

The systematic uncertainties of the extracted asymmetries shown as the error bands in Figs. 5.10, 5.12, 5.11 arise from various sources which can be divided into two classes. One class contains experimental uncertainties, like in the beam and target polarization measurements and in the smearing corrections. The other group of uncertainties comprises contributions from external quantities, like the extraction of the $cos(n\phi)$ moments. The individual contributions to the systematic uncertainty on the inclusive and semi-inclusive asymmetries will be discussed in the following subsections.

5.3.1 Polarization

The average uncertainty on the beam and target polarization are summarized in Tab. 5.2. As the beam and target polarizations appear everywhere as a product, their *fractional* uncertainties can be combined in quadrature. Furthermore, as the average polarization always appears in combination with the luminosity, we can write the total polarization-weighted luminosity as

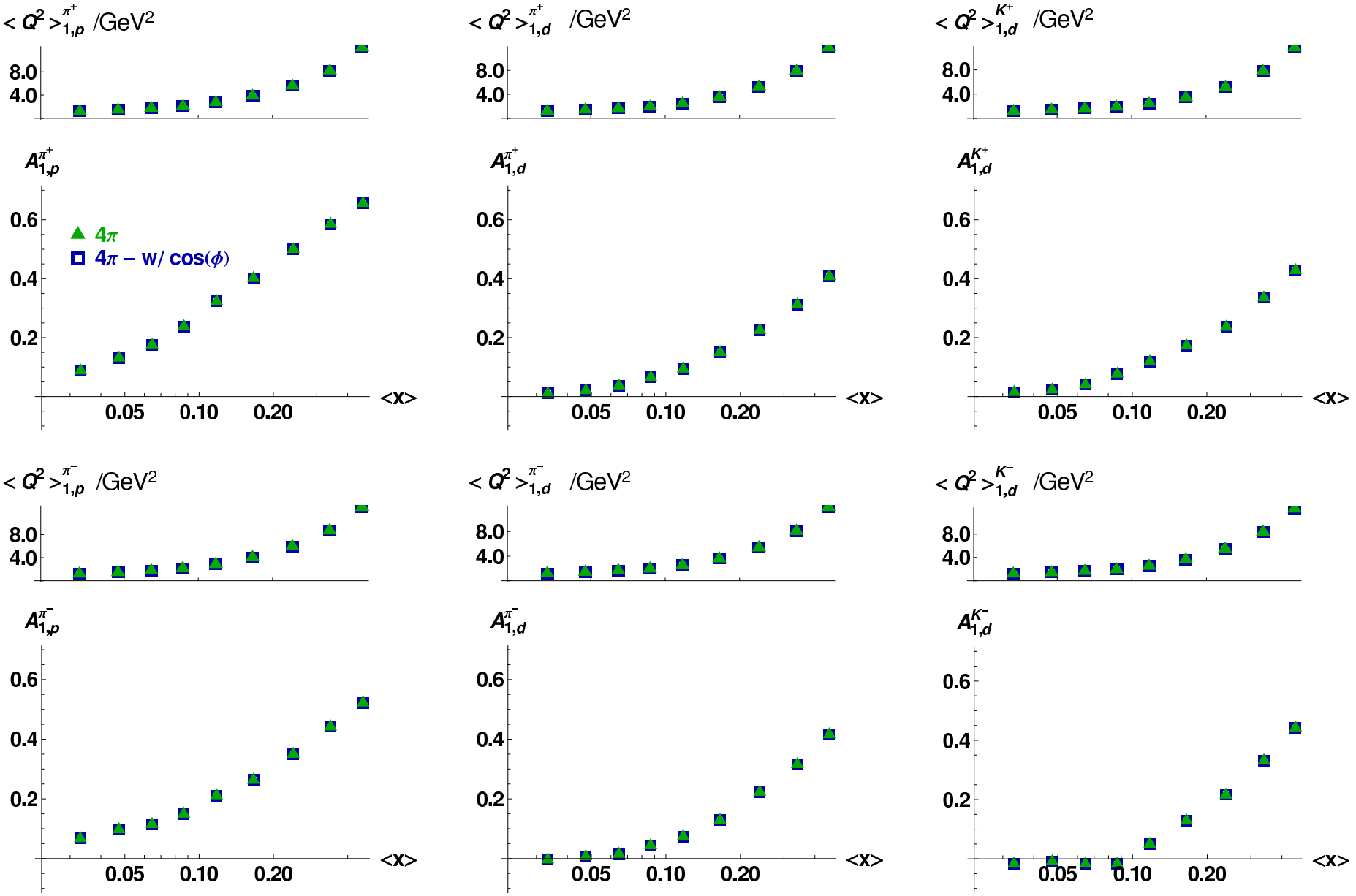

Figure 5.8: Comparison of 4π Born Monte Carlo samples with and without $\cos(\phi)$ weighting. Asymmetries for charged pions from the proton target and both pions and kaons from the deuteron target are shown. Since there is no ϕ-dependent acceptance included, the cosine moments of the unpolarized cross section integrate out over the full ϕ range.

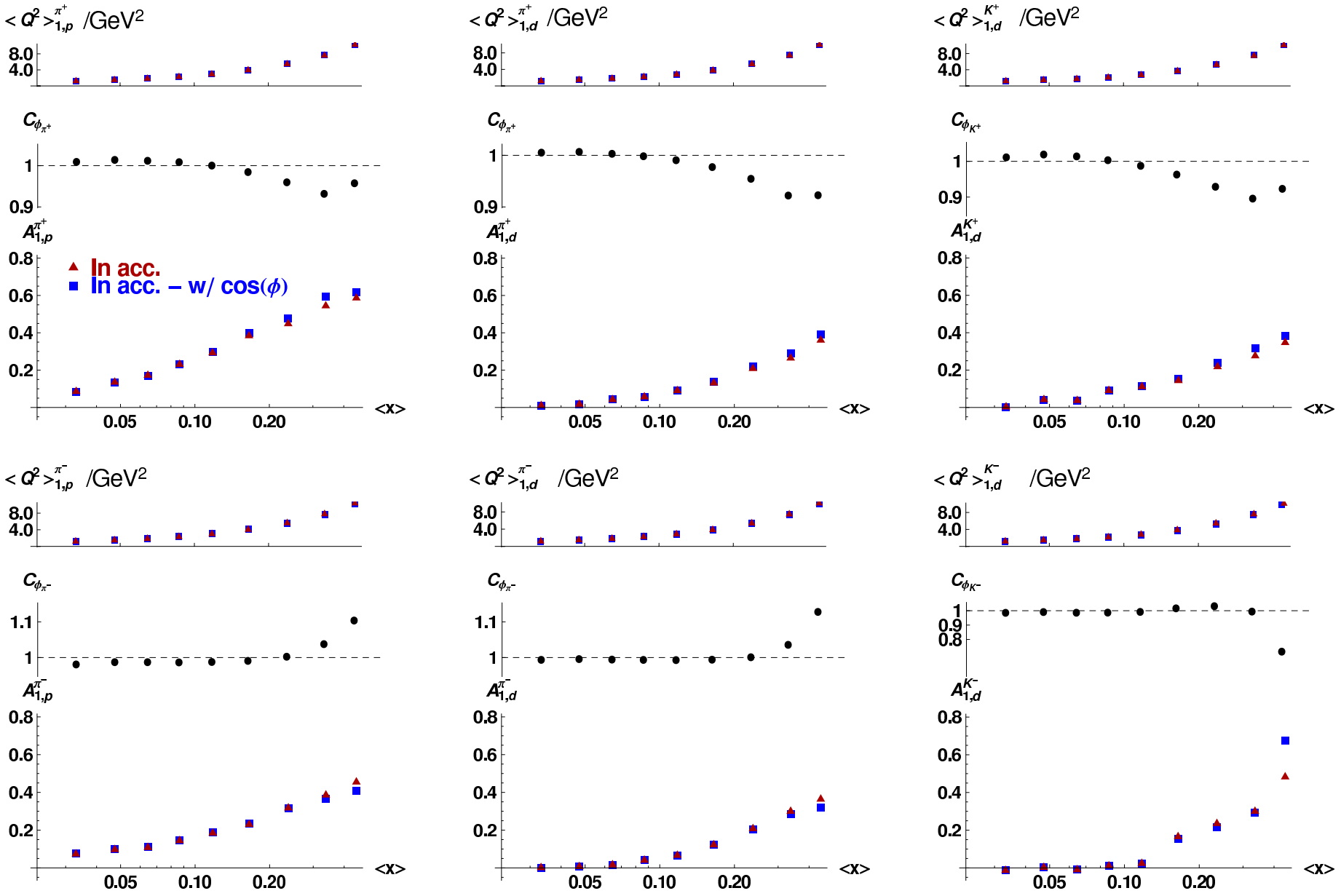

Figure 5.9: Comparison of Born Monte Carlo samples with and without $\cos(\phi)$ weighting in acceptance. Unlike the 4π comparison shown in Fig. 5.8, the nonuniform acceptance of the spectrometer in ϕ creates significant differences between the weighted and unweighted asymmetries. The azimuthal correction factor C_ϕ^h, which is simply the ratio of the two asymmetries, is also shown.

Table 5.2: Fractional uncertainties of beam and target and their quadratic sum by year

	1996	1997	1998	1999	2000
$\delta P_T/P_T$	0.055	0.038	0.075	0.070	0.035
$\delta P_B/P_B$	0.034	0.034	0.034	0.018	0.019
$(\delta P/P)_{tot}$	0.065	0.051	0.082	0.072	0.040

follows:

$$(LP^{\rightarrow}_{\Leftarrow(\Rightarrow)})_{tot} = \sum_{i=years} L_i {}^{\rightarrow}_{\Leftarrow(\Rightarrow)} P_i (1 \pm (\delta P/P)_i). \tag{5.40}$$

The systematic error band is produced by computing azimuthally-corrected (see Chap. 5.3.3) Born asymmetries for both values of $(L\ P^{\rightarrow}_{\Leftarrow(\Rightarrow)})_{tot}$.

5.3.2 RICH unfolding

The limited statistics of the Monte Carlo sample used to extract the smearing matrices gives rise to another source of systematic uncertainty. The influence of the statistical uncertainty of the smearing matrix on the unfolded result is determined using a variational technique. The HERMES RICH group provides four different P-matrix (see Section 4.2.2) for estimating systematic uncertainties. Each of these matrices was produced by running a particular Monte Carlo simulation (`disNG` or `PYTHIA`) and using various background noise patterns (`disNG`, `PYTHIA` or averaged data) added to the simulated hypothetical Čerenkov rings that the RICH algorithm uses to compare with the observed hit pattern. The `disNG_ownBKG` file is the standard P-matrix used in this analysis and is expected to be the most accurate. By generating asymmetries using each of these P-matrices and comparing to the asymmetries using `disNG_ownBKG`, one can estimate the systematic uncertainty from RICH unfolding. This source of the uncertainty is found to contribute negligibly to the total systematic uncertainty of the asymmetry.

5.3.3 Azimuthal correction

Systematic uncertainties of the semi-inclusive asymmetries arising due to the azimuthal correction are tricky to compute exactly, because the $cos(\phi)$ and $cos(2\phi)$ moments have their own uncertainties.

Uncertainties of the correction factor C^h_ϕ were estimated using [64],

$$\sigma^2_{C^h_\phi} = \sum\nolimits_{i,j} \frac{\partial C^h_\phi}{\partial A_i} \frac{\partial C^h_\phi}{\partial A_j} cov(A^{h(2)\phi}_{i(j)}), \tag{5.41}$$

with the known covariance matrix $cov(A^{h(2)\phi}_{i(j)})$. This matrix describes the statistical correlation

between any two parameters $A_{i(j)}^{h(2)\phi}$.

The systematic uncertainty on the semi-inclusive asymmetries due to the azimuthal correction is approximately 3% at large x and becomes negligible for smaller values of x. This uncertainty was added in quadrature to evaluate the total systematic uncertainty in the final asymmetry measurement.

5.4 Results

In this section, the results on inclusive, semi-inclusive hadron and charge separated pion and kaon asymmetries are presented. All results of this work presented here include the corrections described in the previous chapters and the values are listed in App. A-E.

5.4.1 $A_1(x)$

A large fraction of the data, presented here, has been published earlier in [13]. However, there are several changes, due to the new studies, which were produced in other recent HERMES analyses, which lead to some differences with respect to the previous result and give the possibility to improve the quality of data. These changes are:

- improved data productions with better tracking and calibrations,
- new P-matrices for the RICH unfolding together with an updated method of estimation of the systematic uncertainty,
- new parameterizations for $cos\phi$ and $cos2\phi$ moments to correct the final asymmetries due to the non-zero ϕ_h dependence of the unpolarized semi-inclusive cross section.

The most significant improvement is reached in the precision of the semi-inclusive asymmetries from the deuteron target. This is the result of the additional events gained by including the previously excluded semi-inclusive data in the $2-4\ GeV$ momentum range. Also, reducing the lower z cut from 0.2 to 0.1 has improved statistics on the semi-inclusive asymmetries for both targets. In addition, to extend the kinematic range to low values of x, the low Q^2 region ($0.5-1\ GeV^2$) was analyzed.

The inclusive and $\pi^{\pm}$ double spin asymmetries for the proton target as a function of x are shown in Fig. 5.10. Fig. 5.11 shows the inclusive and $\pi^{\pm}, K^{\pm}$ asymmetries for the deuteron target. The hadron asymmetries on the proton and deuteron targets are shown in Fig. 5.12. The $Q^2 < 1\ GeV^2$ region (red squares) and $Q^2 > 1\ GeV^2$ (red circles) region are shown separately. The average kinematics and the results are listed in Tabs. A.2- A.8. The results of COMPASS, the only other experiment which measured asymmetries of identified hadrons [85], are shown for comparison in Fig. 5.11. Fig. 5.12 contains the comparison for charged hadron asymmetries. The two sets of measurements is generally compatible and in the region

of kinematic overlap the statistical precision of the two experiments is generally comparable. The consistency of the results from two experiments illustrates the weak Q^2 dependence of the semi-inclusive asymmetries.

Figs. 5.13-5.14 show the comparison with previous published HERMES result [13]. As expected, the most significant improvement can be seen in the precision of the semi-inclusive asymmetries from the deuteron target. This is a result of the additional events gained by including the previously excluded semi-inclusive data in the 2-4 GeV momentum range. Also, reducing the lower z cut from 0.2 to 0.1 has improved statistics to some degree on the semi-inclusive asymmetries for both targets. Differences in the central values can be attributed to several different causes. First, improved data productions with better tracking and calibrations were used. Second, a different azimuthal correction was applied to the semi-inclusive asymmetries of the published result. Third, the improved EVT RICH algorithm, which is significantly more successful at identifying hadrons in multi-hadron events, was not previously available.

5.4.2 3D asymmetries $A_1(x, z, p_{\perp h})$

As was mentioned before, the cross section for leptoproduction of charged hadrons in semi-inclusive deep-inelastic scattering at fixed beam energy depends on five kinematic variables. Usually, the following variables calculated in the laboratory system are chosen: Q^2, x, z, $p_{\perp h}$ and ϕ_h. Asymmetries presented as a function of one kinematic variable x do not allow to exclude the influence of HERMES acceptance function. Thus part of the physical information is lost. Therefore the study of the global characteristics, for example, the dependence of the asymmetry on z or $p_{\perp h}$ can give new information on the reaction mechanism or take into account the z-dependence of fragmentation functions. Due to the limited statistics it was decided to present the data in 2 and 3-dimensional form. Unlike the 2-dimensional $(x - p_{\perp h})$ asymmetries of the next section, the individual values for 3D semi-inclusive asymmetries have too large error bars to produce meaningful plots, that only the values of 3D binned asymmetries are presented in this thesis (App. C).

5.4.3 $A_1(x, p_{\perp h})$

Recently, semi-inclusive DIS has been shown [71], [72] to be a useful tool to investigate orbital motion of quarks, as reflected in their intrinsic transverse momenta distributions. Dependence of the asymmetry A_1 on the hadron transverse momentum $p_{\perp h}$ can be interesting and useful for understanding the internal structure of the nucleon. The $p_{h_\perp}$ dependence of the double-spin asymmetry, measured for different bins in x will provide a test of the factorization hypothesis and probe the transition from the non-perturbative to perturbative description. Recent measurements of double-spin asymmetries in SIDIS at Jefferson Lab show a significant $p_{\perp h}$-dependence, with a trend being opposite for π^+ and π^- [73]. A possible interpretation of

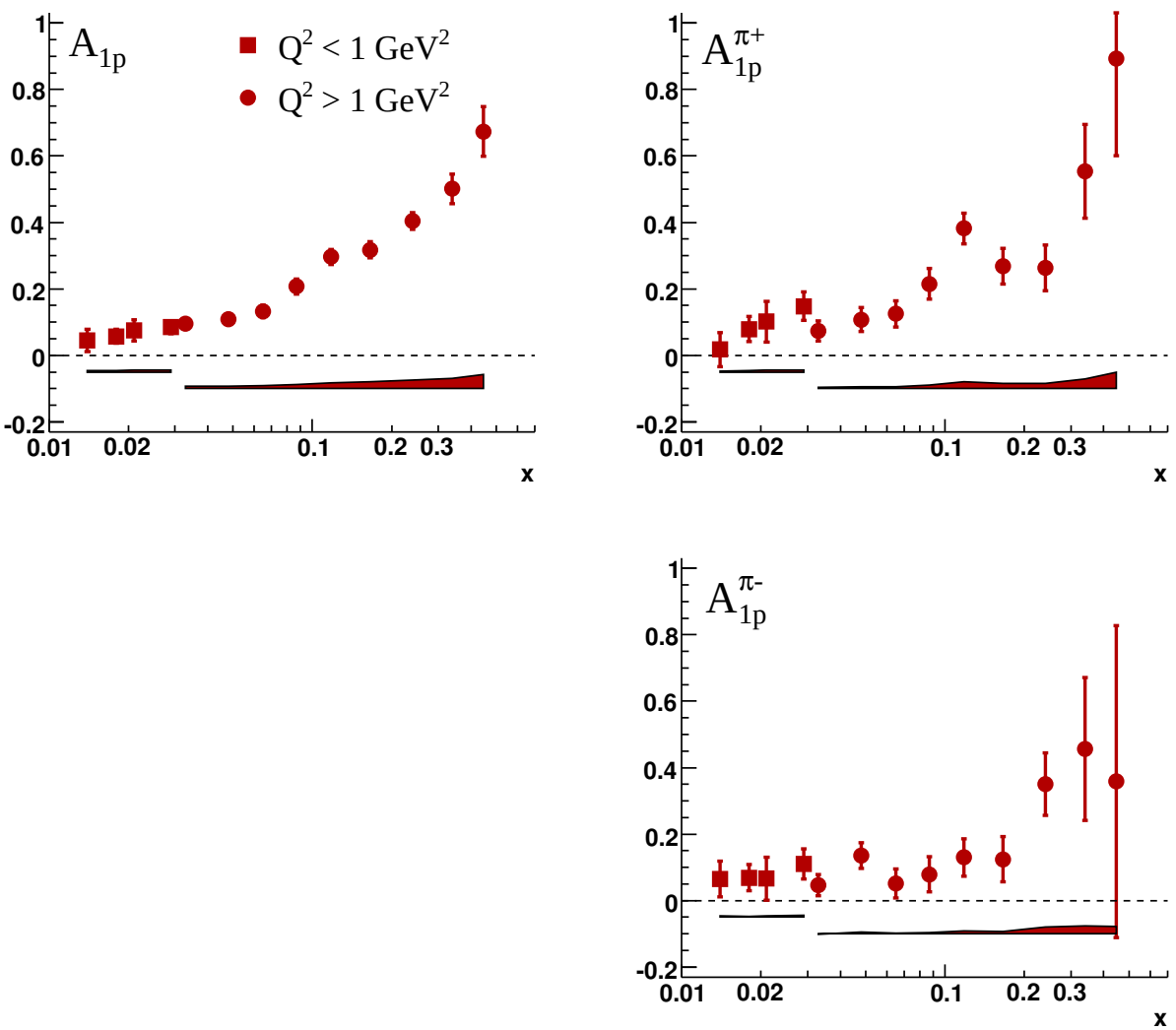

Figure 5.10: The inclusive and semi-inclusive Born level asymmetries on the proton, corrected for instrumental smearing and QED radiative effects. The error bars give the statistical uncertainties, and the colored bands indicate the systematic uncertainty.

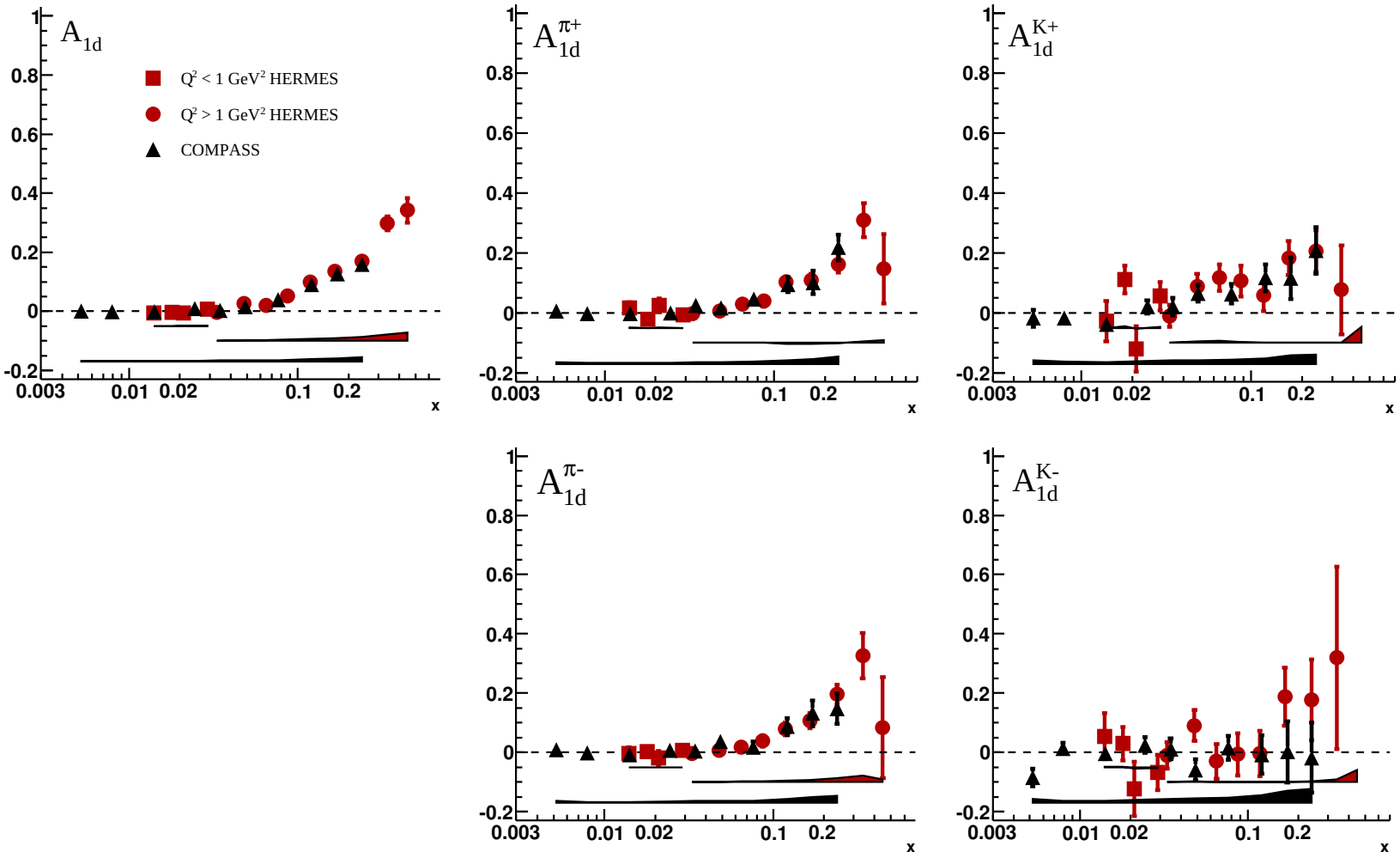

Figure 5.11: The inclusive and semi-inclusive Born level asymmetries on the deuteron, corrected for instrumental smearing and QED radiative effects. The error bars give the statistical uncertainties, and the colored bands indicate the systematic uncertainty. Black triangles and the lowermost bands are taken from the COMPASS publication [85].

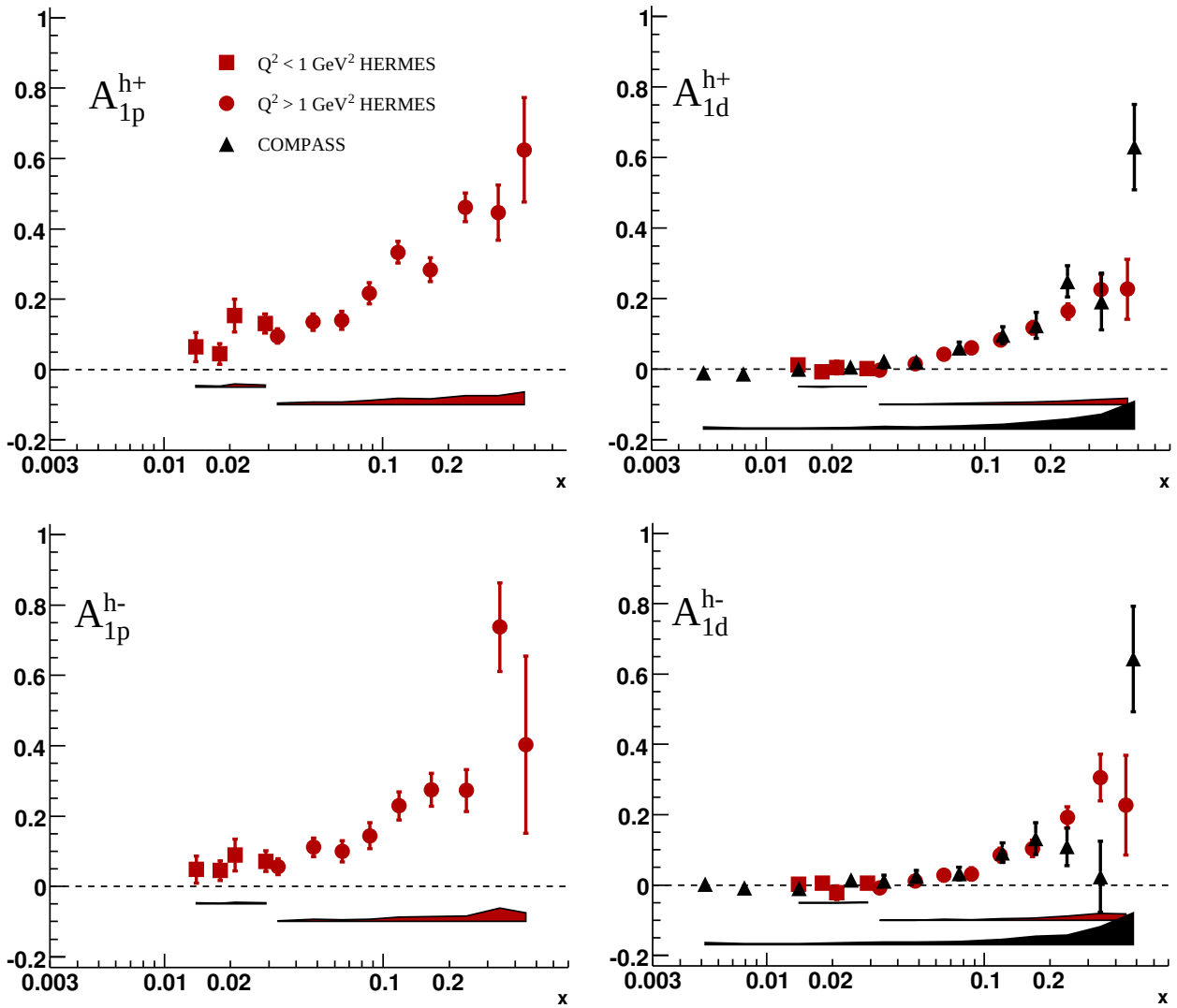

Figure 5.12: The charged hadrons Born level asymmetries for both targets , corrected for instrumental smearing and QED radiative effects. The error bars give the statistical uncertainties, and the colored bands indicate the systematic uncertainty.

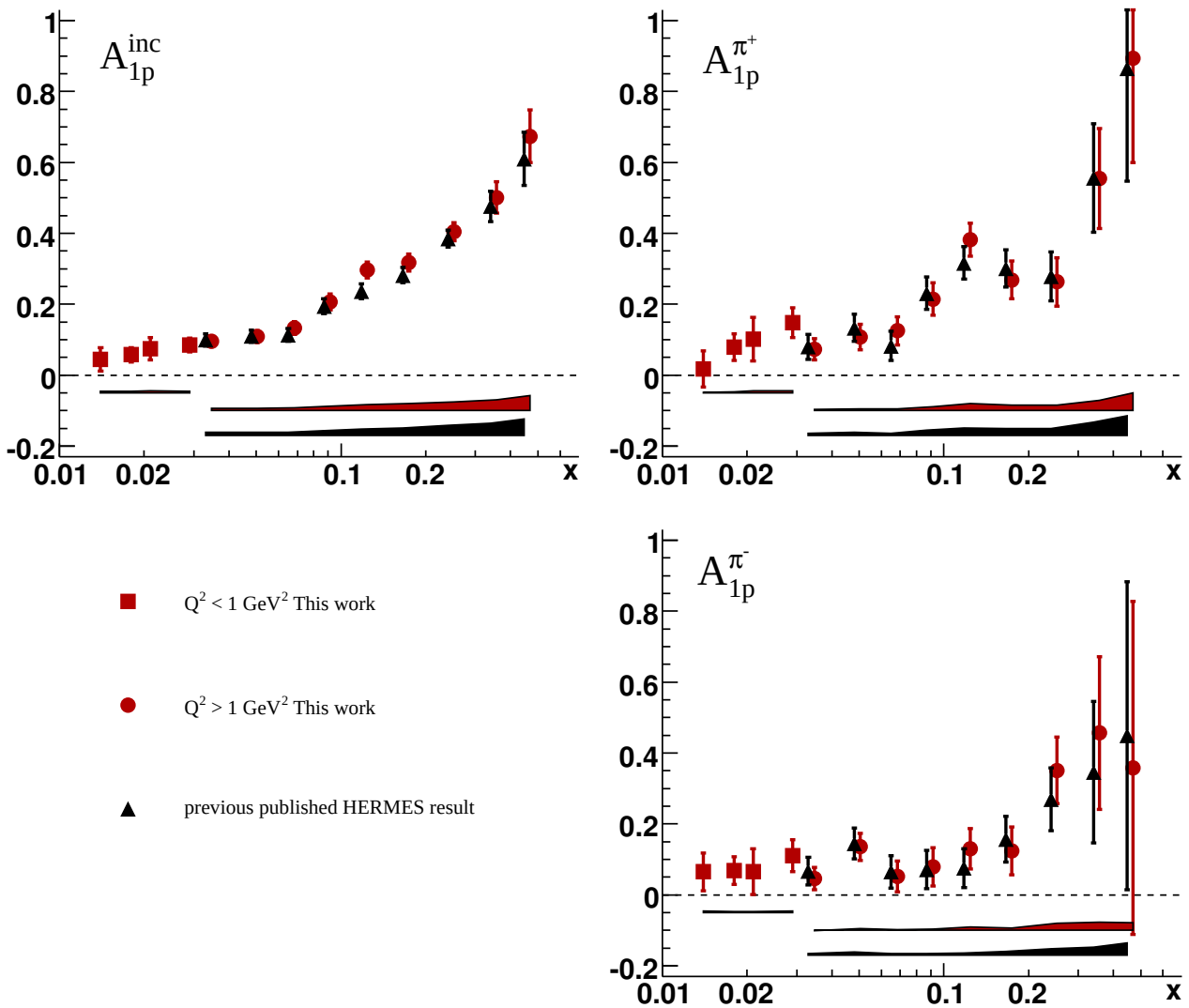

Figure 5.13: The inclusive and semi-inclusive Born level asymmetries on the proton in comparison with previous published HERMES result.

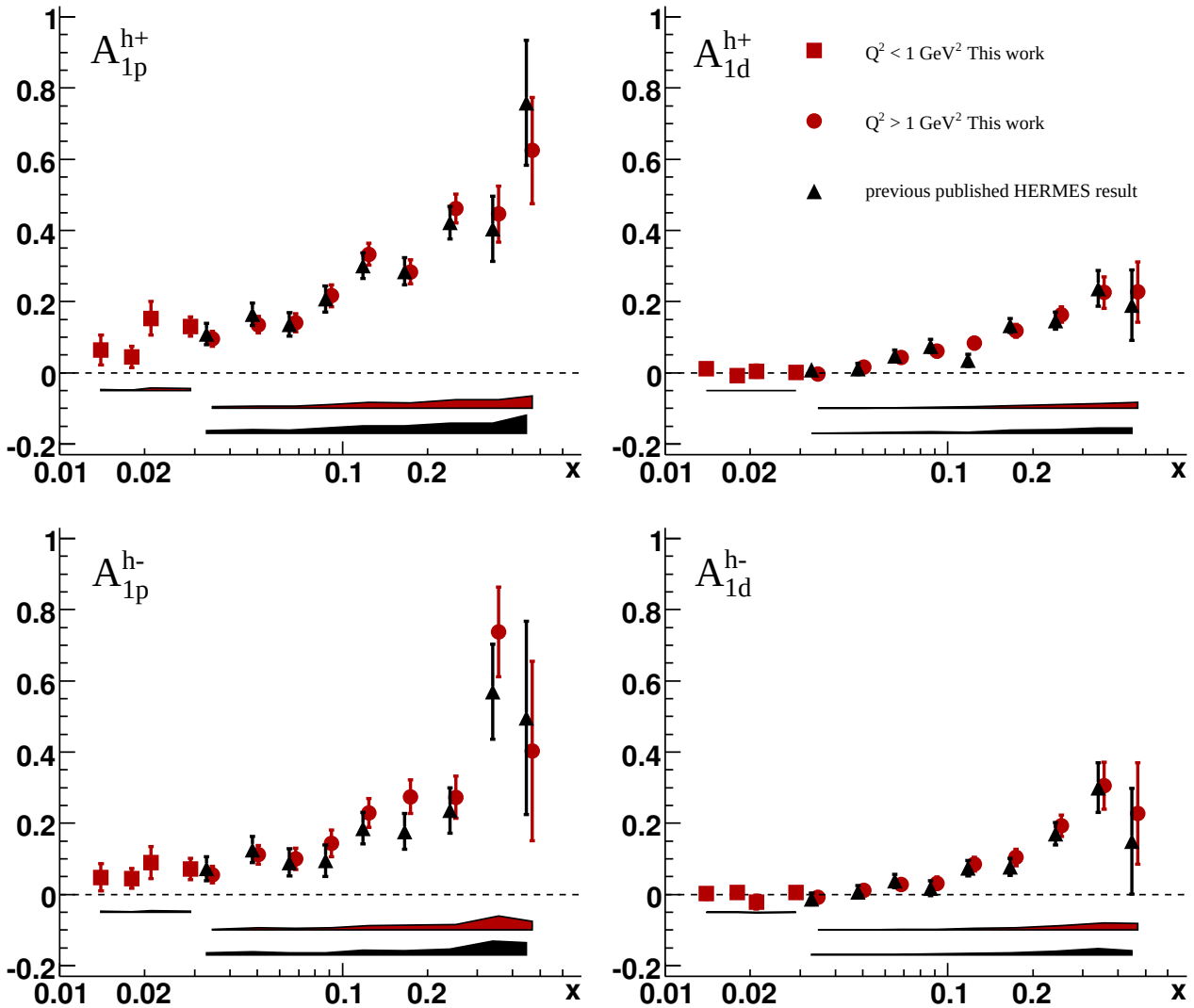

Figure 5.14: The charged hadrons Born level asymmetries for both targets in comparison with previous published HERMES result.

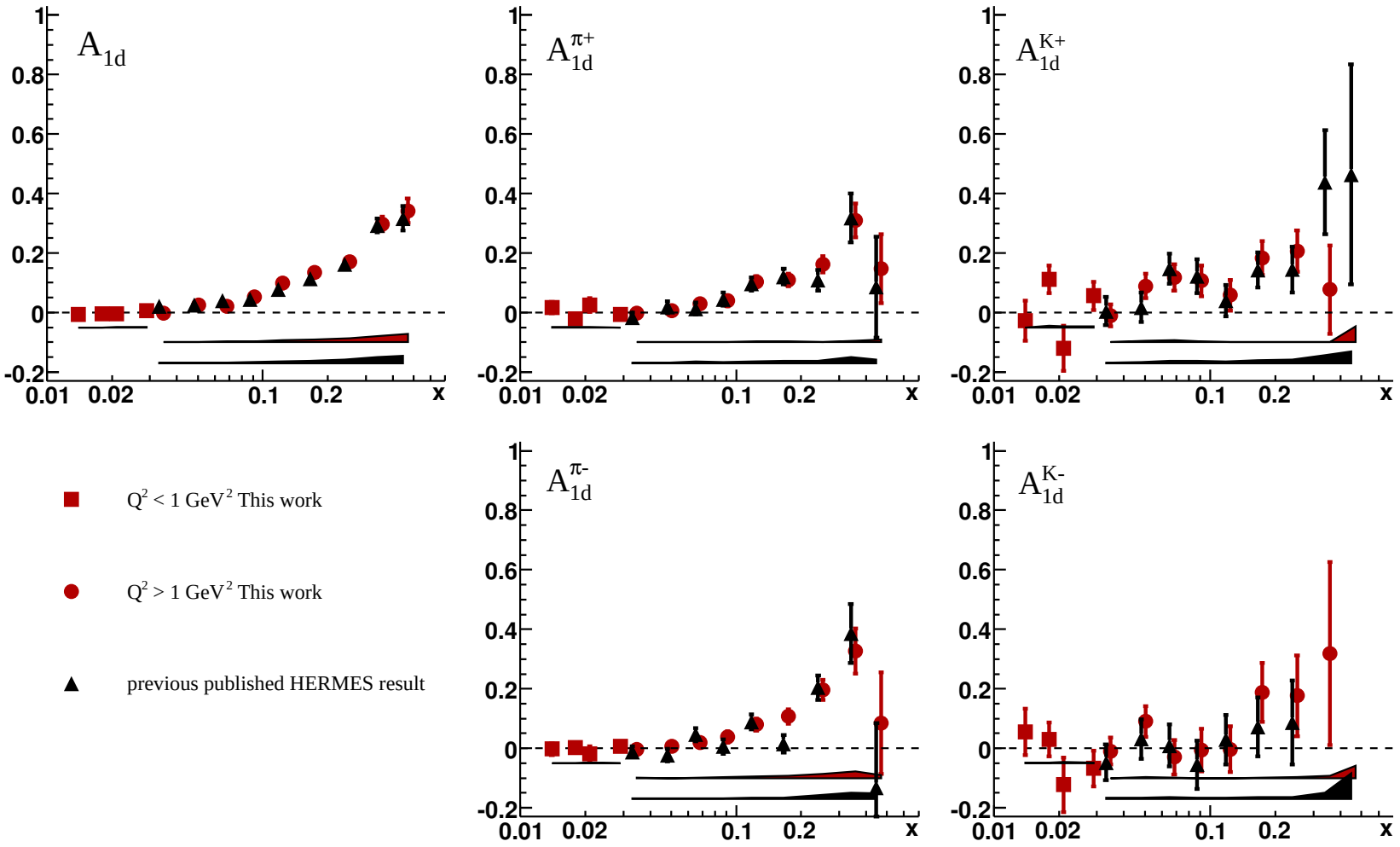

Figure 5.15: The inclusive and semi-inclusive Born level asymmetries on the deuteron in comparison with previous published HERMES result.

the $p_{h_\perp}$-dependence of the double-spin asymmetry may involve different widths of transverse-momentum distributions of quarks with different flavor and polarization [83] resulting from a different orbital structure of quarks polarized in the direction of the proton spin and opposite to it [84].

A 2-dimensional binning in x and $p_{\perp h}$ was chosen for the $A_1(x, p_{\perp h})$ presentation, because it is difficult to distinguish in a 1-dimensional plot the strong dependence of the asymmetry on x from a possible dependence on $p_{\perp h}$.

The double spin asymmetries as a function of $p_{\perp h}$ for the proton and deuteron targets are shown in Fig. 5.16 in three different x ranges:

- $0.023 < x < 0.055$ (red triangles),
- $0.055 < x < 0.100$ (lilac diamonds),
- $0.100 < x < 0.600$ (green squares).

Two upper plots show positive (left) and negative (right) pion asymmetries for the proton target. Central panels illustrate positive (left) and negative (right) pions asymmetries for the deuteron target. Positive and negative kaons are shown in the bottom part of the Fig. 5.16. The error bars give the statistical uncertainties, and the colored bands indicate the systematic uncertainty.

In order to provide a quantitative statement about any potential $p_{h_\perp}$ dependence, the final results have been fitted with simple functions in x, due to the strong dependence of the asymmetry on x, with and without $p_{h_\perp}$ dependence:

- A linear function in x without $p_{h_\perp}$ (Fig. 5.17):
  $A_1^{fit}(x, p_{h_\perp}) = Const(p_{h_\perp}) = C_1 + C_2\ x.$
- A linear function in x and $p_{h_\perp}$ (Fig. 5.18):
  $A_1^{fit}(x, p_{h_\perp}) = C_1 + C_2\ x + C_3\ p_{h_\perp}.$
- A quadratic function of both x and $p_{h_\perp}$ (Fig. 5.19):
  $A_1^{fit}(x, p_{h_\perp}) = C_1 + C_2\ x + C_3\ p_{h_\perp} + C_4\ x^2 + C_5\ p_{h_\perp}^2 + C_6\ x p_{h_\perp}.$

The fit functions are included in the plots of the final Born asymmetries. The values of χ^2 are listed in Tab. 5.3. The higher-order fit functions yield little improvement over the fit linear function in x suggesting little or no $p_{h\perp}$ dependence of the asymmetry.

5.4.4 2D asymmetries $A_1(x, Q^2)$

The average values of kinematical variables which are presented in Tabs. A.2- C.7 show that $< Q^2 >$ is different for each x-value, because x and Q^2 are correlated. That is why each x

	$p \to \pi^+$	$p \to \pi^-$	$d \to \pi^+$	$d \to \pi^-$	$d \to K^+$	$d \to K^-$
$\chi^{2\ (NDF=16)}_{C_1^h+C_2^h x}$	11.5	14.1	39.7	29.5	29.5	26.7
$\chi^{2\ (NDF=15)}_{C_1^h+C_2^h x+C_3^h p_{h\perp}}$	11.5	13.8	38.2	27.9	29.1	24.4
$\chi^{2\ (NDF=12)}_{C_1^h + C_2^h x + C_3^h p_{h\perp} + C_4^h x^2 + C_5^h p_{h\perp} + C_6^h x p_{h\perp}}$	7.78	5.31	36.4	14.9	20.1	16.9

Table 5.3: The value of χ^2 for each functional form fit to the $A_1(x, p_{h\perp})$ data points for each target–final-state-hadron combination.

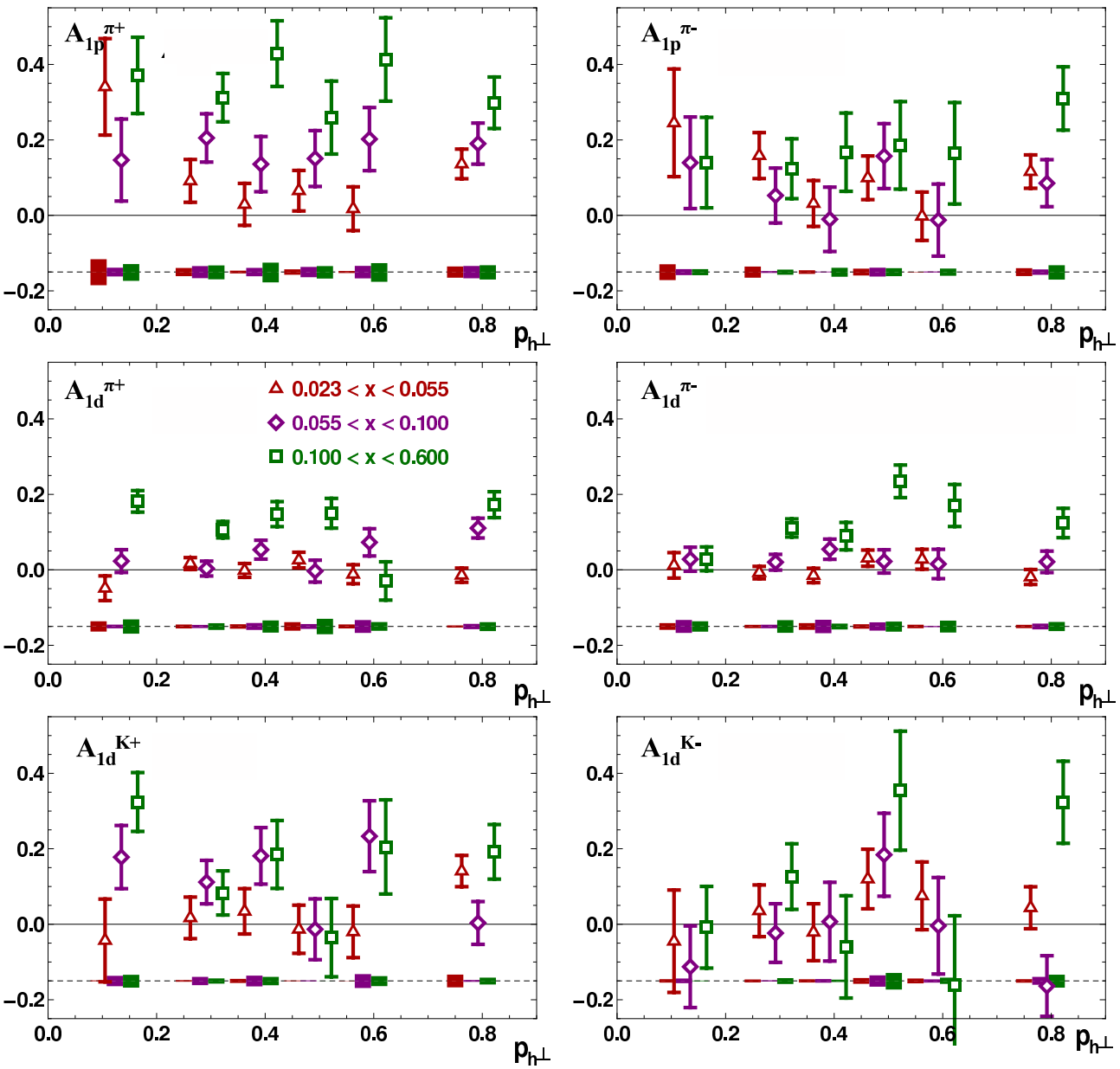

Figure 5.16: $A_1(x, p_{h\perp})$ for charged pion production for proton and deuteron targets and charge kaon production for deuteron target, in three different x ranges.

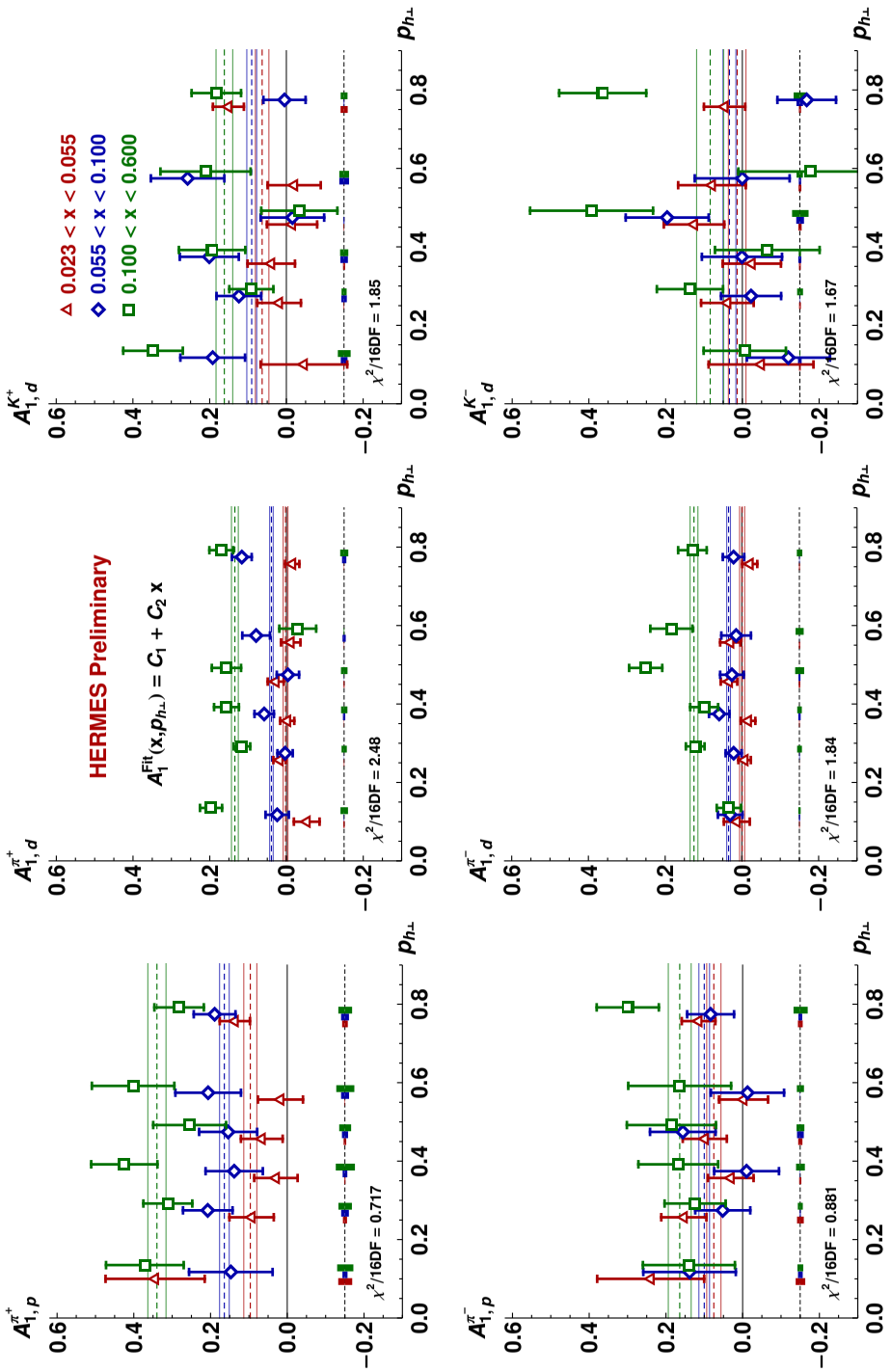

Figure 5.17: Final result for $A_1(x, p_{\perp h})$ fit with a simple linear function in x (dashed) with no $p_{h_\perp}$ dependence. Each fit curve is bounded by a 1-σ error band of the same color. The small solid rectangles represent the systematic uncertainty for the associated data point. The reduced χ^2 values given suggest that this parameterization is adequate to describe the data.

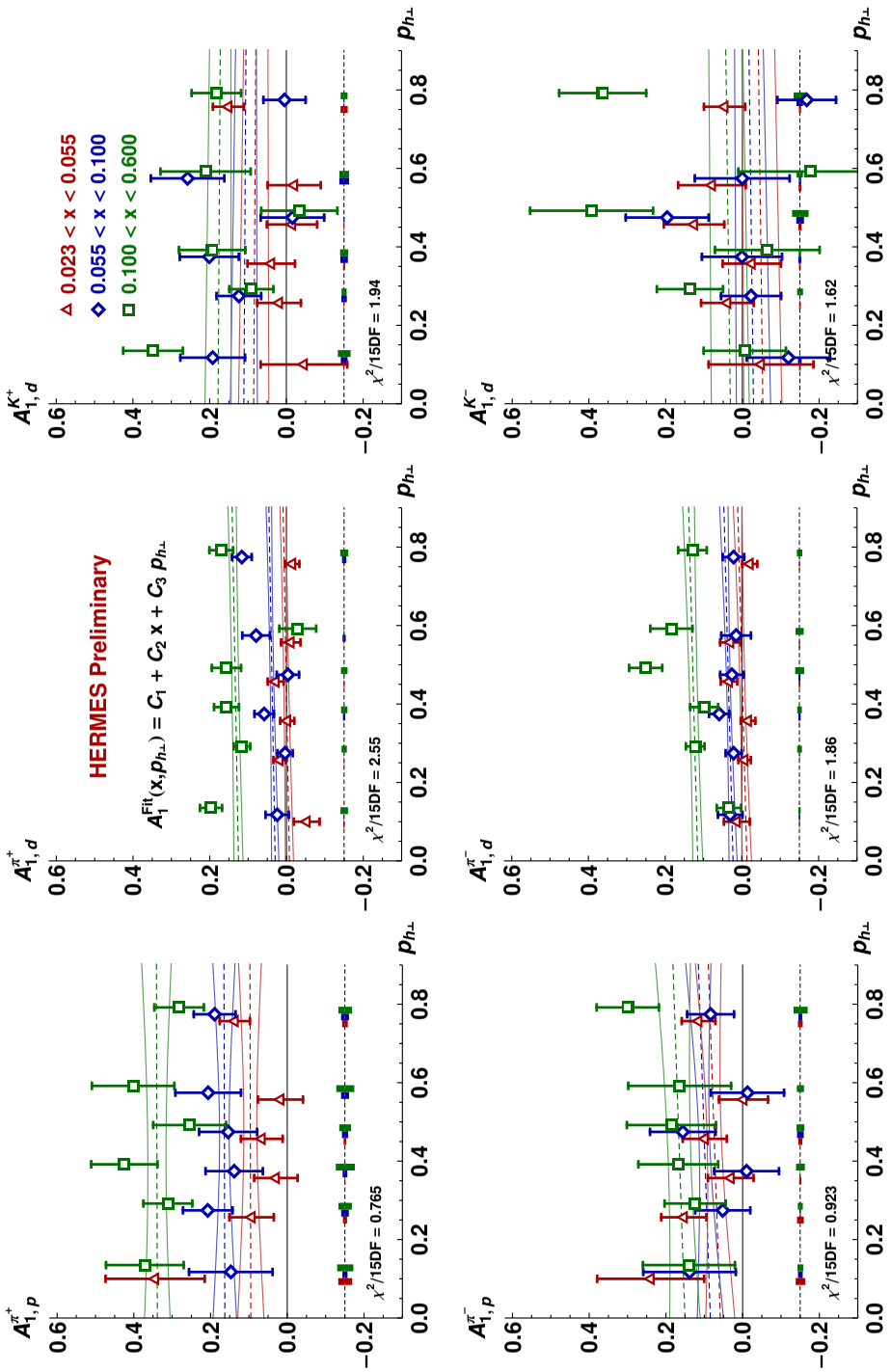

Figure 5.18: Final result for $A_1(x, p_{\perp h})$ fit with a simple linear function in x (dashed) with no $p_{h_\perp}$ dependence. Each fit curve is bounded by a 1-σ error band of the same color. The small solid rectangles represent the systematic uncertainty for the associated data point. The reduced χ^2 values given suggest that this parameterization is adequate to describe the data.

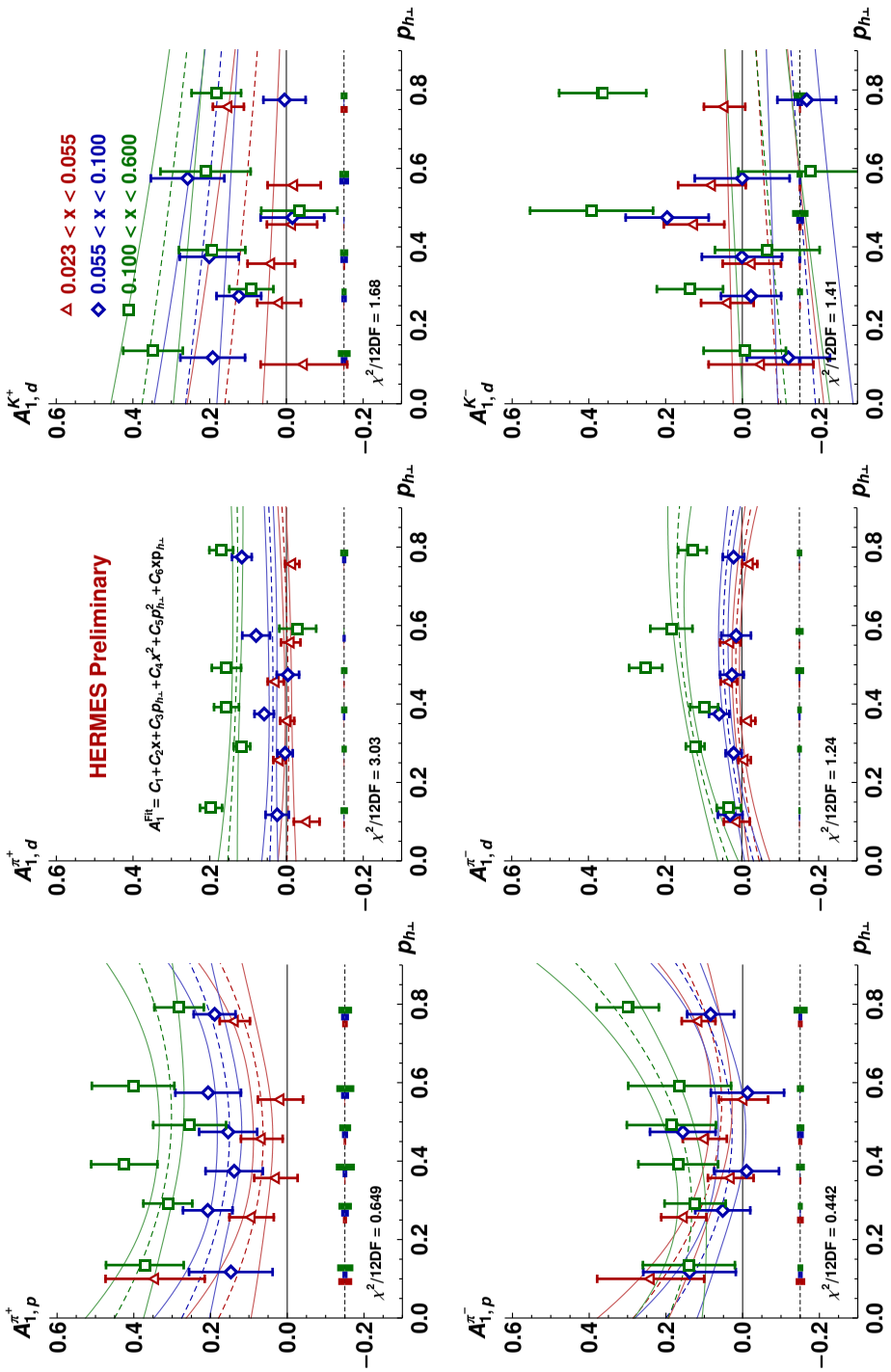

Figure 5.19: Final result for $A_1(x, p_{\perp h})$ fit with a simple linear function in x (dashed) with no $p_{h_\perp}$ dependence. Each fit curve is bounded by a 1-σ error band of the same color. The small solid rectangles represent the systematic uncertainty for the associated data point. The reduced χ^2 values given suggest that this parameterization is adequate to describe the data.

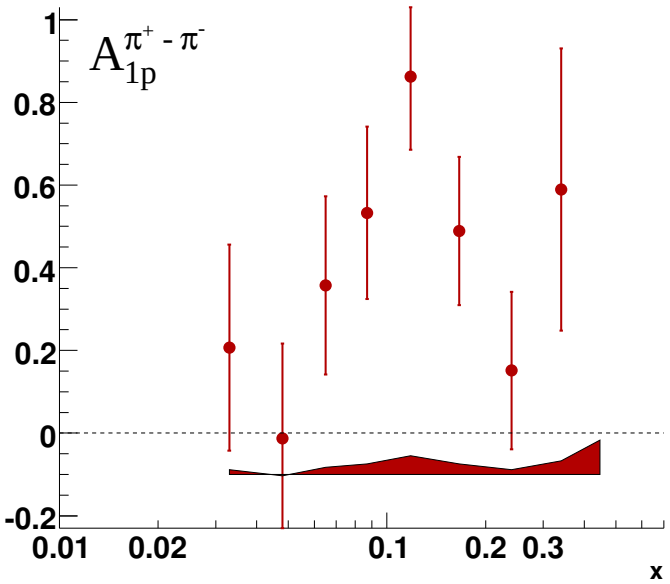

Figure 5.20: The pion-charge-difference asymmetry $A_{1p}^{\pi^+-\pi^-}$ for the proton target. The error bars give the statistical uncertainties, and the colored band indicates the systematic uncertainty.

interval has been divided into two Q^2 bins and 2-dimension $(x - Q^2)$ binned asymmetries have been extracted (see App. D). The bin edges are listed in Tab. D.1. The values of $h^\pm$, $\pi^\pm$ and $K^\pm$ Born asymmetries are listed in Tab. D.2-**??**.

5.4.5 Hadron charge difference asymmetries

Because of its simple and symmetric structure, the deuteron target – one proton and one neutron, provides several opportunities to extract otherwise algebraically buried quantities by employing certain symmetry assumptions. The deuteron is *isoscalar*, that is when one maps the partons to their isospin conjugates ($u \to d$, $d \to u$, $\bar{u} \to \bar{d}$, and, $\bar{d} \to \bar{u}$), the result is still a deuteron.

The asymmetry of the hadron-charge-difference $A_1^{h^+-h^-}$ is one example of taking the advantage of this symmetry. The asymmetry $A_1^{h^+-h^-}$ is defined as a spin asymmetry for the difference of cross sections for positive and negative hadrons

$$A_1^{h^+-h^-} = \frac{(\sigma^{h^+}_{\overrightarrow{\Leftarrow}} - \sigma^{h^-}_{\overrightarrow{\Leftarrow}}) - (\sigma^{h^+}_{\overrightarrow{\Rightarrow}} - \sigma^{h^-}_{\overrightarrow{\Rightarrow}})}{(\sigma^{h^+}_{\overrightarrow{\Leftarrow}} - \sigma^{h^-}_{\overrightarrow{\Leftarrow}}) + (\sigma^{h^+}_{\overrightarrow{\Rightarrow}} - \sigma^{h^-}_{\overrightarrow{\Rightarrow}})}. \tag{5.42}$$

Under certain symmetry assumptions, particularly charge-conjugation invariance in fragmentation, this quantity is equal to the ratio of the sums of the polarized to the unpolarized valence parton densities (see Chap 6.6). The asymmetry $A_1^{h^+-h^-}$ provides not only a Monte-

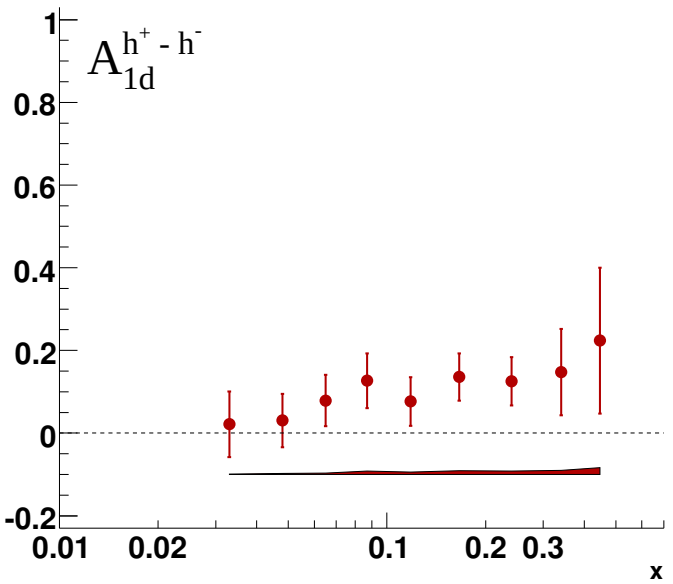

Figure 5.21: The hadron-charge-difference asymmetry $A_{1d}^{h^+-h^-}$ for the deuteron target. The error bars give the statistical uncertainties, and the colored band indicates the systematic uncertainty. The difference between Fig. 5.29 and this plot is that also protons and antiproton are included.

Carlo–free cross-check of the ratio of the linear combinations of the polarized to the unpolarized valence parton densities, which will be computed in Chapter 6.6, but will also allow us to make a critique of the assumptions involved. The recent HERMES isoscalar $\Delta s(x)$ analysis [65] is based on a similar concept.

The asymmetries of the hadron-charge-difference as a function of x are presented in Figs. 5.20-5.23. For the proton target only the pion-charge-difference asymmetry has been extracted (Fig. 5.20). For the deuteron target hadron (Fig. 5.21), pion (Fig. 5.22) and kaon (Fig. 5.23) charge-difference asymmetries are shown. The error bars give the statistical uncertainties, and the colored bands indicate the systematic uncertainty. Hadron RICH unfolding and the azimuthal correction factor were applied in the same way as for the standard asymmetries. Corrections to the asymmetries for higher order QED and detector smearing effects were carried out using an unfolding algorithm as indicated in Chap. 5.2.1. However, there are additional requirements [58] for the smearing matrices in a case of hadron-charge-difference asymmetries.

Check of requirements to the unfolding procedure.

The semi-inclusive double spin asymmetries for positive and negative hadrons h^+ and h^- are defined by

$$A^{h^+} = \frac{\sigma^{h^+}_{\rightarrow\Leftarrow} - \sigma^{h^+}_{\rightarrow\Rightarrow}}{\sigma^{h^+}_{\rightarrow\Leftarrow} + \sigma^{h^+}_{\rightarrow\Rightarrow}}, \qquad A^{h^-} = \frac{\sigma^{h^-}_{\rightarrow\Leftarrow} - \sigma^{h^-}_{\rightarrow\Rightarrow}}{\sigma^{h^-}_{\rightarrow\Leftarrow} + \sigma^{h^-}_{\rightarrow\Rightarrow}}. \tag{5.43}$$

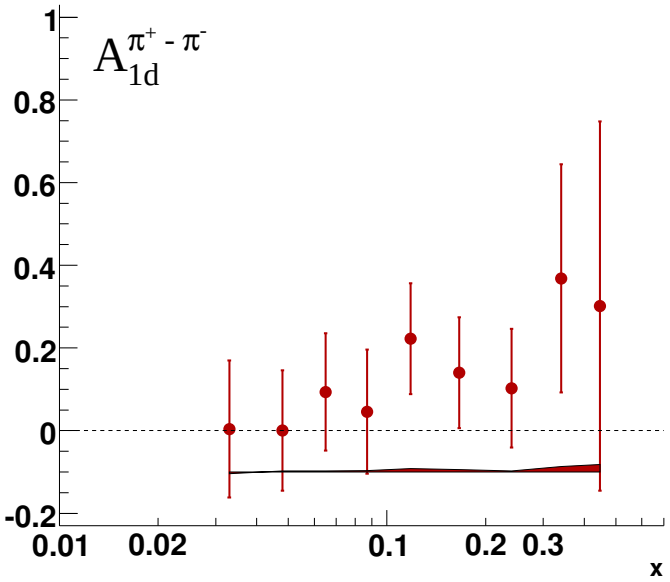

Figure 5.22: The pion-charge-difference asymmetry $A_{1d}^{\pi^+ - \pi^-}$ for the deuteron target. The error bars give the statistical uncertainties, and the colored band indicates the systematic uncertainty.

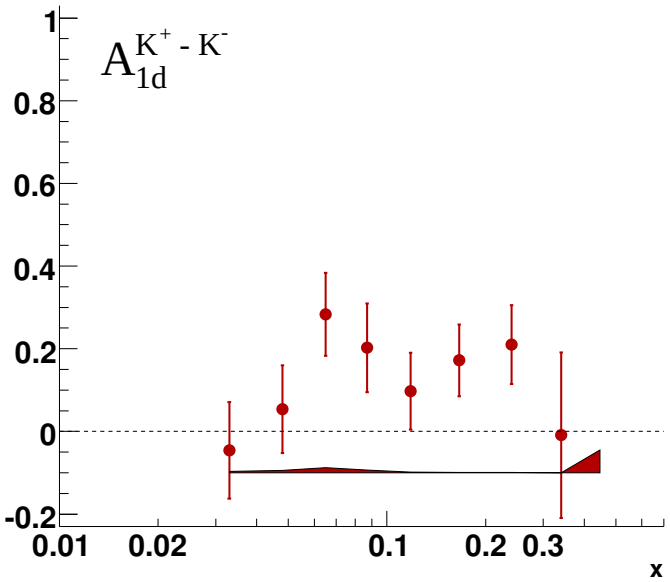

Figure 5.23: The kaon charge-difference asymmetry $A_{1d}^{K^+ - K^-}$ for the deuteron target. The error bars give the statistical uncertainties, and the colored band indicates the systematic uncertainty.

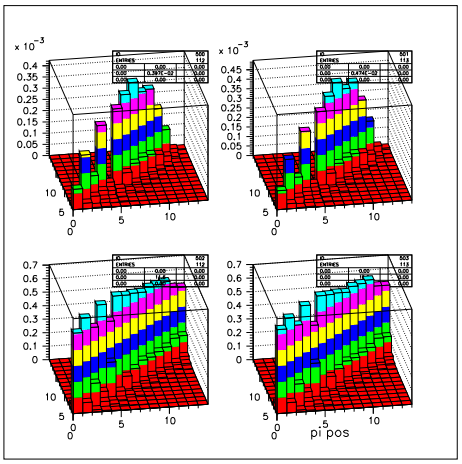

Figure 5.24: Migration matrices $n^{\pi^+}_{\substack{\rightarrow \\ \Rightarrow}}$ (top left) and $n^{\pi^+}_{\substack{\rightarrow \\ \Leftarrow}}$ (top right) and smearing matrices $S^{\pi^+}_{\substack{\rightarrow \\ \Rightarrow}}$ (bottom left) and $S^{\pi^+}_{\substack{\rightarrow \\ \Leftarrow}}$ (bottom right)

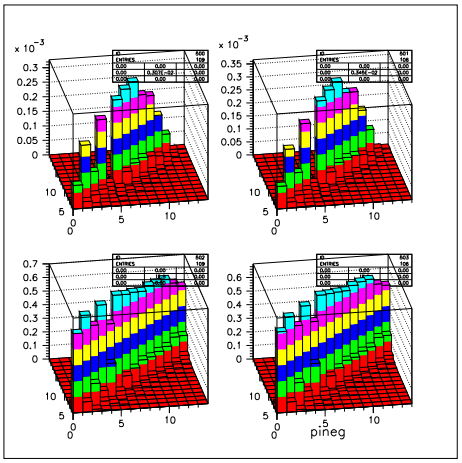

Figure 5.25: Migration matrices $n^{\pi^-}_{\substack{\rightarrow \\ \Rightarrow}}$ (top left) and $n^{\pi^-}_{\substack{\rightarrow \\ \Leftarrow}}$ (top right) and smearing matrices $S^{\pi^-}_{\substack{\rightarrow \\ \Rightarrow}}$ (bottom left) and $S^{\pi^-}_{\substack{\rightarrow \\ \Leftarrow}}$ (bottom right)

In this analysis the hadron-charge-difference asymmetry, which is defined as the spin asymmetry for the difference of the cross sections for positive and negative hadrons, is given:

$$A^{h^+-h^-} = \frac{\left(\sigma^{h^+}_{\substack{\rightarrow \\ \Leftarrow}} - \sigma^{h^-}_{\substack{\rightarrow \\ \Leftarrow}}\right) - \left(\sigma^{h^+}_{\substack{\rightarrow \\ \Rightarrow}} - \sigma^{h^-}_{\substack{\rightarrow \\ \Rightarrow}}\right)}{\left(\sigma^{h^+}_{\substack{\rightarrow \\ \Leftarrow}} - \sigma^{h^-}_{\substack{\rightarrow \\ \Leftarrow}}\right) + \left(\sigma^{h^+}_{\substack{\rightarrow \\ \Rightarrow}} - \sigma^{h^-}_{\substack{\rightarrow \\ \Rightarrow}}\right)}. \tag{5.44}$$

The relation between the difference asymmetries of Eq. 5.44 and the standard hadron asymmetries of Eq. 5.43 is

$$A^{h^+-h^-} = \frac{1}{1-r}\Big(A^{h^+} - rA^{h^-}\Big), \tag{5.45}$$

where

$$r = \frac{\sigma^{h^-}_{\overset{\rightarrow}{\Leftarrow}} + \sigma^{h^-}_{\overset{\rightarrow}{\Rightarrow}}}{\sigma^{h^+}_{\overset{\rightarrow}{\Leftarrow}} + \sigma^{h^+}_{\overset{\rightarrow}{\Rightarrow}}} = \frac{\sigma^{h^-}}{\sigma^{h^+}}. \tag{5.46}$$

It is obvious, that only the case, when $\sigma^{h^+} \neq \sigma^{h^-}$ can be considered.

Corrections to the asymmetries for higher order QED and detector smearing effects were applied in the same way as it was applied to the standard asymmetries (see Chap. 5.2.1). The relation between the Monte Carlo yields for eXperimental kinematics and the Monte Carlo yields for Born level kinematics is

$$n^{X}_{\overset{\rightarrow}{\Rightarrow}}(i) = \sum S_{\overset{\rightarrow}{\Rightarrow}}(i,j) n^{B}_{\overset{\rightarrow}{\Rightarrow}}(j) + n^{B}_{\overset{\rightarrow}{\Rightarrow}}(0), \quad n^{X}_{\overset{\rightarrow}{\Leftarrow}}(i) = \sum S_{\overset{\rightarrow}{\Leftarrow}}(i,j) n^{B}_{\overset{\rightarrow}{\Leftarrow}}(j) + n^{B}_{\overset{\rightarrow}{\Leftarrow}}(0), \tag{5.47}$$

where cross section normalized migration matrices (smearing matrices) are

$$S_{\overset{\rightarrow}{\Rightarrow}}(i,j) = \frac{n_{\overset{\rightarrow}{\Rightarrow}}(i,j)}{n^{B}_{\overset{\rightarrow}{\Rightarrow}}(j)}, \qquad S_{\overset{\rightarrow}{\Leftarrow}}(i,j) = \frac{n_{\overset{\rightarrow}{\Leftarrow}}(i,j)}{n^{B}_{\overset{\rightarrow}{\Leftarrow}}(j)}. \tag{5.48}$$

Figs. 5.24, 5.25 show the migration and smearing matrices for positive and negative pions separately for parallel and anti-parallel case for proton target.

In a case of hadron-charge-difference asymmetry the migration matrices $n_{\overset{\rightarrow}{\Rightarrow}}(i,j)$ and $n_{\overset{\rightarrow}{\Leftarrow}}(i,j)$ for parallel and anti-parallel spin orientation respectively contain the *difference* of the count rates of positive and negative hadrons which fall all into bin i of eXperimental kinematics and bin j of BORN kinematics.

$$n_{\overset{\rightarrow}{\Rightarrow}}(i,j) = n^{h^+}_{\overset{\rightarrow}{\Rightarrow}}(i,j) - n^{h^-}_{\overset{\rightarrow}{\Rightarrow}}(i,j), \quad n_{\overset{\rightarrow}{\Leftarrow}}(i,j) = n^{h^+}_{\overset{\rightarrow}{\Leftarrow}}(i,j) - n^{h^-}_{\overset{\rightarrow}{\Leftarrow}}(i,j). \tag{5.49}$$

The BORN counts rates $n^{B}_{\overset{\rightarrow}{\Rightarrow}}(j)$ and $n^{B}_{\overset{\rightarrow}{\Leftarrow}}(j)$ can be written as the *difference* of BORN count rates of positive and negative hadrons which were extracted from the BORN Monte Carlo dataset (see Fig. 5.26(top plots))

$$n^{Bh^+-h^-}_{\overset{\rightarrow}{\Rightarrow}}(j) = n^{Bh^+}_{\overset{\rightarrow}{\Rightarrow}}(j) - n^{Bh^-}_{\overset{\rightarrow}{\Rightarrow}}(j), \quad n^{Bh^+-h^-}_{\overset{\rightarrow}{\Leftarrow}}(j) = n^{Bh^+}_{\overset{\rightarrow}{\Leftarrow}}(j) - n^{Bh^-}_{\overset{\rightarrow}{\Leftarrow}}(j). \tag{5.50}$$

The Fig. 5.26 (bottom plots) shows that the difference of smearing matrices for positive and negative pions is zero. That is what we expected, because the smearing effects do not depend on the hadron charge. Then we can rewrite the formula 5.47 for hadron-charge-difference asymmetry

$$\begin{aligned} \mathrm{n}^{Xh^+}_{\overset{\rightarrow}{\Rightarrow}(\overset{\rightarrow}{\Leftarrow})}(i) - n^{Xh^-}_{\overset{\rightarrow}{\Rightarrow}(\overset{\rightarrow}{\Leftarrow})}(i) = \\ = \sum S^{h^+}_{\overset{\rightarrow}{\Rightarrow}(\overset{\rightarrow}{\Leftarrow})}(i,j) n^{Bh^+}_{\overset{\rightarrow}{\Rightarrow}(\overset{\rightarrow}{\Leftarrow})}(j) - \sum S^{h^-}_{\overset{\rightarrow}{\Rightarrow}(\overset{\rightarrow}{\Leftarrow})}(i,j) n^{Bh^-}_{\overset{\rightarrow}{\Rightarrow}(\overset{\rightarrow}{\Leftarrow})}(j) + \\ + n^{Bh^+}_{\overset{\rightarrow}{\Rightarrow}(\overset{\rightarrow}{\Leftarrow})}(0) - n^{Bh^-}_{\overset{\rightarrow}{\Rightarrow}(\overset{\rightarrow}{\Leftarrow})}(0) = \end{aligned}$$

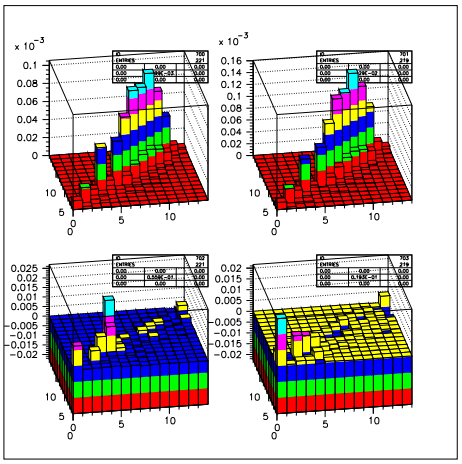

Figure 5.26: Differences of migration matrices $n^{\pi^+}_{\rightarrow\atop\Rightarrow} - n^{\pi^-}_{\rightarrow\atop\Rightarrow}$ (top left) and $n^{\pi^+}_{\rightarrow\atop\Leftarrow} - n^{\pi^-}_{\rightarrow\atop\Leftarrow}$ (top right) and differences of smearing matrices $S^{\pi^+}_{\rightarrow\atop\Rightarrow} - S^{\pi^-}_{\rightarrow\atop\Rightarrow}$ (bottom left) and $S^{\pi^+}_{\rightarrow\atop\Leftarrow} - S^{\pi^-}_{\rightarrow\atop\Leftarrow}$ (bottom right)

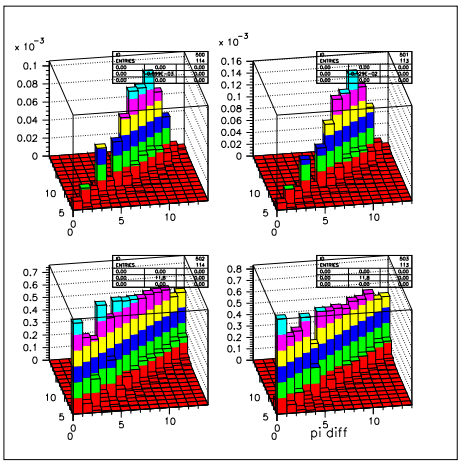

Figure 5.27: Migration matrices $n^{\pi^+-\pi^-}_{\rightarrow\atop\Rightarrow}$ (top left) and $n^{\pi^+-\pi^-}_{\rightarrow\atop\Leftarrow}$ (top right) and smearing matrices $S^{\pi^+-\pi^-}_{\rightarrow\atop\Rightarrow}$ (bottom left) and $S^{\pi^+-\pi^-}_{\rightarrow\atop\Leftarrow}$ (bottom right)

$$=\sum S^{h^+(or\ h^-)}_{\rightarrow\atop\Rightarrow(\Leftarrow)}(i,j)\left(n^{Bh^+}_{\rightarrow\atop\Rightarrow(\Leftarrow)}(j) - n^{Bh^-}_{\rightarrow\atop\Rightarrow(\Leftarrow)}(j)\right) + n^{Bh^+}_{\rightarrow\atop\Rightarrow(\Leftarrow)}(0) - n^{Bh^-}_{\rightarrow\atop\Rightarrow(\Leftarrow)}(0).$$

Based on count rates (Eq. 5.49, 5.50) smearing matrices

$$S^{h^+-h^-}_{\rightarrow\atop\Rightarrow}(i,j) = \frac{\partial\sigma^X_{\rightarrow\atop\Rightarrow}(i)}{\partial\sigma^B_{\rightarrow\atop\Rightarrow}(j)} = \frac{n^{\rightarrow}_{\Rightarrow}(i,j)}{n^B_{\rightarrow\atop\Rightarrow}(j)} = \frac{n^{h^+}_{\rightarrow\atop\Rightarrow}(i,j) - n^{h^-}_{\rightarrow\atop\Rightarrow}(i,j)}{n^{Bh^+}_{\rightarrow\atop\Rightarrow}(j) - n^{Bh^-}_{\rightarrow\atop\Rightarrow}(j)}, \tag{5.51}$$

$$S^{h^+-h^-}_{\rightarrow\atop\Leftarrow}(i,j) = \frac{\partial\sigma^X_{\rightarrow\atop\Leftarrow}(i)}{\partial\sigma^B_{\rightarrow\atop\Leftarrow}(j)} = \frac{n^{\rightarrow}_{\Leftarrow}(i,j)}{n^B_{\rightarrow\atop\Leftarrow}(j)} = \frac{n^{h^+}_{\rightarrow\atop\Leftarrow}(i,j) - n^{h^-}_{\rightarrow\atop\Leftarrow}(i,j)}{n^{Bh^+}_{\rightarrow\atop\Leftarrow}(j) - n^{Bh^-}_{\rightarrow\atop\Leftarrow}(j)} \tag{5.52}$$

are calculated.

The Fig. 5.27 shows migration and smearing matrices for pion charge difference asymmetry. As one can see on the Fig. 5.28:

$$S^{h^+-h^-}_{\Rightarrow(\Leftarrow)}(i,j) \simeq S^{h^+}_{\Rightarrow(\Leftarrow)}(i,j) \simeq S^{h^-}_{\Rightarrow(\Leftarrow)}(i,j). \tag{5.53}$$

Performance of this requirement resolves use of the given in Chap. 5.2.1 unfolding method.

Another method, which allows to unfold the experimental *yields* and then form asymmetries from them, was suggested in [70]. The *yield unfolding* method should give identical result, however there are characteristic features, which make the *asymmetry unfolding* method more attractive. Born asymmetries depend only on raw asymmetries and their uncertainties in a case of *asymmetry unfolding* method. The result, which one can obtain using *yield unfolding* method, depend on the uncertainties of the experimental yields. Because the beam and target polarizations are imperfect, the experimental yields depend on linear combinations of physical lepton-nucleon spin state. Nevertheless, the results from both methods are in a good agreement, when the data sample has enough statistics.

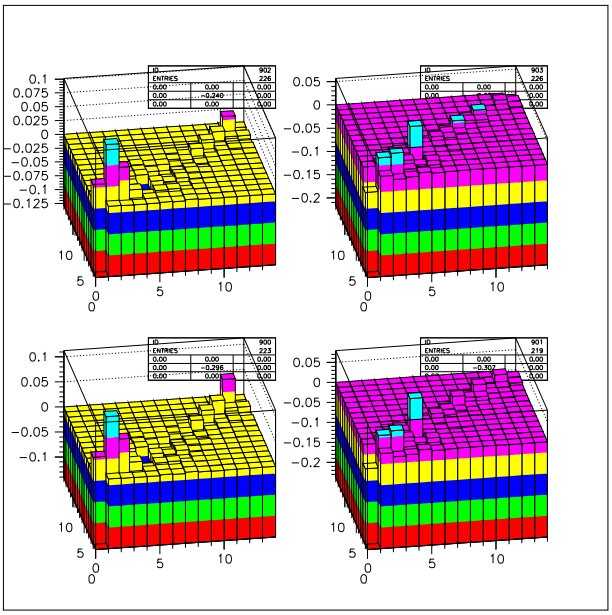

Figure 5.28: Difference of smearing matrices $S^{\pi^+}_{\Rightarrow} - S^{\pi^+-\pi^-}_{\Rightarrow}$ (top left) and $S^{\pi^+}_{\Leftarrow} - S^{\pi^+-\pi^-}_{\Leftarrow}$ (top right), $S^{\pi^-}_{\Rightarrow} - S^{\pi^+-\pi^-}_{\Rightarrow}$ (bottom left) and $S^{\pi^-}_{\Leftarrow} - S^{\pi^+-\pi^-}_{\Leftarrow}$ (bottom right)

The values of asymmetries with their statistical and systematic uncertainties as a function of x with the corresponding average kinematic variables and azimuthal correction factor are presented in Tabs. E.1-E.4.

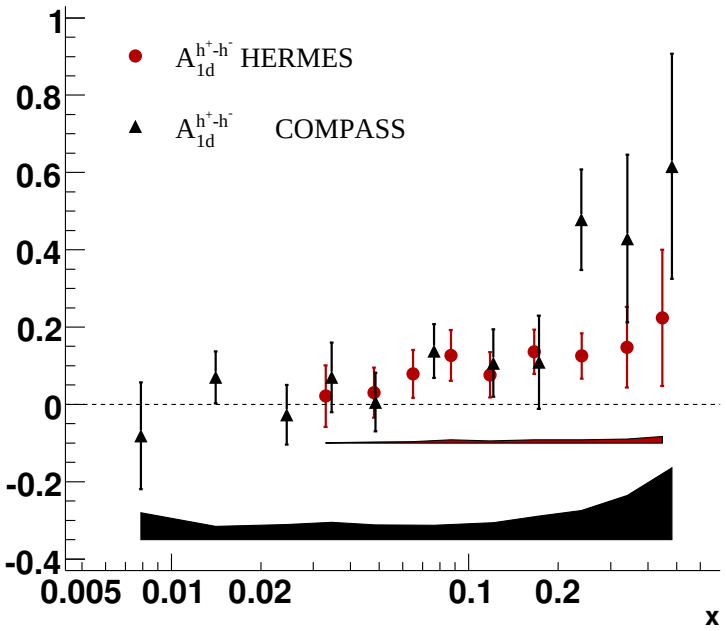

Figure 5.29: The hadron charge-difference asymmetry for deuteron target in comparison with the COMPASS result.

5.4.6 Comparison of result to COMPASS experiment

The COMPASS experiment at CERN measured the semi-inclusive difference asymmetry $A^{h^+-h^-}$ for hadrons of opposite charge [82]. The data were collected in the years 2002-2004 using a 160 GeV polarized muon beam scattered off a large polarized ^6LiD target in the kinematic range $0.006 < x < 0.7$ and $1\ GeV^2 < Q^2 < 100\ GeV^2$. The HERMES result on the difference asymmetry $A_{1d}^{h^+-h^-}$ is shown on Fig. 5.29 as a function of x (red circles) in comparison to the COMPASS result (black triangles) for the difference asymmetry $A_{1d}^{h^+-h^-}$ for unidentified hadrons of opposite charges (where about 10% of the selected hadron sample is protons and antiprotons).

Though the COMPASS data extend the measured region to lower values of x, the two sets of measurements are well compatible and in the region of kinematic overlap the statistical precision of the two experiments is generally comparable. However for $x \leq 0.1$ COMPASS statistical uncertainties are smaller then for HERMES data points, at $x \geq 0.1$ HERMES statistical accuracy is better. The values of systematic uncertainties are slightly different. The main source of systematic uncertainties for HERMES result is the systematic uncertainties in the beam and target polarizations (see Chap. 5.3). In a case of COMPASS measurements the systematic uncertainties arise from the uncertainties, which are related to the dilution factor, which includes the dilution due to radiative events on the deuteron, and to the ratio $R = \sigma_L/\sigma_T$ (see Eq. 2.27), used to calculate the depolarization factor.

Chapter 6

Quark Helicity Distributions

6.1 Formalism of Helicity-Distribution Extraction

The extraction of the polarized quark distributions Δq is based on the LO QCD expressions 2.72 which relate the photon-nucleon asymmetries A_1^h to the polarized $\Delta q(x, Q^2)$ and unpolarized $q(x, Q^2)$ quark distributions and fragmentation functions $D_q^h(Q^2, z)$:

$$A_1^h(x, Q^2, z) = C_R(x, Q^2) \frac{\sum_q e_q^2 \Delta q(x, Q^2) D_q^h(Q^2, z)}{\sum_q e_q^2 q(x, Q^2) D_q^h(Q^2, z)}. \tag{6.1}$$

Compared to Eqs. 2.72 a factor

$$C_R = [1 + R(x, Q^2)]/[1 + \gamma^2] \tag{6.2}$$

appears in this formula since the parameterizations of unpolarized quark distributions q used in Eq. 6.1 were extracted from fits of F_2,

$$F_2(x, Q^2) = \sum_q x e_q^2 q(x, Q^2). \tag{6.3}$$

The structure function F_2 was derived from cross section measurements assuming non-zero values for the ratio R and the kinematic factor γ^2. Using Eq. 2.29, the parameterizations of the parton densities are related to the structure function F_1:

$$F_1(x, Q^2) = \frac{1 + \gamma^2}{1 + R(x, Q^2)} \frac{1}{2x} F_2(x, Q^2) = \frac{1 + \gamma^2}{1 + R(x, Q^2)} \frac{1}{2} \sum_q e_q^2 q(x, Q^2). \tag{6.4}$$

The measured Born asymmetries presented in Ch. 5 were determined in bins of x and integrated over z and Q^2. Then semi-inclusive asymmetry given in Eq. 6.1 can be determined

in bins of x and integrated over z and Q^2 in each bin:

$$A_1^h(x) = C_R(x,Q^2)\frac{\sum_q e_q^2 \int dQ^2 \Delta q(x,Q^2) \int dz \tilde{D}_q^h(Q^2,z)}{\sum_q e_q^2 \int dQ^2 q(x,Q^2) \int dz \tilde{D}_q^h(Q^2,z)}. \tag{6.5}$$

Due to the restricted acceptance of the HERMES spectrometer not all DIS events are detected. The fragmentation functions $\tilde{D}_q^h(Q^2,z)$ in Eq. 6.5 account for the limited acceptance of the spectrometer and the requirements on the hadron momenta for identification with the threshold Čerenkov/RICH (see Chap. 4.2.2). They therefore describe the conditional probability that a quark with momentum fraction x probed at a scale Q^2 will fragment into a hadron of type h within the angular acceptance and within the allowed momentum range.

The semi-inclusive asymmetry can be expressed in terms of quark polarizations $[\Delta q/q](x)$ and purities $P_q^h(x)$:

$$A_1^h(x) = C_R \sum_q \frac{e_q^2 \int dQ^2 q(x,Q^2) \int dz \tilde{D}_q^h(x,Q^2,z)}{\sum_q e_q^2 \int dQ^2 q(x,Q^2) \int dz \tilde{D}_q^h(x,Q^2,z)} \cdot \frac{\int dQ^2 \Delta q(x,Q^2)}{\int dQ^2 q(x,Q^2)} \equiv P_q^h(x) \cdot \frac{\Delta q}{q}(x). \tag{6.6}$$

The introduced purities $P_q^h(x)$ give the conditional probability that a hadron in the acceptance originates from an event where a quark of flavor q was struck. In terms of the unpolarized quark densities and the fragmentation functions they are given as

$$P_q^h(x) = \frac{e_q^2 \int dQ^2 q(x,Q^2) \int dz \tilde{D}_q^h(x,Q^2,z)}{\sum_q e_q^2 \int dQ^2 q(x,Q^2) \int dz \tilde{D}_q^h(x,Q^2,z)}. \tag{6.7}$$

The inclusive asymmetry can be included in this formalism by defining inclusive purities that describe the probability for inclusive scattering off a quark of flavor q:

$$P_q(x) = \frac{e_q^2 \int dQ^2 q(x,Q^2)}{\sum_q e_q^2 \int dQ^2 q(x,Q^2)}. \tag{6.8}$$

The polarized quark distributions are determined by combining the measured Born asymmetries in a system of equations of the form:

$$\overrightarrow{A}_1 = C_R P \overrightarrow{Q}, \tag{6.9}$$

where $\overrightarrow{A}_1$ is vector of measured Born asymmetries of all types and in all bins of x, P is the purity matrix. The vector $\overrightarrow{Q}$ contains the quark polarizations $[\Delta q/q](x)$. Eq. 6.9 is solved for the vector of quark polarizations by minimizing

$$\chi^2 = (\overrightarrow{A}_1 - C_R P \overrightarrow{Q})^T V_A^{-1} (\overrightarrow{A}_1 - C_R P \overrightarrow{Q}), \tag{6.10}$$

where V_A is the covariance matrix of the measured Born asymmetries that includes the corre-

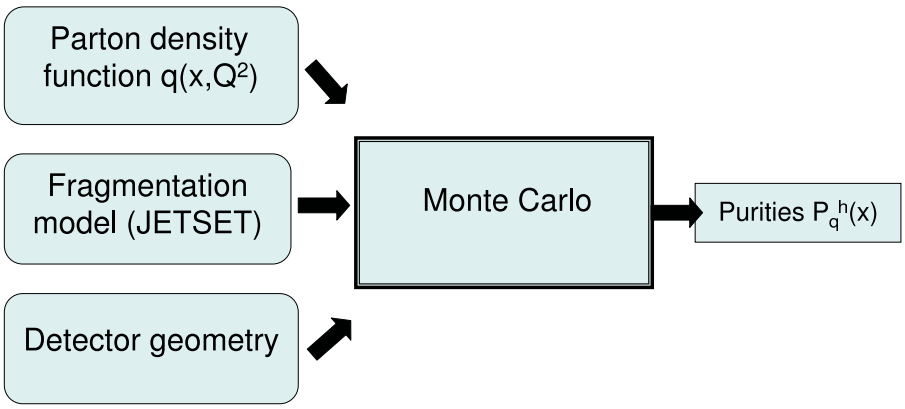

Figure 6.1: A schematic diagram of the generation of purities.

lations of the different types of asymmetries as well as the correlations among the x-bins.

The vector of asymmetries $\overrightarrow{A}_1$. The asymmetry vector combines the inclusive and the semi-inclusive asymmetries on the proton and the deuteron in all bins of x. In each bin, the general form of the vector is

$$\overrightarrow{A}_1(x_i) = \Big(A_{1p}, A_{1p}^{\pi^+}, A_{1p}^{\pi^-}, A_{1d}, A_{1d}^{\pi^+}, A_{1d}^{\pi^-}, A_{1d}^{K^+}, A_{1d}^{K^-}\Big)(x_i). \tag{6.11}$$

The final vector of measured Born asymmetries $\overrightarrow{A}_1$ combines the asymmetries measured in each x-bin consecutively,

$$\overrightarrow{A}_1 = \Big(\overrightarrow{A}_1(x_1), \overrightarrow{A}_1(x_2), ..., \overrightarrow{A}_1(x_n)\Big). \tag{6.12}$$

The asymmetry vector does not include the asymmetries $A_1^{h^\pm}$ of undifferentiated hadrons shown in Fig. 5.12. These asymmetries add little information to the χ^2-minimization, because they are highly correlated with the pion asymmetries and to a smaller extend with the kaon asymmetries.

The purity matrix P . The matrix P contains elements of purities on the proton and deuteron. In each x-bin, it can be separated in a proton and a deuteron sub-matrix. The deuteron sub-matrix is

$$P_d(x_i) = \begin{pmatrix} P_{ud} & P_{\bar{u}d} & P_{dd} & P_{\bar{d}d} & P_{sd} & P_{\bar{s}d} \\ P_{ud}^{\pi^+} & P_{\bar{u}d}^{\pi^+} & P_{dd}^{\pi^+} & P_{\bar{d}d}^{\pi^+} & P_{sd}^{\pi^+} & P_{\bar{s}d}^{\pi^+} \\ P_{ud}^{\pi^-} & P_{\bar{u}d}^{\pi^-} & P_{dd}^{\pi^-} & P_{\bar{d}d}^{\pi^-} & P_{sd}^{\pi^-} & P_{\bar{s}d}^{\pi^-} \\ P_{ud}^{K^+} & P_{\bar{u}d}^{K^+} & P_{dd}^{K^+} & P_{\bar{d}d}^{K^+} & P_{sd}^{K^+} & P_{\bar{s}d}^{K^+} \\ P_{ud}^{K^-} & P_{\bar{u}d}^{K^-} & P_{dd}^{K^-} & P_{\bar{d}d}^{K^-} & P_{sd}^{K^-} & P_{\bar{s}d}^{K^-} \end{pmatrix}(x_i). \tag{6.13}$$

The proton sub-matrix is given by an analogous expression containing only inclusive and pions

values, because the RICH detector was only available for the deuteron target. The total purity matrix is the block-diagonal matrix of these proton and deuteron purity matrices.

The vector of quark polarizations $\overrightarrow{Q}$. The vector $\overrightarrow{Q}(x_i)$ contains the polarizations of the six quark flavors,

$$\overrightarrow{Q}(x_i) = \Big(\frac{\Delta u}{u}(x_i), \frac{\Delta \bar{u}}{\bar{u}}(x_i), \frac{\Delta d}{d}(x_i), \frac{\Delta \bar{d}}{\bar{d}}(x_i), \frac{\Delta s}{s}(x_i), \frac{\Delta \bar{s}}{\bar{s}}(x_i)\Big), \tag{6.14}$$

where as before the total vector $\overrightarrow{Q}$ contains consecutively the values for each x-bin. The vector given here makes no additional symmetry assumption on the quark polarizations.

6.2 Extraction of the Purities

The purities depend on unpolarized physics quantities and on the acceptance function of the detector. This section details the process of the generation of purities, as depicted schematically in Fig. 6.1.

In a first step, DIS events are generated on the parton level with the PYTHIA MC simulation [66], [67]. In this analysis the CTEQ6 parameterization of unpolarized PDFs was used as input for the event generation. This particular parameterization was chosen because of its low initial evolution scale of $Q_0^2 = 0.5\ GeV^2$.

Next, the hadronization of the generated partons is simulated in the JETSET Monte Carlo package [68] which is based on the LUND string model. This model contains several parameters, which have been tuned in a specific procedure for an optimum description of the hadron multiplicity spectra measured at HERMES [69].

In order to model the acceptance of the HERMES detector, the Monte Carlo package HMC has been used. The geometrical acceptance of the spectrometer was modeled with the same cuts on the scattering angle as in the analysis of the data. The *box acceptance* model was augmented by a look-up table, which parameterizes the bending of the charged particles tracks in the field of the spectrometer magnet, depending on the position and momentum of the track. This look-up table was calculated once from tracking many particle trajectories with different starting positions and angles. In this simulation, a measurement of the field of the spectrometer magnet on a fine grid in three dimensions is employed [54].

For a proton and a deuteron target, purities were generated from 10M DIS event samples on each target. Due to the high statistic of the generated samples, the statistical uncertainty on the purity can be neglected when compared to the data.

The results for the one-dimensional x-dependent purities for the proton (black circles) and deuteron (red triangles) for two Q^2 ranges are given in Fig. 6.2. The full points represent the purities for $Q^2 > 1\ GeV^2$, the open points show the purities for low Q^2. For strange quarks (last two columns), the values of purities are increased by a factor of 4.

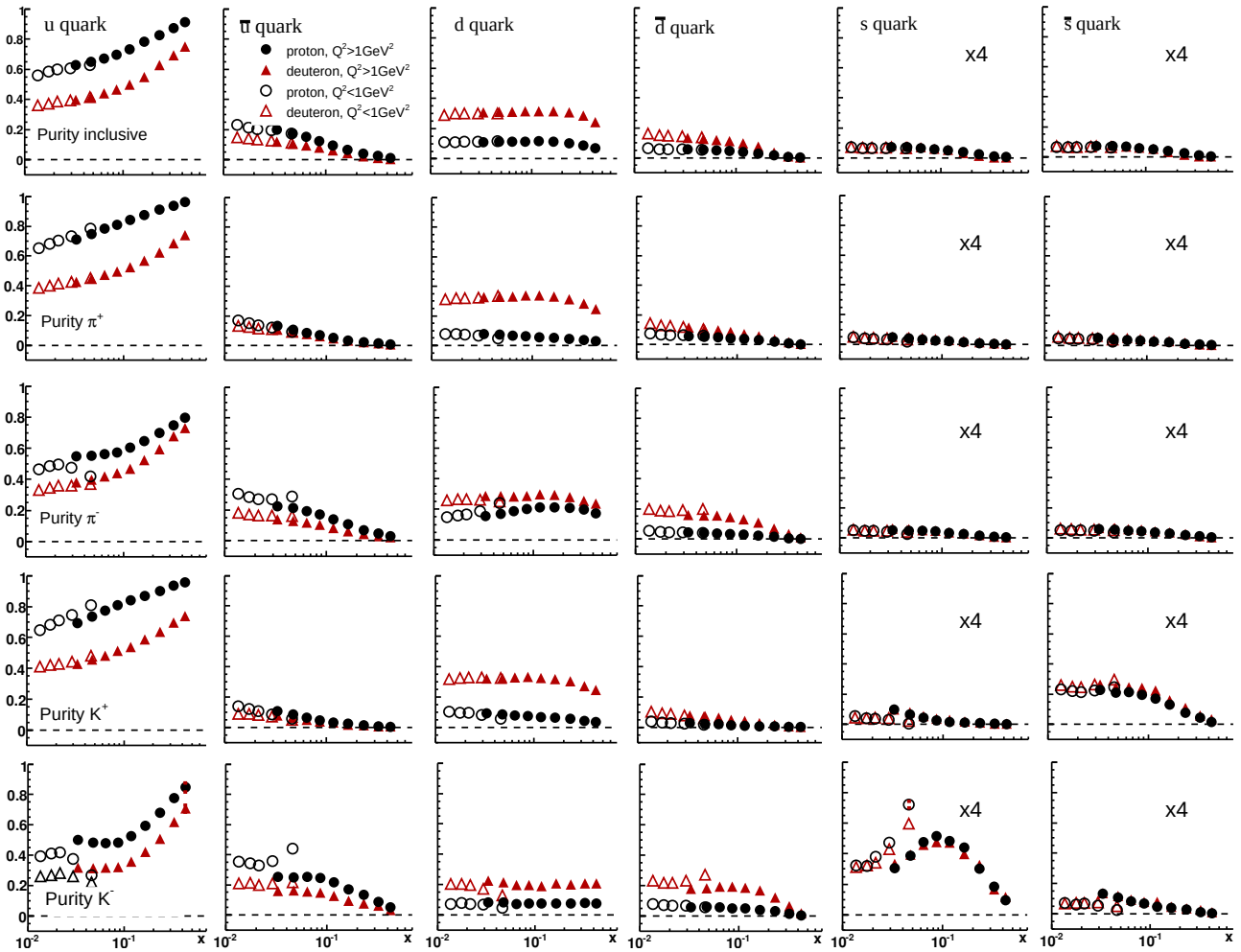

Figure 6.2: Purities in x-bins for the proton target (solid black circles) and deuteron target (solid red triangles) for each quark and asymmetry type for $Q^2 > 1\ GeV^2$. The tuned LUND fragmentation model and the CTEQ6L parameterization of the unpolarized quark distributions have been used in the MC for the generation of the extracted events. Each column corresponds to scattering off a certain quark flavor. Note: for strange quarks (last two columns) the values of purities are increased by a factor of 4. In addition, open symbols show the purities for the range $Q^2 < 1\ GeV^2$.

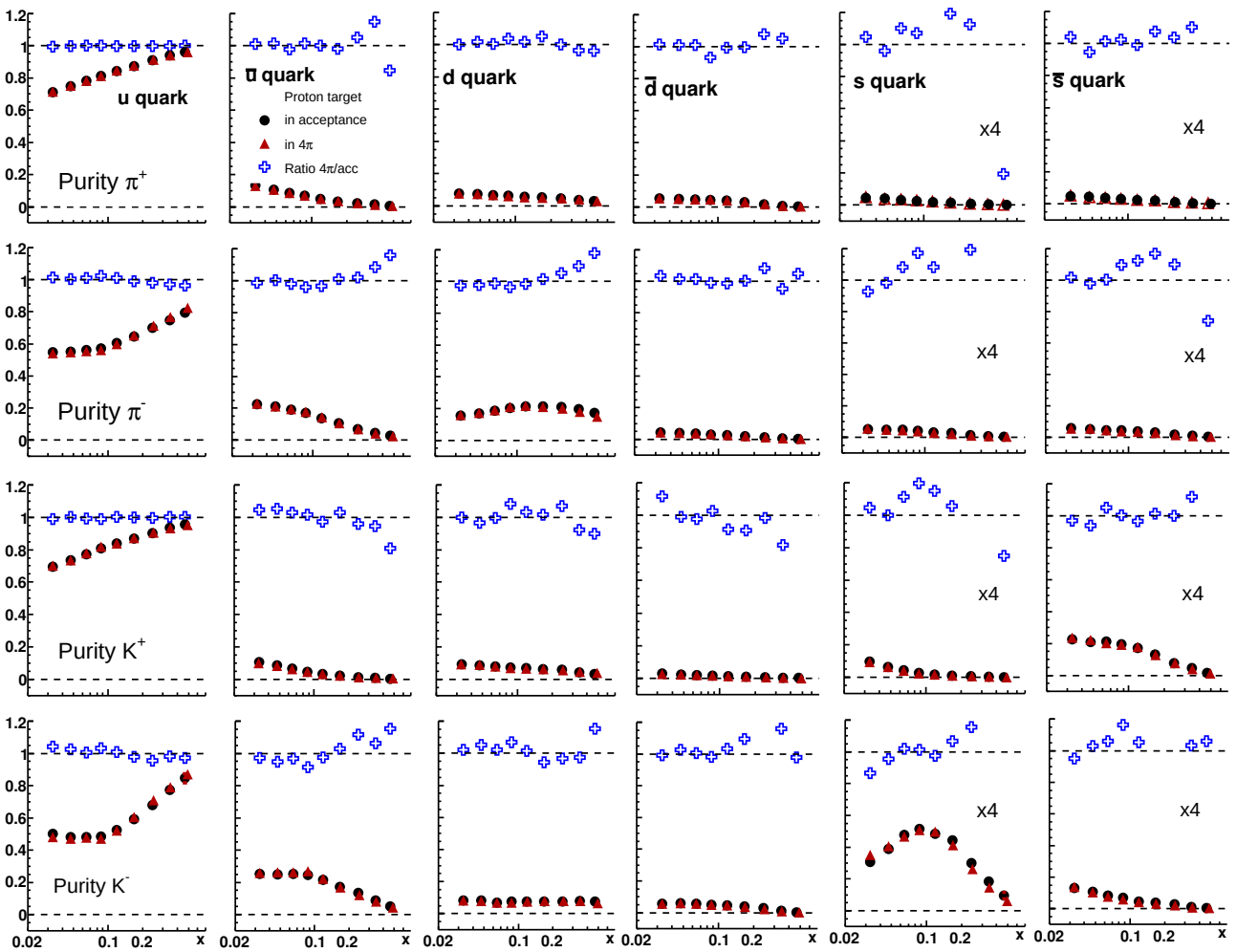

Figure 6.3: Comparison of pion and kaon purities evaluated in the HERMES acceptance (black circles) and in 4π (red triangles) for a proton target. The blue open crosses show the ratio of two purity sets. Note: for strange quarks (last two columns) the values of purities are increased by a factor of 4.

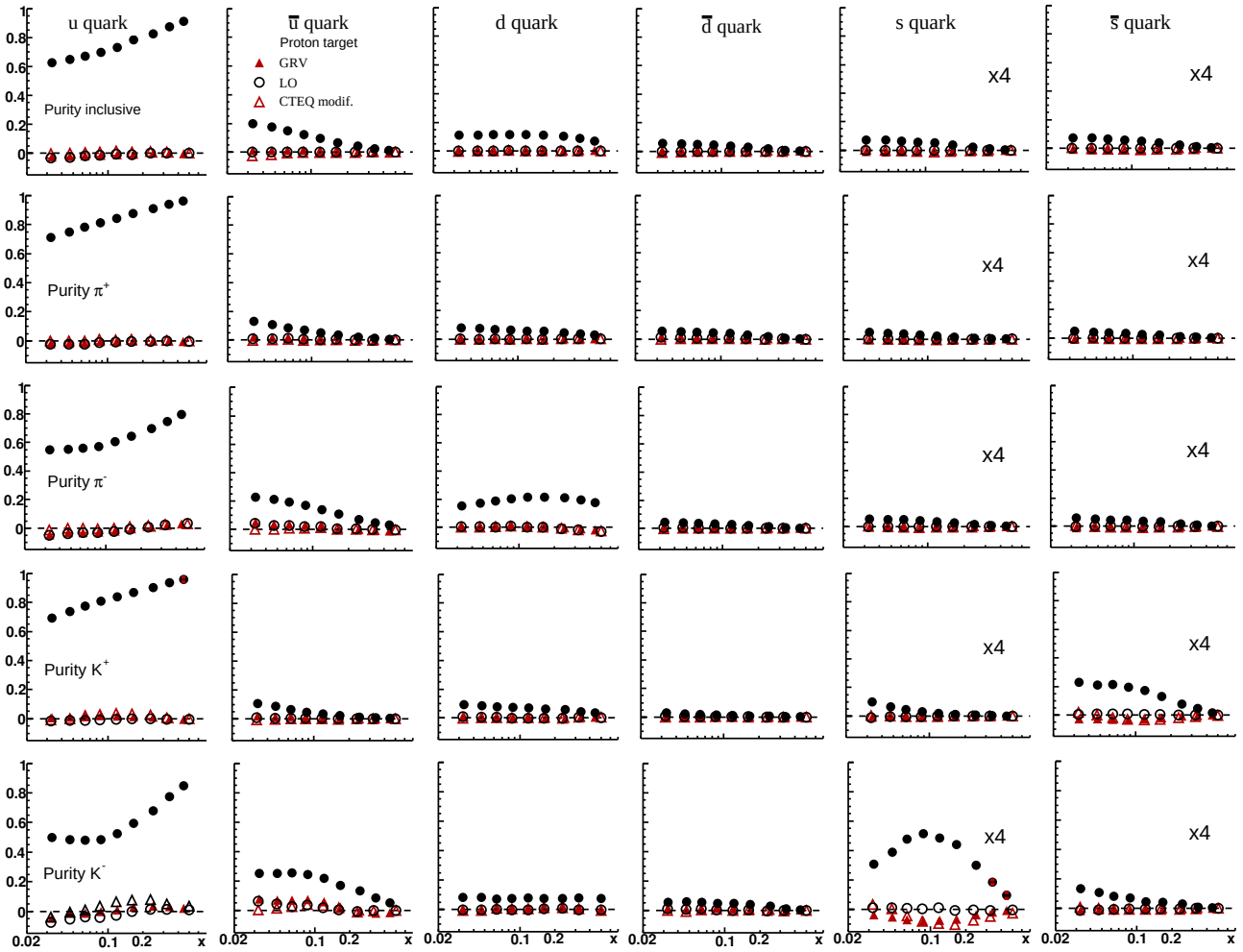

Figure 6.4: The differences between the purity for the proton target calculated using the standard HERMES MC and three purity sets : "LO" (black open circles), "GRV" (red triangles) and "CTEQ modif" (red open triangles). The details are described in the text. For comparison of the differences and the mean values of the purity, black full points represent the purity itself.

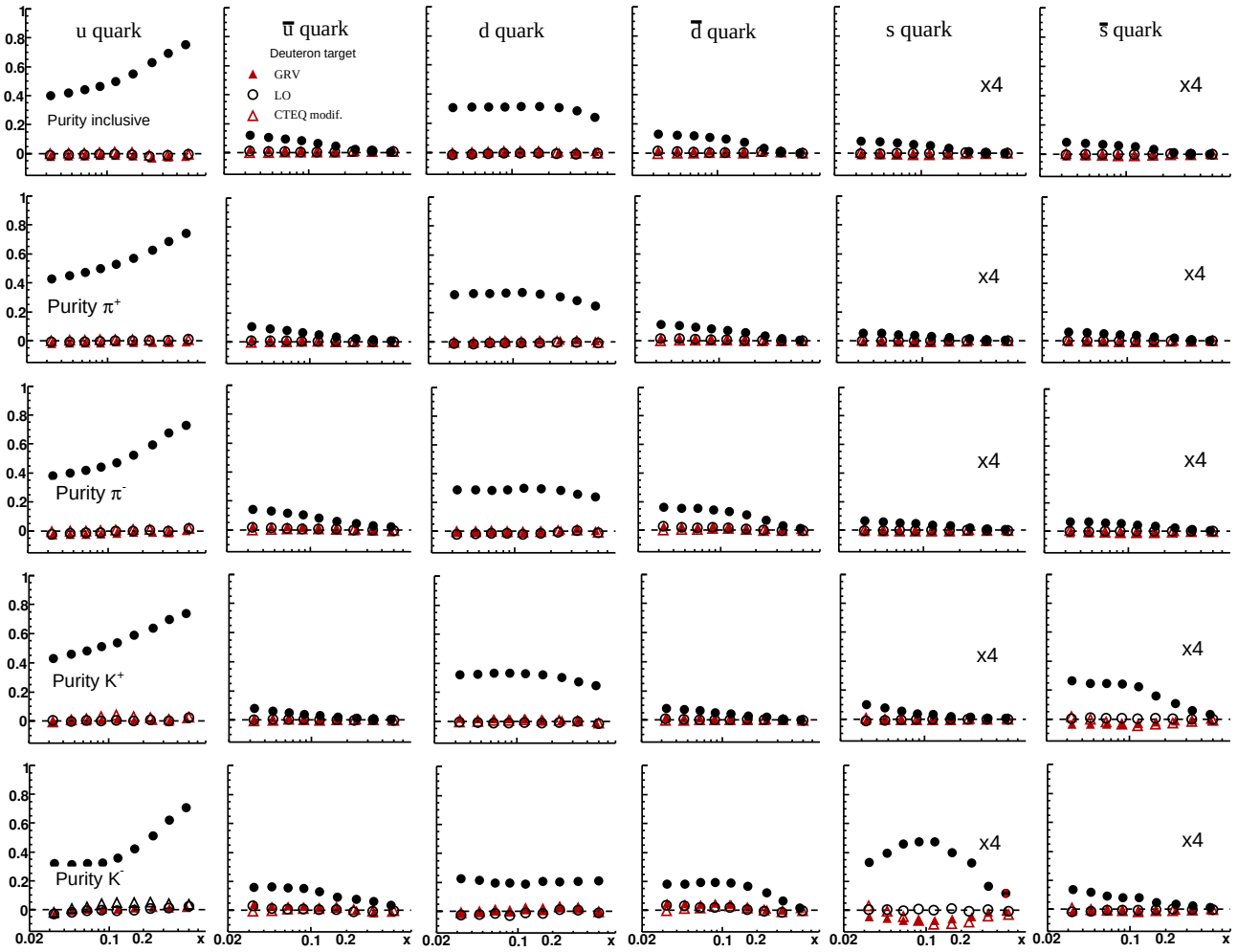

Figure 6.5: Same as for Fig. 6.4 on the deuteron target

6.3 Systematic studies on the purity uncertainties.

One of the main reasons to start this analysis was to make a reliable estimate of the systematic uncertainty due to the purity uncertainties. In the first HERMES publication [13], the uncertainty on the purities due to the JETSET tune uncertainty was estimated by making an essentially-random selection of two MC tunes (old HERMES tune and default tune) and comparing the resulting $\Delta q/q$ values. This tactic completely fails to address the possibility that the multiplicities to which the MC is tuned, may be insensitive to certain correlated combinations of JETSET parameters. In detail these studies are presented in [70].

The *unpolarized PDFs* are also an important part of the purities, and modern sets such as CTEQ6 are accompanied by errors on their fits. These errors should be reflected in the purity uncertainties. This issue and other possible sources of systematic uncertainties are addressed below.

6.3.1 The influence of the spectrometer acceptance on the purities

As described earlier, the influence of the spectrometer acceptance on the Born-level asymmetries A_1 was studied and found to be negligible (see Ch. 5.2.2). The influence of the acceptance on the purities was also investigated. Fig. 6.3 shows the purities evaluated with the 2004c tune in 4π and in the box acceptance to which the asymmetries are unfolded. As has been observed in previous studies, the effect of the acceptance on the purities is found to be negligible. The ratios of the two purity sets which were plotted in addition, show that for u-quarks the effect of acceptance is small and there are only small differences for sea quarks for high x, where the values of purity for sea quarks are small and u-quarks dominate. Then the fragmentation function $\tilde{D}_q^h(Q^2, z)$ in Eq. 6.5 can be replaced with $D_q^h(Q^2, z)$ from Eq. 6.1.

6.3.2 NLO effects

As was mentioned before, the purity method for measuring of quark helicity distributions is a leading-order procedure. A systematic study was performed to estimate the size of NLO effects. The disNG Monte Carlo was run to simulate the leading-order cross section ("LO") with:

- NLO processes turned off;
- $R = \sigma_L/\sigma_T$ set to zero ;
- F_2 computed at LO from the CTEQ6L PDFs.

Alternatively, the LO GRV unpolarized PDFs ("GRV") were used to estimate the systematic uncertainty arising from the choice of unpolarized PDFs. In addition, purities with the CTEQ6LO PFDs were computed using the *modified strange quark densities* ("CTEQ modif"), which were extracted from the HERMES measurement of charged kaon multiplicities in semi-inclusive scattering off a deuteron target [65]. The differences between the standard purities from HERMES MC (black points in Fig. 6.4) and the purities from these simulations ("LO"(open black circles), "GRV"(red full triangles), "CTEQ modif"(red open triangles)) are shown in Fig. 6.4.

The standard purities used in the Δq extraction are seen to be nearly identical, with the only visible variations for the strange quarks in the K^+ and K^- panels. The Fig. 6.5 shows the same effect for the deuteron target.

6.3.3 Dependence of purities on fragmentation functions

The systematic studies, which were described before, are based on MC data, where some parameters were tuned. There is an other method to estimate the systematic uncertainties of the purities. The purities can be calculated analytically, using the parameterizations for parton distributions and fragmentation functions.

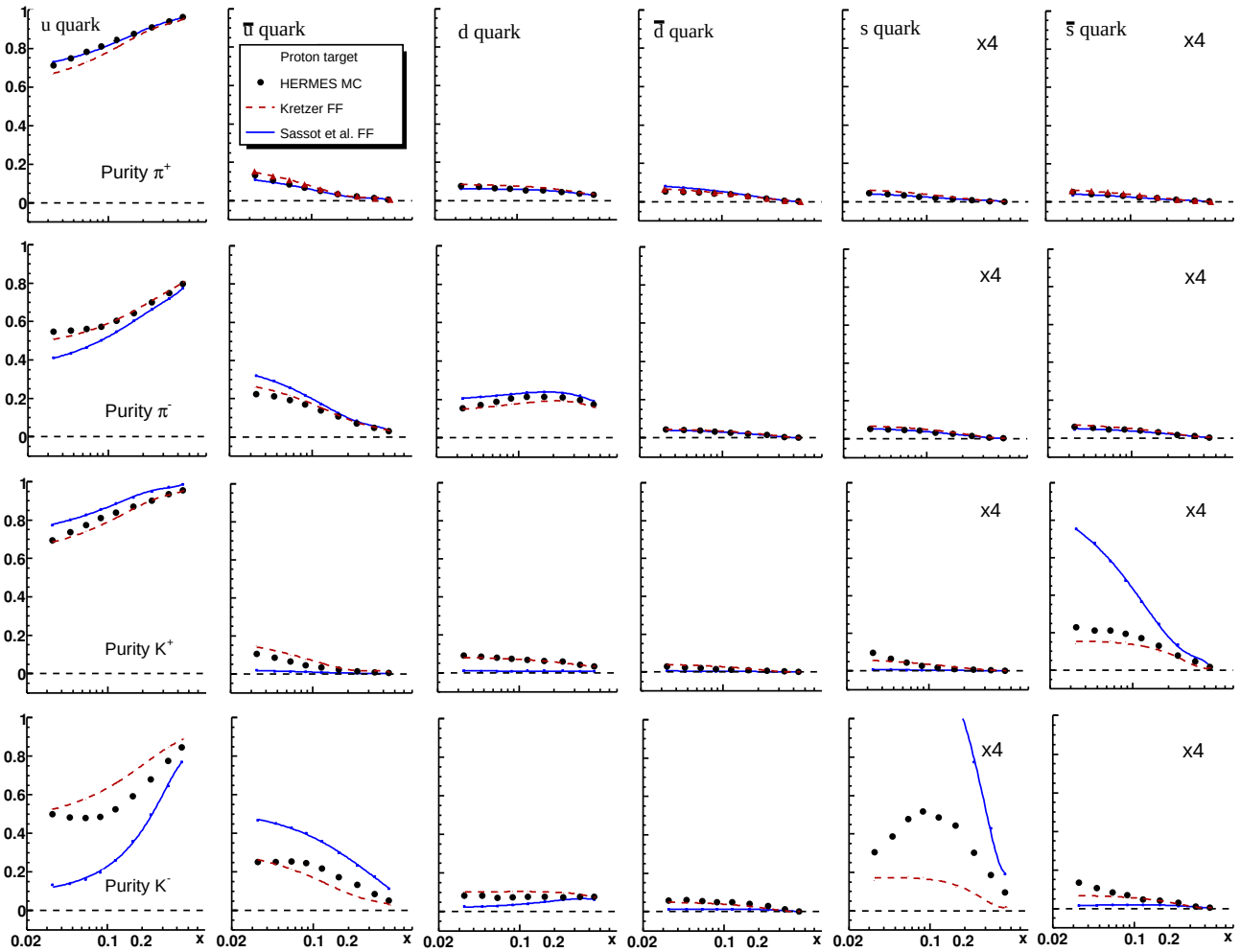

Figure 6.6: Purities for the proton target computed analytically using CTEQ6LO and two fragmentation function parameterizations (Kretzer [74](red dashed line) and Sassot [75](blue solid line)) compared with the HERMES MC-based purities(black points) used in this analysis.

The fragmentation functions (FFs) are an important ingredient in the MC calculation of the purities. In addition, one should consider FFs as another source which contribute to the systematic uncertainty of the purities.

The uncertainties on the purities due to the fragmentation function used in the Monte Carlo simulation were estimated by comparing the MC-based purities used in this analysis and the purities, which have been constructed analytically from the CTEQ PDFs and two different sets of fragmentation functions. Those are the Kretzer FF [74] and the set of FFs from Sassot et al. [75] which was obtained by a fit to the HERMES multiplicities. These analytically-calculated purities are shown on Figs. 6.6 (proton target) and 6.7 (deuteron target). The purities based on the Kretzer FFs are in good agreement with the MC-based purities used in this analysis. The purities based on the Sassot FFs show significant deviation from the MC, particularly for the kaon purities. The influence of the choice of FFs on the polarized distribution functions is

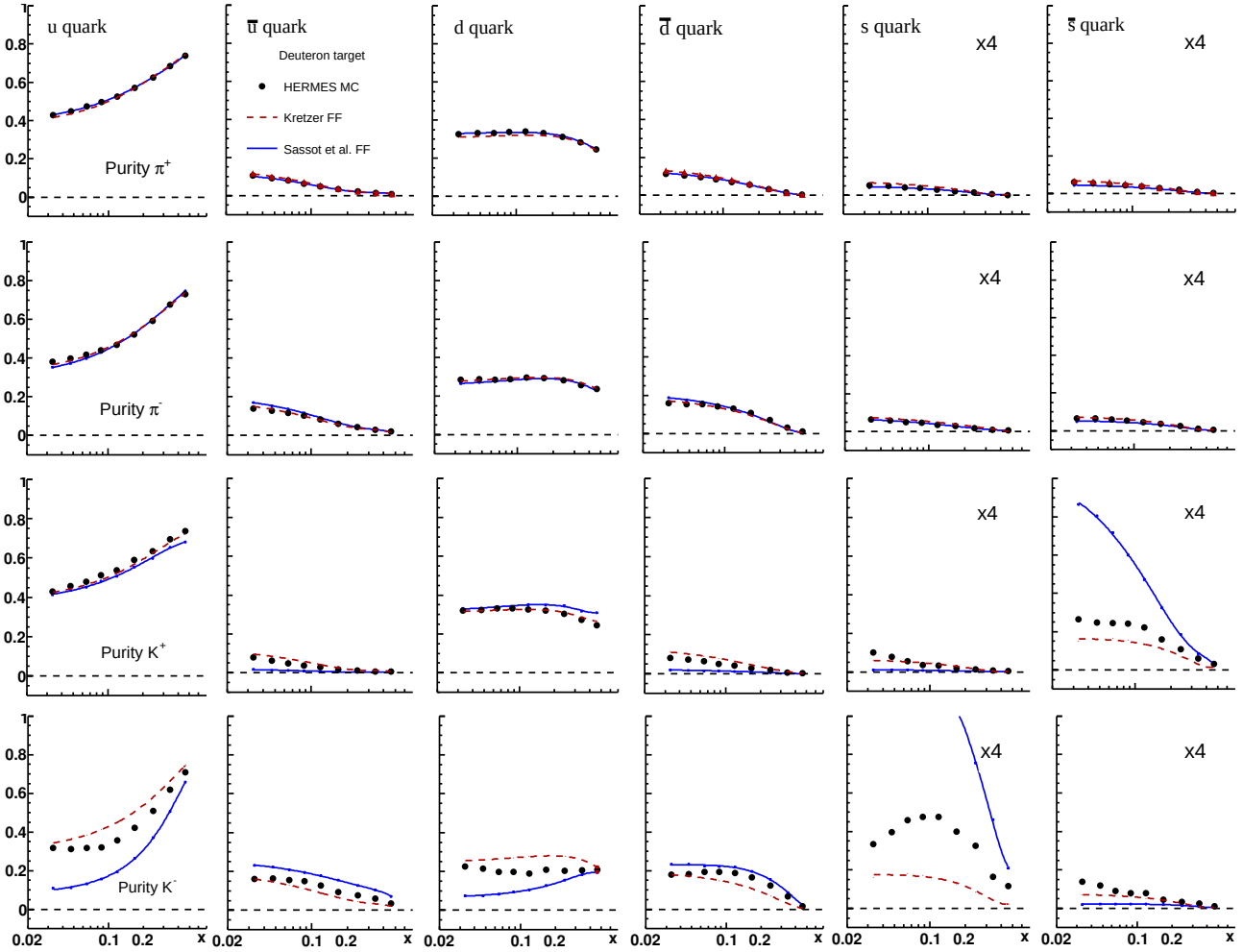

Figure 6.7: Same as for Fig. 6.6 for the deuteron target

discussed in the next chapter.

6.4 Systematic studies on the quark polarizations

Systematic studies of the influence of the unpolarized PDFs on the quark polarization. The aim of these studies was to estimate the effect of the unpolarized PDF errors on the purities. Accordingly, "high" and "low" analytic purities were calculated by varying the CTEQ PDFs to the upper and lower edges of their error bands. The quark polarizations were then extracted using these "high" (red triangles) and "low" (blue squares) purities, as shown in Fig. 6.8. Two different sets of fragmentation functions (left panel : Kretzer FFs; right panel Sassot FFs) have been used. The maximum difference in the extracted mean values for $\Delta q/q$, based on Sassot FFs, at each point in x has been added to the systematic uncertainty on $\Delta q/q$. We are aware that the flavor-correlated variation of the CTEQ PDFs is an arbitrary choice. Ideally, one would use the CTEQ Hessian vectors, and recalculate the PDFs using the fit parameters at each "end" of these 18 Hessians. However the exercise succeeds in obtaining a general impression of the unpolarized PDF uncertainty.

Fig. 6.9 shows the $\Delta q/q$ values obtained from the data using MC purities (black points) in comparison with the results based on analytically calculated purities using parameterizations for fragmentation functions from Kretzer (red triangles) and Sassot (blue squares). For u and d-quarks the mean values for $\Delta q/q$ extracted from different methods are similar. In high x region the results for s-quarks and for $\bar{u}$- and $\bar{d}$-quarks differ due to the significant deviation of the purities which were calculated analytically, particularly for the kaons. The uncertainties changed significantly also. The ratio between the errors of the quark polarizations from the results based on the analytical parameterizations and based on the HERMES MC simulation is shown in Fig. 6.10. This plot shows that the uncertainties on the quark polarizations are very sensitive to the choice of fragmentation functions. Use of the Kretzer fragmentation functions (red stars) increases the uncertainties of the quark polarizations. For the region $x < 0.2$ the uncertainties of the quark polarizations based on the Sassot FFs (blue crosses) become less more than twice.

The constraints on the sea quarks. The system of equations given in Eq. 6.9 is slightly over-constrained, as eight asymmetries are available to determine the polarizations of six quark flavors. Additional assumptions are imposed on the quark flavors in order to improve the precision of the result on the quark polarizations.

The anti-strange polarization was fixed at zero,

$$\Delta\bar{s}(x) = 0, \tag{6.15}$$

because the asymmetries do not provide sufficient constraint on the polarizations of the anti-strange flavor. A comparison of the quark polarizations computed assuming zero anti-strange polarization and without is shown in Fig. 6.11. The results are in a good agreement. But, the uncertainties of computed quark polarizations are substantially larger in a case of the

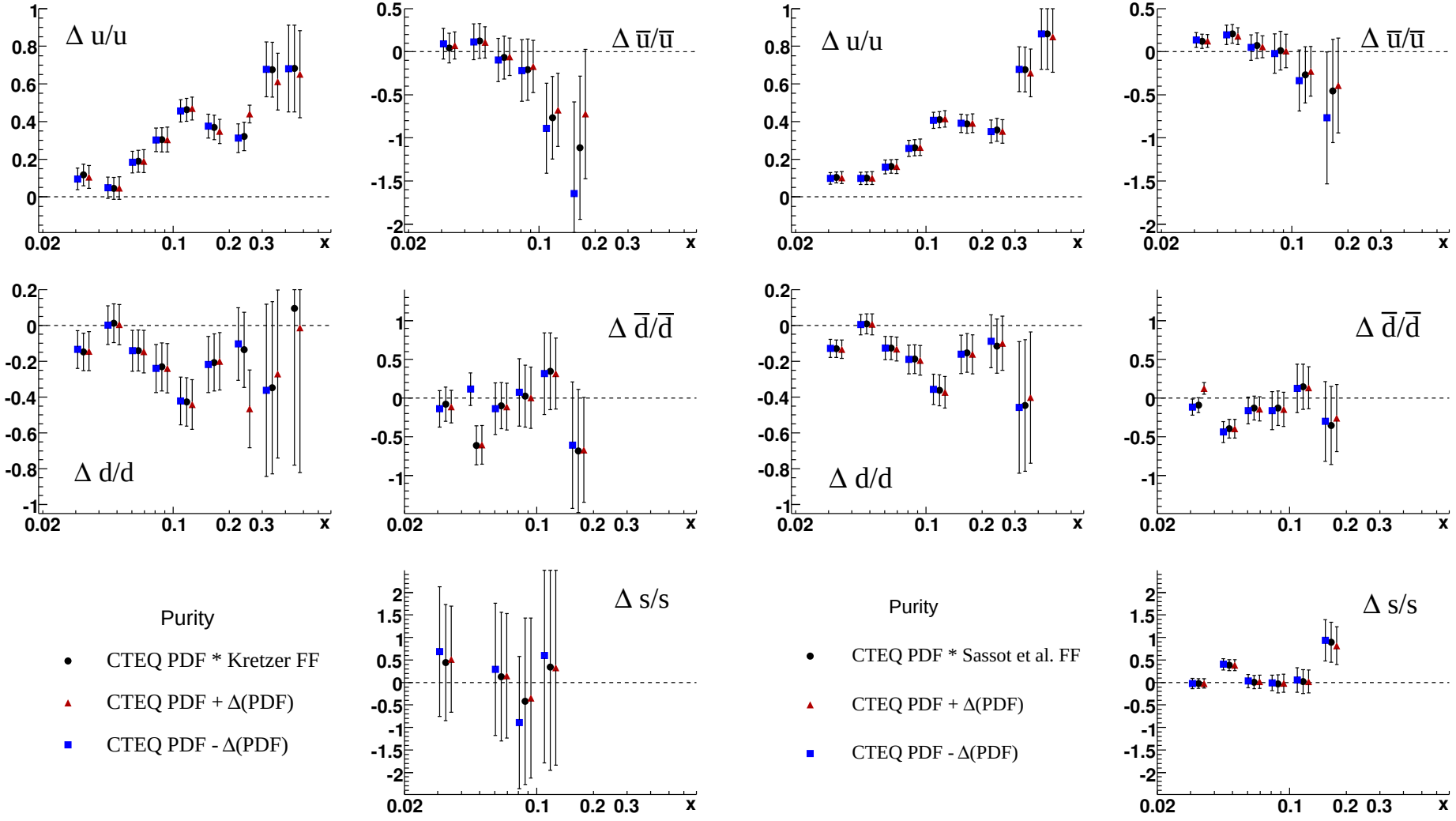

Figure 6.8: The quark polarizations extracted using the analytic purities based on the Kretzer FFs (left) and the Sassot FFs (right) times the CTEQ6LO PDFs varied to the upper and lower edges of their error bars. The red triangles and blue squares were offset in x for presentation. Note: for sea quarks the last three x points are not shown, due to the huge error bars.

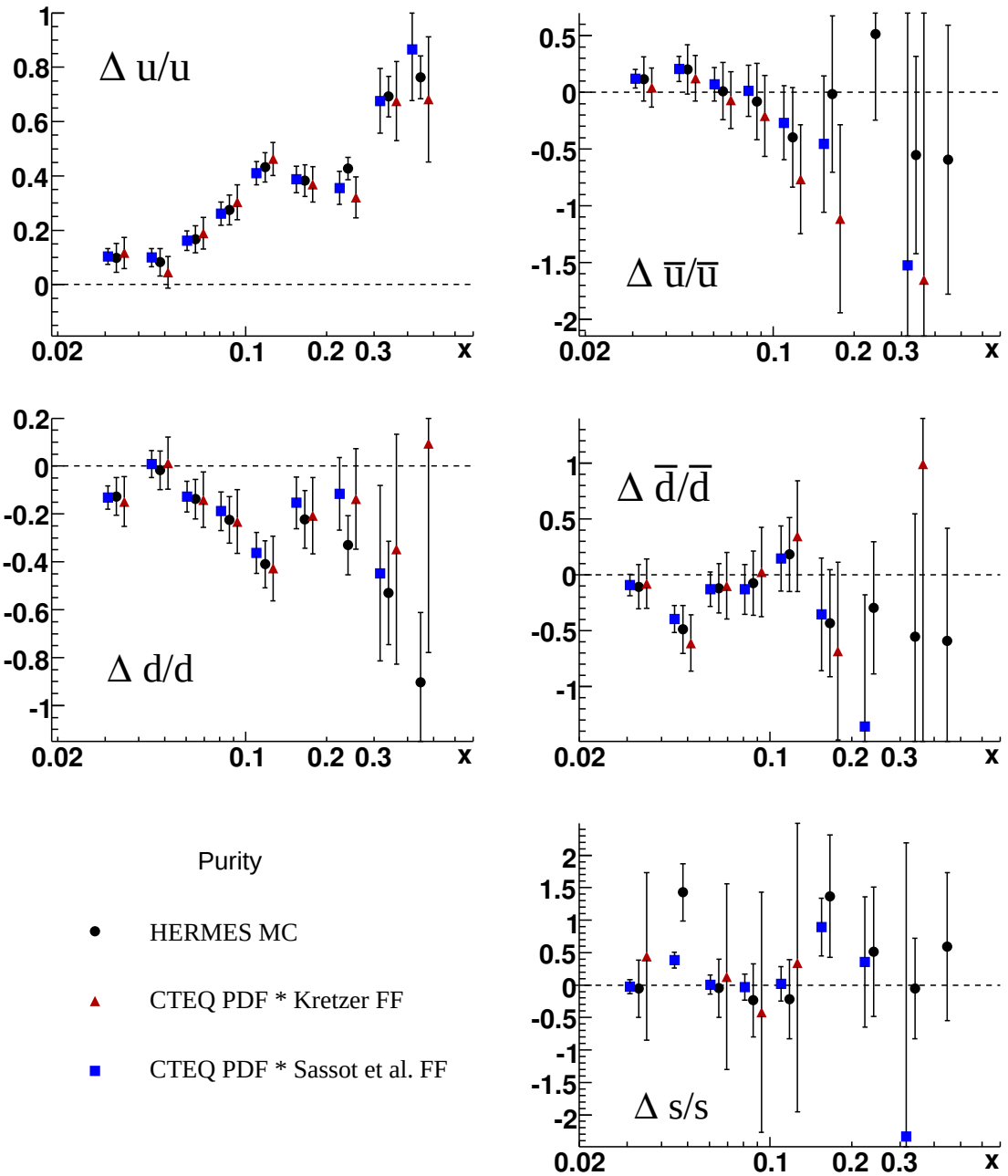

Figure 6.9: Quark polarizations computed from HERMES MC purities (black circles) and from analytically extracted purities with Kretzer FF (red triangles) and Sassot FF (blue squares). The red and blue points were offset in x for presentation.

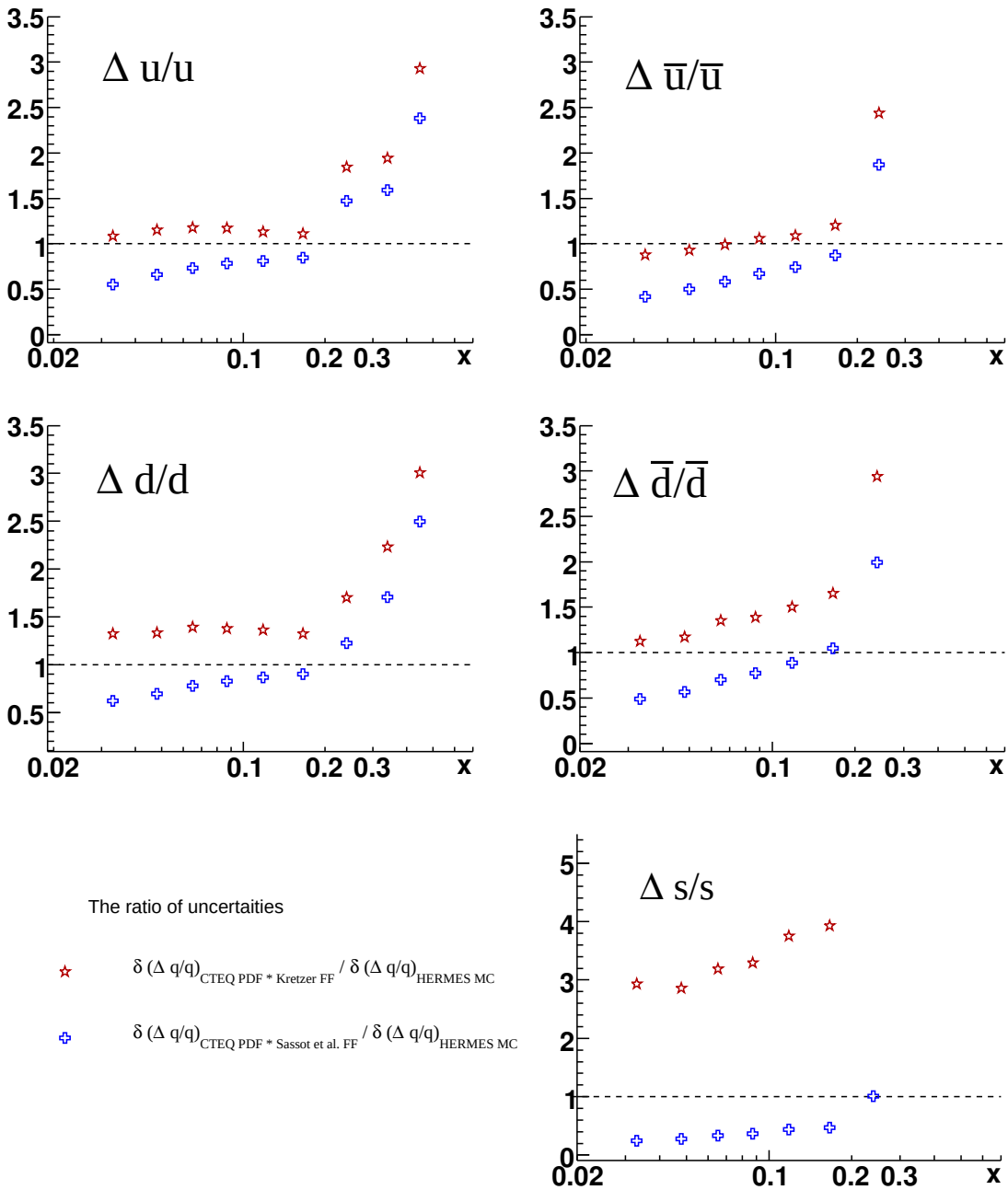

Figure 6.10: The ratio of the uncertainties of the quark polarizations computed from analytically extracted purities with Kretzer FFs (red stars), with Sassot FFs (blue crosses) and from HERMES MC purities.

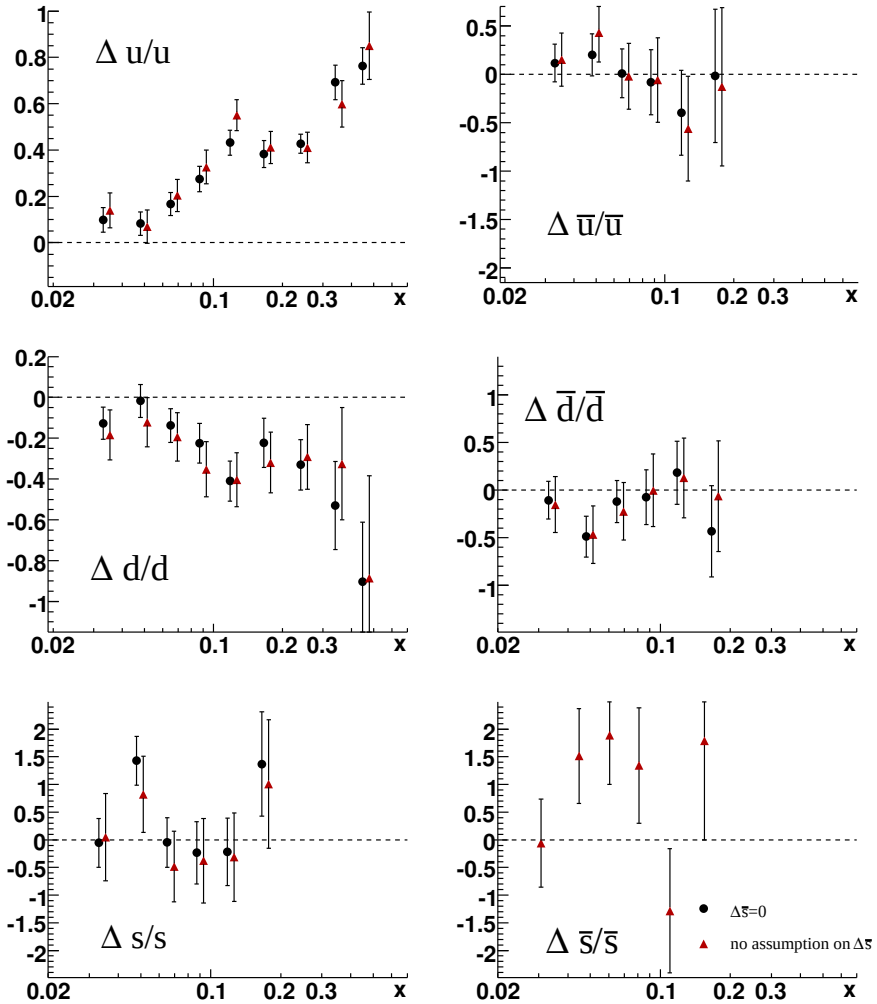

Figure 6.11: Quark polarizations computed assuming zero anti-strange polarization $\Delta\bar{s}(x) = 0$ (black circles) and computed with no assumption on the strange sea (red triangles). The error bars show the statistical uncertainties. The red points were offset in x for presentation. Note: last three x points for sea quarks are not shown, because their uncertainties are large.

assumption of non-zero anti-strange quark polarization.

In a previous analysis [13] in addition the polarizations of the sea flavors were assumed to be zero for $x > 0.3$,

$$\Delta\bar{u}(x) = \Delta\bar{d}(x) = \Delta s(x) = \Delta\bar{s}(x) = 0. \tag{6.16}$$

Uncertainties due to the constraints given in Eq. 6.15 and Eq. 6.16 can be checked by assuming a uniform distribution of the constrained polarization within the limits defined by the unpolarized parton distributions,

$$|\Delta q(x, Q^2)| \leq \frac{1+\gamma^2}{1+R(x, Q^2)} |q(x, Q^2)|, \tag{6.17}$$

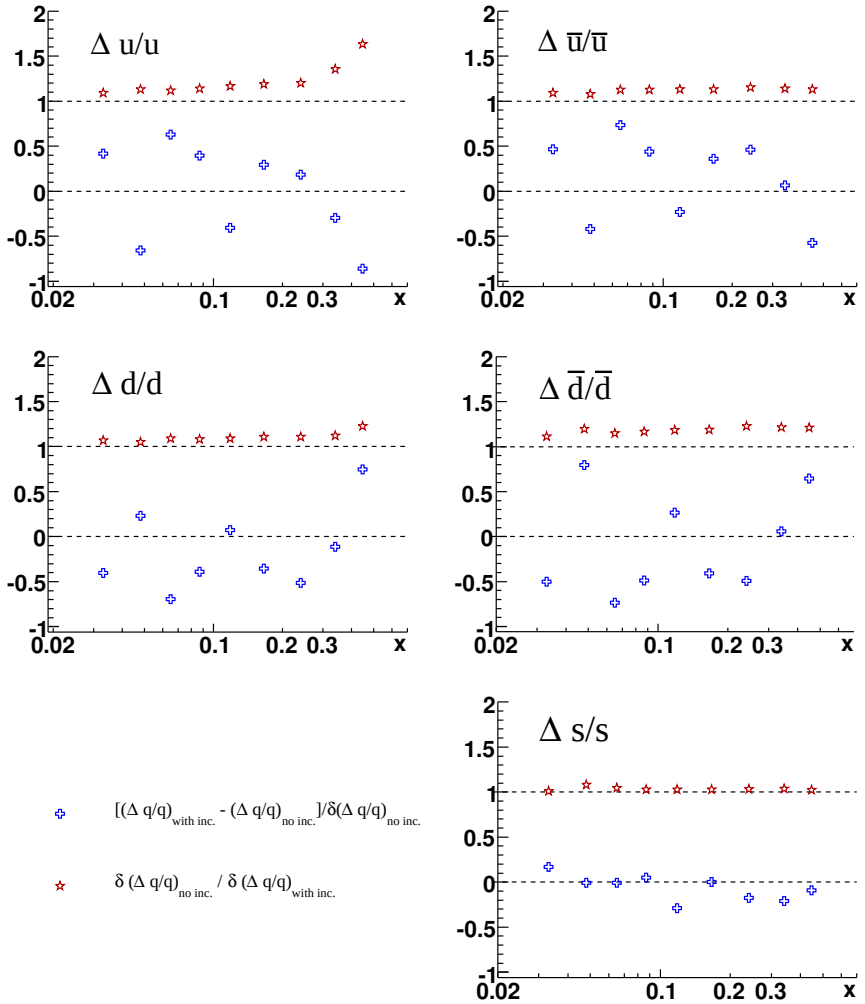

Figure 6.12: The difference (blue crosses) and the ratio (red stars) of quark polarizations computed with and without the inclusive asymmetries.

known as *the positivity limit*. The factor $(1+\gamma^2)/(1+R)$ arises from the definition of the CTEQ6 parameterization. Given these limits, the quark polarizations were evaluated with the positive limits of the positivity constraint and in another fit with the negative limits for $x > 0.3$ given by

$$\frac{\Delta\bar{u}}{\bar{u}}(x_i) = \frac{\Delta\bar{d}}{\bar{d}}(x_i) = \frac{\Delta s}{s}(x_i) = \frac{\Delta\bar{s}}{\bar{s}}(x_i) = \pm\frac{1+\gamma^2}{\sqrt{3}(1+R(x_i))}, \tag{6.18}$$

where the factor of $1/\sqrt{3}$ is the standard deviation of a uniform distribution in the range $[-1,+1]$. The maximum deviation of the resulting quark polarizations and the effect of fixing the $\bar{s}$ polarization at zero were assigned as the systematic uncertainty.

Influence of the inclusive asymmetry The quark polarizations were computed without the inclusive asymmetries in order to detect flaws in the applied models of the asymmetries or in the formalism in general. Both results of the quark polarizations computed with and

without the inclusive asymmetries were compared. The difference in the quark polarizations $(\Delta q/q)_{no\ inc.} - (\Delta q/q)_{with\ inc.}$ divided by the statistical uncertainty $\delta(\Delta q/q)_{no\ inc.}$ is shown in Fig. 6.12 (blue crosses). The two sets of data agree within the statistical uncertainties.

The ratio of the uncertainties of both results of quark polarizations (red stars) is bigger than unity and illustrates that the inclusive asymmetries improve the extracted values. The inclusive polarized DIS is sensitive only to the sum of the quark and anti-quark distributions because the scattering cross section depends on the squared charge of the quarks. The inclusion of inclusive asymmetries in a fit gives the effect especially for the u-quark, which dominates due to the fact that $e_u^2 = 4e_d^2 = 4e_s^2$ and mostly at large values of x, where there is little phase space for the generation of hadrons.

6.5 Results

6.5.1 The quark polarizations $\Delta q/q$: 3D extraction

The primary motivation for the attempt to extract the quark polarizations using the 3D-technique - dividing the semi-inclusive asymmetries and purities into x, z and $p_{\perp h}$ bins - was to better isolate different regions of fragmentation and get more benefit out of the statistics available. Traditionally, one distinguishes two regions for hadron production: the current fragmentation region and the target fragmentation region. Conceptually, one can easily imagine that a high-z, low-$p_{\perp h}$ hadron is more likely related to the current fragmentation. From the other side, the number of hadrons produced from the target remnant increases in the low-z, high-$p_{\perp h}$ region. To make this idea more concrete, the three-dimensional purities are presented using two ways. Fig. 6.13 presents the nine-$z-p_{\perp h}$ bins with the high-z, low-$p_{\perp h}$ or *leading* bins (red circles) and the low-z, high-$p_{\perp h}$ or *remnant* bins (blue triangles) in color. The significant difference in purities between these two bins supports this picture. Fig. 6.14 presents only five of the nine-x bins in order to make space to plot all nine of the $z - p_{\perp h}$ bins in each x position. Three z bins are shown in different colors and symbols: $0.1 < z < 0.35$ (blue triangles), $0.35 < z < 0.5$ (black squares) and $0.5 < z < 0.8$ (red circles). The increasing of the size of the each type of symbols demonstrates $p_{\perp h}$ dependence of purities. The first $p_{\perp h}$-bin ($0.0\ GeV < p_{\perp h} < 0.3\ GeV$) is shown using small symbols, the second bin ($0.3\ GeV < p_{\perp h} < 0.5\ GeV$) is shown with the middle symbols. The large symbols represent the third ($0.5\ GeV < p_{\perp h} < 2.0\ GeV$) bin. One can see that the purities depend on each of these semi-inclusive variables individually.

The comparison between the 1D and 3D extractions, Fig. 6.15, shows that the differences between the methods are small compared with the statistical uncertainties. It was hoped that use of the 3D extraction will improve the statistical errors, as more information is used to constrain the $\Delta q/q$ fit. It was found however, that the improvement of errors is rather small: the reduction is at most 10% of the error, in the lowest x bins.

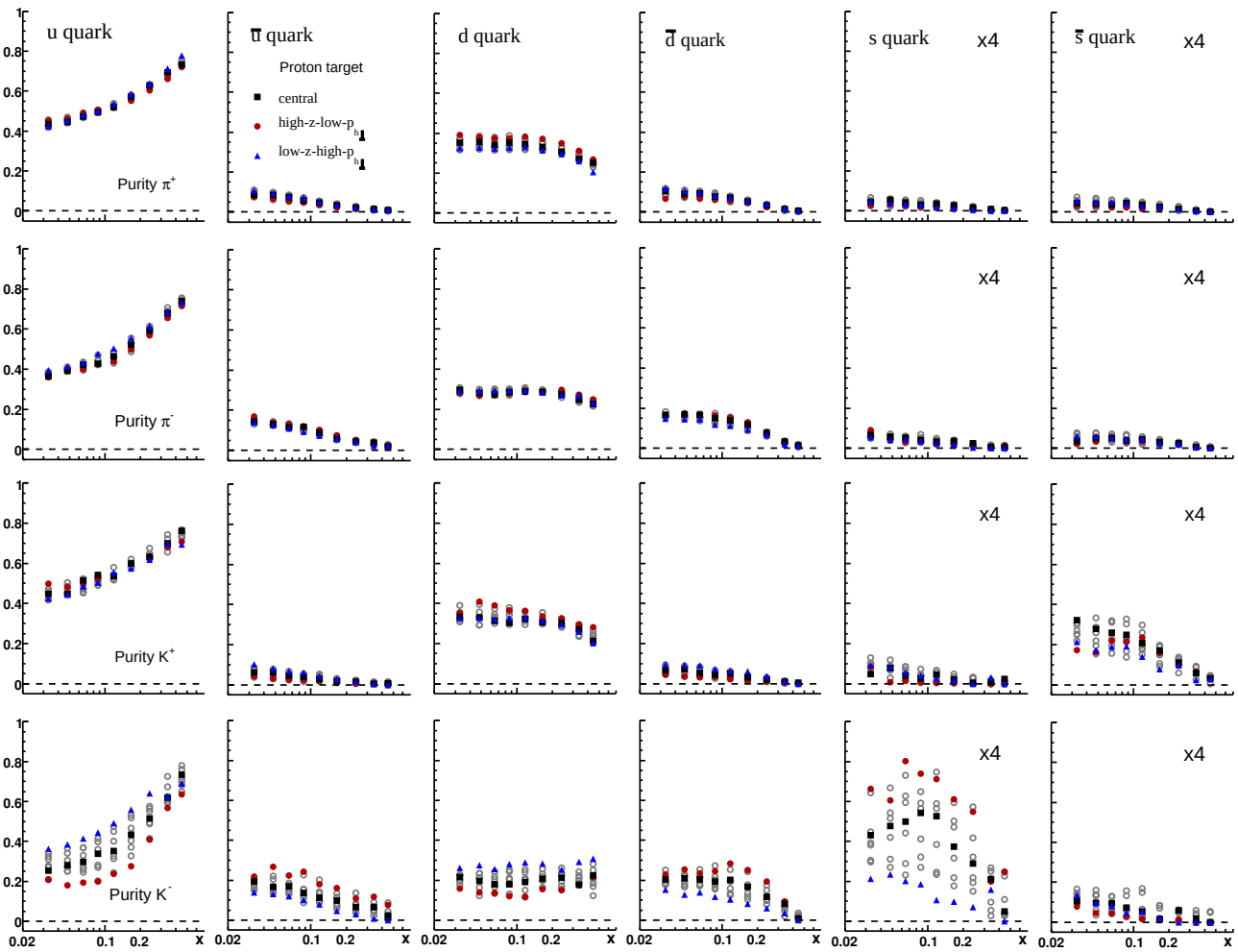

Figure 6.13: Purity in x-bins for the deuteron target. At each x position there are nine points, representing each of the nine $z - p_{\perp h}$ bin combinations. The "leading", high-z-low-$p_{\perp h}$ is plotted in red circles, the "remnant", low-z-high-$p_{\perp h}$, is plotted in blue triangles, and the "central", middle bin of each semi-inclusive variable, is plotted in black squares. All other combinations are shown in gray open circles.

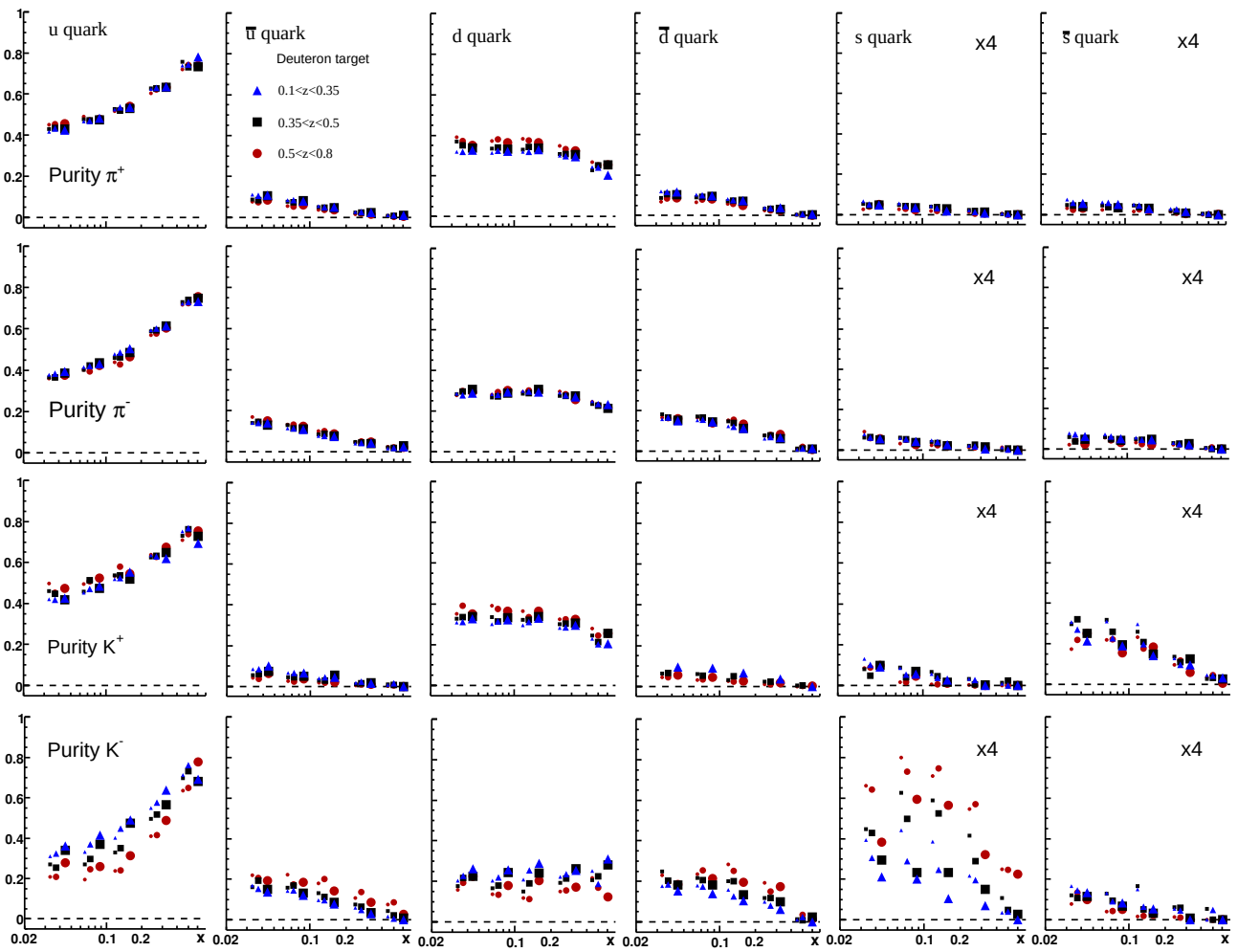

Figure 6.14: Purity in x-bins for the deuteron target. Only five of the nine x-bins are shown in order to make space for points representing all nine semi-inclusive bins. Three z bins are shown in different colors and symbols: $0.1 < z < 0.35$ (blue triangles), $0.35 < z < 0.5$ (black squares) and $0.5 < z < 0.8$ (red circles). The increasing of the size of the each type of symbols demonstrates $p_{\perp h}$ dependence of purities. The first $p_{\perp h}$-bin ($0.0\ GeV < p_{\perp h} < 0.3\ GeV$) is shown using small symbols, the second bin ($0.3\ GeV < p_{\perp h} < 0.5\ GeV$) is shown with the middle symbols. The large symbols represent the third ($0.5\ GeV < p_{\perp h} < 2.0\ GeV$) bin.

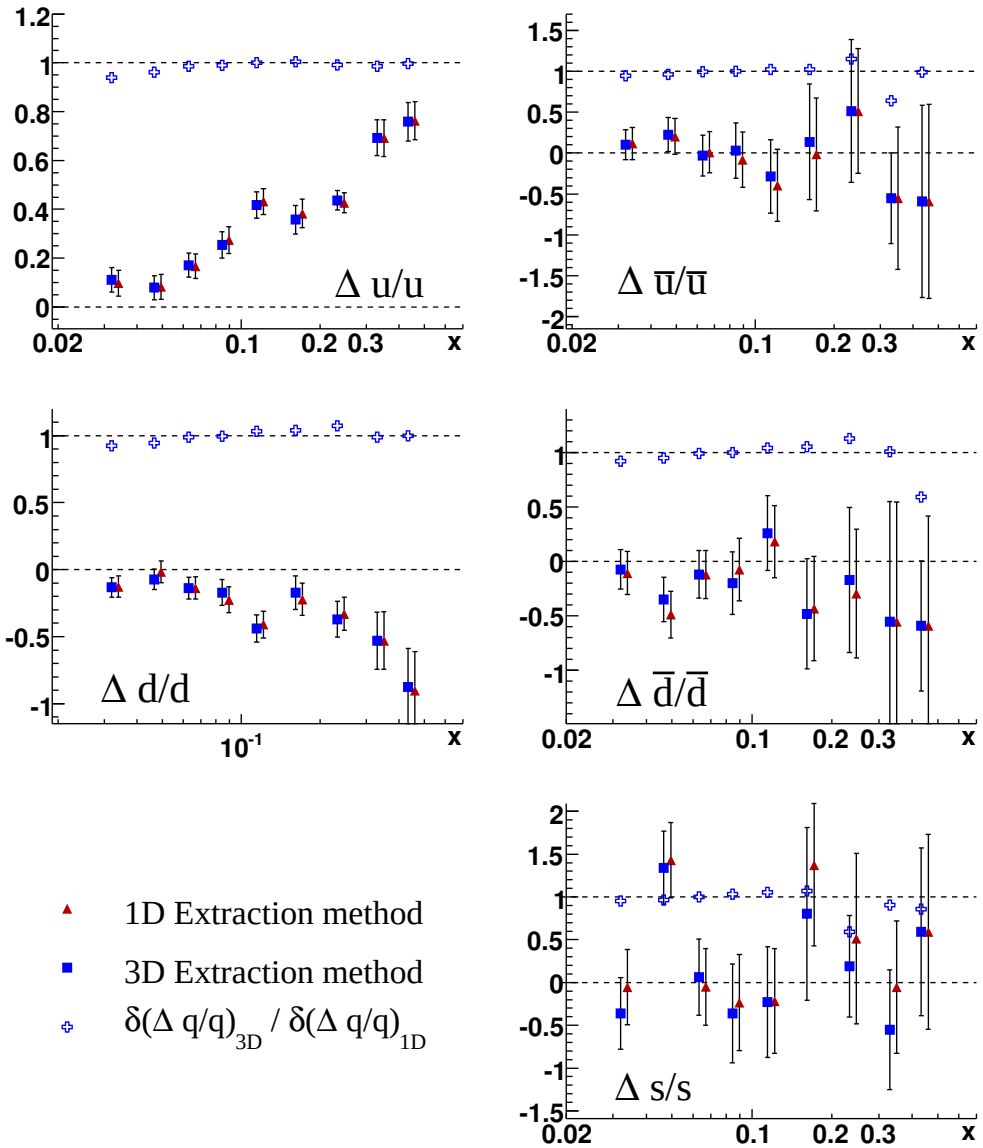

Figure 6.15: Comparison between 1D and 3D $\Delta q/q$. The ratio of the uncertainties $\delta(\Delta q/q)_{3D}/\delta(\Delta q/q)_{1D}$ (blue crosses) shows the improvement of errors at low x for u and d-quarks and at high x for sea quarks.

6.5.2 The quark polarizations

The quark polarizations presented in this section were derived by solving Eq. 6.9, using the set of inclusive and semi-inclusive hadron asymmetries listed in Eq. 6.11. The results for the quark polarization $\Delta q/q$ determined with the 3D ($x - z - p_{\perp h}$-binned) extraction are shown in Fig. 6.16 for two Q^2 ranges ($Q^2 > 1\ GeV^2$ - red squares and $Q^2 < 1\ GeV^2$ - red open circles) as a function of x. These values for quark polarizations were computed assuming zero anti-strange polarization $\Delta\bar{s} = 0$. The previous HERMES published result (black circles) is shown for comparison. Reanalysis of the data with

- open momentum cut;
- new EVT algorithm for RICH which gives more realistic systematic errors;
- double-spin asymmetries which were analyzed and unfolded in a three-dimensional kinematic binning

improves the statistical errors for the quark polarizations.

Systematic uncertainties enter this analysis at many different points and are important components of both the asymmetries and the purities. As a result of the systematic studies, three significant sources of systematic errors on the extracted $\Delta q/q$ values were identified:

- The uncertainty due to the using of the assumption of zero anti-strange polarization $\Delta\bar{s} = 0$;
- The uncertainty in beam and target polarizations, which are main sources of systematic uncertainties for the asymmetries;
- The uncertainty in the unpolarized PDFs, whose influence on the purities was described in the previous chapter.

The upper red bands show the systematic uncertainties for the points for $0.023 < x < 0.3$ from the data where the requirement, that the selected events from the deep-inelastic scattering region $Q^2 > 1\ GeV^2$. The lower Q^2 points are shown in addition. There is no systematic uncertainties in this region, because it is difficult to estimate the uncertainties of unpolarized PDFs. For $x > 0.3$, the asymmetries which were included in a fit, do not provide sufficient constraint on the polarizations of sea quarks. The points for $x > 0.3$ are shown in red open squares in Fig. 6.16 and for these two last x points (red open squares) the huge systematic uncertainties are not shown. The lower black bands are the published systematic uncertainties.

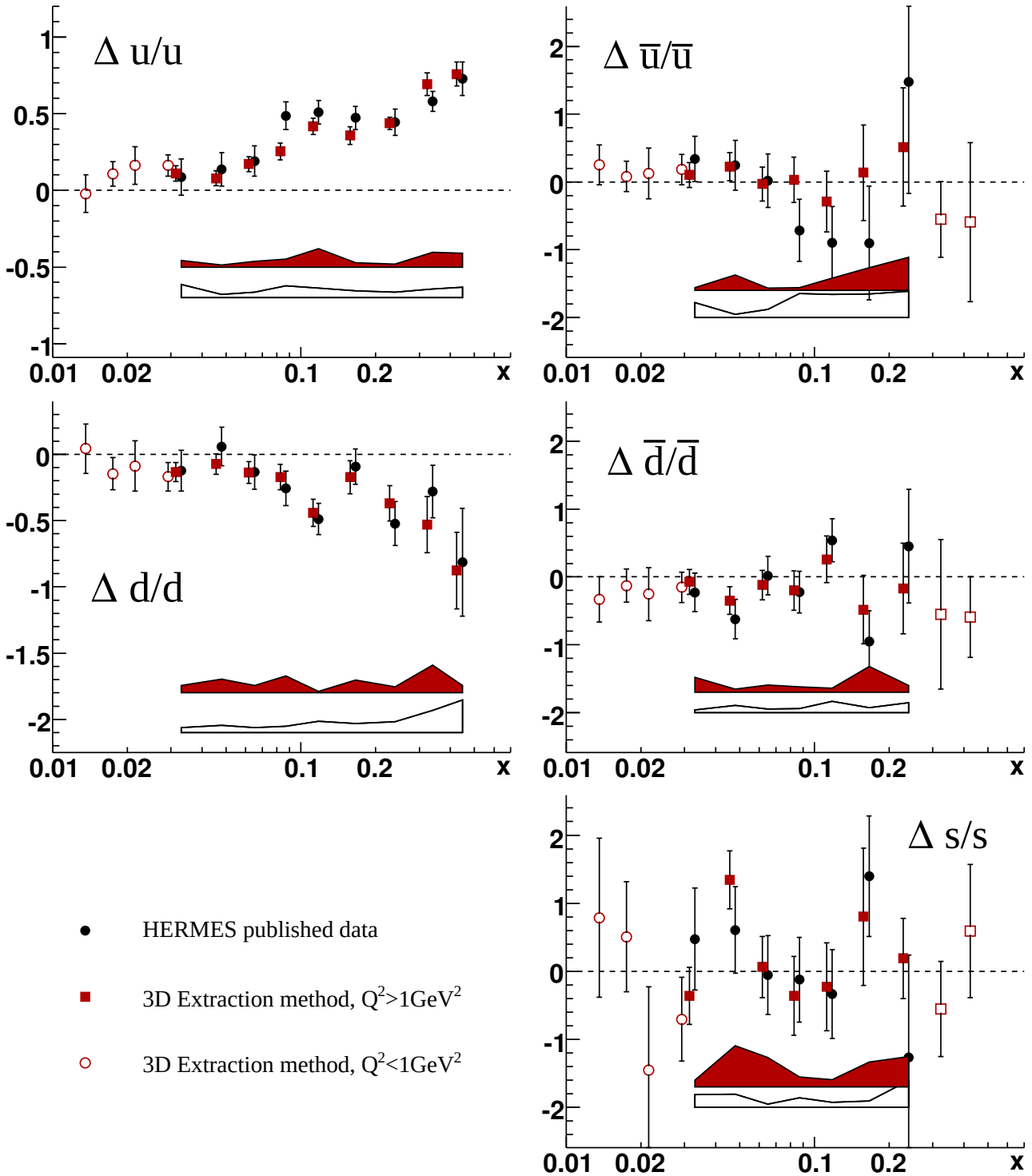

Figure 6.16: The result of polarizations of the quark flavors in the proton for $Q^2 > 1\ GeV^2$ (red squares) and for $Q^2 < 1\ GeV^2$ (red open circles) using the 3D extraction method as a function of x. The published HERMES result [13] (black circles) is shown for comparison. The error bars represent the statistical uncertainties. The upper red bands show the systematic uncertainties due to the using of assumption on the sea quarks, the error on the unpolarized PDFs and the uncertainties on the asymmetries. For the low Q^2 points and for two last x points the systematic uncertainties are not shown (see text). The lower black bands are the published systematic uncertainties.

6.5.3 The polarized parton densities

As discussed in Chapter 2.2, the quark helicities, $\Delta q(x)$, represent the contributions of the individual quark flavors to the spin-dependent structure function $g_1(x)$:

$$g_1(x) = \frac{1}{2}\sum\nolimits_q e_q^2[q^+(x) - q^-(x)] = \frac{1}{2}\sum\nolimits_q e_q^2 \Delta q(x). \tag{6.19}$$

To calculate $\Delta q(x)$, the quark polarizations are multiplied by the unpolarized parton distributions $q(x)$ which are experimentally well established. Furthermore the C_R factor (see Eq. 6.2) must be taken into account.

6.5.4 Comparison with theoretical prediction

The x-weighted helicity distributions $x\Delta q(x)$ are presented in Fig. 6.17. Data for $Q^2 < 1\ GeV^2$ (black circles) and $Q^2 > 1\ GeV^2$ (red squares) are shown separately. The results are compared with the theoretical prediction from the GRSV2000 parameterization (LO, "valence" scenario) [79]. The GRSV result was extracted using the spin asymmetries A_1 of inclusive measurements for the proton, neutron and deuteron from HERMES [80], EMC [5], SMC [36] and SLAC [41]. In the extraction, the ratio of the photo-absorption cross section $R(x, Q^2)$ was set to zero. For the comparison with our results, their results are scaled with $\frac{1}{1+R}$. The theoretical curves, which were calculated for different values of Q^2, show a slow Q^2 dependence for the quark helicity distributions. The HERMES results are in a good agreement with the fit. It should be stressed that HERMES decomposed the separate spin contributions of the quarks and anti-quarks to the nucleon spin x bin by x bin, thanks to the data for asymmetries in semi-inclusive DIS. The theoretical prediction is constrained by the assumption of the functional form. Strong assumptions on the sea quarks are made in the fit. The HERMES result plotted here (Fig. 6.17) was computed without zero anti-strange polarization. The anti-strange helicity distribution is also shown. The low Q^2 points, the anti-strange helicity distribution from the analysis presented in this thesis and the theoretical prediction from the GRVS parameterization do not contradict each other.

6.5.5 Final result for quark helicity distributions

Finally Fig. 6.18 presents the flavor-separated quark helicity distributions (red squares) computed from 3D binned asymmetries. Similarly to the Fig. 6.16, the results presented here were extracted with the constraint $\Delta\bar{s}\equiv 0$. The quark helicity distributions for $Q^2 < 1\ GeV^2$ are shown on the final plot as a open red circles and the sea-quark helicity distributions for $x > 0.3$ as open squares without systematic uncertainties . For comparison the previous published HERMES result is added (black circles). The improvement in statistical uncertainties is well visible.

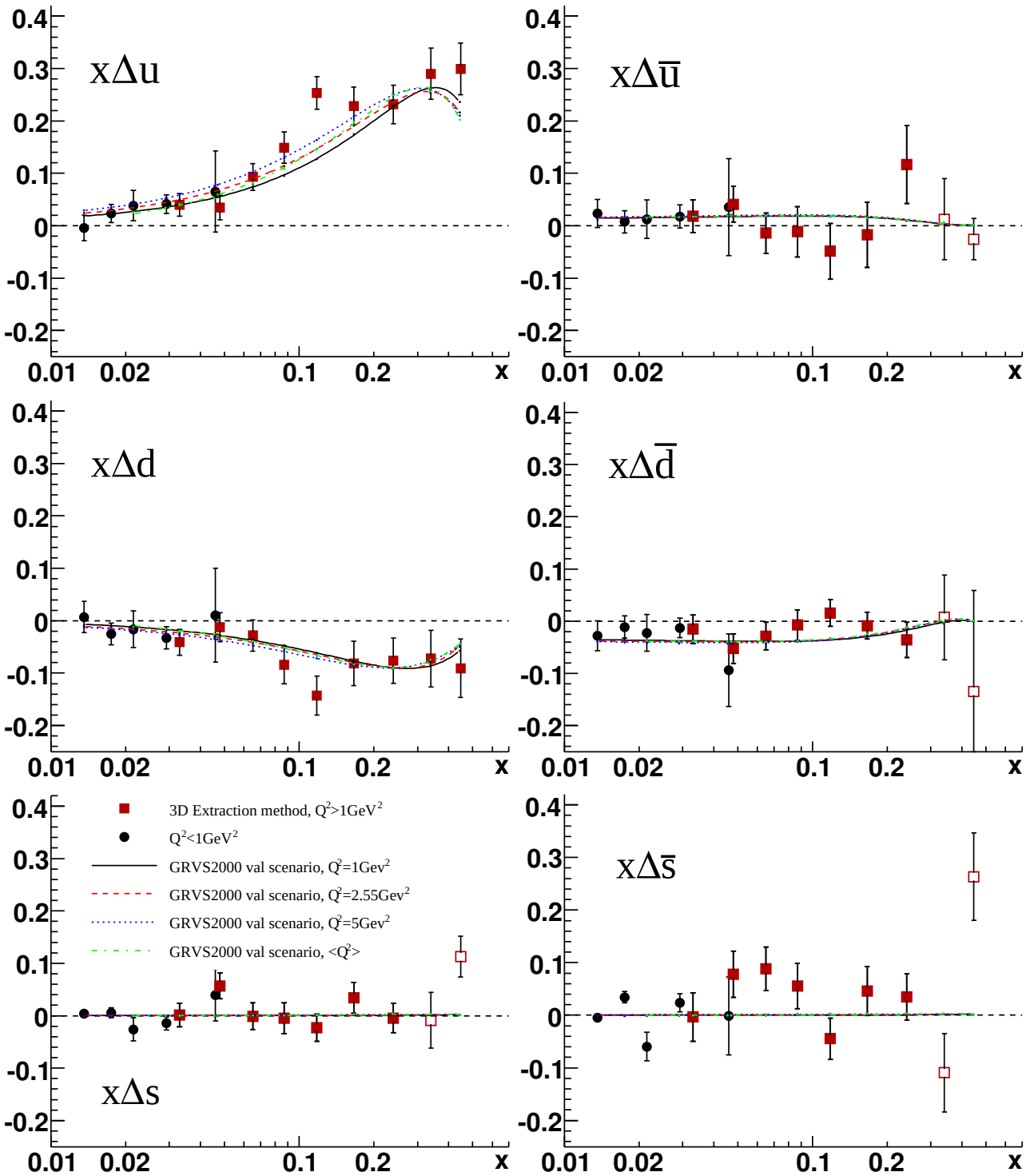

Figure 6.17: The x-weighted helicity distributions from the data for $Q^2 < 1\ GeV^2$ (black circles) and $Q^2 > 1\ GeV^2$ (red squares). The error bars show the statistical uncertainties. Systematic uncertainties are not shown. The data are shown together with the theoretical prediction from the GRSV2000 parameterization [79] for various Q^2 values scaled with $\frac{1}{1+R}$.

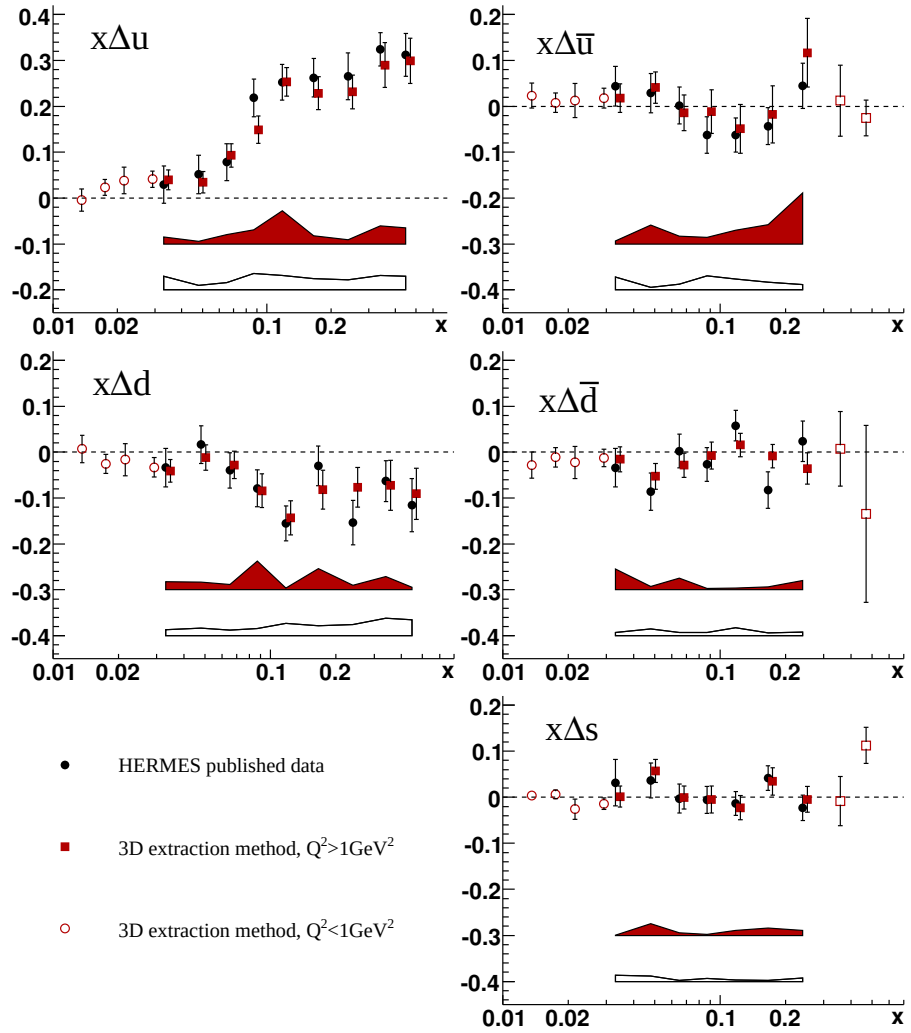

Figure 6.18: The quark helicity distributions $x\Delta q(x)$ for $Q^2 > 1\ GeV^2$ (red squares) and $Q^2 < 1\ GeV^2$ (red open circles) regions evaluated at a common value of $Q^2 = 2.5\ GeV^2$ as a function of x from 3D extraction method are shown in comparison with previous HERMES published result (black circles). The systematic errors are displayed separately as the upper red band. For low Q^2 points and for the sea-quark helicity distributions for two last x points (red open squares) the systematic uncertainties are not shown. The lower black bands are the published systematic uncertainties.

The total systematic uncertainties of the quark helicity densities (red upper bands) include contributions from the input asymmetries and systematic uncertainties on the purities, which arise from the unpolarized parton distributions. The largest contribution comes from the uncertainty in the unpolarized PDFs inside the Monte Carlo model that generates the purities. This significant source of uncertainty was not included in the previously published result (black lower bands).

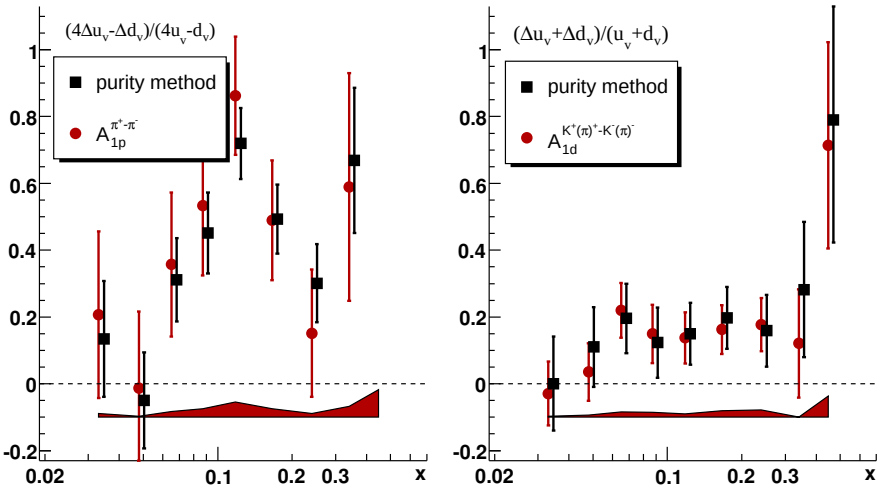

Figure 6.19: Left panel: The pion-charge-difference asymmetry $A_{1p}^{\pi^+-\pi^-}$ (red circles) from proton data in comparison with values for $\frac{4\Delta u_v(x)-\Delta d_v(x)}{4u_v(x)-d_v(x)}$ extracted from the purity method (black squares). Right panel: the combined pion and kaon charge difference asymmetry $A_{1d}^{K^+(\pi)^+-K^-(\pi)^-}$ (red circles) in comparison with extracted from the purity method values for $\frac{\Delta u_v(x)+\Delta d_v(x)}{u_v(x)+d_v(x)}$ from deuteron data. The error bars show the statistical uncertainties. Systematical uncertainties for asymmetries are shown as a red bands. Systematical uncertainties for the purity method are omitted.

6.6 The Hadron-Charge-Difference-Asymmetry Method

In this chapter another method, based on the separation of the quark contributions into *valence* and *sea* quark contributions is presented. The polarized valence quark distributions in the nucleon, $\Delta u_v = \Delta u - \Delta\bar{u}$ and $\Delta d_v = \Delta d - \Delta\bar{d}$ can be extracted using a method that does not rely on the calculation of purities with a Monte Carlo simulation.

6.6.1 The hadron-charge-difference asymmetry. Formalism.

The difference asymmetry approach for the extraction of helicity distributions has been introduced in Ref. [81].

As a first step, one can consider the number of $\pi^+(\pi^-)$ particles $N^{\pi^+}(N^{\pi^-})$ produced in a given bin of x and z in the configuration where the virtual photon and target helicities are antiparallel ($\overrightarrow{\Leftarrow}$) or parallel ($\overrightarrow{\Rightarrow}$). The standard parton model considerations [17] give, up to a constant factor

$$N^{\pi^+}_{p\overrightarrow{\Leftarrow}} \sim \frac{4}{9}u_+D_u^{\pi^+}(z)+\frac{4}{9}\bar{u}_+D_{\bar{u}}^{\pi^+}(z)+\frac{1}{9}d_+D_d^{\pi^+}(z)+\frac{1}{9}\bar{d}_+D_{\bar{d}}^{\pi^+}(z)+\frac{1}{9}s_+D_s^{\pi^+}(z)+\frac{1}{9}\bar{s}_+D_{\bar{s}}^{\pi^+}(z), \quad (6.20)$$

$$N^{\pi^-}_{p\overrightarrow{\Leftarrow}} \sim \frac{4}{9}u_+D_u^{\pi^-}(z)+\frac{4}{9}\bar{u}_+D_{\bar{u}}^{\pi^-}(z)+\frac{1}{9}d_+D_d^{\pi^-}(z)+\frac{1}{9}\bar{d}_+D_{\bar{d}}^{\pi^-}(z)+\frac{1}{9}s_+D_s^{\pi^-}(z)+\frac{1}{9}\bar{s}_+D_{\bar{s}}^{\pi^-}(z), \quad (6.21)$$

$$N^{\pi^+}_{\substack{p\rightarrow\\ \Rightarrow}} \sim \frac{4}{9}u_-D_u^{\pi^+}(z)+\frac{4}{9}\bar{u}_-D_{\bar{u}}^{\pi^+}(z)+\frac{1}{9}d_-D_d^{\pi^+}(z)+\frac{1}{9}\bar{d}_-D_{\bar{d}}^{\pi^+}(z)+\frac{1}{9}s_-D_s^{\pi^+}(z)+\frac{1}{9}\bar{s}_-D_{\bar{s}}^{\pi^+}(z), \quad (6.22)$$

$$N^{\pi^-}_{\substack{p\rightarrow\\ \Rightarrow}} \sim \frac{4}{9}u_-D_u^{\pi^-}(z)+\frac{4}{9}\bar{u}_-D_{\bar{u}}^{\pi^-}(z)+\frac{1}{9}d_-D_d^{\pi^-}(z)+\frac{1}{9}\bar{d}_-D_{\bar{d}}^{\pi^-}(z)+\frac{1}{9}s_-D_s^{\pi^-}(z)+\frac{1}{9}\bar{s}_-D_{\bar{s}}^{\pi^-}(z), \quad (6.23)$$

where $q_+(x)(q_-(x))$ denotes distribution function of a quark with their spin in the same direction as the spin of the nucleon (parallel) or in the opposite direction (antiparallel) and $D_q^h(z)$ the fragmentation function of a quark into hadron h with energy $E_h = z\nu$. The above relations have been obtained with standard assumption that the fragmentation function $D_q^h(z)$ does not depend on the quark helicity i.e. that $D_{q^+}^h(z) = D_{q^-}^h(z)$. Using the isospin and charge conjugation symmetry one can relate various fragmentation functions. Finally, three independent fragmentation functions $D_1(z)$, $D_2(z)$ and $D_3(z)$, correspondingly called favoured, unfavoured and strange quark fragmentation functions are left

$$D_1(z)\equiv D_u^{\pi^+}(z) = D_d^{\pi^-}(z) = D_{\bar{d}}^{\pi^+}(z) = D_{\bar{u}}^{\pi^-}(z), \quad (6.24)$$

$$D_2(z)\equiv D_d^{\pi^+}(z) = D_u^{\pi^-}(z) = D_{\bar{u}}^{\pi^+}(z) = D_{\bar{d}}^{\pi^-}(z), \quad (6.25)$$

$$D_3(z)\equiv D_s^{\pi^+}(z) = D_s^{\pi^-}(z) = D_{\bar{s}}^{\pi^+}(z) = D_{\bar{s}}^{\pi^-}(z). \quad (6.26)$$

In this notation, Eqs. 6.20-6.23 take the form

$$N^{\pi^+}_{\substack{p\rightarrow\\ \Leftarrow}} \sim [\frac{4}{9}u_+ + \frac{1}{9}\bar{d}_+]D_1(z) + [\frac{4}{9}\bar{u}_+ + \frac{1}{9}d_+]D_2(z) + \frac{1}{9}[s_+ + \bar{s}_+]D_3(z), \quad (6.27)$$

$$N^{\pi^-}_{\substack{p\rightarrow\\ \Leftarrow}} \sim [\frac{4}{9}u_+ + \frac{1}{9}\bar{d}_+]D_2(z) + [\frac{4}{9}\bar{u}_+ + \frac{1}{9}d_+]D_1(z) + \frac{1}{9}[s_+ + \bar{s}_+]D_3(z), \quad (6.28)$$

$$N^{\pi^+}_{\substack{p\rightarrow\\ \Rightarrow}} \sim [\frac{4}{9}u_- + \frac{1}{9}\bar{d}_-]D_1(z) + [\frac{4}{9}\bar{u}_- + \frac{1}{9}d_-]D_2(z) + \frac{1}{9}[s_- + \bar{s}_-]D_3(z), \quad (6.29)$$

$$N^{\pi^-}_{\substack{p\rightarrow\\ \Rightarrow}} \sim [\frac{4}{9}u_- + \frac{1}{9}\bar{d}_-]D_2(z) + [\frac{4}{9}\bar{u}_- + \frac{1}{9}d_-]D_1(z) + \frac{1}{9}[s_- + \bar{s}_-]D_3(z). \quad (6.30)$$

For particular combinations of the quantities defined above, namely

$$N^{\pi^+-\pi^-}_{\substack{p\rightarrow\\ \Leftarrow}} \equiv N^{\pi^+}_{\substack{\rightarrow\\ \Leftarrow}} - N^{\pi^-}_{\substack{\rightarrow\\ \Leftarrow}}, \qquad N^{\pi^+-\pi^-}_{\substack{\rightarrow\\ \Rightarrow}} \equiv N^{\pi^+}_{\substack{\rightarrow\\ \Rightarrow}} - N^{\pi^-}_{\substack{\rightarrow\\ \Rightarrow}} \quad (6.31)$$

the sea contribution cancels, and finally

$$N^{\pi^+-\pi^-}_{\substack{p\rightarrow\\ \Leftarrow}} \sim [\frac{4}{9}u_{v+} - \frac{1}{9}d_{v+}][D_1(z) - D_2(z)], \quad (6.32)$$

$$N^{\pi^+-\pi^-}_{\substack{p\rightarrow\\ \Rightarrow}} \sim [\frac{4}{9}u_{v-} - \frac{1}{9}d_{v-}][D_1(z) - D_2(z)], \quad (6.33)$$

where q_v were defined in Eq. 2.50.

The sum of Eqs. 6.32 and 6.33 gives a quantity well known experimentally in terms of

unpolarized valence quark distributions in the proton,

$$N^{\pi^+-\pi^-}_{\substack{p\rightarrow\\ \Leftarrow}} + N^{\pi^+-\pi^-}_{\substack{\rightarrow\\ \Rightarrow}} \sim [\frac{4}{9}u_v - \frac{1}{9}d_v][D_1(z) - D_2(z)], \tag{6.34}$$

while the difference contains information about *polarized* valence quark distributions

$$N^{\pi^+-\pi^-}_{\substack{p\rightarrow\\ \Leftarrow}} - N^{\pi^+-\pi^-}_{\substack{\rightarrow\\ \Rightarrow}} \sim [\frac{4}{9}\Delta u_v - \frac{1}{9}\Delta d_v][D_1(z) - D_2(z)], \tag{6.35}$$

where Δu_v and Δd_v are differences of the valence quark distributions with spin orientation parallel and antiparallel to the spin of the proton.

Then the asymmetry $A_p^{\pi^+-\pi^-}$ can be expressed by the ratio of polarized to unpolarized valence quark distributions in the proton, because the fragmentation functions cancel

$$A_{1p}^{\pi^+-\pi^-}(x) = \frac{4\Delta u_v(x) - \Delta d_v(x)}{4u_v(x) - d_v(x)}. \tag{6.36}$$

where the valence quark densities $(\Delta)u_v(x)$ and $(\Delta)d_v(x)$ were defined in Eqs. 2.50, 2.51.

The resulting values of the difference asymmetry $A_{1p}^{\pi^+-\pi^-}(x)$ as a function of x is shown in Fig. 6.19 (left panel). Since $A_{1p}^{\pi^+-\pi^-}(x)$ can be expressed by the ratio of polarized to unpolarized valence quark distributions in the proton, the extracted values for $\frac{4\Delta u_v(x)-\Delta d_v(x)}{4u_v(x)-d_v(x)}$ at $Q^2 = 2.5\ GeV^2$ determined by the purity method were added for comparison. Both methods agree surprisingly well.

The same calculation can be performed for the deuteron target. Instead of Eqs. 6.27 and 6.28 one can write down the expressions

$$N^{\pi^+}_{\substack{d\rightarrow\\ \Leftarrow}} \sim [u_+ + d_+]\Big(\frac{4}{9}D_1(z) + \frac{1}{9}D_2(z)\Big) + [\bar{u}_+ + \bar{d}_+]\Big(\frac{4}{9}D_2(z) + \frac{1}{9}D_1(z)\Big) + \frac{2}{9}[s_+ + \bar{s}_+]D_3(z), \tag{6.37}$$

$$N^{\pi^-}_{\substack{d\rightarrow\\ \Leftarrow}} \sim [u_+ + d_+]\Big(\frac{4}{9}D_2(z) + \frac{1}{9}D_1(z)\Big) + [\bar{u}_+ + \bar{d}_+]\Big(\frac{4}{9}D_1(z) + \frac{1}{9}D_2(z)\Big) + \frac{2}{9}[s_+ + \bar{s}_+]D_3(z). \tag{6.38}$$

The polarized and unpolarized valence quark distributions in the deuteron are given by

$$N^{\pi^+-\pi^-}_{\substack{d\rightarrow\\ \Leftarrow}} - N^{\pi^+-\pi^-}_{\substack{d\rightarrow\\ \Rightarrow}} \sim [\Delta u_v + \Delta d_v]\Big[\frac{3}{9}D_1(z) - \frac{3}{9}D_2(z)\Big] \tag{6.39}$$

and

$$N^{\pi^+-\pi^-}_{\substack{d\rightarrow\\ \Leftarrow}} + N^{\pi^+-\pi^-}_{\substack{d\rightarrow\\ \Rightarrow}} \sim [u_v + d_v]\Big[\frac{3}{9}D_1(z) - \frac{3}{9}D_2(z)\Big], \tag{6.40}$$

correspondingly. Finally, the asymmetry $A_{1d}^{\pi^+-\pi^-}(x)$ is given

$$A_{1d}^{h^+-h^-}(x) \simeq A_{1d}^{\pi^+-\pi^-}(x) = A_{1d}^{K^+-K^-}(x) = \frac{\Delta u_v(x) + \Delta d_v(x)}{u_v(x) + d_v(x)}, \tag{6.41}$$

where isospin symmetry was used to express the parton densities in the neutron in terms of

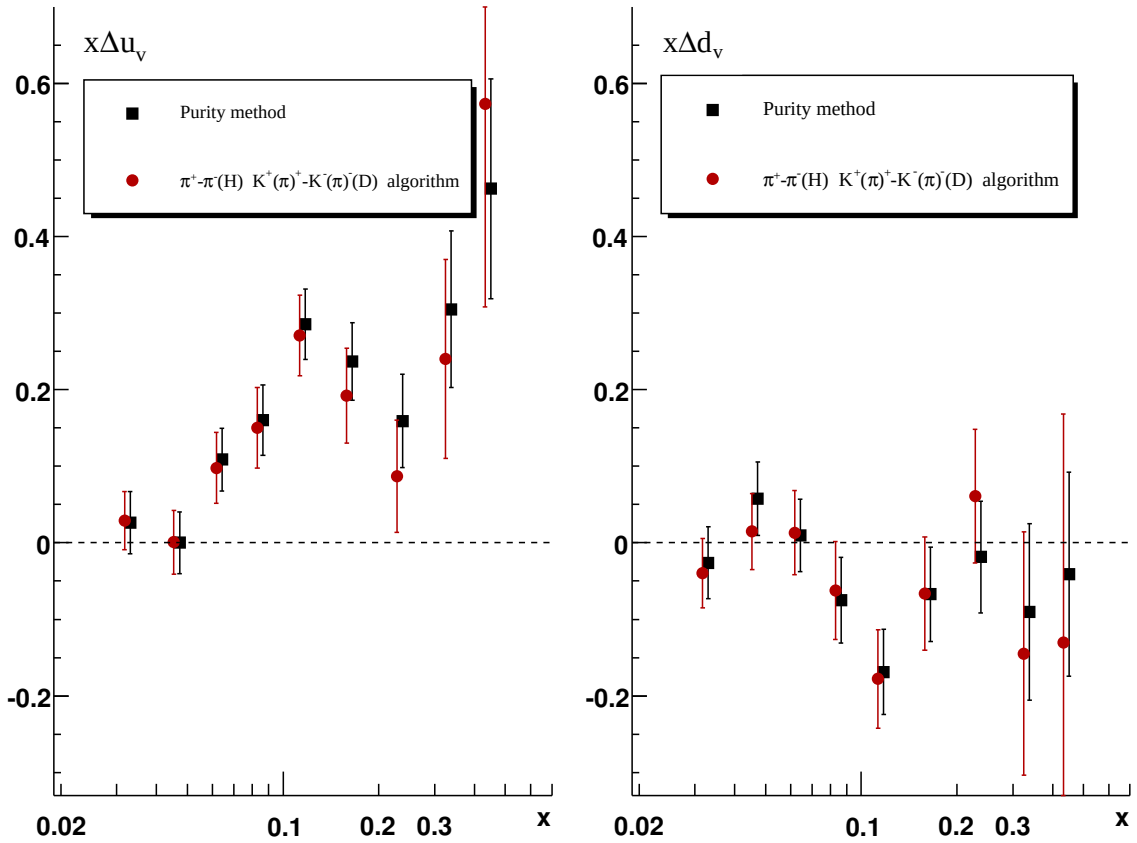

Figure 6.20: Polarized valence quark distributions computed from the charge difference asymmetries (red circles) at $Q^2 = 2.5\ GeV^2$. For comparison, the same densities extracted with the purity algorithm (black squares) are shown slightly offset in x. The error bars represent the statistical uncertainties.

those in the proton. In the case of an isoscalar target and assuming $\Delta s = \Delta\bar{s}$, the difference asymmetries for pions and kaons are both equal to the sum of the valence quark polarizations. Since kaons contribute to the asymmetry in the same way as pions, both pion and kaon data sets were combined (Fig. 6.19 (right panel)).

These two equations 6.36 and 6.41 can be solved for the flavor separated polarized valence quark densities,

$$\Delta u_v(x) = \frac{1}{5}\Big[(4u_v(x) - d_v(x))A_{1p}^{\pi^+-\pi^-}(x) + (u_v(x) + d_v(x))A_{1d}^{\pi^+-\pi^-}(x)\Big], \tag{6.42}$$

$$\Delta d_v(x) = \frac{1}{5}\Big[-(4u_v(x) - d_v(x))A_{1p}^{\pi^+-\pi^-}(x) + 4(u_v(x) + d_v(x))A_{1d}^{\pi^+-\pi^-}(x)\Big]. \tag{6.43}$$

The flavor separated valence quark densities $x\Delta u_v(x)$ and $x\Delta d_v(x)$ at $Q^2 = 2.5\ GeV^2$ determined using these charge-difference asymmetries are presented in Fig. 6.20 (red circles).

The valence quark densities extracted using the purity algorithm are also shown for comparison (black squares). The uncertainties on the valence densities determined here are larger than those on the densities computed with the purity algorithm, particularly for high x. Their large size is due to the computation being based on the charge difference asymmetries of pions and kaon only. In a case of the purity method, as was discussed in Chap. 6.3, the inclusion of the inclusive asymmetries helped to decrease the statistical uncertainties on the quark polarizations for $x > 0.1$. Moreover, the statistical uncertainties arise from the large statistical uncertainty of the asymmetry $A_{1p}^{\pi^+-\pi^-}$, which is included into the Eqs. 6.42, 6.43. Within these uncertainties the result computed with the pion(kaon) charge difference algorithm agree with the results of the purity algorithm. However, this algorithm is not sensitive to the polarization of the quark sea and therefore does not provide a cross check of the measured sea polarizations. Within these limitations the charge difference asymmetry algorithm confirms that the valence quark densities determined with the purity algorithm are not biased by the assumptions which were applied by tuning of Monte Carlo parameters describing the fragmentation processes.

The polarized valence quark distribution $x(\Delta u_v(x) + \Delta d_v(x))$ at $Q^2 = 2.5\ GeV^2$ determined using the asymmetries from Eq. 6.41 is presented in Fig. 6.21 (top plot). The LO parameterization of the DNS fit [75] also shown in the Fig. 6.21, includes all DIS g_1 data from COMPASS data [15] as well as the SIDIS data from SMC [37] and HERMES [13]. Here, the result which is based on charge difference asymmetries gives smaller statistical uncertainties then the uncertainty of the polarized valence quark distribution from purity method, because only deuteron data were used.

In LO the valence quark distribution is related to the polarized structure function g_1^d from inclusive measurements by :

$$\Delta u_v + \Delta d_v = \frac{36}{5}\frac{g_1^d}{(1 - 1.5\omega_D)} - \Big[2(\Delta\bar{u} + \Delta\bar{d}) + \frac{2}{5}(\Delta s + \Delta\bar{s})\Big]. \tag{6.44}$$

The sea contribution to the unpolarized structure function decreases with increasing x and becomes smaller for $x > 0.3$. The polarized sea contribution to the nucleon also becomes negligible in this region. With this assumption the second term in Eq. 6.44 can be neglected for $x > 0.3$ and the values for $\Delta u_v(x) + \Delta d_v(x)$ can be obtained from g_1^d data [14]. The corresponding result are also shown in Fig. 6.21 (top plot, open red points). They agree very well with the DNS curve.

6.6.2 Determination of moments of the distributions

The n^{th} moment $\Delta^{(n)}q(Q^2)$ of a polarized quark distribution $\Delta q(x, Q^2)$ is defined as

$$\Delta^{(n)}q(Q^2)|_{Q_0^2} = \int_0^1 dx\ x^{n-1}\Delta q(x, Q^2)|_{Q_0^2}, \tag{6.45}$$

at a fixed scale $Q_0^2 = 2.5\ GeV^2$.

For the first moments, $n = 1$, the total contribution of each quark flavor to the nucleon spin is determined by integrating the measured parton distributions over the entire x range. The integral of the quark spin distribution in the measured x-region is calculated by integrating the product of the quark polarization at given x-bin, x_i, and the parameterization of the unpolarized distribution $q(x, Q^2)$ as

$$\Delta^{(1)}q(Q^2) = \int_{0.023}^{0.6} dx \Delta q(x, Q^2) = \sum_i \Big[\frac{\Delta q}{q}(x_i) \int_{\xi_i}^{\xi_{i+1}} q(x, Q^2) dx \Big] \tag{6.46}$$

where $\frac{\Delta q}{q}$ was to be assumed constant within each x-bin, i, and independent of Q^2. The integration was performed for $x \in [\xi_i, \xi_{i+1}]$ which defines the boundaries of the bin. The parameterization from CTEQ6L at $Q^2 = 2.5\ GeV^2$ were taken for the unpolarized parton distributions $q(x, Q^2)$.

The first moment of the polarized valence distribution, truncated to the measured x range

$$\Gamma_v(x_{min}) = \int_{x_{min}}^{0.9} dx [\Delta u_v(x) + \Delta d_v(x)], \tag{6.47}$$

derived from the difference asymmetry and from the purity method for $0.023 < x \leq 0.3$ and from g_1^d for $0.3 < x < 0.9$ is shown in Fig. 6.21 (bottom plot). Practically no dependence on the lower limit is observed for $x_{min} < 0.035$.

The resulting values in the measured range $0.023 < x < 0.6$ for the first moment of the helicity distribution separately and for the first moment of the polarized valence distribution in the measured range $0.023 < x < 0.9$ are listed in Table 6.1. The statistical and systematic uncertainties on the moments, $\delta_{\Delta q}^{stat}$ and $\delta_{\Delta q}^{sys}$, are obtained from these covariance matrices as

$$\Big(\delta_{\Delta q}^{stat/sys}\Big)^2 = \sum_{i,j} V_q^{stat/sys} \Big(\frac{\Delta q}{q}(x_i), \frac{\Delta q}{q}(x_j) \Big) \int_{\xi_i}^{\xi_{i+1}} dx q(x, Q^2) \int_{\xi_j}^{\xi_{j+1}} dx q(x, Q^2). \tag{6.48}$$

The effect of the uncertainty on the unpolarized PDFs to the first moments are not included.

For the first moment of the polarized valence distribution it was obtained from the difference asymmetry

$$\Gamma_v(x_{min}) = \int_{x_{min}}^{0.9} dx [\Delta u_v(x) + \Delta d_v(x)] = 0.345 \pm 0.046 \pm 0.04, \tag{6.49}$$

and from the purity method

$$\Gamma_v(x_{min}) = \int_{x_{min}}^{0.9} dx [\Delta u_v(x) + \Delta d_v(x)] = 0.386 \pm 0.073 \pm 0.061. \tag{6.50}$$

These values of Γ_v confirm the COMPASS result obtained at $Q^2 = 10\ GeV^2$ [82], which suggests that $\Delta\bar{u}$ and $\Delta\bar{d}$ are of opposite sign.

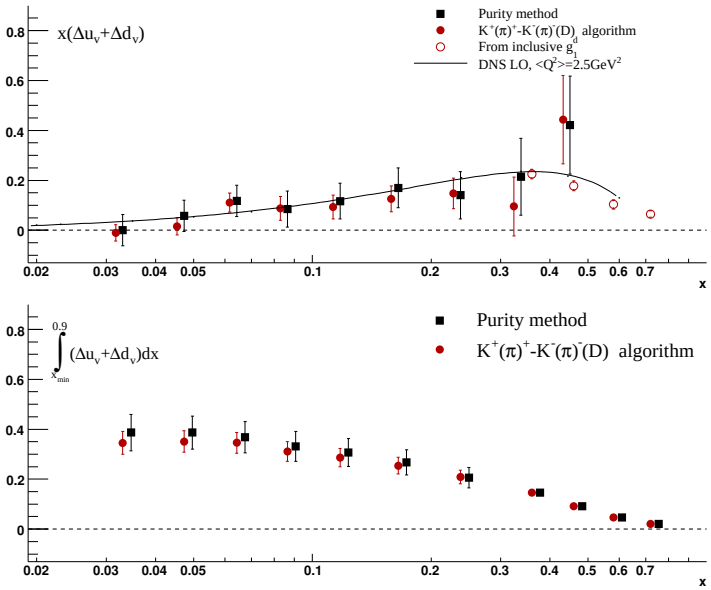

Figure 6.21: Top: Polarized valence quark distribution $x(\Delta u_v(x) + \Delta d_v(x))$ (red circles) evolved to $Q^2 = 2.5\ GeV^2$ according to the DNS fit at LO [75] (line) in comparison with the result obtained from the purity method (black squares). The four additional points (red open circles) at high x are obtained from g_1^d [14]. Bottom: The integral of $\Delta u_v(x) + \Delta d_v(x)$ over the range $0.023 \leq x \leq 0.9$ as a function of the lower x limit, evaluated at $Q^2 = 2.5\ GeV^2$.

The values for the first moments of the helicity distribution from the 3D extraction method are in agreement with published HERMES result. The moments determined in the present analysis have not an improved precision due to the attempt to increase the measured x range for sea flavors. The first moments from analytically calculated purities are smaller due to the restricted x-range, nevertheless the agreement is good. The uncertainty of the strange quark moment is sensitive to the choice of set of fragmentation functions.

Table 6.1: First moments of various helicity distributions in the measured range at a scale of $Q^2 = 2.5\ GeV^2$.

Purity method	3D Extraction
Δu	$0.589 \pm 0.039 \pm 0.065$
Δd	$-0.230 \pm 0.045 \pm 0.068$
Δs	$0.067 \pm 0.030 \pm 0.037$
$\Delta \bar{u}$	$0.044 \pm 0.058 \pm 0.045$
$\Delta \bar{d}$	$-0.046 \pm 0.036 \pm 0.040$
Δu_v	$0.639 \pm 0.084 \pm 0.041$
Δd_v	$-0.149 \pm 0.088 \pm 0.043$
$\Delta u_v + \Delta d_v$	$0.386 \pm 0.073 \pm 0.061$
Difference asymmetry	
Δu_v	$0.613 \pm 0.135 \pm 0.081$
Δd_v	$-0.189 \pm 0.220 \pm 0.105$
$\Delta u_v + \Delta d_v$	$0.345 \pm 0.046 \pm 0.048$

Chapter 7

Conclusions

The study of the nucleon structure via inclusive deep-inelastic scattering played an important role for the establishment of the Quark-Parton Model and subsequently of QCD as the theory of strong interactions. With polarized DIS the spin observables of the nucleon become accessible. A unique insight into the nucleon spin structure is provided by the semi-inclusive DIS process where both the scattered lepton and hadrons produced from the struck quark are detected.

The investigation of the structure of the nucleon was the main goal of the HERMES experiment. Polarized deep-inelastic scattering data on longitudinally polarized hydrogen and deuterium targets have been used to determine double spin asymmetries of cross sections. Inclusive and semi-inclusive asymmetries from both targets were measured, and the separate helicity densities for the up and down and the anti-up, anti-down and strange sea quarks were determined for the first time in [13].

The motivation of this work was the re-analysis of previously published data due to the new systematic studies, which were done by other HERMES groups for better understanding of the HERMES spectrometer performance. The second goal of this work was to consider the sources of statistical and systematic uncertainties in detail and to obtain a realistic estimation of these uncertainties.

The work was split into two parts, which comprise the analysis of the data taken with HERMES detector, the calculation of the final inclusive and semi-inclusive asymmetries, using the full avaible information from the HERMES data and the extraction of separate quark helicity distributions in the nucleon.

In the first part of this thesis work, the final result of inclusive and semi-inclusive virtual photon-nucleon cross section asymmetries were obtained from the analysis of deep-inelastic events taken on polarized proton and deuteron targets. The data cover a kinematic range of $0.023 < x < 0.6$ and $0.5\ GeV^2 < Q^2 < 15\ GeV^2$. The result provides a largely improved statistical precision over the previously published HERMES data. The inclusive and semi-inclusive asymmetries are compatible with result from COMPASS experiment.

Three dimensionally binned SIDIS double-spin asymmetries and asymmetries as a function

of $p_{\perp h}$ are produced. These asymmetries are valuable inputs to world fits being performed by theorists.

In the second part of this work, the purity formalism was introduced as a procedure to extract the polarized quark distributions in the nucleon. The polarization of up, down and sea quarks were determined with improved statistical uncertainties from the measured asymmetries. The latter results were found to be in agreement with an earlier published HERMES result. Before the start of this work it was the hope, that the final semi-inclusive asymmetries can give the possibility to improve the knowledge about the helicity distribution of the strange quark. But unfortunately, the measured asymmetries still do not provide sufficient constraint on the polarizations of sea quarks. Moreover, the systematic studies show the dependence of the result on the choice of the sets of fragmentation functions.

Furthermore the hadron charge difference asymmetries are presented, which in LO QCD provide a measurement of the valence quark polarization. An evaluation of the first moment of the polarized valence distribution is in a very good agreement with the result from the purity method.

Chapter 8

Zusammenfassung

Die Untersuchung der Struktur des Nukleons mittels inklusiver tief-inelastischer Streuung spielte eine wichtige Rolle bei der Etablierung des Quark-Parton Modells and später der Quantenchromodynamik (QCD) als der Theorie der Starken Wechselwirkung. Tief-unelastische Streuung mit polarisierten Quellen und/oder Strahlen ermöglicht den Zugang zu den spinabhängigen Observablen des Nukleons. Der semi-inklusive Prozess, bei dem sowohl das gestreute Lepton als auch die vom getroffenen Quark erzeugten Hadronen nachgewiesen werden, erlaubt einen einmaligen Blick ins Innere des Nukleons.

Die Untersuchung der Struktur des Nukleons ist das Hauptziel des HERMES-Experiments. Daten aus tief-unelastischer Streuung unter Verwendung von longitudinal polarisierten Leptonen-Strahlen und longitudinal polarisierten leichten Wasserstoff- oder Deuterium-Quellen wurden verwendet, um die Doppel-Spin Asymmetrien im Wirkungsquerschnitt zu bestimmen. Für beide Quellen wurden inklusive und semi-inklusive Asymmetrien gemessen. Dabei wurden zum ersten Mal die individuellen Helizitätsverteilungen für up- und down-Quarks und anti-up, anti-down und strange See-Quarks bestimmt [13].

Der Beweggrund der Neu-Analyse der bereits veröffentlichten Daten in der vorliegenden Arbeit sind neuere systematische Studien, die von anderen HERMES-Untergruppen zum besseren Verständnis des HERMES-Spektrometers durchgeführt wurden. Das zweite Ziel dieser Arbeit war es, die statistischen und systematischen Unsicherheiten einer genauen Untersuchung zu unterwerfen, um zu einer realistischen Einschätzung dieser Unsicherheiten zu gelangen.

Die vorliegende Arbeit ist in zwei Teile gegliedert. Im ersten Teil werden die Analyse der mit dem HERMES-Detektor aufgezeichneten Daten und die Berechnung der finalen Ergebnisse der inklusiven und semi-inklusiven Asymmetrien unter Berücksichtigung des kompletten verfügbaren Datensatzes vorgestellt. Im zweiten Teil ist die Extraktion der individuellen Quark-Helizitätsverteilungen des Nukleons beschrieben.

Der erste Teil beschreibt die Bestimmung der finalen Ergebnisse der inklusiven und semi-inklusiven Asymmetrien im virtuellen Photon-Nukleon–Wirkungsquerschnitt aus der Analyse von tief-unelastischen Ereignissen an polarisierten Proton- und Deuteron-Quellen. Die Daten

umfassen den kinematischen Bereich $0.023 < x < 0.6$ und $0.5\ GeV^2 < Q^2 < 15\ GeV^2$. Verglichen mit den zuvor veröffentlichten HERMES-Daten liefert das vorliegende Ergebnis eine wesentlich verbesserte statistische Präzession. Die inklusiven und semi-inklusiven Asymmetrien sind kompatibel mit dem Resultat des COMPASS-Experiments.

Im zweiten Teil der Arbeit wurde der sogenannte Purity-Formalismus eingeführt, eine Prozedur, welche beschreibt, wie die spinabhängigen Quark-Verteilungen des Nukleons extrahiert werden können. Die Polarisationen von up-, down- bzw. See-Quarks wurden mit verbesserten statistischen Unsicherheiten aus den gemessenen Asymmetrien bestimmt. Diese Ergebnisse sind in Übereinstimmung mit dem zuvor veröffentlichten HERMES-Ergebnis. Vor Beginn dieser Arbeit bestand die Hoffnung, dass die finalen semi-inklusiven Asymmetrien die Möglichkeit eröffnen würden, den Kenntnisstand über die Helizitätsverteilung des strange-Quarks zu verbessern. Es stellte sich jedoch heraus, dass die gemessenen Asymmetrien im Rahmen der experimentellen Unsicherheiten die Polarisation der See-Quarks nicht ausreichend festlegen. Zudem weisen systematische Studien darauf hin, dass das Resultat von der Wahl der Fragementationsfunktionen-Sätze abhängt.

Des weiteren wurden die Differenz-Asymmetrien für unterschiedlich geladene Hadronen vorgestellt. Diese Asymmetrien erlauben in führender Ordnung der QCD eine Messung der Polarisation der Valenz-Quarks. Das erste Moment der spinabhängigen Valenzverteilung wurde berechnet. Es ist in sehr guter Übereinstimmung mit dem Resultat, das mit der Purity-Methode erzielt wurde.

Die semi-inklusiven Doppel-Spin Asymmetrien wurden in einem dreidimensionalen Binning extrahiert und zudem als eine Funktion des transversalen Impulses $p_{\perp h}$ des produzierten Hadrons dargestellt. Solche Asymmetrien stellen einen wertvollen Ausgangsdatensatz für theoretische Physiker dar, die Anpassungskurven an die verfügbaren Weltdaten erzeugen.

Appendix A

Results: Asymmetries $A_1(x)$

In this section, the final asymmetries as a function x in two Q^2 intervalls are tabulated. Table A.1 defines the bin numbers and bin edges for x. Listed are the combined asymmetries of the 1996-1997 data-taking periods for the proton target, and 1998-2000 data-taking periods for deuteron target.

Table A.1: 1-Dimensional x binning.

Bin number	x range	Average value of x
	$Q^2 < 1.0\ GeV^2$	
1	0.010-0.015	0.014
2	0.015-0.020	0.018
3	0.020-0.023	0.021
4	0.023-0.040	0.028
5	0.040-0.055	0.046
	$Q^2 > 1.0\ GeV^2$	
6	0.023-0.040	0.033
7	0.040-0.055	0.047
8	0.055-0.075	0.065
9	0.075-0.100	0.087
10	0.100-0.140	0.119
11	0.140-0.200	0.168
12	0.200-0.300	0.245
13	0.300-0.400	0.342
14	0.400-0.600	0.466

Table A.2: Inclusive Born level asymmetries on the proton target

bin	$< x >$	$< Q^2 >$ GeV^2	$\frac{1}{D(1+\eta\gamma)}$	$A_{\|\|,p}$	$A_{1,p}$	$\pm$ stat.	syst.
1	0.014	0.55	1.2625	0.0353	0.0446	0.0337	$^{+0.0041}_{-0.0052}$
2	0.018	0.66	1.3953	0.0415	0.0575	0.0209	$^{+0.0043}_{-0.0050}$
3	0.021	0.77	1.4824	0.0506	0.0744	0.0319	$^{+0.0057}_{-0.0065}$
4	0.029	0.85	1.9036	0.0448	0.0849	0.0190	$^{+0.0051}_{-0.0057}$
5	0.046	0.92	2.9279	0.0709	0.2076	0.0645	$^{+0.0088}_{-0.0098}$
6	0.033	1.21	1.4302	0.0666	0.0954	0.0152	$^{+0.0069}_{-0.0077}$
7	0.048	1.45	1.8214	0.0597	0.1087	0.0165	$^{+0.0075}_{-0.0082}$
8	0.065	1.69	2.2676	0.0586	0.1330	0.0185	$^{+0.0087}_{-0.0094}$
9	0.087	1.94	2.7834	0.0746	0.2070	0.0225	$^{+0.0123}_{-0.0134}$
10	0.118	2.34	3.1374	0.0944	0.2963	0.0227	$^{+0.0178}_{-0.0195}$
11	0.166	3.14	3.0824	0.1031	0.3178	0.0239	$^{+0.0199}_{-0.0219}$
12	0.240	4.49	2.8210	0.1433	0.4046	0.0256	$^{+0.0254}_{-0.0279}$
13	0.340	6.51	2.5109	0.1996	0.5011	0.0445	$^{+0.0314}_{-0.0347}$
14	0.447	9.14	2.2141	0.3054	0.6737	0.0745	$^{+0.0433}_{-0.0481}$

Table A.3: Inclusive Born level asymmetries on the deuteron target

bin	$< x >$	$< Q^2 >$ GeV^2	$\frac{1}{D(1+\eta\gamma)}$	$A_{\|\|,d}$	$A_{1,d}$	$\pm$ stat.	syst.
1	0.014	0.55	1.2624	-0.0044	-0.0055	0.0142	$^{-0.0000}_{+0.0003}$
2	0.017	0.66	1.3849	-0.0029	-0.0041	0.0090	$^{+0.0001}_{-0.0000}$
3	0.021	0.78	1.4718	-0.0037	-0.0054	0.0144	$^{+0.0006}_{-0.0004}$
4	0.029	0.85	1.9028	0.0034	0.0064	0.0086	$^{+0.0006}_{-0.0006}$
5	0.046	0.92	2.9379	0.0066	0.0192	0.0310	$^{+0.0003}_{-0.0003}$
6	0.033	1.22	1.4389	-0.0023	-0.0033	0.0069	$^{+0.0011}_{-0.0008}$
7	0.047	1.47	1.8337	0.0141	0.0258	0.0076	$^{+0.0017}_{-0.0014}$
8	0.065	1.72	2.2630	0.0090	0.0203	0.0088	$^{+0.0019}_{-0.0016}$
9	0.087	1.99	2.7681	0.0187	0.0519	0.0110	$^{+0.0037}_{-0.0029}$
10	0.118	2.40	3.1428	0.0312	0.0979	0.0113	$^{+0.0066}_{-0.0050}$
11	0.166	3.20	3.0659	0.0441	0.1355	0.0121	$^{+0.0094}_{-0.0069}$
12	0.239	4.56	2.8189	0.0603	0.1700	0.0132	$^{+0.0127}_{-0.0092}$
13	0.339	6.56	2.5085	0.1188	0.2979	0.0239	$^{+0.0212}_{-0.0152}$
14	0.445	9.15	2.2082	0.1550	0.3423	0.0415	$^{+0.0276}_{-0.0196}$

Table A.4: Born level asymmetries for hadrons on the proton target

bin	$< x >$	$< Q^2 >$	$\frac{1}{D(1+\eta\gamma)}$	$< z >$	$< p_{h\perp} >$	$C_\phi^{h^+}$	$A_{\parallel,p}^{h^+}$	$A_{1,p}^{h^+}$	$\pm$ stat.	syst.
1	0.014	0.55	1.2655	0.23	0.43	1.001	0.0500	0.0638	0.0421	$^{+0.0039}_{-0.0043}$
2	0.018	0.65	1.4018	0.24	0.41	1.004	0.0314	0.0442	0.0299	$^{+0.0024}_{-0.0027}$
3	0.022	0.77	1.4917	0.25	0.40	1.006	0.1022	0.1530	0.0471	$^{+0.0083}_{-0.0092}$
4	0.030	0.85	1.8851	0.28	0.36	1.007	0.0685	0.1304	0.0274	$^{+0.0064}_{-0.0072}$
5	0.046	0.92	2.8885	0.35	0.29	0.998	-0.0035	-0.0101	0.1037	$^{-0.0033}_{+0.0037}$
6	0.033	1.21	1.4599	0.26	0.40	1.008	0.0650	0.0953	0.0210	$^{+0.0051}_{-0.0057}$
7	0.048	1.45	1.8062	0.29	0.36	1.008	0.0740	0.1350	0.0231	$^{+0.0071}_{-0.0079}$
8	0.065	1.72	2.1243	0.32	0.32	1.003	0.0660	0.1405	0.0257	$^{+0.0074}_{-0.0083}$
9	0.087	2.06	2.4003	0.34	0.31	0.992	0.0911	0.2169	0.0308	$^{+0.0114}_{-0.0127}$
10	0.118	2.58	2.5655	0.36	0.30	0.976	0.1330	0.3333	0.0312	$^{+0.0175}_{-0.0195}$
11	0.166	3.50	2.5284	0.37	0.31	0.954	0.1179	0.2838	0.0345	$^{+0.0161}_{-0.0180}$
12	0.238	4.98	2.3984	0.37	0.31	0.923	0.2086	0.4612	0.0404	$^{+0.0252}_{-0.0281}$
13	0.338	7.09	2.2542	0.37	0.32	0.895	0.2213	0.4464	0.0787	$^{+0.0251}_{-0.0280}$
14	0.448	9.72	2.0500	0.38	0.33	0.902	0.3375	0.6243	0.1486	$^{+0.0355}_{-0.0396}$
bin	$< x >$	$< Q^2 >$	$\frac{1}{D(1+\eta\gamma)}$	$< z >$	$< p_{h\perp} >$	$C_\phi^{h^-}$	$A_{\parallel,p}^{h^-}$	$A_{1,p}^{h^-}$	$\pm$ stat.	syst.
1	0.014	0.55	1.2739	0.24	0.44	0.989	0.0383	0.0481	0.0384	$^{+0.0030}_{-0.0033}$
2	0.018	0.66	1.3956	0.25	0.42	0.991	0.0323	0.0448	0.0277	$^{+0.0020}_{-0.0022}$
3	0.021	0.77	1.4820	0.26	0.41	0.993	0.0605	0.0891	0.0450	$^{+0.0048}_{-0.0053}$
4	0.029	0.85	1.8722	0.29	0.37	0.997	0.0383	0.0716	0.0296	$^{+0.0028}_{-0.0032}$
5	0.046	0.92	2.8937	0.36	0.30	0.999	0.0772	0.2226	0.1272	$^{+0.0091}_{-0.0102}$
6	0.033	1.21	1.4466	0.26	0.41	0.993	0.0388	0.0558	0.0226	$^{+0.0028}_{-0.0031}$
7	0.047	1.47	1.7909	0.29	0.37	0.997	0.0625	0.1114	0.0264	$^{+0.0060}_{-0.0067}$
8	0.065	1.77	2.0477	0.32	0.34	0.997	0.0482	0.0996	0.0300	$^{+0.0052}_{-0.0058}$
9	0.087	2.16	2.3238	0.34	0.32	1.000	0.0619	0.1436	0.0371	$^{+0.0073}_{-0.0081}$
10	0.118	2.74	2.4799	0.35	0.31	1.006	0.0918	0.2289	0.0399	$^{+0.0125}_{-0.0140}$
11	0.165	3.72	2.4458	0.36	0.31	1.010	0.1111	0.2744	0.0468	$^{+0.0143}_{-0.0160}$
12	0.238	5.23	2.3154	0.37	0.32	1.012	0.1162	0.2731	0.0596	$^{+0.0150}_{-0.0167}$
13	0.337	7.35	2.2154	0.37	0.33	1.019	0.3265	0.7373	0.1255	$^{+0.0390}_{-0.0434}$
14	0.445	9.88	2.0752	0.38	0.33	1.046	0.1850	0.4028	0.2520	$^{+0.0248}_{-0.0276}$

Table A.5: Born level asymmetries for pions on the proton target

bin	$< x >$	$< Q^2 >$	$\frac{1}{D(1+\eta\gamma)}$	$< z >$	$< p_{h\perp} >$	$C_\phi^{\pi^+}$	$A_{\parallel,p}^{\pi^+}$	$A_{1,p}^{\pi^+}$	$\pm$ stat.	syst.
1	0.014	0.55	1.2683	0.29	0.50	1.004	0.0139	0.0177	0.0512	$^{+0.0023}_{-0.0026}$
2	0.017	0.66	1.3915	0.31	0.49	1.009	0.0564	0.0792	0.0375	$^{+0.0037}_{-0.0041}$
3	0.021	0.78	1.4718	0.33	0.48	1.012	0.0683	0.1014	0.0611	$^{+0.0058}_{-0.0064}$
4	0.029	0.86	1.8360	0.39	0.45	1.021	0.0788	0.1482	0.0425	$^{+0.0067}_{-0.0073}$
5	0.046	0.92	2.8460	0.53	0.35	1.010	-0.0348	-0.1003	0.2031	$^{-0.0088}_{+0.0103}$
6	0.033	1.22	1.4293	0.32	0.48	1.011	0.0509	0.0738	0.0301	$^{+0.0034}_{-0.0045}$
7	0.047	1.50	1.7435	0.39	0.43	1.015	0.0610	0.1076	0.0357	$^{+0.0048}_{-0.0068}$
8	0.065	1.83	1.9435	0.43	0.40	1.009	0.0640	0.1250	0.0396	$^{+0.0051}_{-0.0083}$
9	0.087	2.27	2.0443	0.47	0.38	0.997	0.1056	0.2148	0.0463	$^{+0.0107}_{-0.0113}$
10	0.118	2.91	2.0743	0.49	0.36	0.982	0.1878	0.3817	0.0468	$^{+0.0199}_{-0.0226}$
11	0.166	3.92	2.0330	0.51	0.36	0.964	0.1376	0.2687	0.0537	$^{+0.0153}_{-0.0146}$
12	0.238	5.46	1.9890	0.52	0.36	0.939	0.1409	0.2632	0.0682	$^{+0.0153}_{-0.0169}$
13	0.338	7.57	1.9742	0.53	0.38	0.916	0.3078	0.5545	0.1412	$^{+0.0298}_{-0.0332}$
14	0.449	10.17	1.8830	0.53	0.38	0.930	0.5111	0.8929	0.2927	$^{+0.0495}_{-0.0552}$
bin	$< x >$	$< Q^2 >$	$\frac{1}{D(1+\eta\gamma)}$	$< z >$	$< p_{h\perp} >$	$C_\phi^{\pi^-}$	$A_{\parallel,p}^{\pi^-}$	$A_{1,p}^{\pi^-}$	$\pm$ stat.	syst.
1	0.014	0.55	1.2685	0.29	0.50	0.982	0.0524	0.0652	0.0531	$^{+0.0039}_{-0.0044}$
2	0.017	0.66	1.3897	0.31	0.50	0.984	0.0503	0.0687	0.0391	$^{+0.0031}_{-0.0034}$
3	0.021	0.78	1.4589	0.32	0.49	0.987	0.0456	0.0659	0.0649	$^{+0.0034}_{-0.0035}$
4	0.029	0.86	1.8354	0.39	0.45	0.997	0.0605	0.1107	0.0455	$^{+0.0053}_{-0.0052}$
5	0.045	0.92	2.8658	0.52	0.36	0.987	-0.0243	-0.0691	0.2323	$^{-0.0018}_{+0.0028}$
6	0.033	1.22	1.4333	0.32	0.48	0.983	0.0328	0.0459	0.0320	$^{+-0.0005}_{-0.0053}$
7	0.047	1.51	1.7187	0.38	0.44	0.990	0.0798	0.1356	0.0386	$^{+0.0056}_{-0.0103}$
8	0.064	1.85	1.9087	0.42	0.41	0.985	0.0275	0.0518	0.0437	$^{+0.0024}_{-0.0032}$
9	0.087	2.32	2.0289	0.45	0.39	0.978	0.0399	0.07911	0.0533	$^{+0.0035}_{-0.0051}$
10	0.118	3.00	2.0489	0.47	0.37	0.978	0.0648	0.1299	0.0564	$^{+0.0095}_{-0.0050}$
11	0.165	4.04	1.9976	0.49	0.37	0.987	0.0628	0.1244	0.0676	$^{+0.0067}_{-0.0079}$
12	0.238	5.62	1.9810	0.50	0.37	1.008	0.1753	0.3508	0.0935	$^{+0.0200}_{-0.0186}$
13	0.338	7.79	1.9854	0.50	0.38	1.051	0.2193	0.4566	0.2155	$^{+0.0235}_{-0.0264}$
14	0.448	10.28	1.9415	0.51	0.38	1.124	0.1639	0.3582	0.4697	$^{+0.0218}_{-0.0243}$

Table A.6: Born level asymmetries for hadrons on the deuteron target

bin	$< x >$	$< Q^2 >$	$\frac{1}{D(1+\eta\gamma)}$	$< z >$	$< p_{h\perp} >$	$C_\phi^{h^+}$	$A_{\parallel,d}^{h^+}$	$A_{1,d}^{h^+}$	$\pm$ stat.	syst.
1	0.011	0.55	1.0151	0.24	0.43	1.002	0.0118	0.0120	0.0154	$^{+0.0001}_{-0.0001}$
2	0.014	0.65	1.1066	0.25	0.41	1.005	-0.0067	-0.0075	0.0109	$^{-0.0002}_{+0.0001}$
3	0.017	0.77	1.1619	0.25	0.40	1.007	0.0040	0.0047	0.0176	$^{+0.0004}_{-0.0003}$
4	0.021	0.85	1.3850	0.28	0.36	1.010	0.0013	0.0018	0.0098	$^{+0.0001}_{-0.0001}$
5	0.028	0.92	1.7902	0.35	0.29	1.003	-0.0104	-0.0188	0.0331	$^{-0.0018}_{+0.0012}$
6	0.033	1.21	1.4573	0.26	0.40	1.007	-0.0019	-0.0028	0.0102	$^{+0.0004}_{-0.0003}$
7	0.048	1.46	1.8077	0.29	0.36	1.008	0.0086	0.0156	0.0114	$^{+0.0009}_{-0.0006}$
8	0.065	1.74	2.1170	0.32	0.33	1.004	0.0202	0.0429	0.0128	$^{+0.0025}_{-0.0016}$
9	0.087	2.09	2.3896	0.35	0.31	0.996	0.0256	0.0609	0.0157	$^{+0.0038}_{-0.0027}$
10	0.118	2.63	2.5582	0.36	0.30	0.984	0.0330	0.0830	0.0162	$^{+0.0053}_{-0.0037}$
11	0.165	3.57	2.5167	0.37	0.30	0.965	0.0486	0.1181	0.0182	$^{+0.0075}_{-0.0053}$
12	0.238	5.05	2.3949	0.37	0.31	0.936	0.0731	0.1637	0.0219	$^{+0.0106}_{-0.0074}$
13	0.338	7.16	2.2487	0.38	0.32	0.900	0.1116	0.2256	0.0443	$^{+0.0147}_{-0.0103}$
14	0.446	9.76	2.0758	0.38	0.32	0.889	0.1232	0.2273	0.0849	$^{+0.0175}_{-0.0123}$
bin	$< x >$	$< Q^2 >$	$\frac{1}{D(1+\eta\gamma)}$	$< z >$	$< p_{h\perp} >$	$C_\phi^{h^-}$	$A_{\parallel,d}^{h^-}$	$A_{1,d}^{h^-}$	$\pm$ stat.	syst.
1	0.012	0.55	1.1330	0.24	0.44	0.999	0.0017	0.0019	0.0161	$^{-0.0003}_{+0.0002}$
2	0.016	0.66	1.2454	0.25	0.42	1.001	0.0046	0.0057	0.0117	$^{+0.0001}_{-0.0001}$
3	0.019	0.77	1.3096	0.26	0.41	1.001	-0.0164	-0.0215	0.0193	$^{-0.0011}_{+0.0007}$
4	0.025	0.85	1.6004	0.29	0.37	1.004	0.0033	0.0053	0.0121	$^{+0.0005}_{-0.0004}$
5	0.034	0.92	2.1767	0.36	0.30	0.999	-0.0109	-0.0237	0.0470	$^{-0.0027}_{+0.0019}$
6	0.033	1.21	1.4485	0.26	0.41	0.998	-0.0060	-0.0086	0.0107	$^{+0.0004}_{-0.0003}$
7	0.047	1.47	1.7896	0.29	0.37	1.000	0.0064	0.0115	0.0125	$^{+0.0003}_{-0.0002}$
8	0.065	1.78	2.0822	0.32	0.34	0.999	0.0133	0.0277	0.0144	$^{+0.0021}_{-0.0015}$
9	0.087	2.17	2.3300	0.34	0.32	0.999	0.0136	0.0317	0.0179	$^{+0.0018}_{-0.0013}$
10	0.118	2.75	2.4891	0.35	0.31	1.006	0.0341	0.0854	0.0194	$^{+0.0048}_{-0.0033}$
11	0.165	3.73	2.4575	0.36	0.31	1.009	0.0419	0.1039	0.0232	$^{+0.0065}_{-0.0045}$
12	0.237	5.25	2.3420	0.37	0.31	1.008	0.0815	0.1925	0.0300	$^{+0.0125}_{-0.0088}$
13	0.337	7.36	2.2242	0.37	0.32	1.019	0.1347	0.3053	0.0663	$^{+0.0198}_{-0.0139}$
14	0.445	9.86	2.0664	0.38	0.33	1.061	0.1038	0.2277	0.1420	$^{+0.0181}_{-0.0127}$

Table A.7: Born level asymmetries for pions on the deuteron target

bin	$< x >$	$< Q^2 >$	$\frac{1}{D(1+\eta\gamma)}$	$< z >$	$< p_{h\perp} >$	$C_\phi^{\pi^+}$	$A_{\parallel,d}^{\pi^+}$	$A_{1,d}^{\pi^+}$	$\pm$ stat.	syst.
1	0.014	0.55	1.2731	0.24	0.43	1.003	0.0134	0.0171	0.0192	$^{+0.0006}_{-0.0004}$
2	0.018	0.66	1.4014	0.25	0.42	1.005	-0.0150	-0.0211	0.0139	$^{-0.0009}_{+0.0006}$
3	0.021	0.77	1.4834	0.26	0.41	1.007	0.0163	0.0244	0.0230	$^{+0.0013}_{-0.0009}$
4	0.029	0.85	1.8684	0.30	0.38	1.010	-0.0036	-0.0068	0.0150	$^{-0.0002}_{+0.0001}$
5	0.045	0.92	2.8759	0.40	0.32	1.000	0.0157	0.0451	0.0686	$^{-0.0002}_{+0.0001}$
6	0.033	1.21	1.4522	0.26	0.41	1.006	-0.0020	-0.0029	0.0113	$^{+0.0002}_{-0.0001}$
7	0.047	1.48	1.7774	0.30	0.37	1.007	0.0031	0.0056	0.0131	$^{+0.0002}_{-0.0003}$
8	0.065	1.80	2.0362	0.34	0.35	1.001	0.0145	0.0295	0.0148	$^{+0.0008}_{-0.0017}$
9	0.087	2.20	2.2354	0.37	0.33	0.990	0.0179	0.0397	0.0180	$^{-0.0000}_{-0.0026}$
10	0.118	2.79	2.3346	0.39	0.33	0.977	0.0456	0.1040	0.0186	$^{+0.0031}_{-0.0072}$
11	0.165	3.77	2.2970	0.40	0.33	0.964	0.0492	0.1089	0.0215	$^{+0.0032}_{-0.0078}$
12	0.238	5.28	2.2204	0.41	0.33	0.942	0.0773	0.1617	0.0270	$^{+0.0018}_{-0.0118}$
13	0.338	7.39	2.1440	0.42	0.34	0.912	0.1583	0.3095	0.0575	$^{+0.0047}_{-0.0196}$
14	0.446	9.92	2.0268	0.42	0.35	0.903	0.0803	0.1471	0.1156	$^{+0.0092}_{-0.0106}$
bin	$< x >$	$< Q^2 >$	$\frac{1}{D(1+\eta\gamma)}$	$< z >$	$< p_{h\perp} >$	$C_\phi^{\pi^-}$	$A_{\parallel,d}^{\pi^-}$	$A_{1,d}^{\pi^-}$	$\pm$ stat.	syst.
1	0.014	0.55	1.2721	0.23	0.43	0.996	-0.0021	-0.0027	0.0194	$^{-0.0007}_{+0.0005}$
2	0.018	0.66	1.3997	0.24	0.41	0.998	0.0016	0.0023	0.0141	$^{-0.0002}_{+0.0001}$
3	0.021	0.77	1.4816	0.25	0.41	0.999	-0.0121	-0.0179	0.0236	$^{-0.0009}_{+0.0006}$
4	0.029	0.85	1.8637	0.29	0.37	1.003	0.0033	0.0062	0.0155	$^{+0.0004}_{-0.0003}$
5	0.045	0.92	2.8785	0.39	0.32	0.995	-0.0283	-0.0809	0.0722	$^{-0.0049}_{+0.0035}$
6	0.033	1.21	1.4465	0.25	0.41	0.995	-0.0028	-0.0040	0.0116	$^{+0.0006}_{-0.0004}$
7	0.047	1.48	1.7715	0.29	0.37	0.997	0.0036	0.0063	0.0136	$^{+0.0001}_{-0.0000}$
8	0.064	1.81	2.0304	0.32	0.35	0.994	0.0092	0.0185	0.0156	$^{+0.0016}_{-0.0011}$
9	0.087	2.23	2.2254	0.35	0.33	0.991	0.0175	0.0387	0.0192	$^{+0.0024}_{-0.0013}$
10	0.118	2.84	2.3410	0.37	0.32	0.995	0.0341	0.0794	0.0208	$^{+0.0052}_{-0.0029}$
11	0.165	3.84	2.3171	0.38	0.32	1.003	0.0460	0.1068	0.0251	$^{+0.0066}_{-0.0036}$
12	0.238	5.37	2.2373	0.39	0.33	1.014	0.0863	0.1958	0.0333	$^{+0.0135}_{-0.0079}$
13	0.337	7.49	2.1575	0.39	0.34	1.052	0.1439	0.3267	0.0765	$^{+0.0219}_{-0.0140}$
14	0.445	9.97	2.0390	0.40	0.34	1.141	0.0362	0.0844	0.1701	$^{+0.0097}_{-0.0064}$

Table A.8: Born level asymmetries for kaons on the deuteron target

bin	$< x >$	$< Q^2 >$	$\frac{1}{D(1+\eta\gamma)}$	$< z >$	$< p_{h\perp} >$	$C_\phi^{K^+}$	$A_{\|\|,d}^{K^+}$	$A_{1,d}^{K^+}$	$\pm$ stat.	syst.
1	0.014	0.55	1.2736	0.29	0.48	1.005	-0.0214	-0.0274	0.0666	$^{-0.0003}_{+0.0002}$
2	0.018	0.65	1.4050	0.31	0.47	1.014	0.0778	0.1109	0.0463	$^{+0.0046}_{-0.0032}$
3	0.022	0.77	1.4996	0.32	0.46	1.017	-0.0788	-0.1203	0.0764	$^{-0.0038}_{+0.0027}$
4	0.029	0.85	1.8984	0.37	0.40	1.030	0.0287	0.0561	0.0476	$^{+0.0032}_{-0.0023}$
5	0.046	0.92	2.8805	0.46	0.32	1.019	0.0047	0.0137	0.1981	$^{-0.0006}_{+0.0004}$
6	0.033	1.21	1.4651	0.32	0.45	1.014	-0.0068	-0.0100	0.0368	$^{+0.0011}_{-0.0008}$
7	0.048	1.46	1.8100	0.37	0.40	1.022	0.0482	0.0891	0.0406	$^{+0.0045}_{-0.0038}$
8	0.065	1.74	2.0858	0.41	0.36	1.014	0.0556	0.1176	0.0441	$^{+0.0062}_{-0.0073}$
9	0.087	2.12	2.2787	0.44	0.34	0.997	0.0468	0.1063	0.0522	$^{+0.0031}_{-0.0079}$
10	0.118	2.70	2.3365	0.46	0.33	0.977	0.0257	0.0586	0.0516	$^{+0.0006}_{-0.0062}$
11	0.166	3.68	2.2756	0.48	0.33	0.948	0.0847	0.1827	0.0567	$^{+0.0008}_{-0.0210}$
12	0.238	5.23	2.1987	0.48	0.33	0.910	0.1032	0.2065	0.0691	$^{+0.0011}_{-0.0215}$
13	0.338	7.42	2.0996	0.50	0.35	0.878	0.0418	0.0771	0.1486	$^{+0.0007}_{-0.0072}$
14	0.445	10.07	2.0224	0.51	0.35	0.890	0.6123	1.1023	0.2973	$^{+0.0544}_{-0.0631}$
bin	$< x >$	$< Q^2 >$	$\frac{1}{D(1+\eta\gamma)}$	$< z >$	$< p_{h\perp} >$	$C_\phi^{K^-}$	$A_{\|\|,d}^{K^-}$	$A_{1,d}^{K^-}$	$\pm$ stat.	syst.
1	0.014	0.55	1.2724	0.28	0.49	0.991	0.0430	0.0543	0.0780	$^{+0.0026}_{-0.0018}$
2	0.018	0.66	1.2992	0.30	0.47	0.989	0.0214	0.0296	0.0564	$^{+0.0023}_{-0.0016}$
3	0.022	0.77	1.4888	0.31	0.46	0.994	-0.0829	-0.1227	0.0924	$^{-0.0043}_{+0.0030}$
4	0.029	0.85	1.8687	0.35	0.41	1.002	-0.0363	-0.0679	0.0595	$^{-0.0027}_{+0.0019}$
5	0.045	0.92	2.8683	0.44	0.33	0.982	-0.0052	-0.0146	0.2745	$^{+0.0008}_{-0.0006}$
6	0.033	1.21	1.4523	0.31	0.46	0.990	-0.0064	-0.0092	0.0449	$^{-0.0001}_{+0.0001}$
7	0.047	1.47	1.7796	0.35	0.41	0.995	0.0511	0.0905	0.0519	$^{+0.0027}_{-0.0037}$
8	0.064	1.78	2.0322	0.38	0.37	0.988	-0.0149	-0.0299	0.0583	$^{-0.0004}_{+0.0011}$
9	0.087	2.20	2.1983	0.41	0.36	0.995	-0.0027	-0.0060	0.0713	$^{-0.0003}_{+0.0007}$
10	0.116	2.83	2.2665	0.43	0.34	1.027	-0.0015	-0.0034	0.0772	$^{-0.0002}_{+0.0005}$
11	0.165	3.86	2.2333	0.43	0.34	1.068	0.0789	0.1883	0.0986	$^{+0.0011}_{-0.0213}$
12	0.236	5.44	2.1686	0.44	0.35	1.081	0.0753	0.1767	0.1363	$^{+0.0032}_{-0.0176}$
13	0.336	7.63	2.1061	0.44	0.35	1.020	0.1485	0.3191	0.3074	$^{+0.0084}_{-0.0250}$
14	0.444	10.01	1.9926	0.46	0.37	0.747	0.7149	1.0635	0.4754	$^{+0.0403}_{-0.0706}$

Appendix B

Results: Asymmetries $A_1(x, p_{h\perp})$

In this section, the final asymmetries as a function $p_{h\perp}$ in three x bins are tabulated. Table B.1 defines the bin numbers and bin edges for x and $p_{h\perp}$. Listed are the combined asymmetries of the 1996-1997 data-taking perionds for the proton target, and 1998-2000 data-taking periods for deuteron target.

Table B.1: 2-Dimensional $x - p_{h\perp}$ binning.

x Bin number	x range
1	0.023-0.055
2	0.055-0.010
3	0.100-0.600
$p_{h\perp}$ Bin number	$p_{h\perp}$ range (GeV)
1	0.00-0.15
2	0.15-0.30
3	0.30-0.40
4	0.40-0.50
5	0.50-0.60
6	0.60-2.0

Table B.2: Semi-Inclusive Born level asymmetries for positive and negative pions on the proton target

bin	$< x >$	$< Q^2 >$	$\frac{1}{D(1+\eta\gamma)}$	$< z >$	$< p_{h\perp} >$	$C_\phi^{\pi^+}$	$A_{\parallel,p}^{\pi^+}$	$A_{1,p}^{\pi^+}$	$\pm$ stat.	syst.
1	0.045	1.30	1.8728	0.39	0.10	1.009	0.1801	0.3405	0.1262	$^{+0.0172}_{-0.0192}$
2	0.042	1.35	1.6707	0.36	0.23	1.018	0.0555	0.0944	0.0581	$^{+0.0052}_{-0.0058}$
3	0.041	1.37	1.5917	0.35	0.35	1.019	0.0196	0.0318	0.0568	$^{+0.0016}_{-0.0018}$
4	0.040	1.38	1.5646	0.34	0.45	1.018	0.0430	0.0684	0.0548	$^{+0.0034}_{-0.0037}$
5	0.040	1.38	1.5438	0.35	0.55	1.016	0.0128	0.0201	0.0590	$^{+0.0009}_{-0.0010}$
6	0.040	1.39	1.5314	0.38	0.76	1.001	0.0905	0.1387	0.0395	$^{+0.0071}_{-0.0079}$
7	0.076	1.85	2.2486	0.47	0.10	1.001	0.0652	0.1467	0.1068	$^{+0.0063}_{-0.0070}$
8	0.076	1.93	2.1275	0.46	0.23	1.004	0.0970	0.2072	0.0644	$^{+0.0096}_{-0.0107}$
9	0.076	2.03	2.0093	0.45	0.35	1.009	0.0663	0.1345	0.0738	$^{+0.0056}_{-0.0063}$
10	0.075	2.12	1.9051	0.43	0.45	1.013	0.0811	0.1565	0.0751	$^{+0.0079}_{-0.0088}$
11	0.074	2.16	1.8431	0.43	0.55	1.013	0.1043	0.1946	0.0844	$^{+0.0095}_{-0.0106}$
12	0.074	2.21	1.8134	0.43	0.75	0.980	0.1055	0.1876	0.0532	$^{+0.0096}_{-0.0107}$
13	0.165	3.90	2.1093	0.49	0.10	0.999	0.1766	0.3721	0.0982	$^{+0.0200}_{-0.0223}$
14	0.166	3.89	2.0799	0.50	0.23	0.989	0.1496	0.3076	0.0638	$^{+0.0164}_{-0.0183}$
15	0.168	3.92	2.0749	0.51	0.35	0.972	0.2063	0.4159	0.0839	$^{+0.0228}_{-0.0255}$
16	0.169	3.96	2.0448	0.51	0.45	0.952	0.1256	0.2445	0.0915	$^{+0.0139}_{-0.0155}$
17	0.170	4.02	1.9755	0.51	0.55	0.936	0.2083	0.3853	0.1011	$^{+0.0208}_{-0.0232}$
18	0.167	4.14	1.9168	0.50	0.74	0.897	0.1552	0.2668	0.0606	$^{+0.0153}_{-0.0170}$
bin	$< x >$	$< Q^2 >$	$\frac{1}{D(1+\eta\gamma)}$	$< z >$	$< p_{h\perp} >$	$C_\phi^{\pi^-}$	$A_{\parallel,p}^{\pi^-}$	$A_{1,p}^{\pi^-}$	$\pm$ stat.	syst.
1	0.045	1.31	1.8698	0.38	0.10	0.981	0.1311	0.2405	0.1377	$^{+0.0116}_{-0.0130}$
2	0.042	1.36	1.6537	0.35	0.23	0.972	0.0989	0.1591	0.0594	$^{+0.0083}_{-0.0092}$
3	0.040	1.37	1.5832	0.34	0.35	0.982	0.0211	0.0327	0.0598	$^{+0.0027}_{-0.0030}$
4	0.040	1.38	1.5375	0.33	0.45	0.993	0.0645	0.0984	0.0577	$^{+0.0051}_{-0.0057}$
5	0.040	1.38	1.5251	0.34	0.55	1.000	0.0005	0.0008	0.0640	$^{+0.0003}_{-0.0003}$
6	0.040	1.39	1.5102	0.37	0.76	0.990	0.0755	0.1129	0.0439	$^{+0.0058}_{-0.0064}$
7	0.076	1.88	2.2374	0.46	0.10	0.993	0.0615	0.1367	0.1188	$^{+0.0057}_{-0.0063}$
8	0.075	1.96	2.1211	0.45	0.23	0.984	0.0255	0.0531	0.0718	$^{+0.0013}_{-0.0015}$
9	0.075	2.05	1.9889	0.43	0.35	0.982	-0.0051	-0.0100	0.0837	$^{-0.0005}_{+0.0005}$
10	0.074	2.14	1.8844	0.42	0.45	0.982	0.0826	0.1529	0.0846	$^{+0.0081}_{-0.0090}$
11	0.074	2.18	1.7992	0.41	0.55	0.984	-0.0085	-0.0151	0.0937	$^{+0.0001}_{-0.0001}$
12	0.074	2.22	1.7667	0.42	0.76	0.967	0.0463	0.0790	0.0600	$^{+0.0044}_{-0.0049}$
13	0.163	3.96	2.0824	0.47	0.10	0.998	0.0664	0.1380	0.1166	$^{+0.0071}_{-0.0079}$
14	0.164	3.94	2.0915	0.48	0.23	0.996	0.0578	0.1204	0.0796	$^{+0.0060}_{-0.0067}$
15	0.164	3.96	2.0439	0.49	0.35	0.997	0.0813	0.1656	0.1025	$^{+0.0106}_{-0.0119}$
16	0.165	4.01	2.0267	0.49	0.45	0.994	0.0910	0.1834	0.1148	$^{+0.0095}_{-0.0106}$
17	0.165	4.08	1.9568	0.49	0.55	0.990	0.0908	0.1759	0.1306	$^{+0.0093}_{-0.0104}$
18	0.162	4.17	1.8853	0.48	0.75	0.961	0.1604	0.2906	0.0798	$^{+0.0164}_{-0.0182}$

Table B.3: Semi-Inclusive Born level asymmetries for positive and negative pions on the deuteron target

bin	$< x >$	$< Q^2 >$	$\frac{1}{D(1+\eta\gamma)}$	$< z >$	$< p_{h\perp} >$	$C_\phi^{\pi^+}$	$A_{\parallel,d}^{\pi^+}$	$A_{1,d}^{\pi^+}$	$\pm$ stat.	syst.
1	0.044	1.31	1.8283	0.25	0.10	1.020	-0.0267	-0.0499	0.0340	$^{-0.0020}_{+0.0014}$
2	0.041	1.35	1.6636	0.24	0.23	1.012	0.0102	0.0171	0.0165	$^{+0.0009}_{-0.0006}$
3	0.041	1.36	1.6171	0.26	0.35	1.007	-0.0009	-0.0015	0.0189	$^{-0.0003}_{+0.0002}$
4	0.041	1.37	1.5945	0.28	0.45	1.006	0.0164	0.0262	0.0213	$^{+0.0015}_{-0.0011}$
5	0.040	1.37	1.5768	0.31	0.55	1.005	-0.0074	-0.0117	0.0257	$^{+0.0005}_{-0.0004}$
6	0.040	1.38	1.5487	0.37	0.75	0.993	-0.0090	-0.0138	0.0191	$^{-0.0005}_{+0.0004}$
7	0.076	1.83	2.3728	0.33	0.10	1.006	0.0101	0.0242	0.0308	$^{+0.0007}_{-0.0005}$
8	0.076	1.94	2.1867	0.34	0.23	1.002	0.0017	0.0038	0.0203	$^{+0.0003}_{-0.0002}$
9	0.075	2.02	2.0753	0.34	0.35	0.997	0.0260	0.0536	0.0255	$^{+0.0033}_{-0.0023}$
10	0.075	2.05	2.0586	0.35	0.45	0.996	-0.0015	-0.0030	0.0295	$^{-0.0003}_{+0.0002}$
11	0.075	2.08	2.0311	0.37	0.55	0.992	0.0364	0.0725	0.0364	$^{+0.0046}_{-0.0032}$
12	0.074	2.15	1.9316	0.41	0.74	0.960	0.0578	0.1060	0.0255	$^{+0.0057}_{-0.0040}$
13	0.160	3.72	2.2820	0.35	0.10	1.002	0.0793	0.1816	0.0290	$^{+0.0105}_{-0.0074}$
14	0.164	3.71	2.3388	0.38	0.23	0.989	0.0457	0.1057	0.0221	$^{+0.0072}_{-0.0051}$
15	0.165	3.73	2.3187	0.41	0.35	0.965	0.0638	0.1424	0.0322	$^{+0.0086}_{-0.0061}$
16	0.165	3.75	2.2961	0.42	0.45	0.942	0.0660	0.1417	0.0377	$^{+0.0086}_{-0.0061}$
17	0.166	3.76	2.3100	0.44	0.55	0.922	-0.0129	-0.0270	0.0465	$^{-0.0009}_{+0.0007}$
18	0.164	3.87	2.2399	0.46	0.73	0.862	0.0795	0.1490	0.0301	$^{+0.0099}_{-0.0069}$
bin	$< x >$	$< Q^2 >$	$\frac{1}{D(1+\eta\gamma)}$	$< z >$	$< p_{h\perp} >$	$C_\phi^{\pi^-}$	$A_{\parallel,d}^{\pi^-}$	$A_{1,d}^{\pi^-}$	$\pm$ stat.	syst.
1	0.043	1.314	1.8179	0.24	0.10	1.000	0.0071	0.0129	0.0342	$^{+0.0010}_{-0.0007}$
2	0.041	1.348	1.6553	0.24	0.23	0.995	-0.0043	-0.0070	0.0168	$^{+0.0002}_{-0.0002}$
3	0.041	1.359	1.6068	0.25	0.35	0.997	-0.0093	-0.0150	0.0194	$^{-0.0009}_{+0.0006}$
4	0.040	1.365	1.5971	0.28	0.45	0.999	0.0198	0.0313	0.0219	$^{+0.0020}_{-0.0014}$
5	0.040	1.370	1.5651	0.31	0.55	1.000	0.0185	0.0289	0.0268	$^{+0.0016}_{-0.0021}$
6	0.040	1.382	1.5329	0.36	0.75	0.991	-0.0124	-0.0188	0.0200	$^{-0.0012}_{+0.0008}$
7	0.076	1.851	2.3703	0.32	0.10	1.003	0.0122	0.0290	0.0324	$^{+0.0017}_{-0.0012}$
8	0.075	1.966	2.1778	0.32	0.23	0.997	0.0094	0.0205	0.0213	$^{+0.0009}_{-0.0006}$
9	0.075	2.038	2.0561	0.33	0.35	0.991	0.0267	0.0544	0.0269	$^{+0.0034}_{-0.0024}$
10	0.074	2.058	2.0303	0.34	0.45	0.992	0.0111	0.0222	0.0311	$^{+0.0027}_{-0.0019}$
11	0.074	2.095	2.0003	0.36	0.55	0.991	0.0079	0.0157	0.0388	$^{-0.0002}_{+0.0002}$
12	0.074	2.159	1.9063	0.40	0.74	0.972	0.0112	0.0207	0.0280	$^{+0.0007}_{-0.0005}$
13	0.158	3.735	2.2976	0.33	0.10	1.011	0.0125	0.0292	0.0322	$^{+0.0032}_{-0.0022}$
14	0.161	3.726	2.3479	0.36	0.22	1.016	0.0474	0.1132	0.0250	$^{+0.0069}_{-0.0048}$
15	0.163	3.751	2.3138	0.39	0.35	1.006	0.0388	0.0902	0.0369	$^{+0.0065}_{-0.0046}$
16	0.163	3.780	2.2928	0.40	0.45	0.998	0.1028	0.2341	0.0435	$^{+0.0126}_{-0.0089}$
17	0.162	3.791	2.3143	0.42	0.55	0.991	0.0742	0.1694	0.0547	$^{+0.0113}_{-0.0080}$
18	0.161	3.897	2.2354	0.44	0.74	0.961	0.0562	0.1198	0.0377	$^{+0.0075}_{-0.0053}$

Table B.4: Semi-Inclusive Born level asymmetries for positive and negative kaons on the deuteron target

bin	$< x >$	$< Q^2 >$	$\frac{1}{D(1+\eta\gamma)}$	$< z >$	$< p_{h\perp} >$	$C_\phi^{K^+}$	$A_{\|\|,d}^{K^+}$	$A_{1,d}^{K^+}$	$\pm$ stat.	syst.
1	0.045	1.29	1.9419	0.33	0.10	1.025	-0.0218	-0.0434	0.1238	$^{-0.0011}_{+0.0008}$
2	0.042	1.33	1.7496	0.33	0.23	1.033	0.0100	0.0180	0.0635	$^{+0.0010}_{-0.0007}$
3	0.041	1.35	1.6608	0.33	0.35	1.033	0.0210	0.0360	0.0692	$^{+0.0030}_{-0.0021}$
4	0.041	1.36	1.6335	0.34	0.45	1.030	-0.0065	-0.0110	0.0731	$^{-0.0008}_{+0.0005}$
5	0.041	1.37	1.5977	0.36	0.55	1.018	-0.0139	-0.0226	0.0771	$^{-0.0001}_{+0.0001}$
6	0.040	1.38	1.5574	0.40	0.76	0.975	0.0893	0.1356	0.0453	$^{+0.0096}_{-0.0068}$
7	0.077	1.78	2.4451	0.40	0.10	1.000	0.0735	0.1798	0.0940	$^{+0.0096}_{-0.0067}$
8	0.076	1.85	2.2843	0.42	0.23	1.005	0.0486	0.1115	0.0648	$^{+0.0078}_{-0.0055}$
9	0.076	1.94	2.1383	0.43	0.35	1.017	0.0843	0.1833	0.0847	$^{+0.0105}_{-0.0074}$
10	0.075	2.00	2.0982	0.43	0.45	1.024	-0.0056	-0.0121	0.0921	$^{-0.0014}_{+0.0010}$
11	0.074	2.04	2.0704	0.43	0.55	1.022	0.1126	0.2384	0.1065	$^{+0.0140}_{-0.0098}$
12	0.074	2.15	1.9352	0.45	0.75	0.960	0.0033	0.0061	0.0605	$^{+0.0012}_{-0.0009}$
13	0.160	3.62	2.3106	0.42	0.10	0.993	0.1401	0.3215	0.0858	$^{+0.0178}_{-0.0125}$
14	0.163	3.61	2.3418	0.46	0.23	0.977	0.0360	0.0824	0.0650	$^{+0.0070}_{-0.0049}$
15	0.165	3.63	2.3043	0.49	0.35	0.948	0.0805	0.1759	0.0937	$^{+0.0109}_{-0.0077}$
16	0.166	3.68	2.2746	0.50	0.45	0.933	-0.0150	-0.0318	0.1065	$^{+0.0001}_{-0.0001}$
17	0.167	3.81	2.2428	0.50	0.55	0.913	0.0922	0.1889	0.1238	$^{+0.0126}_{-0.0088}$
18	0.164	3.95	2.1387	0.51	0.73	0.853	0.0887	0.1620	0.0687	$^{+0.0080}_{-0.0057}$
bin	$< x >$	$< Q^2 >$	$\frac{1}{D(1+\eta\gamma)}$	$< z >$	$< p_{h\perp} >$	$C_\phi^{K^-}$	$A_{\|\|,d}^{K^-}$	$A_{1,d}^{K^-}$	$\pm$ stat.	syst.
1	0.044	1.29	1.9117	0.31	0.10	1.012	-0.0231	-0.0448	0.1512	$^{-0.0025}_{+0.0018}$
2	0.042	1.33	1.7223	0.31	0.23	1.010	0.0204	0.0355	0.0766	$^{+0.0023}_{-0.0016}$
3	0.041	1.35	1.6272	0.31	0.35	1.007	-0.0127	-0.0207	0.0841	$^{-0.0025}_{+0.0017}$
4	0.041	1.36	1.5803	0.32	0.45	0.995	0.0753	0.1184	0.0866	$^{+0.0044}_{-0.0031}$
5	0.040	1.37	1.5519	0.34	0.55	0.979	0.0476	0.0722	0.0963	$^{+0.0036}_{-0.0025}$
6	0.040	1.38	1.5174	0.39	0.76	0.961	0.0277	0.0404	0.0590	$^{+0.0027}_{-0.0019}$
7	0.076	1.80	2.3762	0.37	0.10	1.007	-0.0483	-0.1155	0.1215	$^{-0.0053}_{+0.0037}$
8	0.075	1.89	2.2162	0.39	0.22	1.014	-0.0099 -	0.0223	0.0877	$^{+0.0007}_{-0.0005}$
9	0.074	2.00	2.0884	0.39	0.35	0.996	0.0033	0.0068	0.1153	$^{-0.0041}_{+0.0029}$
10	0.074	2.05	2.0006	0.39	0.45	0.978	0.0928	0.1816	0.1192	$^{+0.0107}_{-0.0075}$
11	0.074	2.08	1.9512	0.40	0.55	0.961	-0.0025	-0.0047	0.1349	$^{+0.0030}_{-0.0022}$
12	0.074	2.16	1.8284	0.43	0.76	0.956	-0.0868	-0.1518	0.0840	$^{-0.0085}_{+0.0060}$
13	0.153	3.58	2.2882	0.38	0.10	1.005	-0.0024	-0.0054	0.1203	$^{+0.0012}_{-0.0008}$
14	0.155	3.59	2.2969	0.42	0.23	1.025	0.0553	0.1303	0.0997	$^{+0.0085}_{-0.0060}$
15	0.157	3.66	2.2819	0.45	0.35	1.046	-0.0263	-0.0627	0.1558	$^{-0.0034}_{+0.0024}$
16	0.157	3.71	2.2111	0.46	0.45	1.059	0.1608	0.3765	0.1837	$^{+0.0246}_{-0.0173}$
17	0.157	3.77	2.1448	0.46	0.55	1.079	-0.0746	-0.1730	0.2145	$^{-0.0096}_{+0.0068}$
18	0.156	3.90	2.0366	0.46	0.75	1.125	0.1583	0.3626	0.1335	$^{+0.0207}_{-0.0146}$

Appendix C

Results: Asymmetries $A_1(x, z, p_{h\perp})$

In this section, the final asymmetries as a function of x in three $p_{h\perp}$ and in three z bins are tabulated. Table C.1 defines the bin numbers and bin edges for z and $p_{h\perp}$. Listed are the combined asymmetries of the 1996-1997 data-taking periods for the proton target, and 1998-2000 data-taking periods for deuteron target. Values of asymmetries and average kinematic variables ordered in groups by horizontal lines according to the different x bins.

Table C.1: The bin edges for z and $p_{h\perp}$ added to form a 3D binning

z Bin number	z range
1	0.10-0.35
2	0.35-0.50
3	0.50-0.80
$p_{h\perp} Binnumber$	$p_{h\perp}$ range (GeV)
1	0.00-0.30
2	0.30-0.50
3	0.50-2.00

Table C.2: Born level asymmetry for positive pions on the proton target

bin	$< x >$	$< Q^2 >$	$\frac{1}{D(1+\eta\gamma)}$	$< z >$	$< p_{h\perp} >$	$C_{\phi}^{\pi^+}$	$A_{\parallel,p}^{\pi^+}$	$A_{1,p}^{\pi^+}$	$\pm$ stat.	syst.
1	0.033	1.22	1.4229	0.26	0.22	1.014	0.0424	0.0611	0.0900	$^{+0.0019}_{-0.0022}$
2	0.033	1.23	1.3754	0.25	0.40	1.004	0.0541	0.0747	0.0595	$^{+0.0042}_{-0.0046}$
3	0.033	1.24	1.3627	0.27	0.65	0.996	0.0457	0.0621	0.0596	$^{+0.0034}_{-0.0038}$
4	0.035	1.17	1.5973	0.41	0.22	1.024	0.1058	0.1730	0.2032	$^{+0.0072}_{-0.0081}$
5	0.034	1.20	1.4998	0.41	0.40	1.025	0.0658	0.1012	0.1234	$^{+0.0046}_{-0.0052}$
6	0.033	1.21	1.4434	0.41	0.71	1.005	0.0943	0.1367	0.0861	$^{+0.0081}_{-0.0091}$
7	0.036	1.14	1.6946	0.59	0.21	1.063	-0.0316	-0.0569	0.3048	$^{-0.0034}_{+0.0037}$
8	0.034	1.17	1.5868	0.59	0.40	1.066	0.0078	0.0132	0.1889	$^{+0.0009}_{-0.0010}$
9	0.034	1.19	1.5129	0.59	0.74	1.058	-0.0101	-0.0162	0.1269	$^{+0.0014}_{-0.0016}$
10	0.047	1.58	1.5793	0.28	0.20	1.013	0.0990	0.1584	0.1032	$^{+0.0104}_{-0.0116}$
11	0.047	1.65	1.4928	0.27	0.40	1.008	0.1059	0.1593	0.0810	$^{+0.0070}_{-0.0078}$
12	0.047	1.67	1.4646	0.28	0.65	0.990	0.0959	0.1391	0.0785	$^{+0.0062}_{-0.0069}$
13	0.048	1.32	2.0167	0.42	0.19	1.011	0.1239	0.2527	0.1572	$^{+0.0133}_{-0.0148}$
14	0.048	1.40	1.8673	0.41	0.40	1.029	-0.0832	-0.1598	0.1356	$^{-0.0062}_{+0.0069}$
15	0.047	1.49	1.7241	0.41	0.69	0.999	0.0584	0.1007	0.1044	$^{+0.0037}_{-0.0042}$
16	0.049	1.26	2.1405	0.61	0.19	1.019	0.0470	0.1025	0.1946	$^{+0.0061}_{-0.0068}$
17	0.048	1.32	2.0356	0.61	0.40	1.060	-0.0570	-0.1231	0.1750	$^{-0.0064}_{+0.0072}$
18	0.048	1.39	1.8612	0.60	0.71	1.070	0.0919	0.1831	0.1305	$^{+0.0109}_{-0.0122}$
19	0.064	2.12	1.5856	0.28	0.20	1.014	0.2543	0.4088	0.1098	$^{+0.0199}_{-0.0222}$
20	0.064	2.23	1.4879	0.27	0.40	1.011	0.0290	0.0436	0.0889	$^{+0.0018}_{-0.0020}$
21	0.064	2.25	1.4514	0.28	0.65	0.987	-0.0184	-0.0264	0.0894	$^{-0.0014}_{+0.0016}$
22	0.065	1.62	2.1910	0.42	0.19	1.006	0.1429	0.3151	0.1496	$^{+0.0130}_{-0.0145}$
23	0.064	1.76	1.9856	0.42	0.39	1.023	0.0300	0.0610	0.1425	$^{+0.0024}_{-0.0027}$
24	0.064	1.89	1.8070	0.42	0.69	0.986	0.0602	0.1072	0.1154	$^{+0.0069}_{-0.0077}$
25	0.065	1.43	2.5731	0.62	0.19	1.003	0.0143	0.0369	0.1751	$^{+0.0036}_{-0.0040}$
26	0.065	1.52	2.3938	0.62	0.39	1.027	0.0693	0.1703	0.1744	$^{+0.0110}_{-0.0123}$
27	0.065	1.66	2.0906	0.62	0.68	1.034	0.0302	0.0652	0.1396	$^{+0.0044}_{-0.0049}$
28	0.087	2.80	1.5555	0.28	0.19	1.013	0.0324	0.0510	0.1195	$^{+0.0019}_{-0.0021}$
29	0.086	2.94	1.4748	0.28	0.40	1.015	0.1309	0.1959	0.1074	$^{+0.0092}_{-0.0102}$
30	0.086	2.99	1.4499	0.28	0.65	0.983	0.1633	0.2327	0.1112	$^{+0.0119}_{-0.0132}$
31	0.087	2.14	2.1368	0.43	0.18	1.004	0.0481	0.1031	0.1541	$^{+0.0051}_{-0.0056}$
32	0.087	2.31	1.9731	0.42	0.39	1.019	0.1013	0.2036	0.1612	$^{+0.0109}_{-0.0121}$
33	0.086	2.49	1.7972	0.42	0.68	0.984	0.0841	0.1488	0.1346	$^{+0.0074}_{-0.0083}$
34	0.087	1.73	2.7702	0.62	0.19	0.987	0.0153	0.0419	0.1894	$^{+0.0025}_{-0.0028}$
35	0.087	1.82	2.5926	0.63	0.39	0.980	0.0862	0.2188	0.1865	$^{+0.0092}_{-0.0102}$
36	0.087	2.01	2.2726	0.63	0.67	0.993	0.3138	0.7083	0.1634	$^{+0.0349}_{-0.0389}$
37	0.118	3.71	1.5541	0.29	0.19	1.012	0.2374	0.3733	0.1230	$^{+0.0180}_{-0.0201}$
38	0.117	3.89	1.4729	0.28	0.39	1.017	0.2655	0.3977	0.1238	$^{+0.0214}_{-0.0239}$
39	0.117	3.94	1.4466	0.28	0.65	0.975	0.3056	0.4310	0.1276	$^{+0.0221}_{-0.0246}$

Table C.2: - continued

bin	$< x >$	$< Q^2 >$	$\frac{1}{D(1+\eta\gamma)}$	$< z >$	$< p_{h\perp} >$	$C_{\phi}^{\pi^+}$	$A_{\parallel,p}^{\pi^+}$	$A_{1,p}^{\pi^+}$	$\pm$ stat.	syst.
40	0.118	2.89	2.0815	0.43	0.18	1.001	0.2029	0.4228	0.1432	$^{+0.0216}_{-0.0241}$
41	0.118	3.07	1.9431	0.42	0.39	1.010	0.0611	0.1199	0.1603	$^{+0.0063}_{-0.0070}$
42	0.118	3.31	1.7725	0.42	0.68	0.975	0.1550	0.2679	0.1446	$^{+0.0137}_{-0.0153}$
43	0.118	2.30	2.6958	0.63	0.19	0.979	0.1797	0.4740	0.1763	$^{+0.0257}_{-0.0286}$
44	0.118	2.31	2.6296	0.64	0.39	0.947	0.2209	0.5498	0.1785	$^{+0.0292}_{-0.0325}$
45	0.118	2.56	2.2858	0.64	0.66	0.941	0.1065	0.2291	0.1553	$^{+0.0143}_{-0.0160}$
46	0.165	5.00	1.5638	0.30	0.19	1.007	0.1536	0.2420	0.1502	$^{+0.0133}_{-0.0148}$
47	0.164	5.20	1.5004	0.30	0.39	1.013	0.0483	0.0735	0.1630	$^{+0.0055}_{-0.0061}$
48	0.163	5.29	1.4642	0.29	0.65	0.955	0.1237	0.1729	0.1749	$^{+0.0087}_{-0.0097}$
49	0.166	4.03	1.9879	0.43	0.19	0.998	0.0484	0.0959	0.1587	$^{+0.0042}_{-0.0047}$
50	0.166	4.21	1.9097	0.43	0.39	0.993	0.1923	0.3646	0.1801	$^{+0.0158}_{-0.0176}$
51	0.165	4.45	1.7731	0.42	0.67	0.955	0.0988	0.1672	0.1704	$^{+0.0115}_{-0.0128}$
52	0.165	3.29	2.5000	0.63	0.19	0.978	0.0893	0.2184	0.1998	$^{+0.0112}_{-0.0124}$
53	0.166	3.24	2.4985	0.64	0.39	0.924	0.2372	0.5474	0.2002	$^{+0.0297}_{-0.0331}$
54	0.166	3.39	2.2672	0.65	0.64	0.873	0.2058	0.4074	0.1737	$^{+0.0223}_{-0.0248}$
55	0.237	6.86	1.5620	0.30	0.18	1.002	-0.0009	-0.0013	0.2211	$^{+0.0010}_{-0.0011}$
56	0.236	7.01	1.5246	0.30	0.39	0.995	0.3882	0.5890	0.2526	$^{+0.0318}_{-0.0355}$
57	0.234	7.07	1.4740	0.30	0.65	0.918	0.1258	0.1702	0.2750	$^{+0.0102}_{-0.0114}$
58	0.239	5.74	1.9152	0.42	0.19	0.993	0.1403	0.2669	0.1969	$^{+0.0137}_{-0.0153}$
59	0.239	5.81	1.8982	0.43	0.39	0.962	0.1747	0.3182	0.2242	$^{+0.0178}_{-0.0198}$
60	0.239	5.98	1.8260	0.43	0.65	0.908	0.3979	0.6598	0.2466	$^{+0.0351}_{-0.0391}$
61	0.238	4.94	2.2220	0.63	0.19	0.980	0.2411	0.5248	0.2377	$^{+0.0289}_{-0.0323}$
62	0.239	4.74	2.3402	0.63	0.40	0.906	-0.0154	-0.0327	0.2463	$^{+0.0031}_{-0.0034}$
63	0.240	4.77	2.2024	0.64	0.64	0.804	0.0302	0.0535	0.1869	$^{+0.0036}_{-0.0040}$
64	0.337	9.39	1.5289	0.31	0.18	0.998	-0.3017	-0.4603	0.4813	$^{-0.0230}_{+0.0256}$
65	0.335	9.29	1.5445	0.31	0.38	0.959	0.7832	1.1606	0.5969	$^{+0.0614}_{-0.0684}$
66	0.336	9.31	1.6209	0.31	0.65	0.857	0.6347	0.8818	0.8257	$^{+0.0460}_{-0.0513}$
67	0.338	8.06	1.8396	0.42	0.19	0.993	0.6043	1.1038	0.3910	$^{+0.0555}_{-0.0618}$
68	0.339	7.84	1.9544	0.43	0.39	0.940	-0.0389	-0.0715	0.4658	$^{-0.0032}_{+0.0037}$
69	0.339	7.70	1.9217	0.43	0.63	0.837	0.3759	0.6048	0.5088	$^{+0.0338}_{-0.0377}$
70	0.338	7.42	2.0061	0.63	0.19	0.988	0.5238	1.0383	0.4981	$^{+0.0546}_{-0.0608}$
71	0.338	6.94	2.2346	0.63	0.40	0.902	0.2682	0.5408	0.4763	$^{+0.0316}_{-0.0352}$
72	0.339	6.67	2.1693	0.64	0.64	0.749	0.2670	0.4338	0.3595	$^{+0.0236}_{-0.0263}$
73	0.448	11.88	1.6006	0.34	0.18	0.993	1.3062	2.0753	0.8053	$^{+0.1083}_{-0.1207}$
74	0.447	11.61	1.6636	0.32	0.46	0.912	0.3834	0.5818	1.3223	$^{+0.0299}_{-0.0333}$
75	0.450	10.66	1.7894	0.42	0.19	1.008	0.2701	0.4872	0.7775	$^{+0.0276}_{-0.0308}$
76	0.449	10.08	2.0304	0.43	0.39	0.950	0.0353	0.0680	1.0543	$^{+0.0068}_{-0.0076}$
77	0.448	9.67	1.8985	0.44	0.63	0.821	0.292	0.4553	1.3480	$^{+0.0286}_{-0.0319}$
78	0.451	10.46	1.9047	0.63	0.20	1.015	0.6800	1.3145	1.1297	$^{+0.0745}_{-0.0831}$
79	0.450	9.82	1.9675	0.63	0.40	0.935	0.5868	1.0799	0.9574	$^{+0.0586}_{-0.0653}$
80	0.448	9.32	2.0194	0.63	0.65	0.758	0.6455	0.9874	0.7602	$^{+0.0543}_{-0.0606}$

Table C.3: Born level asymmetries for negative pions on the proton target

bin	$< x >$	$< Q^2 >$	$\frac{1}{D(1+\eta\gamma)}$	$< z >$	$< p_{h\perp} >$	$C_\phi^{\pi^-}$	$A_{\parallel,p}^{\pi^-}$	$A_{1,p}^{\pi^-}$	$\pm$stat.	syst.
1	0.033	1.22	1.4159	0.26	0.22	0.956 0	.1728	0.2339	0.0884	$^{+0.0113}_{-0.0126}$
2	0.033	1.23	1.3769	0.25	0.40	0.986	0.0250	0.0339	0.0630	$^{+0.0032}_{-0.0035}$
3	0.032	1.24	1.3548	0.27	0.65	0.990	0.1213	0.1626	0.0637	$^{+0.0074}_{-0.0082}$
4	0.035	1.17	1.6004	0.41	0.22	0.962	0.0508	0.0781	0.2056	$^{+0.0022}_{-0.0024}$
5	0.034	1.19	1.4938	0.41	0.40	0.961	-0.1432	-0.2057	0.1318	$^{-0.0110}_{+0.0122}$
6	0.033	1.21	1.4436	0.41	0.72	0.992	-0.0578	-0.0828	0.0957	$^{-0.0037}_{+0.0041}$
7	0.036	1.14	1.7054	0.59	0.21	1.009	-0.1492	-0.2567	0.3085	$^{-0.0160}_{+0.0179}$
8	0.035	1.18	1.5784	0.59	0.40	1.001	0.0154	0.0244	0.1932	$^{+0.0017}_{-0.0019}$
9	0.034	1.19	1.5140	0.58	0.75	1.025	-0.0585	-0.0909	0.1491	$^{-0.0047}_{+0.0052}$
10	0.047	1.58	1.5724	0.28	0.20	0.971	0.1301	0.1986	0.1105	$^{+0.0109}_{-0.0121}$
11	0.047	1.65	1.4869	0.27	0.40	0.989	0.0388	0.0571	0.0835	$^{+0.0023}_{-0.0026}$
12	0.047	1.68	1.4604	0.28	0.65	0.985	0.0672	0.0967	0.0851	$^{+0.0056}_{-0.0062}$
13	0.048	1.33	2.0042	0.41	0.19	0.984	0.0183	0.0361	0.1744	$^{+0.0011}_{-0.0012}$
14	0.048	1.40	1.8562	0.41	0.40	0.981	0.2087	0.3801	0.1489	$^{+0.0203}_{-0.0227}$
15	0.047	1.48	1.7055	0.41	0.70	0.987	0.0093	0.0157	0.1141	$^{+0.0019}_{-0.0021}$
16	0.048	1.26	2.1256	0.61	0.19	1.011	0.1464	0.3146	0.2044	$^{+0.0203}_{-0.0227}$
17	0.048	1.32	2.0158	0.61	0.40	1.029	0.0633	0.1313	0.1913	$^{+0.0077}_{-0.0086}$
18	0.048	1.39	1.8486	0.60	0.72	1.027	0.1068	0.2027	0.1507	$^{+0.0122}_{-0.0136}$
19	0.064	2.12	1.5745	0.28	0.20	0.981	0.0067	0.0103	0.1146	$^{-0.0010}_{+0.0011}$
20	0.064	2.23	1.4739	0.27	0.40	0.991	0.0258	0.0377	0.0981	$^{+0.0018}_{-0.0021}$
21	0.064	2.26	1.4484	0.28	0.65	0.982	0.2106	0.2995	0.0960	$^{+0.0150}_{-0.0167}$
22	0.065	1.62	2.1822	0.42	0.19	0.987	0.0233	0.0501	0.1680	$^{-0.0011}_{+0.0013}$
23	0.064	1.75	1.9732	0.42	0.39	0.976	0.0095	0.0183	0.1602	$^{+0.0033}_{-0.0037}$
24	0.064	1.88	1.7952	0.42	0.69	0.979	-0.0226	-0.0397	0.1300	$^{+0.0002}_{-0.0003}$
25	0.065	1.43	2.5619	0.61	0.19	0.992	0.0828	0.2105	0.1949	$^{+0.0138}_{-0.0154}$
26	0.065	1.52	2.3815	0.61	0.39	0.991	-0.0244	-0.0575	0.1978	$^{-0.0038}_{+0.0042}$
27	0.065	1.66	2.0894	0.61	0.69	0.980	-0.1094	-0.2239	0.1654	$^{-0.0103}_{+0.0115}$
28	0.086	2.80	1.5581	0.28	0.19	0.990	0.1410	0.2175	0.1354	$^{+0.0118}_{-0.0132}$
29	0.086	2.95	1.4699	0.27	0.40	0.997	0.1819	0.2665	0.1251	$^{+0.0128}_{-0.0143}$
30	0.086	2.99	1.4448	0.28	0.65	0.975	-0.0479	-0.0675	0.1213	$^{-0.0033}_{+0.0037}$
31	0.087	2.14	2.1467	0.42	0.18	0.991	0.1027	0.2183	0.1799	$^{+0.0096}_{-0.0107}$
32	0.086	2.31	1.9463	0.42	0.39	0.980	-0.0166	-0.0317	0.1813	$^{-0.0012}_{+0.0013}$
33	0.086	2.48	1.7930	0.42	0.69	0.972	-0.0354	-0.0616	0.1599	$^{-0.0018}_{+0.0020}$
34	0.087	1.76	2.7943	0.62	0.19	0.979	-0.0949	-0.2597	0.2162	$^{-0.0143}_{+0.0160}$
35	0.087	1.81	2.6131	0.63	0.39	0.957	0.0382	0.0955	0.2221	$^{+0.0062}_{-0.0069}$
36	0.087	2.03	2.2495	0.62	0.68	0.945	0.1304	0.2771	0.1989	$^{+0.0142}_{-0.0159}$
37	0.118	3.72	1.5720	0.29	0.19	0.999	-0.0401	-0.0631	0.1433	$^{-0.0033}_{+0.0036}$
38	0.117	3.89	1.4767	0.28	0.39	1.002	0.0211	0.0312	0.1427	$^{+0.0020}_{-0.0023}$
39	0.117	3.95	1.4347	0.28	0.66	0.967	0.2158	0.2996	0.1409	$^{+0.0159}_{-0.0178}$

Table C.3: - continued

bin	$< x >$	$< Q^2 >$	$\frac{1}{D(1+\eta\gamma)}$	$< z >$	$< p_{h\perp} >$	$C_{\phi}^{\pi^-}$	$A_{\parallel,p}^{\pi^-}$	$A_{1,p}^{\pi^-}$	$\pm$ stat.	syst.
40	0.118	2.90	2.0703	0.42	0.19	0.996	0.0248	0.0511	0.1745	$^{+0.0007}_{-0.0008}$
41	0.118	3.08	1.9726	0.42	0.39	0.986	0.0760	0.1479	0.1958	$^{+0.0084}_{-0.0094}$
42	0.117	3.31	1.7942	0.42	0.69	0.974	0.2361	0.4124	0.1755	$^{+0.0214}_{-0.0239}$
43	0.118	2.34	2.7536	0.62	0.19	0.975	0.0205	0.0552	0.2186	$^{+0.0012}_{-0.0013}$
44	0.118	2.37	2.6288	0.63	0.39	0.958	0.0877	0.2207	0.2281	$^{+0.0140}_{-0.0156}$
45	0.118	2.61	2.2611	0.63	0.67	0.939	0.0155	0.0330	0.2067	$^{+0.0056}_{-0.0063}$
46	0.165	5.02	1.5544	0.29	0.18	1.004	0.1608	0.2511	0.1797	$^{+0.0130}_{-0.0145}$
47	0.164	5.21	1.4650	0.29	0.39	1.007	-0.0090	-0.0133	0.1834	$^{+0.0002}_{-0.0002}$
48	0.163	5.29	1.4567	0.29	0.66	0.958	0.1597	0.2229	0.2008	$^{+0.0103}_{-0.0114}$
49	0.166	4.06	1.9901	0.42	0.18	1.001	0.1584	0.3156	0.1945	$^{+0.0171}_{-0.0190}$
50	0.166	4.20	1.9078	0.43	0.39	1.000	0.0383	0.0730	0.2162	$^{+0.0049}_{-0.0054}$
51	0.165	4.47	1.7512	0.42	0.68	0.976	-0.0368	-0.0629	0.2218	$^{-0.0040}_{+0.0044}$
52	0.165	3.35	2.5059	0.62	0.19	0.986	-0.0710	-0.1754	0.2589	$^{-0.0087}_{+0.0097}$
53	0.166	3.33	2.5104	0.63	0.39	0.980	0.0391	0.0963	0.2732	$^{+0.0054}_{-0.0060}$
54	0.166	3.51	2.3507	0.64	0.66	0.958	0.1514	0.3411	0.2555	$^{+0.0196}_{-0.0219}$
55	0.237	6.88	1.5600	0.30	0.18	1.007	0.2567	0.4031	0.2641	$^{+0.0212}_{-0.0236}$
56	0.236	7.03	1.5140	0.30	0.39	1.006	0.1576	0.2400	0.3229	$^{+0.0131}_{-0.0146}$
57	0.234	7.08	1.5032	0.30	0.66	0.943	0.2566	0.3637	0.3420	$^{+0.0185}_{-0.0206}$
58	0.238	5.76	1.9090	0.42	0.19	1.011	0.2152	0.4152	0.2497	$^{+0.0210}_{-0.0234}$
59	0.239	5.84	1.8396	0.43	0.39	1.022	0.3010	0.5662	0.2763	$^{+0.0295}_{-0.0329}$
60	0.239	5.98	1.8782	0.43	0.66	0.994	-0.0282	-0.0527	0.3275	$^{+0.0002}_{-0.0002}$
61	0.238	5.06	2.2692	0.62	0.19	1.006	0.1010	0.2307	0.3370	$^{+0.0126}_{-0.0140}$
62	0.238	4.86	2.4157	0.62	0.40	1.020	0.1035	0.2550	0.3814	$^{+0.0124}_{-0.0138}$
63	0.240	4.93	2.3042	0.63	0.65	1.011	0.1953	0.4550	0.3541	$^{+0.0231}_{-0.0258}$
64	0.337	9.42	1.5959	0.31	0.18	1.008	-0.0080	-0.0129	0.6587	$^{-0.0036}_{+0.0041}$
65	0.335	9.32	1.5753	0.31	0.38	1.005	0.2637	0.4175	0.8359	$^{+0.0238}_{-0.0265}$
66	0.336	9.37	1.5394	0.31	0.66	0.948	0.0768	0.1121	1.0330	$^{+0.0071}_{-0.0079}$
67	0.338	8.11	1.8432	0.42	0.19	1.034	0.1842	0.3511	0.5474	$^{+0.0197}_{-0.0220}$
68	0.338	7.88	1.9482	0.43	0.39	1.066	0.0919	0.1909	0.6584	$^{+0.0094}_{-0.0105}$
69	0.338	7.76	1.9590	0.43	0.65	1.052	1.1389	2.3462	0.7541	$^{+0.1235}_{-0.1377}$
70	0.337	7.52	2.0620	0.61	0.19	1.040	-0.1910	-0.4096	0.6544	$^{-0.0224}_{+0.0250}$
71	0.337	7.13	2.1573	0.62	0.40	1.082	0.5945	1.3873	0.7669	$^{+0.0718}_{-0.0800}$
72	0.339	6.94	2.3637	0.63	0.66	1.091	-0.0134	-0.0346	0.8235	$^{-0.0022}_{+0.0024}$
73	0.446	11.89	1.6113	0.32	0.18	1.022	0.3751	0.6176	1.6545	$^{+0.0350}_{-0.0391}$
74	0.446	11.64	1.5498	0.32	0.47	1.028	-1.8760	-2.9879	1.7502	$^{-0.1519}_{+0.1693}$
75	0.449	10.66	1.8734	0.42	0.19	1.077	-0.2176	-0.4393	1.2582	$^{-0.0187}_{+0.0209}$
76	0.450	10.15	1.9932	0.43	0.39	1.152	0.0335	0.0770	1.4915	$^{+0.0068}_{-0.0075}$
77	0.449	9.88	1.9543	0.43	0.64	1.151	-0.0217	-0.0487	1.4349	$^{-0.0138}_{+0.0154}$
78	0.448	10.51	1.8089	0.62	0.20	1.096	0.0304	0.0604	1.2312	$^{+0.0078}_{-0.0087}$
79	0.447	9.90	2.0329	0.62	0.40	1.165	1.3232	3.1339	1.5596	$^{+0.1619}_{-0.1804}$
80	0.446	9.39	2.2266	0.63	0.66	1.190	0.1958	0.5187	1.8008	$^{+0.0421}_{-0.0470}$

Table C.4: Born level asymmetries for positive pions on the deuteron target

bin	$< x >$	$< Q^2 >$	$\frac{1}{D(1+\eta\gamma)}$	$< z >$	$< p_{h\perp} >$	$C_\phi^{\pi^+}$	$A_{\parallel,d}^{\pi^+}$	$A_{1,d}^{\pi^+}$	$\pm$ stat.	syst.
1	0.033	1.20	1.4735	0.19	0.21	1.015	-0.0004	-0.0006	0.0225	$^{+0.0003}_{-0.0002}$
2	0.033	1.22	1.4274	0.21	0.39	0.999	0.0025	0.0035	0.0203	$^{+0.0007}_{-0.0005}$
3	0.033	1.23	1.3954	0.25	0.63	0.987	0.0202	0.0278	0.0266	$^{+0.0024}_{-0.0017}$
4	0.035	1.16	1.5976	0.41	0.21	1.015	-0.0898	-0.1457	0.0983	$^{-0.0085}_{+0.0060}$
5	0.034	1.20	1.5008	0.41	0.40	1.013	0.0125	0.0191	0.0618	$^{+0.0012}_{-0.0008}$
6	0.033	1.21	1.4438	0.41	0.71	1.001	-0.0661	-0.0956	0.0431	$^{-0.0039}_{+0.0027}$
7	0.036	1.14	1.6908	0.60	0.21	1.074	-0.0141	-0.0256	0.1477	$^{-0.0063}_{+0.0044}$
8	0.034	1.17	1.5709	0.59	0.40	1.069	0.0536	0.0899	0.0895	$^{+0.0018}_{-0.0013}$
9	0.034	1.190	1.5018	0.59	0.74	1.063	0.0030	0.0049	0.0602	$^{-0.0019}_{+0.0013}$
10	0.047	1.47	1.7962	0.21	0.19	1.010	-0.0002	-0.0003	0.0251	$^{+0.0002}_{-0.0001}$
11	0.047	1.54	1.6939	0.22	0.39	0.998	0.0074	0.0126	0.0253	$^{+0.0001}_{-0.0001}$
12	0.047	1.60	1.6088	0.26	0.62	0.977	0.0118	0.0186	0.0344	$^{+0.0014}_{-0.0010}$
13	0.048	1.32	2.0596	0.41	0.19	1.008	0.0464	0.0963	0.0802	$^{+0.0056}_{-0.0040}$
14	0.048	1.40	1.8842	0.41	0.40	1.017	-0.0014	-0.0027	0.0694	$^{-0.0006}_{+0.0004}$
15	0.047	1.48	1.7378	0.41	0.69	0.992	0.0101	0.0174	0.0528	$^{+0.0018}_{-0.0013}$
16	0.049	1.27	2.1357	0.61	0.19	1.033	0.0196	0.0433	0.0971	$^{+0.0009}_{-0.0007}$
17	0.048	1.33	2.0094	0.61	0.40	1.076	0.0002	0.0004	0.0884	$^{+0.0008}_{-0.0005}$
18	0.048	1.39	1.8406	0.61	0.70	1.082	-0.0669	-0.1332	0.0657	$^{-0.0058}_{+0.0041}$
19	0.064	1.84	2.0094	0.22	0.18	1.007	-0.0025	-0.0050	0.0276	$^{-0.0003}_{+0.0002}$
20	0.064	1.96	1.8656	0.23	0.39	0.998	0.0240	0.0446	0.0298	$^{+0.0029}_{-0.0021}$
21	0.064	2.06	1.7428	0.26	0.62	0.969	0.0695	0.1175	0.0404	$^{+0.0067}_{-0.0047}$
22	0.065	1.53	2.4724	0.42	0.18	1.001	0.0062	0.0154	0.0783	$^{+0.0011}_{-0.0008}$
23	0.065	1.69	2.1755	0.42	0.39	1.004	0.0689	0.1504	0.0761	$^{+0.0091}_{-0.0064}$
24	0.064	1.83	1.9546	0.42	0.68	0.972	0.0078	0.0149	0.0602	$^{+0.0017}_{-0.0012}$
25	0.065	1.44	2.5834	0.62	0.19	1.009	0.0096	0.0251	0.0894	$^{+0.0012}_{-0.0008}$
26	0.065	1.53	2.3728	0.62	0.39	1.029	-0.0572	-0.1396	0.0902	$^{-0.0068}_{+0.0048}$
27	0.065	1.67	2.0914	0.62	0.68	1.030	0.0082	0.0176	0.0724	$^{+0.0010}_{-0.0007}$
28	0.087	2.34	2.1227	0.23	0.18	1.008	0.0137	0.0294	0.0326	$^{+0.0018}_{-0.0013}$
29	0.086	2.53	1.9382	0.23	0.39	0.996	0.0093	0.0179	0.0368	$^{+0.0018}_{-0.0012}$
30	0.086	2.63	1.8691	0.27	0.62	0.960	0.0642	0.1152	0.0508	$^{+0.0072}_{-0.0051}$
31	0.087	1.84	2.8121	0.42	0.18	0.999	0.0036	0.0101	0.0868	$^{+0.0019}_{-0.0013}$
32	0.087	2.08	2.4251	0.42	0.39	0.993	-0.0526	-0.1266	0.0897	$^{-0.0068}_{+0.0048}$
33	0.087	2.28	2.1915	0.42	0.67	0.959	0.0749	0.1573	0.0771	$^{+0.0087}_{-0.0061}$
34	0.087	1.71	2.9137	0.62	0.19	0.979	-0.0040	-0.0113	0.0988	$^{+0.0002}_{-0.0001}$
35	0.087	1.78	2.6927	0.63	0.39	0.965	0.0617	0.1603	0.0994	$^{+0.0071}_{-0.0050}$
36	0.087	2.01	2.2898	0.63	0.67	0.978	0.0456	0.1021	0.0828	$^{+0.0059}_{-0.0041}$
37	0.118	3.08	2.1275	0.24	0.17	1.010	0.0637	0.1369	0.0327	$^{+0.0076}_{-0.0053}$
38	0.117	3.31	1.9599	0.24	0.39	0.991	0.0573	0.1114	0.0401	$^{+0.0070}_{-0.0049}$
39	0.117	3.38	1.97 41	0.27	0.62	0.944	0.0414	0.0771	0.0578	$^{+0.0057}_{-0.0040}$

Table C.4: - continued

bin	$< x >$	$< Q^2 >$	$\frac{1}{D(1+\eta\gamma)}$	$< z >$	$< p_{h\perp} >$	$C_{\phi}^{\pi^+}$	$A_{\parallel,d}^{\pi^+}$	$A_{1,d}^{\pi^+}$	$\pm$ stat.	syst.
40	0.118	2.41	2.9200	0.42	0.18	1.002	0.0644	0.1885	0.0857	$^{+0.0115}_{-0.0081}$
41	0.118	2.63	2.6103	0.42	0.39	0.987	0.0256	0.0660	0.0963	$^{+0.0053}_{-0.0037}$
42	0.117	2.89	2.3732	0.42	0.67	0.936	0.0282	0.0627	0.0890	$^{+0.0045}_{-0.0032}$
43	0.118	2.21	2.9705	0.62	0.19	0.962	-0.0402	-0.1150	0.0976	$^{-0.0064}_{+0.0045}$
44	0.119	2.22	2.9289	0.63	0.39	0.928	0.0184	0.0500	0.1001	$^{+0.0012}_{-0.0008}$
45	0.118	2.50	2.4377	0.63	0.65	0.910	0.0562	0.1247	0.0853	$^{+0.0081}_{-0.0057}$
46	0.165	4.18	2.0866	0.24	0.17	1.007	0.0506	0.1063	0.0376	$^{+0.0062}_{-0.0043}$
47	0.165	4.37	2.0056	0.25	0.39	0.980	0.0960	0.1886	0.0527	$^{+0.0092}_{-0.0065}$
48	0.164	4.40	2.0963	0.27	0.62	0.915	-0.0359	-0.0689	0.0781	$^{-0.0026}_{+0.0018}$
49	0.165	3.42	2.6841	0.42	0.19	1.000	0.0312	0.0836	0.0907	$^{+0.0049}_{-0.0035}$
50	0.166	3.52	2.6270	0.42	0.38	0.976	-0.0026	-0.0067	0.1104	$^{-0.0001}_{+0.0001}$
51	0.165	3.86	2.4111	0.42	0.66	0.913	0.0302	0.0664	0.1088	$^{+0.0024}_{-0.0017}$
52	0.165	3.21	2.7023	0.62	0.19	0.962	0.0811	0.2109	0.1080	$^{+0.0141}_{-0.0099}$
53	0.166	3.13	2.7732	0.63	0.39	0.906	0.0989	0.2485	0.1137	$^{+0.0153}_{-0.0107}$
54	0.167	3.34	2.4673	0.64	0.64	0.845	0.0597	0.1243	0.0927	$^{+0.0099}_{-0.0070}$
55	0.238	5.78	2.0457	0.25	0.18	0.995	0.0978	0.1991	0.0489	$^{+0.0119}_{-0.0084}$
56	0.238	5.74	2.0995	0.26	0.38	0.953	0.0931	0.1862	0.0743	$^{+0.0111}_{-0.0078}$
57	0.236	5.79	2.1937	0.28	0.62	0.865	0.1390	0.2638	0.1128	$^{+0.0149}_{-0.0105}$
58	0.237	5.08	2.3842	0.42	0.19	0.993	0.0026	0.0062	0.1105	$^{+0.0032}_{-0.0023}$
59	0.239	4.94	2.5374	0.42	0.39	0.952	0.0812	0.1962	0.1296	$^{+0.0147}_{-0.0104}$
60	0.239	5.17	2.4094	0.42	0.65	0.861	0.0702	0.1455	0.1390	$^{+0.0104}_{-0.0073}$
61	0.237	4.90	2.3374	0.62	0.19	0.964	0.0410	0.0925	0.1352	$^{+0.0052}_{-0.0037}$
62	0.238	4.69	2.4792	0.63	0.39	0.891	0.0156	0.0344	0.1395	$^{+0.0005}_{-0.0004}$
63	0.240	4.70	2.4166	0.64	0.64	0.782	0.1116	0.2110	0.1107	$^{+0.0131}_{-0.0092}$
64	0.337	7.93	2.0014	0.25	0.18	0.975	0.1688	0.3294	0.1090	$^{+0.0204}_{-0.0144}$
65	0.338	7.43	2.2351	0.29	0.38	0.911	0.2910	0.5927	0.1644	$^{+0.0366}_{-0.0257}$
66	0.337	7.60	2.2199	0.29	0.61	0.805	-0.1834	-0.3276	0.2584	$^{-0.0229}_{+0.0161}$
67	0.337	7.54	2.1185	0.42	0.19	0.988	0.4463	0.9340	0.2290	$^{+0.0536}_{-0.0377}$
68	0.338	7.04	2.3274	0.42	0.39	0.925	0.0266	0.0572	0.2556	$^{-0.0000}_{+0.0000}$
69	0.338	6.95	2.3513	0.43	0.63	0.789	0.0691	0.1283	0.2748	$^{+0.0085}_{-0.0060}$
70	0.337	7.38	2.0566	0.62	0.20	0.969	0.0526	0.1049	0.2899	$^{+0.0083}_{-0.0058}$
71	0.337	7.01	2.1812	0.63	0.40	0.886	0.1005	0.1941	0.2697	$^{+0.0152}_{-0.0107}$
72	0.339	6.74	2.2668	0.63	0.64	0.723	0.0578	0.0947	0.2128	$^{+0.0072}_{-0.0050}$
73	0.446	10.35	1.9352	0.25	0.19	0.960	0.1457	0.2707	0.2269	$^{+0.0201}_{-0.0141}$
74	0.444	9.56	2.1334	0.27	0.42	0.866	0.1521	0.2809	0.2793	$^{+0.0221}_{-0.0155}$
75	0.446	10.37	1.9045	0.42	0.20	0.989	0.1082	0.2037	0.4450	$^{+0.0173}_{-0.0121}$
76	0.445	9.52	2.1309	0.42	0.39	0.913	0.0191	0.0372	0.5140	$^{+0.0026}_{-0.0018}$
77	0.444	9.22	2.1596	0.43	0.63	0.749	-0.4158	-0.6730	0.5382	$^{0.0375}_{+0.0263}$
78	0.450	10.40	1.8859	0.63	0.20	0.989	0.0319	0.0595	0.6043	$^{+0.0068}_{-0.0048}$
79	0.450	9.87	1.9746	0.63	0.40	0.900	-0.0076	-0.0134	0.5451	$^{+0.0025}_{-0.0018}$
80	0.447	9.41	2.1343	0.63	0.64	0.709	0.1199	0.1815	0.4045	$^{+0.0148}_{-0.0104}$

Table C.5: Born level asymmetries for negative pions on the deuteron target

bin	$< x >$	$< Q^2 >$	$\frac{1}{D(1+\eta\gamma)}$	$< z >$	$< p_{h\perp} >$	$C_\phi^{\pi^-}$	$A_{\parallel,d}^{\pi^-}$	$A_{1,d}^{\pi^-}$	$\pm$ stat.	syst.
1	0.033	1.20	1.4680	0.18	0.21	0.993	-0.0066	-0.0096	0.0226	$^{+0.0004}_{-0.0003}$
2	0.033	1.22	1.4208	0.21	0.39	0.996	0.0022	0.0031	0.0208	$^{+0.0006}_{-0.0004}$
3	0.033	1.23	1.3893	0.25	0.63	0.990	0.0400	0.0550	0.0272	$^{+0.0038}_{-0.0027}$
4	0.035	1.16	1.5945	0.41	0.21	0.985	-0.0947	-0.1487	0.1006	$^{-0.0048}_{+0.0034}$
5	0.034	1.19	1.4985	0.41	0.40	0.978	-0.0515	-0.0755	0.0638	$^{-0.0023}_{+0.0016}$
6	0.033	1.21	1.4447	0.41	0.72	0.997	-0.0262	-0.0377	0.0451	$^{-0.0022}_{+0.0016}$
7	0.036	1.14	1.7004	0.59	0.21	1.069	0.1084	0.1970	0.1555	$^{+0.0118}_{-0.0083}$
8	0.034	1.17	1.5535	0.59	0.40	1.041	-0.0677	-0.1096	0.0896	$^{-0.0030}_{+0.0021}$
9	0.034	1.19	1.4952	0.59	0.75	1.042	-0.0274	-0.0426	0.0643	$^{-0.0017}_{+0.0012}$
10	0.047	1.47	1.7935	0.20	0.19	0.996	-0.0109	-0.0194	0.0257	$^{-0.0008}_{+0.0005}$
11	0.047	1.53	1.6894	0.22	0.39	0.996	0.0056	0.0094	0.0262	$^{+0.0005}_{-0.0004}$
12	0.047	1.60	1.6002	0.26	0.63	0.983	0.0060	0.0095	0.0354	$^{-0.0005}_{+0.0004}$
13	0.048	1.32	2.0480	0.41	0.19	0.993	0.0698	0.1418	0.0843	$^{+0.0070}_{-0.0049}$
14	0.048	1.40	1.8829	0.41	0.40	0.992	0.0782	0.1460	0.0709	$^{+0.0077}_{-0.0054}$
15	0.047	1.48	1.7306	0.41	0.70	0.986	0.0124	0.0212	0.0556	$^{+0.0007}_{-0.0005}$
16	0.048	1.27	2.1245	0.61	0.19	1.033	0.0303	0.0665	0.1019	$^{+0.0032}_{-0.0022}$
17	0.048	1.34	2.0049	0.60	0.40	1.046	0.0001	0.0002	0.0916	$^{-0.0065}_{+0.0045}$
18	0.048	1.40	1.8320	0.60	0.72	1.044	-0.0904	-0.1730	0.0729	$^{-0.0091}_{+0.0064}$
19	0.064	1.83	2.0089	0.22	0.18	0.997	0.0163	0.0327	0.0287	$^{+0.0025}_{-0.0018}$
20	0.064	1.95	1.8511	0.23	0.39	0.999	0.0278	0.0514	0.0312	$^{+0.0037}_{-0.0026}$
21	0.064	2.06	1.7403	0.26	0.62	0.984	0.0210	0.0360	0.0427	$^{+0.0032}_{-0.0023}$
22	0.065	1.53	2.4840	0.42	0.18	0.992	-0.0060	-0.0147	0.0819	$^{-0.0015}_{+0.0010}$
23	0.065	1.68	2.1665	0.42	0.39	0.976	-0.0785	-0.1658	0.0798	$^{-0.0068}_{+0.0048}$
24	0.064	1.83	1.9617	0.42	0.69	0.981	-0.0310	-0.0596	0.0659	$^{-0.0037}_{+0.0026}$
25	0.065	1.45	2.5918	0.61	0.19	1.008	0.0161	0.0421	0.0976	$^{+0.0015}_{-0.0010}$
26	0.065	1.53	2.3658	0.61	0.39	1.001	0.0146	0.0347	0.0947	$^{+0.0007}_{-0.0005}$
27	0.065	1.68	2.0644	0.61	0.69	0.992	0.0207	0.0425	0.0790	$^{+0.0029}_{-0.0021}$
28	0.087	2.35	2.1122	0.23	0.18	1.005	0.0242	0.0513	0.0340	$^{+0.0024}_{-0.0017}$
29	0.086	2.53	1.9173	0.23	0.39	1.001	0.0417	0.0801	0.0389	$^{+0.0055}_{-0.0039}$
30	0.086	2.65	1.8497	0.27	0.62	0.984	0.0015	0.0027	0.0536	$^{-0.0015}_{+0.0011}$
31	0.087	1.85	2.8263	0.42	0.18	1.000	0.0063	0.0177	0.0923	$^{+0.0011}_{-0.0008}$
32	0.087	2.08	2.4386	0.42	0.39	0.975	0.0458	0.1088	0.0982	$^{+0.0088}_{-0.0062}$
33	0.086	2.28	2.1613	0.42	0.68	0.985	0.0302	0.0643	0.0853	$^{+0.0011}_{-0.0008}$
34	0.087	1.73	2.9412	0.62	0.19	0.982	-0.0536	-0.1548	0.1087	$^{-0.0064}_{+0.0045}$
35	0.087	1.80	2.6881	0.62	0.39	0.956	-0.0110	-0.0284	0.1113	$^{-0.0005}_{+0.0003}$
36	0.087	2.03	2.2836	0.62	0.68	0.947	0.0245	0.0530	0.0941	$^{+0.0013}_{-0.0009}$
37	0.118	3.07	2.1298	0.24	0.17	1.014	0.0065	0.0140	0.0353	$^{+0.0022}_{-0.0016}$
38	0.117	3.32	1.9508	0.24	0.39	1.001	0.0664	0.1297	0.0436	$^{+0.0070}_{-0.0050}$
39	0.117	3.39	1.9674	0.27	0.62	0.982	0.1202	0.2324	0.0629	$^{+0.0137}_{-0.0096}$

Table C.5: - continued

bin	$< x >$	$< Q^2 >$	$\frac{1}{D(1+\eta\gamma)}$	$< z >$	$< p_{h\perp} >$	$C_{\phi}^{\pi^-}$	$A_{\parallel,d}^{\pi^-}$	$A_{1,d}^{\pi^-}$	$\pm$ stat.	syst.
40	0.118	2.41	2.9536	0.42	0.18	1.017	-0.0240	-0.0721	0.0951	$^{-0.0056}_{+0.0039}$
41	0.118	2.64	2.6274	0.42	0.39	0.996	0.0476	0.1247	0.1076	$^{+0.0058}_{-0.0041}$
42	0.117	2.92	2.3799	0.42	0.67	0.994	0.0000	0.0000	0.0997	$^{-0.0002}_{+0.0001}$
43	0.118	2.23	3.0239	0.62	0.19	0.975	0.0467	0.1378	0.1129	$^{+0.0087}_{-0.0061}$
44	0.118	2.25	2.9257	0.62	0.39	0.956	0.0907	0.2535	0.1197	$^{+0.0128}_{-0.0090}$
45	0.118	2.52	2.4960	0.63	0.66	0.932	0.0113	0.0263	0.1068	$^{+0.0033}_{-0.0023}$
46	0.165	4.19	2.0951	0.24	0.17	1.019	0.0565	0.1207	0.0417	$^{+0.0058}_{-0.0041}$
47	0.165	4.38	2.0054	0.25	0.39	1.001	0.0725	0.1456	0.0583	$^{+0.0081}_{-0.0057}$
48	0.164	4.40	2.0853	0.27	0.62	0.974	0.0220	0.0447	0.0862	$^{+0.0022}_{-0.0015}$
49	0.165	3.44	2.7421	0.42	0.19	1.027	0.0398	0.1121	0.1069	$^{+0.0056}_{-0.0039}$
50	0.166	3.54	2.6491	0.42	0.39	1.027	-0.0325	-0.0885	0.1305	$^{-0.0018}_{+0.0012}$
51	0.165	3.90	2.4221	0.42	0.67	0.991	0.0590	0.1415	0.1293	$^{+0.0097}_{-0.0068}$
52	0.165	3.24	2.7433	0.62	0.19	0.985	0.0378	0.1020	0.1324	$^{+0.0065}_{-0.0046}$
53	0.166	3.18	2.8491	0.62	0.39	0.975	0.0697	0.1935	0.1468	$^{+0.0125}_{-0.0088}$
54	0.166	3.41	2.5449	0.63	0.65	0.940	0.0343	0.0820	0.1312	$^{+0.0050}_{-0.0035}$
55	0.237	5.80	2.0393	0.24	0.18	1.021	0.0542	0.1128	0.0557	$^{+0.0078}_{-0.0055}$
56	0.238	5.74	2.1201	0.26	0.38	1.010	0.0519	0.1112	0.0868	$^{+0.0078}_{-0.0055}$
57	0.236	5.80	2.1344	0.28	0.62	0.973	0.1672	0.3471	0.1242	$^{+0.0198}_{-0.0139}$
58	0.237	5.11	2.4218	0.42	0.19	1.039	0.0777	0.1954	0.1385	$^{+0.0133}_{-0.0094}$
59	0.239	5.00	2.5781	0.42	0.39	1.055	0.2448	0.6656	0.1718	$^{+0.0384}_{-0.0270}$
60	0.238	5.26	2.4192	0.42	0.65	1.000	0.1637	0.3962	0.1747	$^{+0.0279}_{-0.0196}$
61	0.237	4.97	2.3845	0.62	0.19	1.002	0.0888	0.2120	0.1760	$^{+0.0147}_{-0.0103}$
62	0.237	4.73	2.5461	0.62	0.40	1.004	0.0047	0.0120	0.1942	$^{-0.0001}_{+0.0001}$
63	0.240	4.81	2.4973	0.63	0.65	0.964	0.0542	0.1306	0.1746	$^{+0.0090}_{-0.0063}$
64	0.337	7.98	2.0049	0.24	0.18	1.042	0.2122	0.4431	0.1288	$^{+0.0258}_{-0.0181}$
65	0.338	7.41	2.2315	0.27	0.38	1.056	0.001	0.0023	0.2170	$^{+0.0066}_{-0.0047}$
66	0.337	7.72	2.1967	0.28	0.61	0.997	0.1857	0.4065	0.3201	$^{+0.0289}_{-0.0203}$
67	0.336	7.57	2.1347	0.42	0.19	1.066	-0.0325	-0.0739	0.2955	$^{-0.0023}_{+0.0016}$
68	0.337	7.12	2.3518	0.42	0.39	1.104	0.2607	0.6752	0.3520	$^{+0.0309}_{-0.0217}$
69	0.338	7.04	2.3454	0.42	0.64	1.051	-0.0175	-0.0433	0.4155	$^{+0.0071}_{-0.0050}$
70	0.337	7.52	2.0635	0.62	0.19	1.039	0.0134	0.0286	0.3912	$^{+0.0100}_{-0.0070}$
71	0.337	7.08	2.2446	0.62	0.40	1.063	0.2626	0.6262	0.4243	$^{+0.0376}_{-0.0264}$
72	0.339	6.83	2.3157	0.63	0.65	1.032	0.3480	0.8315	0.3708	$^{+0.0512}_{-0.0360}$
73	0.446	10.40	1.9325	0.25	0.19	1.112	-0.0292	-0.0627	0.2992	$^{+0.0023}_{-0.0016}$
74	0.443	9.55	2.1324	0.27	0.42	1.142	0.1521	0.3705	0.3969	$^{+0.0233}_{-0.0164}$
75	0.445	10.40	1.9784	0.42	0.19	1.128	-0.1382	-0.3084	0.6096	$^{-0.0187}_{+0.0131}$
76	0.444	9.57	2.0955	0.42	0.39	1.207	0.2558	0.6470	0.7768	$^{+0.0538}_{-0.0378}$
77	0.444	9.36	2.1667	0.42	0.64	1.158	0.0965	0.2421	0.9413	$^{+0.0097}_{-0.0068}$
78	0.448	10.50	1.9192	0.62	0.20	1.112	0.3811	0.8135	0.8076	$^{+0.0506}_{-0.0356}$
79	0.447	9.89	1.9884	0.62	0.40	1.179	0.1467	0.3440	0.9319	$^{+0.0212}_{-0.0149}$
80	0.446	9.43	2.1844	0.63	0.66	1.158	-0.5669	-1.4345	0.8624	$^{-0.0716}_{+0.0503}$

Table C.6: Born level asymmetries for positive kaons on the deuteron target

bin	$< x >$	$< Q^2 >$	$\frac{1}{D(1+\eta\gamma)}$	$< z >$	$< p_{h\perp} >$	$C_\phi^{K^+}$	$A_{||,d}^{K^+}$	$A_{1,d}^{K^+}$	$\pm$ stat.	syst.
1	0.034	1.20	1.5040	0.23	0.21	1.026	0.0058	0.0090	0.0971	$^{+0.0024}_{-0.0017}$
2	0.033	1.22	1.4320	0.24	0.40	1.012	-0.0319	-0.0463	0.0777	$^{-0.0021}_{+0.0014}$
3	0.033	1.23	1.3918	0.27	0.65	0.970	0.0185	0.0250	0.0788	$^{+0.0028}_{-0.0020}$
4	0.035	1.17	1.6145	0.41	0.22	1.071	0.0385	0.0665	0.2629	$^{+0.0056}_{-0.0039}$
5	0.034	1.19	1.5067	0.41	0.40	1.051	0.1584	0.2510	0.1787	$^{+0.0143}_{-0.0100}$
6	0.033	1.21	1.4408	0.41	0.72	0.999	-0.0378	-0.0544	0.1001	$^{+0.0023}_{-0.0016}$
7	0.036	1.14	1.6724	0.61	0.22	1.101	0.1654	0.3047	0.3980	$^{+0.0255}_{-0.0179}$
8	0.034	1.18	1.5429	0.60	0.40	1.052	-0.2230	-0.3620	0.2264	$^{-0.0202}_{+0.0142}$
9	0.034	1.19	1.4930	0.60	0.74	1.017	-0.0545	-0.0827	0.1231	$^{-0.0028}_{+0.0020}$
10	0.048	1.44	1.8636	0.24	0.19	1.011	0.0455	0.0857	0.0979	$^{+0.0050}_{-0.0035}$
11	0.047	1.54	1.7078	0.25	0.39	1.015	-0.0123	-0.0213	0.0962	$^{+0.0001}_{-0.0000}$
12	0.047	1.61	1.5868	0.28	0.64	0.950	0.0816	0.1230	0.0996	$^{+0.0085}_{-0.0060}$
13	0.048	1.33	2.0327	0.42	0.19	1.050	-0.0686	-0.1464	0.1950	$^{-0.0099}_{+0.0070}$
14	0.048	1.43	1.8664	0.42	0.39	1.064	0.1288	0.2556	0.1795	$^{+0.0111}_{-0.0078}$
15	0.047	1.50	1.7161	0.42	0.69	0.993	0.0890	0.1517	0.1242	$^{+0.0064}_{-0.0045}$
16	0.048	1.27	2.0886	0.62	0.19	1.053	-0.1870	-0.4113	0.2408	$^{-0.0283}_{+0.0199}$
17	0.048	1.33	1.9720	0.62	0.40	1.075	0.0268	0.0567	0.2078	$^{+0.0045}_{-0.0032}$
18	0.048	1.41	1.8131	0.62	0.71	1.086	0.1919	0.3780	0.1376	$^{+0.0241}_{-0.0170}$
19	0.064	1.78	2.1208	0.25	0.18	1.001	0.0439	0.0932	0.1014	$^{+0.0077}_{-0.0054}$
20	0.064	1.96	1.8815	0.26	0.39	1.020	0.0535	0.1026	0.1095	$^{+0.0048}_{-0.0034}$
21	0.064	2.09	1.7536	0.28	0.63	0.953	0.0533	0.0890	0.1196	$^{+0.0049}_{-0.0034}$
22	0.065	1.57	2.3936	0.42	0.18	1.024	0.1209	0.2963	0.1779	$^{+0.0176}_{-0.0123}$
23	0.065	1.74	2.1144	0.42	0.39	1.046	0.0565	0.1250	0.1925	$^{+0.0080}_{-0.0056}$
24	0.064	1.87	1.8865	0.42	0.68	0.977	0.0316	0.0583	0.1389	$^{+0.0051}_{-0.0036}$
25	0.065	1.46	2.4925	0.63	0.19	1.008	0.1560	0.3921	0.2150	$^{+0.0247}_{-0.0173}$
26	0.065	1.53	2.2907	0.63	0.39	1.048	-0.0009	-0.0023	0.2007	$^{+0.0036}_{-0.0025}$
27	0.065	1.68	2.0562	0.62	0.68	1.064	0.0258	0.0564	0.1510	$^{+0.0046}_{-0.0032}$
28	0.087	2.27	2.1904	0.26	0.17	1.007	0.0908	0.2002	0.1181	$^{+0.0132}_{-0.0093}$
29	0.086	2.54	1.9532	0.26	0.39	1.019	-0.0096	-0.0190	0.1396	$^{-0.0014}_{+0.0010}$
30	0.086	2.68	1.8909	0.28	0.63	0.945	0.0776	0.1387	0.1559	$^{+0.0112}_{-0.0079}$
31	0.087	1.92	2.6354	0.42	0.18	1.013	0.0272	0.0725	0.2003	$^{+0.0014}_{-0.0010}$
32	0.087	2.15	2.2837	0.42	0.39	1.022	0.1173	0.2739	0.2187	$^{+0.0151}_{-0.0106}$
33	0.087	2.37	2.0527	0.42	0.68	0.967	-0.0447	-0.0888	0.1748	$^{-0.0080}_{+0.0056}$
34	0.087	1.75	2.7367	0.63	0.19	0.980	-0.0592	-0.1588	0.2122	$^{-0.0086}_{+0.0061}$
35	0.087	1.82	2.5547	0.64	0.39	0.979	0.0843	0.2110	0.2193	$^{+0.0117}_{-0.0083}$
36	0.087	2.07	2.2493	0.63	0.66	1.015	0.0913	0.2085	0.1668	$^{+0.0148}_{-0.0104}$
37	0.118	3.01	2.1603	0.26	0.17	1.015	-0.0160	-0.0350	0.1165	$^{-0.0029}_{+0.0021}$
38	0.117	3.35	1.9576	0.27	0.39	1.008	0.0422	0.0832	0.1511	$^{+0.0108}_{-0.0076}$
39	0.117	3.52	1.9243	0.28	0.63	0.932	0.1071	0.1920	0.1740	$^{+0.0089}_{-0.0063}$

Table C.6: - continued

bin	$< x >$	$< Q^2 >$	$\frac{1}{D(1+\eta\gamma)}$	$< z >$	$< p_{h\perp} >$	$C_\phi^{K^+}$	$A_{\|\|,d}^{K^+}$	$A_{1,d}^{K^+}$	$\pm$ stat.	syst.
40	0.118	2.50	2.6818	0.42	0.19	1.010	0.0528	0.1430	0.1920	$^{+0.0116}_{-0.0082}$
41	0.119	2.73	2.3355	0.43	0.39	1.009	0.0707	0.1666	0.2122	$^{+0.0068}_{-0.0048}$
42	0.117	3.09	2.1646	0.42	0.67	0.948	0.0340	0.0698	0.1921	$^{+0.0013}_{-0.0009}$
43	0.118	2.28	2.7226	0.63	0.19	0.951	0.1156	0.2992	0.2040	$^{+0.0194}_{-0.0137}$
44	0.118	2.29	2.6998	0.64	0.39	0.937	-0.1048	-0.2652	0.2029	$^{-0.0149}_{+0.0105}$
45	0.118	2.62	2.3009	0.64	0.65	0.951	0.0584	0.1278	0.1647	$^{+0.0032}_{-0.0022}$
46	0.165	4.11	2.1033	0.27	0.17	1.016	0.1156	0.2469	0.1291	$^{+0.0159}_{-0.0112}$
47	0.164	4.44	1.9448	0.28	0.39	0.984	0.1813	0.3470	0.1843	$^{+0.0183}_{-0.0129}$
48	0.164	4.63	1.9408	0.29	0.62	0.906	0.2078	0.3653	0.2351	$^{+0.0241}_{-0.0170}$
49	0.165	3.55	2.4714	0.42	0.19	0.998	0.1485	0.3666	0.2002	$^{+0.0195}_{-0.0137}$
50	0.166	3.70	2.2957	0.43	0.39	0.980	-0.0038	-0.0086	0.2305	$^{-0.0027}_{+0.0019}$
51	0.165	4.04	2.2863	0.42	0.66	0.905	0.1332	0.2757	0.2315	$^{+0.0202}_{-0.0142}$
52	0.166	3.28	2.5353	0.64	0.19	0.934	-0.0208	-0.0492	0.2145	$^{-0.0009}_{+0.0006}$
53	0.166	3.22	2.5826	0.64	0.39	0.885	0.0057	0.0131	0.2174	$^{+0.0065}_{-0.0046}$
54	0.166	3.52	2.2564	0.64	0.64	0.852	0.0701	0.1347	0.1763	$^{+0.0091}_{-0.0064}$
55	0.237	5.74	2.0661	0.27	0.18	1.016	0.2529	0.5307	0.1686	$^{+0.0343}_{-0.0241}$
56	0.238	5.86	2.0634	0.29	0.38	0.957	-0.0357	-0.0706	0.2884	$^{-0.0040}_{+0.0028}$
57	0.234	6.15	2.0046	0.30	0.61	0.843	0.0094	0.0159	0.3490	$^{+0.0001}_{-0.0001}$
58	0.238	5.27	2.2679	0.42	0.19	0.973	0.1837	0.4054	0.2307	$^{+0.0177}_{-0.0125}$
59	0.238	5.11	2.3389	0.43	0.39	0.937	0.1858	0.4073	0.2886	$^{+0.0246}_{-0.0173}$
60	0.239	5.43	2.1777	0.43	0.64	0.826	0.0790	0.1421	0.2850	$^{+0.0093}_{-0.0065}$
61	0.237	4.98	2.2417	0.63	0.19	0.922	-0.2399	-0.4961	0.2499	$^{-0.0257}_{+0.0181}$
62	0.238	4.82	2.3540	0.64	0.39	0.845	0.0249	0.0495	0.2461	$^{+0.0010}_{-0.0013}$
63	0.239	4.90	2.2412	0.64	0.63	0.746	0.1809	0.3026	0.1972	$^{+0.0200}_{-0.0138}$
64	0.336	7.97	1.9414	0.27	0.18	1.001	0.1239	0.2407	0.3849	$^{+0.0094}_{-0.0066}$
65	0.338	7.45	2.1913	0.29	0.38	0.970	-0.4232	-0.8996	0.7531	$^{-0.0492}_{+0.0346}$
66	0.336	8.22	1.9217	0.31	0.61	0.792	-0.3278	-0.4987	1.1126	$^{-0.0208}_{+0.0146}$
67	0.337	7.61	2.0498	0.42	0.19	0.950	0.1876	0.3654	0.4708	$^{+0.0220}_{-0.0155}$
68	0.337	7.14	2.1711	0.43	0.39	0.899	-0.0201	-0.0392	0.5769	$^{-0.0023}_{+0.0016}$
69	0.339	7.06	2.1239	0.43	0.62	0.768	-0.0918	-0.1498	0.6524	$^{-0.0140}_{+0.0098}$
70	0.338	7.56	2.0467	0.64	0.19	0.923	-0.1758	-0.3322	0.5022	$^{-0.0194}_{+0.0137}$
71	0.338	7.19	2.1863	0.64	0.40	0.816	0.6324	1.1284	0.5117	$^{+0.0664}_{-0.0467}$
72	0.338	6.99	2.2772	0.64	0.63	0.671	-0.1641	-0.2506	0.3954	$^{-0.0119}_{+0.0084}$
73	0.442	10.12	1.9551	0.29	0.27	0.993	0.7638	1.4828	0.6825	$^{+0.0865}_{-0.0609}$
74	0.447	10.39	2.0621	0.42	0.19	0.944	1.5482	3.0130	1.0247	$^{+0.1830}_{-0.1289}$
75	0.445	9.66	2.0418	0.43	0.39	0.863	0.3774	0.6653	1.0063	$^{+0.0455}_{-0.0320}$
76	0.445	9.31	2.1893	0.43	0.62	0.739	1.0361	1.6760	1.1806	$^{+0.1081}_{-0.0761}$
77	0.449	10.61	1.9589	0.64	0.19	0.963	-0.1360	-0.2566	1.0832	$^{-0.0128}_{+0.0090}$
78	0.446	10.03	2.0406	0.64	0.39	0.855	0.3032	0.5290	0.9831	$^{+0.0363}_{-0.0255}$
79	0.445	9.64	2.0350	0.64	0.63	0.698	0.4605	0.6541	0.8544	$^{+0.0393}_{-0.0276}$

Table C.7: Born level asymmetries for negative kaons on the deuteron target

bin	$< x >$	$< Q^2 >$	$\frac{1}{D(1+\eta\gamma)}$	$< z >$	$< p_{h\perp} >$	$C_\phi^{K^-}$	$A_{||,d}^{K^-}$	$A_{1,d}^{K^-}$	$\pm$ stat.	syst.
1	0.034	1.20	1.4984	0.23	0.21	0.994	-0.0156	-0.0232	0.1120	$^{+0.0014}_{-0.0010}$
2	0.033	1.22	1.4326	0.24	0.40	1.004	0.0199	0.0287	0.0920	$^{+0.0026}_{-0.0018}$
3	0.033	1.23	1.3812	0.27	0.65	0.958	0.0619	0.0818	0.0932	$^{+0.0005}_{-0.0003}$
4	0.035	1.16	1.6018	0.41	0.21	0.961	-0.2107	-0.3243	0.2732	$^{-0.0156}_{+0.0110}$
5	0.034	1.20	1.4881	0.41	0.40	0.980	-0.358	-0.5220	0.2049	$^{-0.0266}_{+0.0187}$
6	0.033	1.21	1.4225	0.41	0.73	0.993	0.0137	0.0194	0.1364	$^{+0.0028}_{-0.0020}$
7	0.035	1.13	1.6684	0.60	0.21	1.036	0.3188	0.5511	0.5235	$^{+0.0240}_{-0.0169}$
8	0.034	1.18	1.5118	0.60	0.40	1.025	0.2033	0.3150	0.3183	$^{+0.0231}_{-0.0162}$
9	0.034	1.19	1.4657	0.59	0.75	1.027	-0.0769	-0.1157	0.1841	$^{-0.0047}_{+0.0033}$
10	0.047	1.45	1.8641	0.24	0.19	1.032	0.0041	0.0079	0.1245	$^{-0.0024}_{+0.0017}$
11	0.047	1.54	1.6835	0.25	0.39	0.998	0.0771	0.1295	0.1143	$^{+0.0022}_{-0.0015}$
12	0.047	1.62	1.5778	0.27	0.64	0.923	0.0641	0.0934	0.1173	$^{+0.0053}_{-0.0037}$
13	0.048	1.34	2.0275	0.42	0.19	0.993	0.0974	0.1960	0.2428	$^{+0.0152}_{-0.0107}$
14	0.047	1.42	1.8584	0.41	0.40	1.010	0.1459	0.2737	0.2424	$^{+0.0066}_{-0.0046}$
15	0.047	1.50	1.6790	0.42	0.71	0.986	0.0588	0.0975	0.1605	$^{+0.0129}_{-0.0090}$
16	0.048	1.27	2.0295	0.61	0.19	1.008	0.0451	0.0922	0.3230	$^{+0.0053}_{-0.0037}$
17	0.048	1.33	1.9079	0.61	0.40	0.995	-0.0352	-0.0668	0.2982	$^{-0.0048}_{+0.0034}$
18	0.047	1.41	1.7817	0.60	0.71	1.006	-0.0063	-0.0112	0.2157	$^{+0.0002}_{-0.0001}$
19	0.065	1.79	2.0646	0.25	0.18	1.026	-0.0702	-0.1486	0.1299	$^{-0.0075}_{+0.0053}$
20	0.064	1.99	1.8356	0.25	0.39	0.985	0.0501	0.0907	0.1312	$^{+0.0060}_{-0.0042}$
21	0.064	2.10	1.6971	0.28	0.64	0.921	-0.0353	-0.0553	0.1443	$^{-0.0001}_{+0.0000}$
22	0.065	1.54	2.4157	0.42	0.18	0.997	0.0445	0.1072	0.244460	$^{+0.0112}_{-0.0079}$
23	0.064	1.75	2.1694	0.42	0.40	1.002	0.0953	0.2071	0.2663	$^{+0.0111}_{-0.0078}$
24	0.064	1.87	1.8479	0.42	0.70	1.001	-0.0411	-0.0759	0.1915	$^{-0.0014}_{+0.0010}$
25	0.065	1.46	2.4618	0.62	0.19	0.994	-0.0568	-0.1389	0.3142	$^{-0.0069}_{+0.0048}$
26	0.065	1.55	2.2574	0.63	0.39	0.965	0.0218	0.0476	0.3387	$^{-0.0017}_{+0.0012}$
27	0.065	1.67	1.9655	0.61	0.69	0.936	-0.1420	-0.2614	0.2113	$^{-0.0141}_{+0.0099}$
28	0.086	2.30	2.1603	0.25	0.17	1.004	-0.0192	-0.0417	0.1450	$^{-0.0016}_{+0.0011}$
29	0.086	2.58	1.9175	0.26	0.39	0.981	-0.0155	-0.0291	0.1707	$^{-0.0033}_{+0.0023}$
30	0.086	2.70	1.7525	0.28	0.64	0.940	0.0776	0.1280	0.1788	$^{+0.0048}_{-0.0033}$
31	0.087	1.94	2.6417	0.42	0.18	1.008	-0.0893	-0.2377	0.2848	$^{-0.0089}_{+0.0063}$
32	0.086	2.19	2.3135	0.42	0.39	0.996	0.1030	0.2374	0.3207	$^{+0.0083}_{-0.0058}$
33	0.086	2.36	2.0794	0.42	0.69	1.028	0.0243	0.0521	0.2684	$^{+0.0070}_{-0.0049}$
34	0.087	1.76	2.6690	0.63	0.19	1.021	0.1147	0.3126	0.3670	$^{+0.0225}_{-0.0158}$
35	0.087	1.83	2.5530	0.63	0.39	1.004	0.0848	0.2174	0.3849	$^{+0.0061}_{-0.0043}$
36	0.087	2.04	2.1154	0.63	0.69	0.940	-0.2739	-0.5450	0.2720	$^{-0.0297}_{+0.0209}$
37	0.118	3.07	2.1374	0.26	0.17	0.992	-0.0311	-0.0659	0.1439	$^{-0.0042}_{+0.0029}$
38	0.117	3.40	1.8845	0.26	0.39	0.978	-0.0349	-0.0643	0.1835	$^{-0.0041}_{+0.0029}$
39	0.117	3.53	1.8330	0.28	0.64	0.968	0.1774	0.3147	0.2113	$^{+0.0174}_{-0.0122}$

Table C.7: - continued

bin	$< x >$	$< Q^2 >$	$\frac{1}{D(1+\eta\gamma)}$	$< z >$	$< p_{h\perp} >$	$C_\phi^{K^-}$	$A_{\|\|,d}^{K^-}$	$A_{1,d}^{K^-}$	$\pm$ stat.	syst.
40	0.117	2.55	2.7142	0.42	0.19	1.035	0.1290	0.3625	0.2872	$^{+0.0224}_{-0.0157}$
41	0.118	2.86	2.4517	0.42	0.38	1.019	-0.2429	-0.6067	0.3364	$^{-0.0297}_{+0.0209}$
42	0.118	3.06	2.1670	0.42	0.70	1.055	-0.1073	-0.2454	0.3058	$^{-0.0139}_{+0.0098}$
43	0.117	2.28	2.7054	0.63	0.19	1.066	-0.0288	-0.0830	0.3813	$^{-0.0049}_{+0.0035}$
44	0.118	2.34	2.7336	0.63	0.39	1.086	0.1366	0.4056	0.4621	$^{+0.0206}_{-0.0144}$
45	0.118	2.65	2.2637	0.63	0.66	1.078	0.0229	0.0559	0.3534	$^{+0.0000}_{-0.0000}$
46	0.165	4.18	2.0801	0.26	0.17	0.985	-0.0027	-0.0055	0.1638	$^{+0.0008}_{-0.0006}$
47	0.164	4.48	1.9725	0.27	0.39	0.976	0.2359	0.4540	0.2506	$^{+0.0281}_{-0.0198}$
48	0.164	4.68	1.8591	0.29	0.63	1.031	0.3173	0.6082	0.3259	$^{+0.0395}_{-0.0277}$
49	0.164	3.66	2.5479	0.42	0.19	1.052	0.0611	0.1639	0.3468	$^{+0.0075}_{-0.0053}$
50	0.166	3.85	2.5267	0.42	0.39	1.078	-0.0037	-0.0101	0.4683	$^{-0.0024}_{+0.0017}$
51	0.165	4.08	2.1258	0.42	0.69	1.150	0.3927	0.9600	0.4087	$^{+0.0518}_{-0.0365}$
52	0.164	3.33	2.5255	0.62	0.19	1.074	-0.0660	-0.1790	0.4802	$^{-0.0028}_{+0.0019}$
53	0.165	3.26	2.5463	0.63	0.39	1.160	0.0573	0.1693	0.5404	$^{+0.0115}_{-0.0081}$
54	0.165	3.54	2.3024	0.63	0.66	1.255	-0.1122	-0.3243	0.5407	$^{-0.0154}_{+0.0108}$
55	0.235	5.83	2.0470	0.26	0.17	0.980	0.1562	0.3132	0.2278	$^{+0.0178}_{-0.0125}$
56	0.237	5.97	2.1197	0.28	0.38	1.009	0.2693	0.5762	0.4177	$^{+0.0380}_{-0.0267}$
57	0.234	6.15	1.8263	0.30	0.64	1.095	0.0756	0.1513	0.5332	$^{+0.0078}_{-0.0055}$
58	0.237	5.45	2.2826	0.42	0.19	1.022	-0.0439	-0.1023	0.4300	$^{-0.00403}_{+0.0028}$
59	0.239	5.37	2.3201	0.42	0.39	1.096	-0.0535	-0.1363	0.5173	$^{-0.0099}_{+0.0070}$
60	0.237	5.58	2.2487	0.42	0.66	1.208	-0.1888	-0.5131	0.6597	$^{-0.0366}_{+0.0257}$
61	0.235	5.13	2.2229	0.62	0.20	1.032	0.2508	0.5754	0.6697	$^{+0.0305}_{-0.0214}$
62	0.235	4.84	2.4268	0.62	0.40	1.175	0.1531	0.4366	0.8066	$^{+0.0345}_{-0.0242}$
63	0.237	4.82	2.2547	0.63	0.65	1.325	-0.0470	-0.1406	0.8037	$^{+0.0043}_{-0.0030}$
64	0.334	7.98	1.9413	0.27	0.18	0.918	0.3675	0.6551	0.5364	$^{+0.0365}_{-0.0257}$
65	0.337	7.70	2.2495	0.29	0.38	0.999	0.2128	0.4784	0.9767	$^{+0.0303}_{-0.0213}$
66	0.336	8.39	1.8805	0.30	0.62	1.105	-0.6089	-1.2655	1.6376	$^{-0.0735}_{+0.0517}$
67	0.334	7.91	2.0062	0.42	0.19	0.936	-0.372	-0.6989	0.8173	$^{-0.0446}_{+0.0314}$
68	0.337	7.37	2.2489	0.42	0.40	1.045	1.0930	2.5685	1.0563	$^{+0.1499}_{-0.1055}$
69	0.338	7.58	2.3659	0.43	0.66	1.271	0.0050	0.0152	1.6401	$^{-0.0111}_{+0.0078}$
70	0.334	7.56	2.0637	0.62	0.19	0.915	0.2284	0.4315	1.3717	$^{+0.0383}_{-0.0269}$
71	0.335	7.30	2.2047	0.63	0.40	0.961	-0.7289	-1.5438	1.4963	$^{-0.0826}_{+0.0580}$
72	0.337	7.00	2.1229	0.63	0.65	1.271	0.0214	0.0576	1.6899	$^{-0.0069}_{+0.0048}$
73	0.441	10.26	1.9718	0.29	0.28	0.719	0.8397	1.1906	0.8449	$^{+0.0724}_{-0.0510}$
74	0.443	10.51	1.7250	0.42	0.19	0.585	-0.6500	-0.6559	0.9880	$^{-0.0355}_{+0.0249}$
75	0.443	9.94	2.0411	0.42	0.39	0.708	0.7864	1.1358	1.4410	$^{+0.0553}_{-0.0389}$
76	0.445	9.27	2.0997	0.42	0.65	1.106	1.3403	3.1113	1.9898	$^{+0.1714}_{-0.1207}$
77	0.444	10.40	1.6911	0.63	0.19	0.609	0.8786	0.9056	2.4509	$^{+0.0491}_{-0.0345}$
78	0.444	9.89	2.1944	0.62	0.40	0.693	1.6969	2.5819	2.2083	$^{+0.1503}_{-0.1059}$
79	0.444	9.39	2.0840	0.63	0.65	0.947	0.4335	0.8560	2.2612	$^{+0.0759}_{-0.0534}$

Appendix D

Results: Asymmetries $A_1(x, Q^2)$

In this section, the final asymmetries as a function of x in two Q^2 bins are tabulated. Table D.1 defines the bin numbers and bin edges for x and Q^2. Listed are the combined asymmetries of the 1996-1997 data-taking periods for the proton target, and 1998-2000 data-taking periods for deuteron target.

Table D.1: 2-Dimensional $x - Q^2$ binning.

Bin number	x range	Q^2 range (GeV^2)
1	0.023-0.040	1.0-1.2
2	0.040-0.055	1.0-1.5
3	0.055-0.075	1.0-1.7
4	0.075-0.100	1.0-2.0
5	0.100-0.140	1.0-3.0
6	0.140-0.200	1.0-4.0
7	0.200-0.300	1.0-6.0
8	0.300-0.400	1.0-8.0
9	0.400-0.600	4.0-10.0
10	0.023-0.040	1.2-20.0
11	0.040-0.055	1.5-20.0
12	0.055-0.075	1.7-20.0
13	0.075-0.100	2.0-20.0
14	0.100-0.140	3.0-20.0
15	0.140-0.200	4.0-20.0
16	0.200-0.300	6.0-20.0
17	0.300-0.400	8.0-20.0
18	0.400-0.600	10.0-20.0

Table D.2: Semi-Inclusive Born level asymmetries for positive and negative hadrons on the proton target

bin	$< x >$	$< Q^2 >$	$\frac{1}{D(1+\eta\gamma)}$	$< z >$	$< p_{h\perp} >$	$C_\phi^{h^+}$	$A_{\|\|,p}^{h^+}$	$A_{1,p}^{h^+}$	$\pm$ stat.	syst.
1	0.032	1.09	1.5443	0.26	0.39	1.008	0.0615	0.0958	0.0338	$^{+0.0055}_{-0.0061}$
2	0.047	1.24	2.1166	0.30	0.33	1.006	0.0463	0.0986	0.0386	$^{+0.0056}_{-0.0062}$
3	0.064	1.36	2.7258	0.34	0.28	0.996	0.0592	0.1607	0.0510	$^{+0.0088}_{-0.0098}$
4	0.086	1.55	3.2980	0.37	0.27	0.977	0.0191	0.0617	0.0665	$^{+0.0027}_{-0.0030}$
5	0.116	2.14	3.2123	0.37	0.28	0.961	0.1055	0.3257	0.0514	$^{+0.0169}_{-0.0189}$
6	0.163	2.89	3.1439	0.38	0.28	0.932	0.0731	0.2142	0.0566	$^{+0.0123}_{-0.0137}$
7	0.234	4.37	2.7574	0.37	0.30	0.902	0.2019	0.5022	0.0568	$^{+0.0270}_{-0.0301}$
8	0.334	6.26	2.5369	0.37	0.32	0.868	0.2024	0.4455	0.1093	$^{+0.0255}_{-0.0284}$
9	0.432	8.39	2.3074	0.37	0.35	0.869	0.2718	0.5451	0.2515	$^{+0.0319}_{-0.0356}$
10	0.035	1.36	1.3453	0.25	0.41	1.008	0.0739	0.1002	0.0310	$^{+0.0056}_{-0.0062}$
11	0.048	1.78	1.4118	0.26	0.40	1.010	0.1074	0.1531	0.0281	$^{+0.0082}_{-0.0091}$
12	0.065	2.19	1.5723	0.28	0.37	1.011	0.0835	0.1327	0.0264	$^{+0.0071}_{-0.0079}$
13	0.087	2.71	1.6970	0.30	0.34	1.009	0.1477	0.2528	0.0287	$^{+0.0137}_{-0.0153}$
14	0.120	3.79	1.5787	0.30	0.34	1.007	0.1847	0.2937	0.0307	$^{+0.0155}_{-0.0173}$
15	0.169	5.01	1.6260	0.32	0.31	0.995	0.1849	0.2992	0.0356	$^{+0.0165}_{-0.0184}$
16	0.248	7.11	1.6037	0.33	0.30	0.976	0.2323	0.3634	0.0512	$^{+0.0197}_{-0.0219}$
17	0.346	9.29	1.6578	0.36	0.28	0.953	0.2754	0.4349	0.1066	$^{+0.0231}_{-0.0257}$
18	0.466	11.60	1.7382	0.38	0.29	0.942	0.4103	0.6721	0.1780	$^{+0.0363}_{-0.0404}$
bin	$< x >$	$< Q^2 >$	$\frac{1}{D(1+\eta\gamma)}$	$< z >$	$< p_{h\perp} >$	$C_\phi^{h^-}$	$A_{\|\|,p}^{h^-}$	$A_{1,p}^{h^-}$	$\pm$ stat.	syst.
1	0.031	1.09	1.5346	0.27	0.41	0.994	0.0345	0.0526	0.0360	$^{+0.0032}_{-0.0036}$
2	0.047	1.25	2.1036	0.31	0.34	0.998	0.0598	0.1256	0.0451	$^{+0.0071}_{-0.0080}$
3	0.064	1.37	2.7003	0.35	0.30	0.997	0.0328	0.0883	0.0624	$^{+0.0055}_{-0.0062}$
4	0.086	1.57	3.2416	0.38	0.28	1.002	0.0567	0.1840	0.0858	$^{+0.0087}_{-0.0097}$
5	0.116	2.16	3.1526	0.38	0.29	1.011	0.0645	0.2054	0.0698	$^{+0.0113}_{-0.0126}$
6	0.162	2.92	3.0896	0.38	0.30	1.021	0.0513	0.1619	0.0824	$^{+0.0080}_{-0.0089}$
7	0.232	4.44	2.6889	0.38	0.31	1.026	0.0853	0.2353	0.0889	$^{+0.0127}_{-0.0142}$
8	0.333	6.28	2.5162	0.37	0.34	1.043	0.2986	0.7834	0.1909	$^{+0.0411}_{-0.0458}$
9	0.429	8.33	2.3182	0.38	0.36	1.073	0.0637	0.1584	0.4348	$^{+0.0136}_{-0.0152}$
10	0.035	1.36	1.3418	0.25	0.42	0.992	0.0460	0.0613	0.0335	$^{+0.0029}_{-0.0032}$
11	0.048	1.78	1.4050	0.26	0.41	0.994	0.0690	0.0964	0.0317	$^{+0.0051}_{-0.0057}$
12	0.065	2.19	1.5623	0.28	0.38	0.997	0.0612	0.0953	0.0306	$^{+0.0047}_{-0.0052}$
13	0.087	2.73	1.6811	0.29	0.35	0.998	0.0700	0.1174	0.0343	$^{+0.0062}_{-0.0069}$
14	0.120	3.79	1.5720	0.30	0.35	0.999	0.1377	0.2162	0.0381	$^{+0.0117}_{-0.0131}$
15	0.169	5.04	1.6105	0.31	0.33	0.994	0.1940	0.3104	0.0456	$^{+0.0163}_{-0.0181}$
16	0.248	7.13	1.5951	0.33	0.31	0.984	0.1851	0.2906	0.0693	$^{+0.0155}_{-0.0173}$
17	0.346	9.29	1.6549	0.35	0.29	0.978	0.3907	0.6327	0.1491	$^{+0.0331}_{-0.0369}$
18	0.467	11.56	1.7483	0.38	0.30	1.015	0.3270	0.5805	0.2918	$^{+0.0316}_{-0.0353}$

Table D.3: Semi-Inclusive Born level asymmetries for positive and negative pions on the proton target

bin	$< x >$	$< Q^2 >$	$\frac{1}{D(1+\eta\gamma)}$	$< z >$	$< p_{h\perp} >$	$C_\phi^{\pi^+}$	$A_{\|\|,p}^{\pi^+}$	$A_{1,p}^{\pi^+}$	$\pm$ stat.	syst.
1	0.031	1.09	1.5167	0.32	0.47	1.014	0.0301	0.0462	0.0489	$^{+0.0025}_{-0.0028}$
2	0.046	1.26	2.0720	0.43	0.40	1.019	0.0362	0.0765	0.0648	$^{+0.0039}_{-0.0044}$
3	0.063	1.40	2.6077	0.50	0.35	1.002	0.0507	0.1324	0.0928	$^{+0.0064}_{-0.0071}$
4	0.085	1.63	3.0360	0.56	0.33	0.970	0.0263	0.0776	0.1314	$^{+0.0018}_{-0.0020}$
5	0.115	2.35	2.7556	0.55	0.33	0.957	0.1373	0.3618	0.0952	$^{+0.0190}_{-0.0212}$
6	0.160	3.19	2.6885	0.56	0.34	0.929	0.0948	0.2367	0.1117	$^{+0.0114}_{-0.0127}$
7	0.229	4.80	2.3791	0.55	0.35	0.909	0.0983	0.2126	0.1126	$^{+0.0129}_{-0.0144}$
8	0.332	6.66	2.3337	0.55	0.39	0.877	0.2731	0.5587	0.2389	$^{+0.0303}_{-0.0338}$
9	0.430	8.64	2.2322	0.55	0.43	0.884	0.4509	0.8901	0.6487	$^{+0.0511}_{-0.0569}$
10	0.035	1.37	1.3370	0.31	0.49	1.008	0.0769	0.1037	0.0440	$^{+0.0055}_{-0.0062}$
11	0.048	1.79	1.3970	0.33	0.47	1.011	0.0866	0.1224	0.0419	$^{+0.0065}_{-0.0073}$
12	0.065	2.22	1.5376	0.36	0.44	1.014	0.0821	0.1281	0.0402	$^{+0.0067}_{-0.0075}$
13	0.087	2.78	1.6409	0.39	0.41	1.014	0.1395	0.2321	0.0447	$^{+0.0121}_{-0.0135}$
14	0.120	3.83	1.5514	0.39	0.40	1.012	0.2315	0.3633	0.0484	$^{+0.0193}_{-0.0215}$
15	0.168	5.08	1.5878	0.42	0.37	1.001	0.1704	0.2710	0.0572	$^{+0.0148}_{-0.0165}$
16	0.247	7.19	1.5692	0.44	0.35	0.986	0.1927	0.2983	0.0839	$^{+0.0163}_{-0.0181}$
17	0.344	9.49	1.6112	0.47	0.33	0.969	0.3466	0.5413	0.1738	$^{+0.0282}_{-0.0314}$
18	0.461	11.82	1.6855	0.50	0.33	0.967	0.5409	0.8818	0.3205	$^{+0.0472}_{-0.0526}$
bin	$< x >$	$< Q^2 >$	$\frac{1}{D(1+\eta\gamma)}$	$< z >$	$< p_{h\perp} >$	$C_\phi^{\pi^-}$	$A_{\|\|,p}^{\pi^-}$	$A_{1,p}^{\pi^-}$	$\pm$ stat.	syst.
1	0.031	1.09	1.5077	0.33	0.48	0.986	0.011	0.017	0.0517	$^{+0.0012}_{-0.0014}$
2	0.046	1.26	2.0638	0.42	0.41	0.998	0.079	0.163	0.0721	$^{+0.0093}_{-0.0104}$
3	0.063	1.40	2.60559	0.49	0.35	0.980	-0.019	-0.048	0.1061	$^{-0.0015}_{+0.0017}$
4	0.085	1.63	3.0281	0.55	0.33	0.955	0.076	0.220	0.1520	$^{+0.0104}_{-0.0116}$
5	0.115	2.35	2.7506	0.533	0.34	0.964	0.045	0.119	0.1181	$^{+0.0065}_{-0.0073}$
6	0.160	3.19	2.6850	0.55	0.34	0.980	-0.035	-0.091	0.1469	$^{-0.0048}_{+0.0054}$
7	0.229	4.79	2.3925	0.53	0.36	1.016	0.110	0.268	0.1643	$^{+0.0133}_{-0.0149}$
8	0.331	6.64	2.3348	0.53	0.40	1.086	0.183	0.463	0.3895	$^{+0.0227}_{-0.0254}$
9	0.427	8.60	2.2150	0.53	0.43	1.177	0.006	0.0161	1.0106	$^{+0.0044}_{-0.0049}$
10	0.035	1.37	1.3336	0.30	0.49	0.980	0.060	0.0778	0.0469	$^{+0.0037}_{-0.0041}$
11	0.048	1.80	1.3900	0.32	0.48	0.982	0.085	0.1155	0.0446	$^{+0.0063}_{-0.0070}$
12	0.065	2.23	1.5298	0.35	0.44	0.988	0.051	0.0765	0.0442	$^{+0.0037}_{-0.0041}$
13	0.087	2.80	1.6299	0.38	0.42	0.990	0.028	0.0449	0.0515	$^{+0.0025}_{-0.0028}$
14	0.119	3.84	1.5436	0.38	0.41	0.993	0.087	0.1331	0.0575	$^{+0.0072}_{-0.0080}$
15	0.168	5.12	1.5723	0.40	0.38	0.994	0.131	0.2051	0.0697	$^{+0.0113}_{-0.0126}$
16	0.245	7.19	1.5620	0.42	0.36	0.998	0.245	0.3819	0.1070	$^{+0.0202}_{-0.0225}$
17	0.342	9.34	1.6294	0.45	0.33	1.012	0.263	0.4342	0.2434	$^{+0.0229}_{-0.0255}$
18	0.463	11.49	1.7452	0.48	0.34	1.083	0.266	0.5038	0.5050	$^{+0.0282}_{-0.0315}$

Table D.4: Semi-Inclusive Born level asymmetries for positive and negative hadrons on the deuteron target

bin	$< x >$	$< Q^2 >$	$\frac{1}{D(1+\eta\gamma)}$	$< z >$	$< p_{h\perp} >$	$C_\phi^{h^+}$	$A_{\parallel,d}^{h^+}$	$A_{1,d}^{h^+}$	$\pm$ stat.	syst.
1	0.032	1.09	1.1842	0.26	0.39	1.008	0.0021	0.0025	0.0125	$^{+0.0006}_{-0.0004}$
2	0.047	1.25	1.4697	0.31	0.33	1.009	-0.0025	-0.0037	0.0134	$^{-0.0003}_{+0.0002}$
3	0.064	1.37	1.6612	0.34	0.29	1.000	0.0165	0.0273	0.0160	$^{+0.0017}_{-0.0012}$
4	0.086	1.55	1.7626	0.37	0.27	0.986	0.0287	0.0498	0.0189	$^{+0.0028}_{-0.0020}$
5	0.116	2.14	1.6348	0.38	0.28	0.974	0.0084	0.0134	0.0141	$^{+0.0010}_{-0.0007}$
6	0.163	2.90	1.5118	0.38	0.29	0.950	0.0440	0.0632	0.0148	$^{+0.0039}_{-0.0027}$
7	0.233	4.38	1.3412	0.38	0.30	0.920	0.0525	0.0648	0.0151	$^{+0.0042}_{-0.0029}$
8	0.334	6.27	1.2328	0.38	0.33	0.877	0.0594	0.0642	0.0305	$^{+0.0046}_{-0.0032}$
9	0.432	8.38	1.1402	0.37	0.35	0.859	0.0624	0.0611	0.0702	$^{+0.0062}_{-0.0044}$
10	0.035	1.36	1.0556	0.25	0.41	1.005	-0.0064	-0.0068	0.0118	$^{+0.0001}_{-0.0001}$
11	0.048	1.78	1.0857	0.26	0.40	1.007	0.0215	0.0235	0.0105	$^{+0.0015}_{-0.0010}$
12	0.065	2.18	1.1731	0.28	0.37	1.008	0.0219	0.0259	0.0096	$^{+0.0016}_{-0.0011}$
13	0.087	2.72	1.2189	0.30	0.34	1.005	0.0284	0.0348	0.0103	$^{+0.0024}_{-0.0017}$
14	0.120	3.79	1.1396	0.30	0.34	1.003	0.0676	0.0773	0.0111	$^{+0.0048}_{-0.0034}$
15	0.169	5.01	1.1335	0.32	0.32	0.992	0.0600	0.0675	0.0128	$^{+0.0044}_{-0.0031}$
16	0.248	7.12	1.0974	0.34	0.30	0.974	0.1250	0.1336	0.0185	$^{+0.0083}_{-0.0058}$
17	0.346	9.30	1.0715	0.37	0.29	0.948	0.2205	0.2240	0.0379	$^{+0.0134}_{-0.0094}$
18	0.463	11.55	1.0138	0.39	0.29	0.925	0.1905	0.1786	0.0598	$^{+0.0116}_{-0.0081}$
bin	$< x >$	$< Q^2 >$	$\frac{1}{D(1+\eta\gamma)}$	$< z >$	$< p_{h\perp} >$	$C_\phi^{h^-}$	$A_{\parallel,d}^{h^-}$	$A_{1,d}^{h^-}$	$\pm$ stat.	syst.
1	0.031	1.08	1.3424	0.26	0.41	1.000	0.0019	0.0026	0.0150	$^{+0.0009}_{-0.0006}$
2	0.047	1.25	1.7408	0.31	0.34	1.003	0.0091	0.0160	0.0179	$^{+0.0003}_{-0.0002}$
3	0.064	1.37	2.0487	0.35	0.30	0.999	0.0019	0.0040	0.0230	$^{+0.0011}_{-0.0008}$
4	0.086	1.56	2.2494	0.38	0.28	0.999	0.0065	0.0146	0.0292	$^{+0.0007}_{-0.0005}$
5	0.116	2.16	2.1396	0.38	0.29	1.010	0.0343	0.0741	0.0234	$^{+0.0036}_{-0.0025}$
6	0.162	2.92	2.0648	0.38	0.29	1.019	0.0427	0.0898	0.0276	$^{+0.0054}_{-0.0038}$
7	0.232	4.43	1.8628	0.37	0.31	1.020	0.0692	0.1314	0.0310	$^{+0.0085}_{-0.0060}$
8	0.333	6.31	1.7740	0.37	0.33	1.041	0.0994	0.1835	0.0706	$^{+0.0120}_{-0.0084}$
9	0.431	8.37	1.7278	0.38	0.36	1.091	0.0756	0.1425	0.1911	$^{+0.0129}_{-0.0091}$
10	0.035	1.36	1.1823	0.25	0.42	0.995	-0.0135	-0.0159	0.0140	$^{-0.0001}_{+0.0001}$
11	0.048	1.78	1.2372	0.26	0.41	0.996	0.0042	0.0052	0.0132	$^{+0.0002}_{-0.0001}$
12	0.065	2.19	1.3525	0.28	0.38	0.999	0.0223	0.0301	0.0125	$^{+0.0020}_{-0.0014}$
13	0.087	2.73	1.4284	0.30	0.35	0.999	0.0182	0.0260	0.0138	$^{+0.0016}_{-0.0011}$
14	0.120	3.80	1.3450	0.30	0.35	0.998	0.0333	0.0447	0.0155	$^{+0.0030}_{-0.0021}$
15	0.169	5.03	1.3643	0.31	0.32	0.993	0.0444	0.0602	0.0188	$^{+0.0038}_{-0.0027}$
16	0.248	7.11	1.3517	0.33	0.31	0.984	0.1129	0.1502	0.0292	$^{+0.0093}_{-0.0065}$
17	0.346	9.33	1.3963	0.35	0.30	0.982	0.2073	0.2841	0.0676	$^{+0.0176}_{-0.0124}$
18	0.463	11.63	1.4398	0.38	0.30	1.028	0.1382	0.2045	0.1336	$^{+0.0138}_{-0.0097}$

Table D.5: Semi-Inclusive Born level asymmetries for positive and negative pions on the deuteron target

bin	$< x >$	$< Q^2 >$	$\frac{1}{D(1+\eta\gamma)}$	$< z >$	$< p_{h\perp} >$	$C_\phi^{\pi^+}$	$A_{\|\|,d}^{\pi^+}$	$A_{1,d}^{\pi^+}$	$\pm$ stat.	syst.
1	0.032	1.09	1.5397	0.27	0.40	1.007	0.0015	0.0024	0.0180	$^{+0.0007}_{-0.0005}$
2	0.047	1.25	2.0906	0.32	0.35	1.008	-0.0114	-0.0241	0.0228	$^{-0.0014}_{+0.0010}$
3	0.064	1.38	2.6742	0.38	0.31	0.995	0.0095	0.0252	0.0328	$^{+0.0020}_{-0.0014}$
4	0.085	1.58	3.1822	0.43	0.30	0.972	0.0094	0.0291	0.0453	$^{+0.0014}_{-0.0010}$
5	0.116	2.20	3.0291	0.43	0.30	0.962	0.0208	0.0605	0.0350	$^{+0.0034}_{-0.0024}$
6	0.162	2.98	2.9597	0.44	0.31	0.944	0.0470	0.1314	0.0401	$^{+0.0075}_{-0.0052}$
7	0.233	4.49	2.6052	0.43	0.33	0.924	0.0537	0.1292	0.0412	$^{+0.0078}_{-0.0055}$
8	0.334	6.37	2.4484	0.43	0.36	0.888	0.0971	0.2110	0.0865	$^{+0.0129}_{-0.0091}$
9	0.432	8.44	2.2792	0.43	0.38	0.875	0.0613	0.1223	0.2038	$^{+0.0117}_{-0.0082}$
10	0.035	1.36	1.3456	0.25	0.42	1.005	-0.0048	-0.0065	0.0169	$^{-0.0002}_{+0.0001}$
11	0.048	1.78	1.4091	0.26	0.40	1.006	0.0202	0.0287	0.0157	$^{+0.0017}_{-0.0012}$
12	0.065	2.19	1.5646	0.28	0.38	1.006	0.0190	0.0298	0.0149	$^{+0.0018}_{-0.0013}$
13	0.087	2.73	1.6768	0.31	0.36	1.003	0.0259	0.0435	0.0166	$^{+0.0031}_{-0.0021}$
14	0.120	3.80	1.5646	0.31	0.35	1.000	0.0712	0.1114	0.0180	$^{+0.0070}_{-0.0049}$
15	0.169	5.03	1.6087	0.33	0.33	0.992	0.0552	0.0880	0.0217	$^{+0.0055}_{-0.0039}$
16	0.248	7.13	1.5891	0.35	0.32	0.976	0.1221	0.1894	0.0326	$^{+0.0117}_{-0.0082}$
17	0.346	9.31	1.6454	0.38	0.30	0.954	0.2547	0.3997	0.0730	$^{+0.0238}_{-0.0168}$
18	0.463	11.58	1.7241	0.42	0.31	0.934	0.0999	0.1610	0.1368	$^{+0.0117}_{-0.0082}$
bin	$< x >$	$< Q^2 >$	$\frac{1}{D(1+\eta\gamma)}$	$< z >$	$< p_{h\perp} >$	$C_\phi^{\pi^-}$	$A_{\|\|,d}^{\pi^-}$	$A_{1,d}^{\pi^-}$	$\pm$ stat.	syst.
1	0.031	1.09	1.5326	0.26	0.40	0.998	0.0018	0.0028	0.0184	$^{+0.0009}_{-0.0007}$
2	0.047	1.25	2.0874	0.31	0.35	1.001	0.0088	0.0183	0.0238	$^{+0.0005}_{-0.0003}$
3	0.063	1.38	2.6705	0.37	0.31	0.993	-0.0029	-0.0077	0.0346	$^{+0.0005}_{-0.0004}$
4	0.085	1.59	3.1827	0.41	0.30	0.985	0.0039	0.0121	0.0489	$^{+0.0006}_{-0.0004}$
5	0.116	2.22	3.0403	0.41	0.30	0.996	0.0259	0.0785	0.0394	$^{+0.0042}_{-0.0029}$
6	0.162	3.00	2.9799	0.42	0.31	1.011	0.0574	0.1728	0.0477	$^{+0.0092}_{-0.0065}$
7	0.232	4.54	2.6163	0.41	0.33	1.029	0.0777	0.2090	0.0522	$^{+0.0135}_{-0.0095}$
8	0.333	6.42	2.4555	0.41	0.35	1.085	0.1002	0.2669	0.1206	$^{+0.0177}_{-0.0124}$
9	0.431	8.45	2.2894	0.40	0.38	1.185	0.0468	0.1271	0.3173	$^{+0.0134}_{-0.0094}$
10	0.035	1.36	1.3425	0.25	0.42	0.992	-0.0076	-0.0102	0.0172	$^{+0.0002}_{-0.0002}$
11	0.048	1.78	1.4073	0.26	0.40	0.993	-0.0016	-0.0022	0.0162	$^{-0.0002}_{+0.0001}$
12	0.065	2.20	1.5594	0.28	0.37	0.995	0.0184	0.0286	0.0157	$^{+0.0021}_{-0.0014}$
13	0.087	2.74	1.6717	0.30	0.35	0.996	0.0257	0.0428	0.0178	$^{+0.0025}_{-0.0018}$
14	0.120	3.80	1.5643	0.30	0.35	0.995	0.0403	0.0628	0.0197	$^{+0.0042}_{-0.0030}$
15	0.168	5.04	1.6053	0.32	0.33	0.992	0.0360	0.0573	0.0244	$^{+0.0036}_{-0.0025}$
16	0.247	7.13	1.5899	0.33	0.31	0.988	0.1071	0.1683	0.0381	$^{+0.0104}_{-0.0073}$
17	0.346	9.35	1.6442	0.36	0.30	1.002	0.2165	0.3565	0.0896	$^{+0.0221}_{-0.0155}$
18	0.463	11.66	1.7217	0.38	0.30	1.098	0.0272	0.0514	0.1894	$^{+0.0051}_{-0.0036}$

Table D.6: Semi-Inclusive Born level asymmetries for positive and negative kaons on the deuteron target

bin	$< x >$	$< Q^2 >$	$\frac{1}{D(1+\eta\gamma)}$	$< z >$	$< p_{h\perp} >$	$C_\phi^{K^+}$	$A_{\|\|,d}^{K^+}$	$A_{1,d}^{K^+}$	$\pm$ stat.	syst.
1	0.032	1.09	1.5530	0.34	0.44	1.018	0.0172	0.0273	0.0580	$^{+0.0048}_{-0.0034}$
2	0.047	1.24	2.1090	0.40	0.37	1.030	0.0067	0.0145	0.0687	$^{+0.0003}_{-0.0002}$
3	0.064	1.37	2.6819	0.45	0.32	1.014	0.0610	0.1659	0.0916	$^{+0.0116}_{-0.0082}$
4	0.086	1.57	3.1680	0.49	0.30	0.985	-0.0171	-0.0534	0.1242	$^{-0.0044}_{+0.0031}$
5	0.116	2.18	2.9668	0.49	0.31	0.966	0.0439	0.1258	0.0929	$^{+0.0074}_{-0.0052}$
6	0.162	2.95	2.9167	0.50	0.31	0.924	0.0680	0.1832	0.1054	$^{+0.0124}_{-0.0087}$
7	0.233	4.45	2.5778	0.50	0.33	0.884	0.0569	0.1297	0.1052	$^{+0.0072}_{-0.0050}$
8	0.333	6.33	2.4180	0.51	0.36	0.831	0.1082	0.2175	0.2264	$^{+0.0119}_{-0.0083}$
9	0.432	8.43	2.2651	0.51	0.40	0.810	0.5100	0.9363	0.5598	$^{+0.0614}_{-0.0432}$
10	0.035	1.36	1.3521	0.32	0.46	1.009	-0.0294	-0.0401	0.0554	$^{-0.0020}_{+0.0014}$
11	0.048	1.78	1.4203	0.33	0.44	1.012	0.0963	0.1384	0.0492	$^{+0.0083}_{-0.0058}$
12	0.065	2.18	1.5810	0.36	0.41	1.014	0.0608	0.0976	0.0452	$^{+0.0062}_{-0.0044}$
13	0.087	2.71	1.7005	0.38	0.38	1.008	0.0809	0.1386	0.0489	$^{+0.0088}_{-0.0062}$
14	0.120	3.78	1.5787	0.39	0.37	0.996	0.0083	0.0131	0.0513	$^{+0.0013}_{-0.0009}$
15	0.169	5.01	1.6145	0.41	0.35	0.984	0.1102	0.1751	0.0582	$^{+0.0110}_{-0.0077}$
16	0.248	7.12	1.5945	0.44	0.33	0.965	0.1734	0.2668	0.0857	$^{+0.0167}_{-0.0117}$
17	0.346	9.31	1.6412	0.47	0.31	0.955	-0.0404	-0.0634	0.1938	$^{-0.0037}_{+0.0026}$
18	0.463	11.59	1.7461	0.52	0.31	0.962	0.7308	1.2270	0.3810	$^{+0.0722}_{-0.0508}$
bin	$< x >$	$< Q^2 >$	$\frac{1}{D(1+\eta\gamma)}$	$< z >$	$< p_{h\perp} >$	$C_\phi^{K^-}$	$A_{\|\|,d}^{K^-}$	$A_{1,d}^{K^-}$	$\pm$ stat.	syst.
1	0.032	1.09	1.5374	0.32	0.46	0.995	0.0340	0.0520	0.0723	$^{+0.0030}_{-0.0021}$
2	0.047	1.25	2.0987	0.38	0.38	1.003	0.0667	0.1405	0.0923	$^{+0.0054}_{-0.0038}$
3	0.064	1.37	2.6601	0.43	0.33	0.984	-0.0357	-0.0936	0.1280	$^{-0.0016}_{+0.0011}$
4	0.085	1.58	3.1233	0.46	0.31	1.003	0.0802	0.2513	0.1849	$^{+0.0150}_{-0.0105}$
5	0.116	2.20	2.9314	0.46	0.32	1.054	0.0067	0.0206	0.1527	$^{-0.0010}_{+0.0007}$
6	0.162	2.98	2.8637	0.47	0.33	1.126	-0.0012	-0.0038	0.2029	$^{+0.0022}_{-0.0015}$
7	0.232	4.49	2.5396	0.46	0.35	1.131	0.0066	0.0190	0.2311	$^{+0.0023}_{-0.0016}$
8	0.333	6.38	2.3905	0.46	0.37	1.053	0.1767	0.4448	0.5109	$^{+0.0242}_{-0.0170}$
9	0.430	8.45	2.2815	0.48	0.42	0.752	0.8677	1.4878	1.9152	$^{+0.0834}_{-0.0587}$
10	0.035	1.36	1.3498	0.30	0.47	0.983	-0.0548	-0.0727	0.0662	$^{-0.0035}_{+0.0024}$
11	0.048	1.78	1.4123	0.31	0.46	0.985	0.0331	0.0460	0.0607	$^{+0.0023}_{-0.0016}$
12	0.065	2.19	1.5619	0.34	0.42	0.990	-0.0067	-0.0104	0.0588	$^{-0.0007}_{+0.0005}$
13	0.087	2.72	1.6778	0.36	0.39	0.988	-0.0483	-0.0801	0.0660	$^{-0.0048}_{+0.0034}$
14	0.120	3.79	1.5646	0.36	0.38	0.987	-0.0038	-0.0058	0.0717	$^{+0.0008}_{-0.0006}$
15	0.168	5.02	1.6172	0.38	0.36	0.996	0.1627	0.2621	0.0915	$^{+0.0158}_{-0.0111}$
16	0.248	7.11	1.6000	0.39	0.35	1.001	0.1754	0.2809	0.1447	$^{+0.0172}_{-0.0121}$
17	0.345	9.34	1.6615	0.42	0.33	0.975	0.1078	0.1747	0.3559	$^{+0.0117}_{-0.0082}$
18	0.464	11.66	1.7161	0.45	0.33	0.742	0.6300	0.8018	0.7625	$^{+0.0497}_{-0.0350}$

Appendix E

Hadron charge difference asymmetry

Table E.1: Pions charge difference asymmetry on the proton target

bin	$< x >$	$< Q^2 >$	$\frac{1}{D(1+\eta\gamma)}$	$< z >$	$< p_{h\perp} >$	$C_{\phi}^{\pi^+-\pi^-}$	$A_{\|\|,p}^{\pi^+-\pi^-}$	$A_{1,p}^{\pi^+-\pi^-}$	$\pm$ stat.	syst.
1	0.033	1.22	1.4328	0.32	0.48	1.165	0.123313	0.2067	0.2489	$^{+0.0112}_{-0.0125}$
2	0.047	1.50	1.7362	0.39	0.43	1.114	-0.007812	-0.0133	0.2297	$^{-0.0030}_{+0.0033}$
3	0.064	1.83	1.9356	0.43	0.40	1.082	0.172113	0.3572	0.2158	$^{+0.0175}_{-0.0195}$
4	0.087	2.29	2.0400	0.47	0.38	1.044	0.249157	0.5328	0.2082	$^{+0.0252}_{-0.0281}$
5	0.118	2.94	2.0699	0.49	0.36	0.990	0.420272	0.8626	0.1771	$^{+0.0450}_{-0.0501}$
6	0.165	3.95	2.0267	0.51	0.36	0.924	0.261339	0.4892	0.1792	$^{+0.0255}_{-0.0285}$
7	0.238	5.50	1.9890	0.52	0.36	0.840	0.090487	0.1512	0.1904	$^{+0.0112}_{-0.0125}$
8	0.338	7.65	1.9663	0.53	0.38	0.756	0.395789	0.5892	0.3410	$^{+0.0329}_{-0.0367}$
9	0.449	10.20	1.8791	0.53	0.38	0.739	1.112169	1.5434	0.8365	$^{+0.0828}_{-0.0923}$

Table E.2: Hadrons charge difference asymmetry on the deutron target

bin	$< x >$	$< Q^2 >$	$\frac{1}{D(1+\eta\gamma)}$	$< z >$	$< p_{h\perp} >$	$C_\phi^{h^+-h^-}$	$A_{\|\|,d}^{h^+-h^-}$	$A_{1,d}^{h^+-h^-}$	$\pm$ stat.	syst.
1	0.033	1.21	1.4573	0.26	0.40	1.040	0.0141	0.0214	0.0796	$^{+0.0005}_{-0.0004}$
2	0.047	1.46	1.8077	0.29	0.36	1.032	0.0164	0.0306	0.0646	$^{+0.0027}_{-0.0019}$
3	0.065	1.75	2.1170	0.32	0.33	1.015	0.0367	0.0787	0.0619	$^{+0.0035}_{-0.0025}$
4	0.087	2.11	2.3896	0.35	0.31	0.990	0.0535	0.1266	0.0660	$^{+0.0083}_{-0.0058}$
5	0.118	2.66	2.5582	0.36	0.30	0.951	0.0314	0.0765	0.0589	$^{+0.0059}_{-0.0042}$
6	0.165	3.65	2.5167	0.37	0.30	0.908	0.0594	0.1358	0.0571	$^{+0.0088}_{-0.0062}$
7	0.238	5.22	2.3949	0.37	0.31	0.853	0.0613	0.1253	0.0585	$^{+0.0080}_{-0.0056}$
8	0.338	7.24	2.2487	0.38	0.32	0.789	0.0833	0.1478	0.1045	$^{+0.0098}_{-0.0069}$
9	0.445	9.80	2.0758	0.38	0.32	0.758	0.1421	0.2238	0.1763	$^{+0.0168}_{-0.0118}$

Table E.3: Pions charge difference asymmetry on the deutron target

bin	$< x >$	$< Q^2 >$	$\frac{1}{D(1+\eta\gamma)}$	$< z >$	$< p_{h\perp} >$	$C_\phi^{\pi^+-\pi^-}$	$A_{\|\|,d}^{\pi^+-\pi^-}$	$A_{1,d}^{\pi^+-\pi^-}$	$\pm$ stat.	syst.
1	0.033	1.21	1.4522	0.26	0.41	1.041	0.0026	0.0039	0.1656	$^{-0.0042}_{+0.0029}$
2	0.047	1.48	1.7774	0.30	0.37	1.017	0.0002	0.0003	0.1460	$^{+0.0022}_{-0.0016}$
3	0.064	1.80	2.0362	0.34	0.35	1.029	0.0447	0.0936	0.1416	$^{+0.0023}_{-0.0036}$
4	0.087	2.20	2.2354	0.37	0.33	1.035	0.0198	0.0458	0.1502	$^{+0.0035}_{-0.0040}$
5	0.118	2.80	2.3346	0.39	0.33	1.015	0.0938	0.2224	0.1345	$^{+0.0082}_{-0.0155}$
6	0.165	3.82	2.2970	0.40	0.33	0.993	0.0615	0.1403	0.1339	$^{+0.0059}_{-0.0109}$
7	0.238	5.30	2.2204	0.41	0.33	0.965	0.0479	0.1027	0.1437	$^{+0.0028}_{-0.0069}$
8	0.338	7.40	2.1440	0.42	0.34	0.889	0.1932	0.3683	0.2762	$^{+0.0134}_{-0.0217}$
9	0.446	9.92	2.0268	0.42	0.35	0.743	0.2000	0.3012	0.4465	$^{+0.0180}_{-0.0187}$

Table E.4: Kaons charge difference asymmetry on the deutron target

bin	$< x >$	$< Q^2 >$	$\frac{1}{D(1+\eta\gamma)}$	$< z >$	$< p_{h\perp} >$	$C_\phi^{K^+-K^-}$	$A_{\|\|,d}^{K^+-K^-}$	$A_{1,d}^{K^+-K^-}$	$\pm$ stat.	syst.
1	0.033	1.21	1.4650	0.32	0.45	1.096	-0.0284	-0.0456	0.1167	$^{+0.0029}_{-0.0022}$
2	0.047	1.47	1.8100	0.37	0.40	1.087	0.0274	0.0540	0.1059	$^{+0.0059}_{-0.0045}$
3	0.065	1.75	2.0858	0.41	0.36	1.058	0.1282	0.2829	0.1003	$^{+0.0124}_{-0.0159}$
4	0.087	2.15	2.2787	0.44	0.34	0.999	0.0889	0.2023	0.1071	$^{+0.0061}_{-0.0151}$
5	0.118	2.73	2.3365	0.46	0.33	0.928	0.0449	0.0972	0.0928	$^{+0.0012}_{-0.0104}$
6	0.165	3.71	2.2756	0.48	0.33	0.851	0.0888	0.1719	0.0868	$^{+0.0006}_{-0.0197}$
7	0.238	5.30	2.1987	0.48	0.33	0.806	0.1188	0.2101	0.0952	$^{+0.0007}_{-0.0216}$
8	0.336	7.45	2.0996	0.50	0.35	0.811	-0.0053	-0.0090	0.2003	$^{-0.0003}_{+0.0010}$
9	0.445	10.07	2.0224	0.51	0.35	0.940	0.5753	1.0934	0.4277	$^{+0.0549}_{-0.0632}$

Bibliography

[1] M. Gell-Mann. A schematic model of baryons and mesons. *Phys. Lett.* **8**, 214 (1964).

[2] G. Zweig. An SU(3) model for strong interaction symmetry and its breaking. 2.CERN-TH-412.

[3] R. P. Feynman. Very high-energy collisions of hadrons. *Phys. Rev. Lett.* **23**, 1415 (1969).

[4] M. J. Alguard *et al.* (SLAC). Deep inelastic scattering of polarized electrons by polarized protons. *Phys. Rev. Lett.* **37**, 1261 (1976).

[5] J. Ashman *et al.* (EMC). A measurement of the spin asymmetry an determination of the structure function g_1 in deep inelastic muon proton scattering. *Phys. Lett.* **B 206**, 364 (1988).

[6] R. P. Feymann. Photon-hadron interations. *Reading*, 1972.

[7] E. D. Bloom *et al.* (SLAC). High-energy inelastic e-p scattering at 6° and 10°. *Phys. Rev. Lett.* **23**, 930 (1969).

[8] M. Breidenbach *et al.* (SLAC) Observed behavior of highly inelastic electron-proton scattering. *Phys. Rev. Lett.* **23**, 935 (1969).

[9] J. R. Ellis and R. L. Jaffe. A sum rule for deep inelastic electroproduction from polarized protons. *Phys. Rev.* **D 9**, 1444 (1974).

[10] M. J. Alguard *et al.* (SLAC). Deep inelastic *ep* asymmetry measurements and comparison with the bjorken sum rule and models of the proton spin structure. *Phys. Rev. Lett.* **41**, 70 (1978).

[11] G. Baum *et al.* (SLAC). A new measurement of deep inelastic *ep* asymmetries. *Phys. Rev. Lett.* **51**, 1135 (1983).

[12] J. Ashman *et al.* (EMC). An investigation of the spin structure of the proton in deep inelastic scattering of polarized muons on polarized protons. *Nucl. Phys.* **B 328**, 1 (1989).

[13] A. Airapetian *et al.* (HERMES). Quark helicity distributions in the nucleon for *up*, *down*, and *strange* quarks from semi-inclusive deep-inelastic scattering. *Phys. Rev.* **D 71**, 012003 (2005).

[14] A. Airapetian *et al.* (HERMES). Precise determination of the spin structure function g_1 of the proton, deuteron and neutron. *Phys. Rev.* **D 75**, 012007 (2007).

[15] E. S Ageev *et al.* (COMPASS). Measurement of the spin structure of the deuteron in the DIS region. *Phys. Lett.* **B 612**, 154 (2005).

[16] V. Yu. Alexakhin *et al.* (COMPASS). Spin asymmetry A_1^d and the spin-dependent structure function g1d of the deuteron at low values of x and Q^2. *Phys. Lett.* **B 647**, 330 (2007).

[17] F. E. Close. An introduction to quarks and partons. Academic press, (1979).

[18] F. Halzen, A. D. Martin. Quarks and leptons. John Wiley Sons, (1984).

[19] M. Düren. The HERMES Experiment: From the Design to the First Results, Habilitation, Universität Erlangen-Nürnberg. HERMES-95-02, (1995).

[20] X. Zheng *et al.* (JLAB). Precision measurement of the neutron spin asymmetries and spin-dependent structure functions in the valence quark region. *Phys. Rev.* **C 70**, 065207 (2004).

[21] M. Anselmino, A. Efremov, E. Leader. The theory and phenomenology of polarized deep-inelastic scattering. *Phys. Rep.* **261**, 1 (1995). Erratum *ibid.*, **281**, 399 (1997).

[22] J. J. Aubert *et al.* (EMC). The ratio of the nucleon structure functions F_2^N for iron and deuterium. *Phys. Lett.* **B 123**, 275 (1983).

[23] L.W. Whitlow, E.M. Riordan, S. Dasu, S. Rock, A. Bodek. (SLAC). Precise measurements of the proton an deuteron structure functions from a global analysis of the deep inelastic scattering cross sections. *Phys. Lett.* **B 6282**, 475 (1992).

[24] A.C. Benvenuti *et al.* (BCDMS). A high statistics measurement of the proton structure functions $F_2(x, Q^2)$ and r from deep inelastic muon scattering at high Q^2. *Phys. Lett.* **B 6223**, 485 (1989).

[25] M. Arneodo *et al.* (NMC). Measurement of the proton and deuteron structure functions, $F_2(p)$ and $F_2(d)$, and of the ratio $\sigma(L)/\sigma(T)$. *Nucl. Phys.* **B 483**, 3 (1997).

[26] M.R. Adams *et al.* (E665). Proton and deuteron structure functions in muon scattering at 470 GeV. *Phys. Rev.* **D 54**, 3006 (1996).

[27] D.D. Gabbert. Determination of the structure function F_2 at HERMES. DESY-THESIS-2008-041, Dissertation, Universität Hamburg, (2008).

[28] A. Aktas *et al.* (H1). Measurement of the proton structure function F_2 at low Q^2 in QED compton scattering at HERA. *Phys. Lett.* **B 598**, 159 (2004).

[29] S. Chekanov *et al.* (ZEUS). Measurement of the neutral current cross section and F_2 structure function for deep inelastic e^+p scattering at HERA. *Eur.Phys. J.* **C21**, 443 (2001).

[30] J. Breitweg *et al.* (ZEUS). Measurement of the proton structure function F_2 at very low Q^2 at HERA. *Phys. Lett.* **B 487**, 53 (2000).

[31] V. Tvaskis. (JLab). Longitudinal-Transverse Separation of Deep-Inelastic Scattering at low Q^2 on Nucleons and Nuclei. Dissertation, Vrije Universiteit Amsterdam, (2004).

[32] B. Adeva *et al.* (SMC). Spin asymmetries A_1 and structure functions g_1 of the proton and the deuteron from polarized high energy muon scattering. *Phys. Rev.* **D 58**, 112001 (1998).

[33] W.M. Yao *et al.* The Review of Particle Physics. Journal of Physics, **G 33**, 1 (2006).

[34] K. Abe *et al.* (E143). Measurement of $R = \sigma_L/\sigma_T$ for $0.03 < x < 0.1$ and fit to world data. *Phys. Lett.* **B 452**, 194 (1999).

[35] Jr. Callan, Curtis G. and D.J. Gross. High-energy electroproduction and constitution of the electric current. *Phys. Rev. Lett.* **22**, 156 (1969).

[36] B. Adeva *et al.* (SMC). Spin asymmetries A_1 of the proton and the deuteron in the low x and low Q^2 region from polarized high energy muon scattering. *Phys. Rev.* **D 60**, 072004 (1999). Erratum ibid. **D 62**, 079902 (2000).

[37] B. Adeva *et al.* (SMC). A next-to-leading order QCD analysis of the spin structure function g_1. *Phys. Rev.* **D 58**, 112002 (1998).

[38] B. Adeva *et al.* (SMC). Erratum: Spin asymmetries A_1 of the proton and the deuteron in the low x and low Q^2 region from polarized high energy muon scattering. *Phys. Rev.* **D 62**, 07990 (2000).

[39] K.Abe *et al.* (E143). Measurement of the proton and deuteron spin structure functions g_1 and g_2. *Phys. Rev.* **D 58**, 112003 (1998).

[40] P.L. Anthony *et al.* (E155). Measurement of the deuteron spin structure function $g_1^d(x)$ for $1(GeV/c)^2 < Q^2 < 40(GeV/c)^2$. *Phys. Lett.* **B 463**, 339 (1999).

[41] P.L. Anthony *et al.* (E155). Measurement of the Q^2 dependence of the proton and neutron spin structure function g_1^p and g_1^n. *Phys. Lett.* **B 493**, 19 (2000).

[42] K. Ackerstaff *et al.* (HERMES). Measurement of the Neutron Spin Structure Function g_1^n with a Polarized ^{3}He Internal Target . *Phys. Lett.* **B 404**, 383 (1997).

[43] P. Anthony *et al.* (E142). Deep Inelastic Scattering of Polarized Electrons by Polarized ^{3}He and the Study of the Neutron Spin Structure. *Phys. Rev.* **D 54**, 6620 (1996).

[44] K. Abe *et al.* (E154). Precision Determination of the Neutron Spin Structure Function g_1^n. *Phys. Rev. Lett.* **79**, 26 (1997).

[45] K. Ackerstaff *et al.* The HERMES spectrometer. *Nucl. Instrum. Meth.* **A 417**, 230 (1998).

[46] A.A. Sokolov, I.M. Ternov. On polarization and spin effects in the theory of synchrotron radiation. *Phys.Dokl.* **8**, 1203 (1964).

[47] A. Airapetian *et al.* (HERMES). The HERMES polarized hydrogen and deuterium gas target in the HERA electron storage ring. *Nucl. Instrum. Meth.* **A 540**, 68 (2005).

[48] C. Baumgarten *et al.* (HERMES Target Group). An atomic beam polarimeter to measure the nuclear polarization in the HERMES gaseous polarized hydrogen and deuterium target. *Nucl. Instrum. Meth.* **A 482**, 606 (2002).

[49] C. Baumgarten. Aufbau und Kalibration eines Gasanalysators für das HERMES-Wasserstoff target. Diplomarbeit, Universität Hamburg, (1996), HERMES-96-068.

[50] H. Kolster. The HERMES Caseous Internal Polarized Proton Target and its use in the HERA Positron Storage Ring. Dissertation, Ludwig-Maximilians-Universität München, (1998), HERMES-98-009.

[51] A. Nass *et al.* The HERMES polarized atomic beam source. *Nucl. Instrum. Meth.* **A 505**, 633 (2003).

[52] T. Benisch *et al.* The luminosity monitor of the HERMES experiment at DESY. *Nucl. Instrum. Meth.* **A 471**, 314 (2001).

[53] J.D. Jackson. Classical Electrodynamics. John Wiley and Sons, (1975).

[54] W. Wander. Reconstruction of high energy scattering events in the HERMES experiment. PhD thesis, Friedrich-Alexander-Universität Erlangen-Nürnberg, DESY-THESIS-97-31, (1996).

[55] J. Wendland. Polarized Parton Distribution Measured at HERMES Experiment. PhD thesis, Simon Fraser University, DESY-THESIS-2003-032, (2003).

[56] D. Adams *et al.* (SMC). Spin structure of the proton from polarized inclusive deep-inelastic muon proton scattering. *Phys. Rev.* **D 56**, 5330 (1997).

[57] I. Akushevich, H. Böttcher and D. Ryckbosch. RADGEN 1.0: Monte Carlo generator for radiative events in DIS on polarized and unpolarized targets. hep-ph/9906408, (1998).

[58] A. Miller. Applying radiative corrections to rations of cross sections for DIS. unpublished, (2002).

[59] D. Boer, P. J. Mulders. Time-reversal odd distribution functions in leptoproduction. *Phys. Rev.* **D 57**, 5780 (1998).

[60] R. N. Cahn. Azimuthal dependence in leptoproduction: a simple parton model calculation. *Phys. Lett.* **B 78**, 269 (1978).

[61] F. Giordano, R. Lamb. Measurement of azymithal asymmetries of the unpolarized cross section. HERMES Release Report, (2008).

[62] F. Giordano, R. Lamb. Measurement of azymithal asymmetries of the unpolarized cross section at HERMES. *in Proceedings of the 18th International Symposium on Spin Physics*, 225 (2009).

[63] A. Bacchetta *et al.* Semi-inclusive deep inelastic scattering at small transverse momentum. Journal of High Energy Physics, 093 (2007).

[64] C. Amsler *et al.* Particle Data Group. *Phys. Lett.* **B 667**, 1 (2008).

[65] A. Airapetian *et al.* (HERMES). Measurement of Parton Distributions of Strange Quarks in the Nucleon from Charged-Kaon Production in Deep-Inelastic Scattering on the Deuteron. *Phys. Lett.* **B 666**, 446 (2008).

[66] T. Sjöstrand *et al.* High-energy-physics event generation with PYTHIA 6.1. Comput. Phys. Commun. **135**, 238 (2001).

[67] T. Sjöstrand, L. Lönnblad, S Mrenna and P. Skands. PYTHIA 6.3: Physics and manual. hep-ph/0308153, (2003).

[68] T. Sjöstrand. High-energy-physics event generation with PYTHIA 5.7 and JETSET 7.4. Comput. Phys. Commun. **82**, 74 (1994).

[69] A. Hillenbrand. Measurement and Simulation of the Fragmentation process at HERMES. PhD thesis, Friedrich-Alexander-Universität Erlangen-Nürnberg, DESY-THESIS-2005-035, (2005).

[70] J. G. Rubin. Polarization, Motion and Fragmentation: Exploring the Role of Quarks in the Nucleon Through Semi-Inclusive Longitudinal Spin Asymmetries as HERMES. PhD thesis, DESY-THESIS-2009-045, (2009).

[71] S. J. Brodsky, D. S. Hwang, I. Schmidt. Final-state interactions and single-spin asymmetries in semi-inclusive deep inelastic scattering. *Phys. Lett.* **D 530**, 99 (2002).

[72] J. C. Collins. Leading-twist single-transverse-spin asymmetries: Drell-Yan and deep-inelastic scattering. *Phys. Lett.* **D 536**, 43 (2002).

[73] P. E. Bosted. Factorization and transverse Momentum in SIDIS at JLab. *Nucl. Phys.* **A 782**, 142 (2007).

[74] S. Kretzer. Fragmentation functions from flavor-inclusive and flavor-tagged e^+e^- annihilations. *Phys. Rev.* **D 62**, 054001 (2000).

[75] D. de Florian, R. Sassot, M. Stratmann. Global analysis of fragmentation functions for pions and kaons and their uncertainties. *Phys. Rev.* **D 75**, 114010 (2007).

[76] E. Leader. The longitudinal spin structure of the nucleon. Proceedings of the International school of physics "Enrico Fermi", Course CLXVII, 263 (2008).

[77] Y. Goto *et al.* Polarized parton distribution function in the nucleon. *Phys. Rev.* **D 62**, 034017 (2000).

[78] S. L. Adler. Axial-Vector Vertex in Sinor Electrodynamics. *Phys. Rev.* **177**, 2426 (1969).

[79] M. Glück, E. Reya, M. Stratmann, W. Vogelsang. Models for the polarized parton distributions of the nucleon. *Phys. Rev.* **D 63**, 094005 (2001).

[80] A. Airapetian *et al.* (HERMES). Measurement of the proton spin structure function g_1^p with a pure hydrogen target. *Phys. Lett.* **B 442**, 484 (1998).

[81] L. Frankfurt *et al.* The valence and strange-sea quark spin distributions in the nucleon from semi-inclusive deep inelastic scattering. *Phys. Lett.* **B 230**, 141 (1989).

[82] M. Alekseev *et al.* (COMPASS). The polarized valence quark distribution from semi-inclusive DIS. *Phys. Lett.* **B 660**, 458 (2008).

[83] M. Anselmino, A. Efremov, A. Kotzinian, B. Parsamyan. Transverse momentum dependence of the quark helicity distributions and the Cahn effect in double-spin asymmetry A_{LL} in semi-inclusive DIS. *Phys. Rev.* **D 74**, 074015 (2006).

[84] S. J. Brodsky, M. Burkardt, I. Schmidt. QCD constraints on the shape of polarized quark and gluon distributions. *Nucl. Phys.* **B 441**, 197 (1995).

[85] M. Alekseev *et al.* (COMPASS). Flavour Separation of Helicity Distributions from Deep Inelastic Muon-Deuteron Scattering. *Phys. Lett.* **B 680**, 217 (2009).

Acknowledgements

This work could not have been completed without the help of many people.

I would like to express my gratitude to Stanislav Belostotski, who gave me the opportunity to join the analysis group at HERMES.

I would like to thank my advisor Elke Aschenauer, who helped me a lot in understanding HERMES physics and data analysis. Even being overloaded with other tasks, she always found time to answer my questions about HERMES. I am grateful to Elke for her relation to my family and especially to my son. Days when Quax was at DESY were the happiest ones for Dima.

This thesis would have not been possible without my co-workers in the Δq group: Naomi Makins and Josh Rubin. Josh was the one I worked in closer contact with, and we were able to carry on the analysis even being separated by eight time zones. Mutual cross checking between us was very useful for improvements in the analysis.

It has been a great pleasure to work with Delia Hasch, Caroline Riedl, Francesca Giordano, Charlotte Van Hulse and Armine Rostomyan. My special thanks go to Ami and Elke for careful reading of and giving advises for the thesis.

I am very grateful to my doctoral advisor, Professor Klaus Rith, for his support and the excellent combination of freedom and guidance which he gave me during my work on this thesis over the last years. I am thankful to HERMES management, Klaus Rith and Yorck Holler in particular, for possibility to have a very nice office in Bld.36. Together with my son we did a lot of work there.

And last but not least I want to express my deepest gratitude towards my family and friends. Towards Prof.Nikolaj Nikolaev and his wife Lyudmila, thanks for all the lovely dinners and support in difficult situations. Towards Peter Kravtsov and Alexander Vassiliev, who put a lot of happy moments in my life. Towards my parents for their love and the wise decision not to stir to me to become the physicist.

The main words I would like to tell to my beloved husband and my son, the most important two persons in my life. I am forever grateful to Sasha. It is important, that he believed that "I can manage" even when I was not even sure. His care and support were the main components of my succesful work. Thanks to my son for his interest in my work and for his patience. I will never forget the first letter he wrote me during my collaboration meeting talk in 2a/2 in 2004.

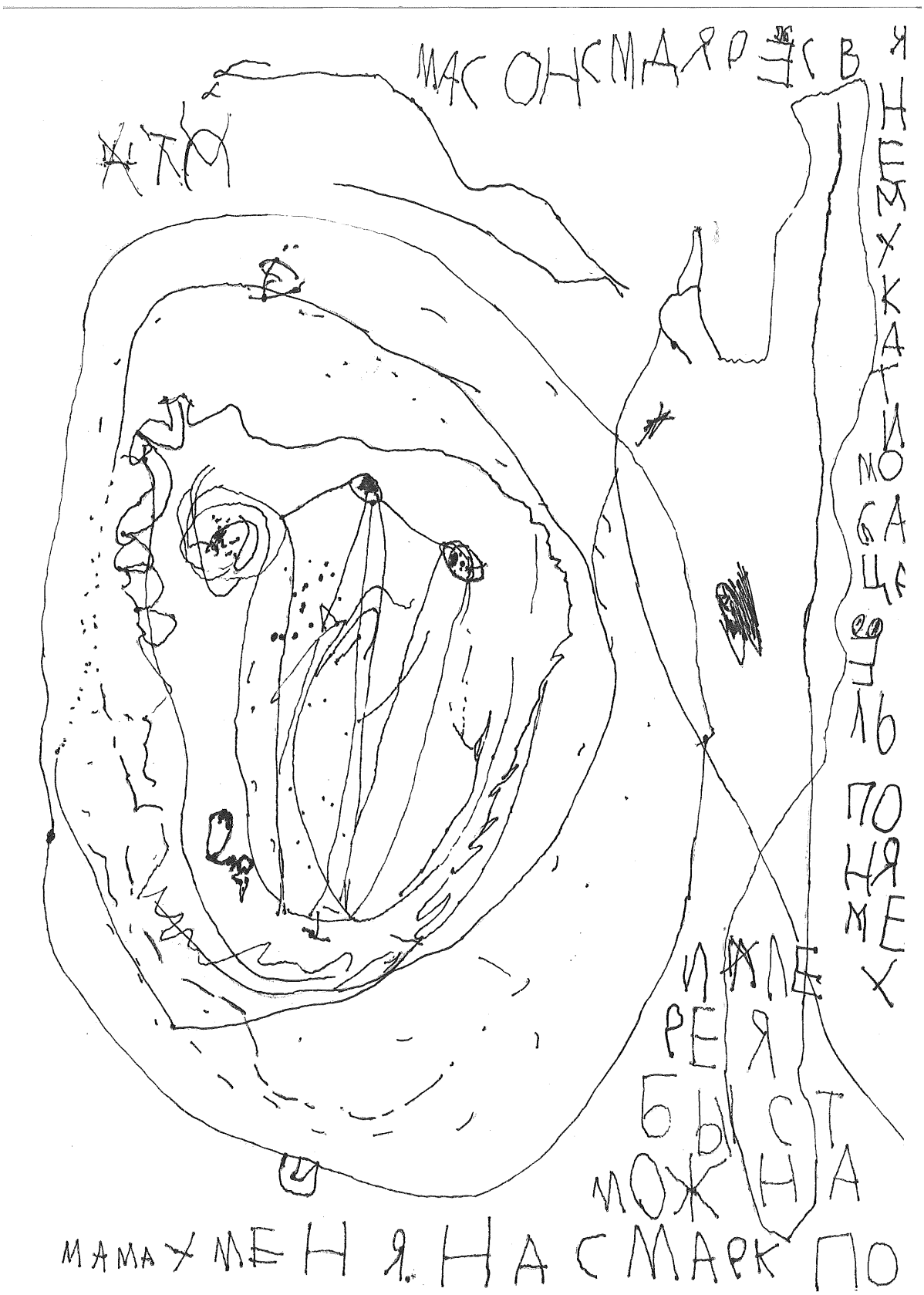
МАС ОНСМАЯРЭГВ
ЯНЕМХКАТИ
МОСАЦ
ЛЬ
ПОНЯМЕХ
ИЛЕ
РЕЯ
БЫСТ
МОЖНА
МАМАХМЕНЯ НАСМАРК ПО